

The University of Nottingham
School of Physics & Astronomy



**INVESTIGATION OF STRUCTURAL AND OPTICAL
PROPERTIES OF DILUTE GaAsBi AND InGaAsBi
SEMICONDUCTOR NANOSTRUCTURES GROWN BY
MOLECULAR BEAM EPITAXY**

by

AMRA ALI ABUTALIB ALHASSNI

M. Sc (Physics of Materials)

Thesis submitted to the University of Nottingham

for the degree of Doctor of Philosophy

February 2023

ABSTRACT

This thesis investigates the optical and structural properties of GaAs_{1-x}Bi_x thin epitaxial layers and self-assembled InGa(Bi)As quantum dots (QDs) grown on conventional (100) GaAs substrates by Molecular Beam Epitaxy (MBE). The GaAs_{1-x}Bi_x epilayers were grown at different substrate temperatures. The InGa(Bi)As QDs were formed via the Stranski-Krastanov (S-K) growth mode using bismuth as a surfactant.

Photoluminescence (PL) measurements showed that the GaAs_{1-x}Bi_x PL spectra exhibit two different behaviours depending on the growth temperature, namely, red and blue shift were observed as the growth temperature increases from 300 °C to 325 °C, and from 325 °C to 365 °C, respectively. Moreover, the Bi composition in the studied samples were determined and calculated from the PL data. The results showed that Bi incorporation into the GaAs host lattice is very sensitive to the growth temperature and varied from 2.3% to 4.7%, and from 4.7 % to 2.8% for a growth temperature in the range 300 °C - 325°C and 325 °C - 365 °C, respectively. These findings were supported by Scanning Electron Microscopy (SEM) results which showed that the samples with the highest surface concentrations of droplets are those with the lowest concentrations of Bi (samples grown at T_G= 300 °C, 310 °C and 365 °C). This means that for these growth temperatures a lower concentration of Bi was incorporated into the GaAs structure. However, the sample with the highest concentration of bismuth (4.7%) which was grown at 325 °C, showed a lower number of both surface droplets and self-aligned trailing nanotracks. These results are also consistent with Raman measurement which demonstrated that as the content of Bi increases, first there is a slight redshift and

then a blueshift of the longitudinal optical (LO) phonon peak, which can be explained by the Bi-induced tensile and/or compressive stress. The optimum growth temperature for maximum Bi incorporation was found to be 325 °C (4.7%). The integrated PL intensity as a function of inverse temperature confirmed two types of defects. The first type is related to lattice disorder and the other related to Bi clusters.

The effect of gamma radiation dose on the structural and optical properties of dilute GaAs_{1-x}Bi_x thin epitaxial layers grown at different substrate temperatures by MBE on conventional (100) GaAs was also investigated. This study investigates the interaction of gamma radiation with GaAs_{1-x}Bi_x III-V semiconductor alloys, which have enormous potential use in ionizing radiation detectors that can be monitored through both optical and electrical measurements. From Raman measurements, it was found that the concentration of holes increased when the samples were irradiated. This result is in good agreement with the PL results, which showed that the intensity of the main peak increases after irradiation, indicating that the optical properties have improved for all samples. Furthermore, the X-ray diffraction (XRD) data demonstrated that for irradiated GaAs_{1-x}Bi_x samples, their crystallographic quality was slightly worse after irradiation. This is due to the fact that radiation induces several types of defects, including structural defects. This result is consistent with PL results, which demonstrated that GaAs_{1-x}Bi_x samples have the largest PL full width at half maximum (FWHM) for all irradiated samples. This finding demonstrates that irradiated samples have worse quality compared to non-irradiated samples.

The effects of gamma radiation dose (30 kGy and 50 kGy) on self-assembled InGaAs/GaAs QDs formed at various growth temperatures ($T_G = 510\text{ }^\circ\text{C}$, $482\text{ }^\circ\text{C}$, $450\text{ }^\circ\text{C}$) with and without exposure to bismuth flux have been investigated. The PL results showed that for irradiation dose of 30 kGy, the QDs PL emission energy exhibit a blue shift of around 10 meV for sample grown without Bi, however, no blue shifts are detected in the PL of QDs for all samples grown with Bi surfactant at different growth temperatures. Interestingly, the PL emissions of QDs and wetting layers disappeared after the irradiation dose was increased to 50kGy for a sample grown without Bi. In contrast, for samples grown with a Bi surfactant the PL QDs emissions were still observed, however, their intensities were reduced by factors between 1.5 to 2. In general, gamma radiation treatment has better effect on the QDs samples grown under a Bi flux than the samples grown without Bi. The particular radiation dose of 30 kGy resulted in an improvement of the optical properties of all samples grown with Bi as a surfactant, as evidenced by a large increase in the QDs PL intensity after radiation. Furthermore, a growth temperature of $510\text{ }^\circ\text{C}$ for InGaAs QDs was found to be optimal for both as-grown and gamma irradiated samples in terms of optical efficiency.

PUBLICATIONS

1. Dilute GaAs_{1-x}Bi_x epilayers grown at different growth temperatures by Molecular Beam Epitaxy: Potential application as gamma-radiation sensors.
[Amra Alhassni](#), Jorlandio F. Felix, John Fredy, Sultan Alhassan, Haifa Alghamdi, Amjad Almunyif, Mohamed Henini. Submitted to Applied Surface Science (2023).
2. Investigation of the effect of gamma radiation on the electrical and optical properties of dilute GaAs_{1-x}Bi_x grown on Molecular Beam Epitaxy.
Sultan Alhassan, Faisal S Al Mashary, Jorlandio Francisco Felix, Walter de Azevedo, [Amra Alhassni](#), Amjad Almunyif, Saud Alotaibi, Abdulaziz Almalki, Maryam Alhuwayz, Haifa Alghamdi, Noor Al Saqri, Igor P. Kazakov, Hind Albalawi, and Mohamed Henini. Submitted to Radiation Physics and Chemistry (2023).
3. Effect of substrate materials on the electrical properties of self-assembled InAs quantum dot-based laser structures.
Al Huwayz, DA Jameel, S Alotaibi, S Alhassan, A Almalki, N Al Saqri, Y Al Saleh, [Amra Alhassni](#), A Almunyif, OM Lemine, A Salhi, M Henini
Applied physics A (2023)

4. Effect of bismuth surfactant on the structural, morphological and optical properties of self-assembled InGaAs quantum dots grown by Molecular Beam Epitaxy on GaAs (001) substrates.

Haifa Alghamdi, [Amra Alhassni](#), Sultan Alhassan, Amjad Almunyif, Alexey V. Klekovkin, Igor N. Trunkin, Alexander L. Vasiliev, Helder V. A. Galeti, Yara Galvão Gobato, Igor P. Kazakov, Mohamed Henini. Journal of Alloys and Compounds **905**, 164015 (2022).

5. Optical properties of self-assembled InAs quantum dots based P-I-N structures grown on GaAs and Si substrates by Molecular Beam Epitaxy.

M. Al Huwayz, H.V.A Galeti, OM Lemine, KH Ibnaouf, A Alkaoud, Y Alaskar, A Salhi, S Alhassan, S Alotaibi, A Almalki, A Almunyif, [Amra Alhassni](#), DA Jameel, Y Galvão Gobato, M Henini. Journal of Luminescence 251, 119155 (2022).

6. Investigation of the effect of substrate orientation on the structural, electrical and optical properties of n-type GaAs_{1-x}Bi_x layers grown by Molecular Beam Epitaxy.

Sultan Alhassan, Daniele de Souza, [Amra Alhassni](#), Saud Alotaibi, Abdulaziz Almalki, Maryam Alhuwayz, Igor P. Kazakov, Elkhan. M. Pashaev, Alexey V. Klekovkin, Sergio Souto, Yara Galvão Gobato, Noor Al Saqri, Helder Vinicius Avanço Galeti, Faisal S Al Mashary, Hind Albalawi, Norah Alwadai, and Mohamed Henini. Journal of Alloys and Compounds **885**, 161019 (2021).

7. Structural and optical properties of n-type and p-type GaAs_(1-x)Bi_x thin films grown by molecular beam epitaxy on (311)B GaAs substrates.

Daniele de Souza, Sultan Alhassan, Saud Alotaibi, **Amra Alhassni**, Amjad Almuniyif, Igor P. Kazakov, Alexey V. Klekovkin, Sergey A. Zinov'ev, Igor A. Likhachev, Elkhan. M. Pashaev, Sergio Souto, Yara Galvão Gobato, Helder Vinicius Avanço Galeti, Mohamed Henini. *Semiconductor Science and Technology* **36**, 075018 (2021).

8. Effect of thermal annealing on the optical and structural properties of (311)B and (001) GaAsBi/GaAs single quantum wells grown by MBE.

Haifa Alghamdi, Vanessa Orsi Gordo, Martin Schidbauer, Jorlandio F. Felix, Sultan Alhassan, **Amra Alhassni**, Gabriela Augusta Prando, Horacio Coelho-Junior, Mustafa Gunes, Helder Vinicus Avanco Galeti, Yara Galvao Gobato, and Mohamed Henini. *Journal of Applied Physics* 127, 125704 (2020).

9. The effect of strain and spatial Bi distribution on the band alignment of GaAsBi single quantum well structure.

M. Gunes, O. Donmez, G. Gumus, A. Erol, H. Alghamdi, S. Alhassan, **Amra Alhassni**, S. Alotaibi, M. Schmidbauer, H.V.A Galeti, M. Henini. *Physica B: Physics of Condensed Matter* **602**, 412487 (2020)

10. Raman spectroscopy of GaSb_{1-x}Bi_x alloys with high Bi content.

I Ammar, N Sfina, M Fnaiech, Fangxing Zha, Qiuying Zhang, Haoguang Dai, Xiaolei Zhang, Li Yue, Shumin Wang, Jun Shao, GB Stringfellow,

Daniele De Souza, Sultan Alhassan, Saud Alotaibi, **Amra Alhassni**, Amjad Almunyif, Hind Albalawi, Igor P Kazakov, Alexey V Klekovkin, Sergey A ZinovEv, Igor A Likhachev, Elkhan M Pashaev, Sergio Souto, Yara Galvão Gobato, Helder Vinicius Avanço Galeti, Mohamed Henini. Applied Physics Letters **20**, 202103(2020).

11. Investigation of Deep Defects and Their Effects on the Properties of NiO/B- Ga₂O₃ Heterojuncion Diodes.

Abdulaziz Almalki, Labeled Madani, Nouredine Sengouga, Sultan Saleh Alhassan, Saud Alotaibi, **Amra Alhassni**, Amjad Almunyif, Jasbinder Chauhan, Mohamed Henini, Helder Vinicius Avanço Galeti, Yara Galvão Gobato, Marcio Peron Franco de Godoy, Marcelo Barbosa de Andrade, Sérgio Souto, Hong Zhou, Boyan Wang, Ming Xiao, Yuan Qin, Yuhao Zhang. (In progress).

CONFERENCE PRESENTATIONS

POSTER PRESENTATIONS

- The Effect of Bismuth (Bi) as Surfactant on the Optical Properties of InAs/In(Bi)As Single Quantum Dots Grown on (100) GaAs Substrate.
The 10th International Workshop on Bismuth-Containing Semiconductors, Toulouse, France, July 21-24 (2019).
- Optical properties of In(Bi)As QDs grown on GaAs (100) substrates.
11th International Conference on Quantum Dots (QD2020), Munich, Germany, December 7 -11 (2020).
- The Effect of the Growth Rate on the Optical Properties of Self-Assembled InAs Quantum Dots Grown by Molecular Beam Epitaxy on GaAs (100) Substrates.
12th International Conference “Nanomaterials: Applications & Properties (IEEE NAP-2022)”, that was held in Kraków, Poland on September 11-16, 2022.

ACKNOWLEDGEMENTS

“All praise is due to Allah, the Lord of the Worlds”

I would like to express my sincere gratitude to my supervisor, Prof. **Mohamed Henini**, for the continuous support of my Ph.D study and research, for his patience, motivation, enthusiasm, and immense knowledge. His guidance and advice were invaluable during the research and writing of this thesis. Also, I owe him a debt of gratitude for providing me with different opportunities during my PhD, such as attendance at international conferences where I presented my work and explored collaborations with a variety of groups from around the world independently and confidently.

I would like to express my gratitude to the **Saudi Cultural Bureau** in the United Kingdom and the **Higher Education Ministry** in Saudi Arabia for awarding me an Overseas PhD Scholarship and for their generous funding. This opportunity would not have been possible without their assistance. In addition, I would like to express my gratitude to **Al-Baha University** in Saudi Arabia for providing me with financial assistance during my PhD studies at the University of Nottingham.

I would like to thank all my collaborators; Prof. **Jorlandio F. Felix** (University of Brasilia, Brazil) for exposing my samples to gamma radiation and for XRD and Raman characterization and for useful discussions, Prof. **Igor Kazakov** (Lebedev Physical Institute, Moscow, Russia) for providing me with samples investigated in this thesis, Prof. **Helder Galeti** (Federal University of São Carlos, Brazil) for his helpful support to learn PL technique; and all other collaborators named in the

publications list. Also I would like to express my gratitude to all my colleagues in the School of Physics and Astronomy for their support and friendship during my PhD studies.

Most importantly, I would like to thank my beloved mother **Rahmah Alhassni** and beloved father **Ali Alhassni** who believed and supported me in realizing my dream, and deepest gratitude to my brothers **Mohamed, Abutalib and Hussain** and my sisters for sharing this journey with me from the beginning to the end. Without their encouragement and support, I would not be able to complete this journey.

Finally, I would like to express my gratitude to my husband, **Abutalib**, and to my little angel daughter, **Diyala**, for patience and understanding throughout my research. Without their help, love and care, I would not have the ability to succeed. Thank you is not enough for always believing in my ability to succeed and for accompanying me during this journey.

TABLE OF CONTENTS

CHAPTER 1: INTRODUCTION	1
1.1 INTRODUCTION.....	1
1.2 MOTIVATION	3
1.3 SCHEME OF THE THESIS	5
REFERENCES.....	7
CHAPTER 2: FUNDAMENTAL CONCEPTS AND PRINCIPLES OF SEMICONDUCTORS	11
2.1 INTRODUCTION.....	11
2.2 INTRINSIC AND EXTRINSIC SEMICONDUCTORS	15
2.3 ENERGY BANDGAP	18
2.4 CRYSTAL STRUCTURE OF SEMICONDUCTORS.....	20
2.4.1 Types of Basic Lattice.....	22
2.4.2 Miller Indices for Crystal Planes.....	26
2.4.3 Conventional and Non-Conventional Planes	28
2.5 DIRECT AND INDIRECT ENERGY BANDGAP.....	30
2.6 EFFECT OF TEMPERATURE ON ENERGY BANDGAP	32
2.7 MODIFICATION OF BAND STRUCTURE.....	33
2.7.1 Alloys	33
2.7.1.1 Vegard's Law	35
2.7.1.2 Graded Gap Semiconductor Structures.....	35

2.7.2	Heterostructures.....	36
2.7.2.1	Band Alignment	37
2.7.2.1.1	Straddled Alignment or Type I.....	37
2.7.2.1.2	Staggered Alignment or Type II.....	37
2.7.2.1.3	Broken Gap Alignment or Type III	38
2.7.2.2	Anderson’s rule	38
2.8	GENERAL PROPERTIES OF SELECTED SEMICONDUCTORS MATERIALS INVESTIGATED IN THIS WORK.....	40
2.8.1	Gallium Arsenide (GaAs).....	40
2.8.2	Indium Gallium Arsenide (InGaAs).....	43
2.8.3	Dilute Bismide Materials.....	44
2.8.4	Properties of InGaBiAs	46
2.9	Optical properties of semiconductors.....	48
2.10	Absorption Processes	48
	REFERENCES.....	51
	CHAPTER 3: THE OPTICAL PROPERTIES AND GROWTH OF LOW DIMENSIONAL SEMICONDUCTOR STRUCTURES.....	57
3.1	INTRODUCTION.....	57
3.2	QUANTUM CONFINEMENT.....	59
3.3	DENSITY OF STATES	59
3.4	OPTICAL PROCESSES IN LOW DIMENSIONAL SEMICONDUCTOR STRUCTURES	62

3.4.1	Absorption in Semiconductor Nanostructures	62
3.4.2	Photoluminescence Process in Nanostructures	62
3.5	CARRIER DYNAMICS IN LOW DIMENSIONAL SEMICONDUCTOR STRUCTURES	65
3.6	EPITAXIAL GROWTH OF LOW DIMENSIONAL SEMICONDUCTOR STRUCTURES	66
3.6.1	Molecular Beam Epitaxy.....	67
3.6.2	MBE Growth of Bi Based III-V Structures.....	69
3.6.3	Growth of Quantum Well Structures.....	70
3.6.4	Growth of Quantum Wires	72
3.6.5	Growth of Quantum Dots	73
	REFERENCES	77
	CHAPTER 4: EXPERIMENTAL TECHNIQUES.....	80
4.1	PHOTOLUMINESCENCE.....	80
4.1.1	Principles of Photoluminescence.....	80
4.1.2	System Hardware Implementation	87
4.1.2.1	Spectrometer and Detectors	88
4.1.2.2	Lasers and Optics	90
4.1.2.3	Cryostat and Temperature Controller	91
4.1.2.4	Computer Interface	92
4.1.2.5	System Controlling Software	92
4.1.3	Photoluminescence Measurements.....	92

4.2	STRUCTURAL CHARACTERIZATION	93
4.2.1	X-ray Diffraction	93
4.2.1.1	Principle of XRD	93
4.2.2	Scanning Electron Microscopy (SEM).....	96
4.2.3	Raman Spectroscopy	97
	REFERENCES	100
CHAPTER 5: THE EFFECT OF GROWTH TEMPERATURE ON THE		
STRUCTURAL AND OPTICAL PROPERTIES OF DILUTE GaAs_{1-x}Bi_x		
EPILAYERS GROWN BY MOLECULAR BEAM EPITAXY102		
5.1	INTRODUCTION.....	102
5.2	EXPERIMENTAL DETAILS.....	105
5.3	RESULTS AND DISCUSSION	107
5.3.1	Structural Characteristics	107
5.3.1.1	X-ray Diffraction (XRD)	107
5.3.1.2	Scanning Electron Microscopy (SEM)	109
5.3.2	Optical Properties	111
5.3.2.1	Raman Spectroscopy.....	111
5.3.2.2	Photoluminescence.....	115
5.3.2.2.1	Low-Temperature Photoluminescence of GaAs _(1-x) Bi _x Thin Film Samples.....	115
5.3.2.2.2	Excitation Power Dependence of Photoluminescence of GaAs _(1-x) Bi _x Epilayers Grown at Different Growth Temperatures	123

5.3.2.2.3	Temperature Dependence Of Photoluminescence of GaAs _(1-x) Bi _x Thin Films Grown At Different Temperatures	126
5.4	CONCLUSION	134
	REFERENCES	136
 CHAPTER 6: INVESTIGATION OF THE EFFECT OF GAMMA RADIATION ON THE STRUCTURAL AND OPTICAL PROPERTIES OF DILUTE GaAs_{1-x}Bi_x EPILAYERS GROWN AT DIFFERENT GROWTH TEMPERATURES BY MOLECULAR BEAM EPITAXY		
6.1	INTRODUCTION	143
6.2	SAMPLE DETAILS	144
6.3	RESULTS AND DISCUSSION	145
6.3.1	Structural Characteristics	145
6.3.2	Optical Properties	146
6.3.2.1	Raman Measurements	146
6.3.2.2	Photoluminescence	149
6.4	CONCLUSION	163
	REFERENCES	166
 CHAPTER 7: INVESTIGATION OF THE EFFECT OF GAMMA RADIATION ON THE OPTICAL PROPERTIES OF SELF-ASSEMBLED InGaAs QUANTUM DOTS GROWN ON (100) GaAs SUBSTRATES BY MOLECULAR BEAM EPITAXY USING BISMUTH AS A SURFACTANT		
7.1	INTRODUCTION	170

7.2	SAMPLE DETAILS.....	172
7.3	RESULTS AND DISCUSSION	176
7.3.1	Effect of Bismuth as a Surfactant and Gamma Radiation on the Optical Properties of InGa(Bi)As Quantum Dots	176
7.3.2	Effect of Growth Temperatures and Gamma Radiation on the Optical Properties of InGa(Bi)As Quantum Dots	186
7.4	CONCLUSION	196
	REFERENCES.....	198
	CHAPTER 8: CONCLUSIONS AND FUTURE WORK.....	203
8.1	GaAsBi EPILAYERS.....	203
8.2	InGaAs QUANTUM DOTS.....	204
8.3	FUTURE WORK SUGGESTIONS	205
	REFERENCES	209

CHAPTER 1: INTRODUCTION

This chapter will provide a brief introduction to the semiconductor materials investigated in this work, and the motivation and the outline of the thesis.

1.1 INTRODUCTION

Numerous materials, including III-V compound semiconductors (such as GaAs or InP), elemental semiconductors (such as Si), dominate the modern photonics and microelectronics markets, respectively [1, 2]. Recent studies have shown that the majority of semiconductor devices are fabricated on silicon (Si) [3]. However, Si has some fundamental limitations, including an indirect bandgap that affects photon emission efficiency and lower carrier mobility. However, GaAs is considered as one of the most central semiconductor material amongst the III-V compounds for research investigations due to its superior semiconducting properties. For example, GaAs has a direct bandgap of 1.42 eV at room temperature and higher carrier mobility. These properties provide a wide range of applications in the fields of optoelectronic devices for both light detection and light emitting, and high-speed transistors [4]. One of the most important properties of GaAs is the ability to tailor its bandgap through the formation of ternary compounds (e.g., $\text{GaAs}_{1-x}\text{Bi}_x$, $\text{Al}_x\text{Ga}_{1-x}\text{As}$, $\text{In}_x\text{Ga}_{1-x}\text{As}$). Indeed, the III-V compound semiconductors and their ternary or quaternary (e.g., $\text{Ga}_x\text{In}_{1-x}\text{Al}_y\text{N}_y$) alloys provide a wide range of bandgap energies, which are especially important when a specific bandgap energy is required. These properties enable III-V semiconductors to be used in photonic devices such as laser diodes, optical detectors, and solar cells. In addition, the interest in the III-V compound semiconductors has been increasing since their first commercial advent in the early 1980's, particularly in the non-equilibrium growth techniques such as

molecular beam epitaxy (MBE) which offers enormous tailoring capabilities for device fabrication by forming compound materials from these semiconductors [5]. These compounds are usually grown in heterojunction systems as epitaxial layers on substrates such as GaAs or InP e.g., $\text{GaAs}_{1-x}\text{Bi}_x$ on GaAs, or $\text{Ga}_x\text{In}_{1-x}\text{As}_y\text{N}_{1-y}$ on InP. The mismatch between the lattice constants of the epitaxial layer and the substrate is one of the most important parameters that must be considered during the epitaxial growth of heterostructures. A large lattice mismatch causes dislocations in the epitaxial layer.

GaAs is also used as a substrate material for the epitaxial growth of many III-V semiconductors such as GaAsBi and InGaAs. The properties of GaAs have a significant impact on the following properties and epitaxial layer growth. Another property of GaAs is that its bandgap energy can be tuned by introducing a small amount of bismuth. As a result, dilute bismide GaAsBi is formed. As it is well-known, bismuth is the heaviest element in the Group V of the periodic table, and it is not commonly used in device fabrication. Furthermore, using Bi as a surfactant during the growth of GaAs at low temperatures has proven to enhance surface migration, to reduce the density of defects and to suppress the formation of traps in GaAs. Additionally, the growth of epitaxial layers on the conventional plane (100) GaAs substrates using different growth temperatures has generated a wealth of information on the growth mechanisms of epitaxial layers. In fact, the use of different growth temperatures for the growth of epitaxial semiconductor alloys has a major effect on their properties. In particular, the structural and optical properties of III-V compound semiconductor structures are found to change and/or improve by growing at different temperatures. Photoluminescence and Raman methods are used to investigate the optical properties of semiconductor alloys. The study

presented in this thesis relates to the characterization of semiconductor alloys based on III-V semiconductors, namely GaAsBi epilayers and $\text{In}_{0.52}\text{Ga}_{0.48}\text{As}$ quantum dots grown on (100) GaAs substrate, using optical and structural methods.

1.2 MOTIVATION

$\text{GaAs}_{1-x}\text{Bi}_x$ alloys are a new class of emerging III-V semiconductors which have attracted an increasing interest [6, 7] because their bandgaps can be engineered for numerous potential applications in electronics, photonics and spintronic. A few percent of Bi incorporated into GaAs, i.e. $\text{GaAs}_{1-x}\text{Bi}_x$ with x being the Bi composition, leads to a giant bowing in the bandgap energy (~ 88 meV/% Bi) [8], as well as an increase of the spin-orbit band splitting [9, 10]. These remarkable properties such as reduction of the bandgap make GaAsBi a suitable material for several device applications such as multi-junction solar cells [11], photonic devices [8] and long-wavelength optoelectronic devices [12]. It is well known that the growth temperature of III-V alloys can significantly influence their crystalline quality. In fact, substitutional incorporation of Bi into the host lattice of III-V compounds requires low growth temperatures. However, the growth of $\text{GaAs}_{1-x}\text{Bi}_x$ is more complicated than the growth of conventional III-V alloys. This is mainly due to the high tendency of Bi to surface segregate during growth, which requires the growth temperature to be lowered to < 400 °C [13]. Epitaxial growth of III-V compounds at low growth temperatures causes an increased density of defects as well as it leads to degradation of the optical quality of the alloys [13]. The purpose of this study is to investigate the effect of the growth temperature (ranging from 300 °C to 365 °C) on the optical and structural properties of $\text{GaAs}_{1-x}\text{Bi}_x$ thin

epitaxial films grown on semi-insulating (100) GaAs substrates by MBE by using different techniques such as scanning electron microscopy (SEM), X-ray diffraction (XRD), Photoluminescence (PL), Raman spectroscopy and hole concentration measurements (Chapter 5).

The second motivation of this work involves an investigation of the effect of gamma radiation (γ) dose on the structural and optical properties of the above GaAs_{1-x}Bi_x samples using the same experimental techniques (Chapter 6).

Furthermore, self-assembled InGaAs quantum dots (QDs) grown on (100) GaAs have allowed for significant advances in optoelectronic devices [14-17]. However, further advancements in QD-based devices are needed to control QD size, uniformity, and density, all of which affect QD electronic states. QD density and size are influenced by a variety of growth conditions such as substrate temperature, growth interruptions, and growth rate [18-21]. Increasing the substrate temperature during QD growth, for example, usually results in larger QDs due to an increase in the In adatom diffusion length. Another method for controlling QD size and density during growth is to use a surfactant [22]. Bi is a good surfactant because the larger Bi atoms do not incorporate into the InAs QDs or the surrounding GaAs matrix. Bi atoms, acting as a surfactant, can smoothen the GaAs surface and interfaces of heterostructures during growth. Additionally, they reduce point defects and impurities in the matrix, which reduces non-radiative recombination centres and improves the optical properties of matrix materials [23]. In addition, when a semiconductor is exposed to high-energy radiation, vacancies, clusters of defects, and dislocations are produced as lattice defects, which could modify the material parameters and hence the properties of devices such as p-i-n detectors and solar

cells. For example, detector devices are commonly subjected to high radiation doses, and the material radiation tolerance is an important factor to consider when selecting detector materials. Therefore, in this work, the effects of gamma radiation doses (30 KiloGray (kGy) and 50 kGy (1Gy= J/Kg)) and Bi surfactant on the optical properties of self-assembled $\text{In}_x\text{GaAs}_{1-x}$ QDs grown at different growth temperatures on (100) GaAs substrates have also been studied (Chapter 7).

1.3 SCHEME OF THE THESIS

The thesis is structured as follows:

Chapter 1 covers the research motivations and structure of the thesis.

Chapter 2 presents a description of the fundamental concepts of semiconductors, including their crystal structures and the optical processes, the concept of the bandgap, the nature of the energy gap and some general properties of GaAs, GaAsBi and InGa(Bi)As. Additionally, the properties of heterostructures are also discussed.

Chapter 3 offers information on the fundamental concepts of low-dimensional semiconductor structures, such as their fabrication by molecular beam epitaxial and characteristics.

Chapter 4 describes the experimental methods and techniques that were used in this study including X-ray diffraction (XRD), scanning electron microscopy (SEM), Raman and photoluminescence (PL) spectroscopy techniques.

Chapter 5 presents PL, XRD, Raman and SEM results, obtained on a set of $\text{GaAs}_{1-x}\text{Bi}_x/\text{GaAs}$ epilayers grown at different growth temperatures on (100) GaAs substrates.

Chapter 6 reports the effect of gamma radiation dose on the optical and structural properties of $\text{GaAs}_{1-x}\text{Bi}_x$ epilayer grown at different growth temperatures on (100) GaAs substrates using XRD, hole concentration measurements, Raman spectroscopy and PL techniques.

Chapter 7 presents the effects of Bi as surfactant and gamma radiation doses on the optical properties of $\text{In}_x\text{GaAs}_{1-x}$ QDs grown at different growth temperatures on (100) GaAs substrate using PL spectroscopy.

Chapter 8 includes a summary of the work presented in this thesis as well as suggestions for future research.

REFERENCES

- [1] D. Liang, J.E. Bowers, Recent progress in lasers on silicon, *Nature photonics*, **4**, 511-517 (2010).
- [2] Z. Zhou, B. Yin, J. Michel, On-chip light sources for silicon photonics, *Light: Science & Applications*, **4**, e358-e358 (2015).
- [3] Y.B. Bolkhovityanov, O.P. Pchelyakov, GaAs epitaxy on Si substrates: modern status of research and engineering, *Physics-Uspekhi*, **51**, 437 (2008).
- [4] S. Adachi, *Properties of semiconductor alloys: group-IV, III-V and II-VI semiconductors*, John Wiley & Sons, 2009.
- [5] H. Ünlü, A thermodynamic model for determining pressure and temperature effects on the bandgap energies and other properties of some semiconductors, *Solid-state electronics*, **35**, 1343-1352 (1992).
- [6] D. Cooke, F. Hegmann, E. Young, T. Tiedje, Electron mobility in dilute GaAs bismide and nitride alloys measured by time-resolved terahertz spectroscopy, *Applied physics letters*, **89**, 122103 (2006).
- [7] K. Oe, Characteristics of semiconductor alloy GaAs_{1-x}Bi_x, *Japanese Journal of Applied Physics*, **41**, 2801 (2002).
- [8] S. Francoeur, M.-J. Seong, A. Mascarenhas, S. Tixier, M. Adamcyk, T. Tiedje, Band gap of GaAs_{1-x}Bi_x, $0 < x < 3.6\%$, *Applied physics letters*, **82**, 3874-3876 (2003).

- [9] Z. Batool, K. Hild, T. Hosea, X. Lu, T. Tiedje, S. Sweeney, The electronic band structure of GaBiAs/GaAs layers: Influence of strain and band anti-crossing, *Journal of Applied Physics*, **111**, 113108 (2012).
- [10] B. Fluegel, S. Francoeur, A. Mascarenhas, S. Tixier, E. Young, T. Tiedje, Giant spin-orbit bowing in GaAs $1-x$ Bi x , *Physical review letters*, **97**, 067205 (2006).
- [11] Z. Zhou, D.F. Mendes, R.D. Richards, F. Bastiman, J.P. David, Absorption properties of GaAsBi based p-i-n heterojunction diodes, *Semiconductor Science and Technology*, **30**, 094004 (2015).
- [12] V. Pačebutas, K. Bertulis, A. Bičiūnas, A. Krotkus, Low-temperature MBE-grown GaBiAs layers for terahertz optoelectronic applications, *physica status solidi c*, **6**, 2649-2651 (2009).
- [13] X. Lu, D. Beaton, R. Lewis, T. Tiedje, M. Whitwick, Effect of molecular beam epitaxy growth conditions on the Bi content of GaAs $1-x$ Bi x , *Applied Physics Letters*, **92**, 192110 (2008).
- [14] A.V. Barve, J. Montaya, Y. Sharma, T. Rotter, J. Shao, W.-Y. Jang, S. Meesala, S.J. Lee, S. Krishna, High temperature operation of quantum dots-in-a-well infrared photodetectors, *Infrared Physics & Technology*, **54**, 215-219 (2011).
- [15] N. Kirstaedter, N. Ledentsov, M. Grundmann, D. Bimberg, V. Ustinov, S. Ruvimov, M. Maximov, P.S. Kop'ev, Z.I. Alferov, U. Richter, Low threshold, large To injection laser emission from (InGa) As quantum dots, *Electronics Letters*, **30**, 1416-1417 (1994).

- [16] Z. Mi, C. Wu, J. Yang, P. Bhattacharya, Molecular beam epitaxial growth and characteristics of 1.52 μ m metamorphic InAs quantum dot lasers on GaAs, *Journal of Vacuum Science & Technology B: Microelectronics and Nanometer Structures Processing, Measurement, and Phenomena*, **26**, 1153-1156 (2008).
- [17] D. Pan, E. Towe, S. Kennerly, Normal-incidence intersubband (In, Ga) As/GaAs quantum dot infrared photodetectors, *Applied Physics Letters*, **73**, 1937-1939 (1998).
- [18] K. Akahane, N. Yamamoto, Formation of InAs quantum dots at ultrahigh growth rates, *Physica E: Low-dimensional Systems and Nanostructures*, **42**, 2735-2738 (2010).
- [19] P. Joyce, T. Krzyzewski, G. Bell, T. Jones, S. Malik, D. Childs, R. Murray, Effect of growth rate on the size, composition, and optical properties of InAs/GaAs quantum dots grown by molecular-beam epitaxy, *Physical Review B*, **62**, 10891 (2000).
- [20] S. Kiravittaya, Y. Nakamura, O. Schmidt, Photoluminescence linewidth narrowing of InAs/GaAs self-assembled quantum dots, *Physica E: Low-dimensional Systems and Nanostructures*, **13**, 224-228 (2002).
- [21] H. Saito, K. Nishi, S. Sugou, Shape transition of InAs quantum dots by growth at high temperature, *Applied Physics Letters*, **74**, 1224-1226 (1999).
- [22] J. Massies, N. Grandjean, Surfactant effect on the surface diffusion length in epitaxial growth, *Physical Review B*, **48**, 8502 (1993).

[23] H. Okamoto, T. Tawara, H. Gotoh, H. Kamada, T. Sogawa, Growth and characterization of telecommunication-wavelength quantum dots using Bi as a surfactant, *Japanese Journal of Applied Physics*, **49**, 06GJ01 (2010).

CHAPTER 2: FUNDAMENTAL CONCEPTS AND PRINCIPLES OF SEMICONDUCTORS

This chapter covers the fundamental concepts of semiconductors, such as crystal structure and optical processes. It describes the principles of the bandgap, the nature of the energy gap (i.e. direct or indirect bandgap), temperature dependent energy gap and some general features of GaAs, GaAsBi and InGaBiAs. This chapter further emphasises the importance of heterostructures in understanding the optical properties of quantum dots studied in this work.

2.1 INTRODUCTION

Semiconductors have become a popular subject for fundamental study in recent decades, leading to their usage in a wide range of electrical and optical devices. Personal computers (CPUs, memory), laser diodes for data transmission, and DVD and CD players are all examples of these technologies. Semiconductor applications can be found on the roads, in our homes, in our schools, and even in our wallets. Semiconductor research continues to stimulate interest at all levels of science due to its wide range of applications.

Solid state materials can be classified in general based on the value of the energy gap between their valence and conduction bands. Most materials have energy gaps in the range from zero to a few electron volts (eV). According to this classification, materials having an energy gap of ~ 0 eV are referred to as metals. In contrast, materials with energy gap more than 3 eV are known to be insulators, whereas the semiconducting materials have energy gap ranging from ~ 0.1 eV to ~ 3 eV.

It is worth to mention that an intrinsic semiconducting material behaves as an insulator at absolute zero temperature ($T=0K$), however, their electrical conductivity increases significantly as the temperature increases. Furthermore, electrical conductivity can be controlled by using light of specific wavelengths or by introducing small amounts of specific impurities known as dopants. These properties are very different from those of metals, which have high densities of free electrons. The electrical conductivity of metals, which is many orders of magnitude greater than semiconductor conductivity, has a weak temperature dependence and is unaffected by low levels of illumination or impurities. Semiconductor materials are divided into two types based on their chemical composition: elemental semiconductors and compound semiconductors. Elemental semiconductors are those composed of single species of atoms, such as silicon (Si), germanium (Ge), and diamond (C) (possesses some semiconductor properties), and belong to the group IV of the periodic table of elements (see Figure 2.1). Some of the properties of elemental semiconductors are shown in Table 2.1.

		III	IV	V	VI	
1		5 10.811 B Boron	6 12.011 C Carbon	7 14.007 N Nitrogen	8 15.999 O Oxygen	
2		13 26.982 Al Aluminium	14 28.086 Si Silicon	15 30.974 P Phosphorus	16 32.065 S Sulphur	
3	II	30 65.39 Zn Zinc	31 69.723 Ga Gallium	32 72.64 Ge Germanium	33 74.922 As Arsenic	34 78.96 Se Selenium
4		48 112.41 Cd Cadmium	49 114.82 In Indium	50 118.71 Sn Tin	51 121.76 Sb Antimony	52 127.6 Te Tellurium
5		80 200.59 Hg Mercury	81 204.38 Tl Thallium	82 207.2 Pb Lead	83 208.98 Bi Bismuth	84 209 Po Polonium

Figure 2.1: Group II through VI of the periodic Table of the elements.

Table 2.1: Chemical Formula, energy gap (E_g) at 300K, lattice constant (a), structure of lattice and energy gap type.

Materials	Chemical Formula	E_g (eV)	a (nm)	Structure	Type
Silicon	Si	1.12	0.543	Cubic	Indirect
Germanium	Ge	0.664	0.566	Cubic	Indirect
Diamond	C	5.48	0.357	Cubic	Indirect

There are, however, numerous compound semiconductor materials, which are composed of two or more elements. For instance, elements of group III and V are used to provide important compound semiconductors such as GaAs which is a combination of gallium (Ga) from column III and arsenide (As) from column V. Compound semiconductors formed with two elements are known as “binary compounds” such as GaAs, AlAs and InAs. In addition, for those semiconductors which have more than two elements, they are known as “ternary compounds” such as GaAsBi and AlGaAs, and semiconductors with four elements are called quaternary, for example GaInAsP. Another important class of semiconductors is known as II-VI compound materials, which include zinc oxide (ZnO) and mercury zinc telluride (HgZnTe). Table 2.2 lists the most common III-V compounds as well as their properties.

Table 2.2: Chemical Formula, energy gap, lattice constant, structure of crystal and bandgap type at T= 300K of most important III-V compound semiconductors [1].

Material	Chemical Formula	E_g (eV)	a (nm)	Structure	Type
Gallium arsenide	GaAs	1.424	0.565	Cubic	Direct
Indium arsenide	InAs	0.354	0.606	Cubic	Direct
Aluminium arsenide	AlAs	2.15	0.566	Cubic	Indirect
Gallium nitride	GaN	3.44	a=0.318, c=0.517	Hexagonal	Direct
Indium Nitride	InN	1.89	a=0.354, c=0.870	Hexagonal	Direct

Many of the compound semiconductors have some specific electrical and optical properties which can be controlled by (i) changing the temperature (i.e. thermal excitation), (ii) optical excitation (i.e. excitation with photons having energies higher than the energy gap (E_g)), and (iii) introducing impurities into their crystal lattice (i.e. doping). The following section introduces an additional category of semiconductor classification based on doping type.

2.2 INTRINSIC AND EXTRINSIC SEMICONDUCTORS

An intrinsic semiconductor, also known as an undoped semiconductor, is a semiconductor that is completely free of dopant species. In intrinsic semiconductors the number of excited electrons in the conduction band (n) is equal to the number of holes in the valence band (p).

$$n = p = n_i \quad 2.1$$

where n_i is the intrinsic carrier concentration.

At zero Kelvin temperature (0K), intrinsic semiconductors behave as insulators because the valence band is completely filled, and the conduction band is completely empty, hence there is no charge carrier flow to contribute to conductivity unless photo-excitation or a thermal excitation is used. However, at specific temperature, electrons from the valence band (VB) may have enough thermal energy to be excited to the conduction band (CB). At room temperature (RT), few electrons have enough thermal energy to jump from VB to CB. For example, intrinsic Si and GaAs have n_i values equal to $1.5 \times 10^{10} \text{ cm}^{-3}$ and $1.8 \times 10^6 \text{ cm}^{-3}$, respectively at RT.

Extrinsic semiconductors, also known as doped semiconductors, are made by introducing various atoms (dopant atoms) into the host crystal. As shown in Figure 2.2 for a silicon semiconductor with four electrons in its outermost shell, there are two types of extrinsic materials that can be created.

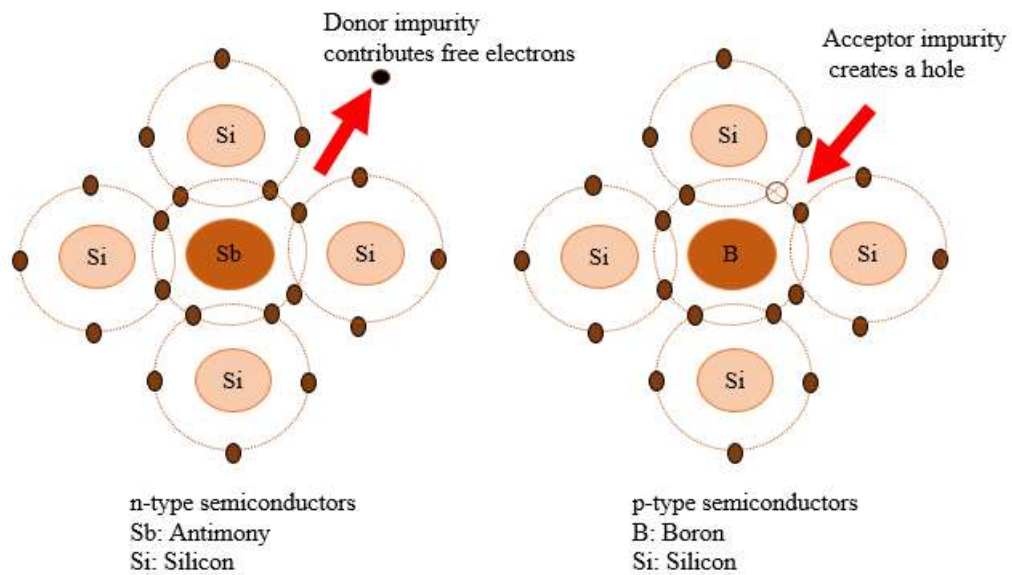


Figure 2.2: P-type and N-type extrinsic silicon.

- (1) P-type material: the dopant atoms incorporated into the semiconductor crystal are referred to as acceptor atoms. As acceptor atoms for silicon, Boron (B), Gallium (Ga), or Aluminium (Al) can be used. These atoms are from column III of the periodic table and have three electrons in the outermost shell. When these atoms are added to the silicon crystal, one electron in the silicon valence band can simply jump to one of the acceptor atoms' valence shells, leaving a negatively charged acceptor atom behind. This negatively charged acceptor atom is fixed and does not contribute to electrical conduction. Majority carrier holes are generated in p-type materials, contributing to the hole concentration (p). The activation energy is low at RT, therefore all of the combined acceptor atoms will accept one electron from the valence band. As a result, excess free hole density (p_0) in the valence band for a p-type material at RT is provided by:

$$p_0 \approx N_A(cm^{-3}) \quad 2.2$$

where N_A is the acceptor concentration.

(2) n-type material: donor atoms are the dopant atoms that are added to the semiconductor crystal. Phosphorus (P), Antimony (Sb), and Arsenide (As) are utilised as donors in silicon. The outermost shell of these donor atoms has five electrons, and they are found in column V of the periodic table. One electron of the donor atom can simply jump to the conduction band of silicon leaving the donor atom positively charged. The positively charged donor atom is fixed and has no effect on the electrical conduction. This procedure is sometimes referred to as "ionisation" or "activation" of the donor atoms because the energy is so low in comparison to the silicon bandgap that it can simply be ionised at room temperature. Electrons are the majority carriers in n-type materials and contribute to the electron concentration (n). In addition, at $T \neq 0K$ for an n-type material, the extra free electrons from dopant atoms can be thermally excited from their states within the forbidden bandgap that are placed slightly below the bottom of the conduction band, resulting in an increase in the free electrons density (n_0).

$$n_0 \approx N_D(cm^{-3}) \quad 2.3$$

where N_D is the donor concentration.

2.3 ENERGY BANDGAP

The bandgap, also known as an energy gap in solid state physics, is an energy range (a forbidden energy region) in a solid where no electron state can exist. The energy-wave vector (E - k) relationship is commonly used to represent this region. In general, the bandgap (E_g) in insulators and semiconductors refers to the energy difference between the top of the valence band (E_v) and the bottom of the conduction band (E_c). The shape of the conduction band and valence band at edge near $k=0$ is approximately parabolic (the conduction band is empty and the valence band is filled). The energy of the conduction (E_c) and valence (E_v) bands can be calculated as follows:

$$E_c = E_g + \frac{h^2 k^2}{8\pi^2 m_e^*} \quad 2.4$$

$$E_v = E_g - \frac{h^2 k^2}{8\pi^2 m_h^*} \quad 2.5$$

where h is the Plank's constant, m_e^* and m_h^* are the effective mass of electron and hole, respectively.

Energy (E) - momentum (P) relationship is described as:

$$E = \frac{P^2}{2m^*} \quad 2.6$$

The effective mass can be found from the second derivative of E with respect to P

$$m_e^* = \left(\frac{d^2 E}{dp^2} \right)^{-1} \quad 2.7$$

A similar expression can be found for holes (with subscript h instead of e). Electrons and holes are treated as free particles by assigning them a modified mass, the effective mass, which combines their potential and kinetic energies into a single kinetic-like energy. In GaAs, as an example, the effective mass of electrons and holes is given by $m_e^* = 0.067m_0$ and $m_h^* = 0.035m_0$, where m_0 is the mass of the free electron. At zero Kelvin, the valence band is full, and the conduction band is completely empty, then electrons cannot move in solid due to a large bandgap between both bands, and the material behaves as an insulator. Above zero Kelvin, some electrons have enough energy to transfer from the valence band to the conduction band and contribute to the electrical conduction process. The Fermi level is the probability of occupying energy levels in the valence and conduction bands. The intrinsic semiconductor acts as a perfect insulator at absolute zero temperature. However, as the temperature rises, free electrons and holes are created. The number of holes in the valence band in an undoped or pure semiconductor is equal to the number of electrons in the conduction band. As a result, the probability of occupying energy levels in the conduction and valence bands is equal. As a result, as shown in Figure 2.3, the Fermi level for an undoped semiconductor is in the middle of the forbidden band. Figure 2.3 depicts a simplified energy–band structure and Fermi level for undoped semiconductors. The energy of an electron is defined as positive when measured upwards, and the energy of a hole is defined as positive when measured downwards.

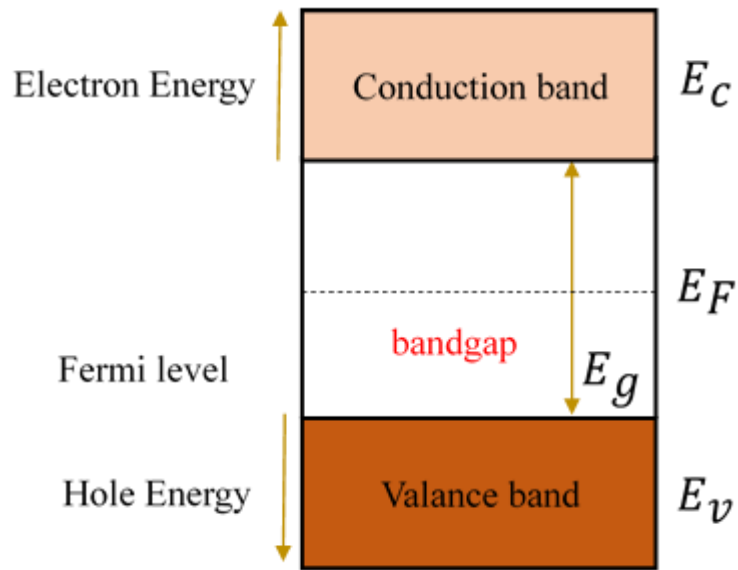


Figure 2.3: simplified energy–band structures and Fermi level of undoped semiconductors.

The electron-carrier concentration in an intrinsic semiconductor is equal to the hole-carrier concentration. This can be written as $p = n = n_i$,

where p is the concentration of hole carriers, n is the concentration of electron carriers, and n_i is the concentration of intrinsic carriers. The Fermi level for intrinsic semiconductor is given as,

$$E_F = \frac{E_C + E_V}{2} \quad 2.8$$

where E_F is the Fermi level energy.

2.4 CRYSTAL STRUCTURE OF SEMICONDUCTORS

A crystal is a material with an orderly and periodic arrangement of atoms in three-dimensional space. The arrangement of atoms in a crystal is known as its crystal structure. To describe the crystal structure, two basic concepts are introduced.

1. A lattice is a set of points in space that form a periodic structure.
2. The basis or building block of atoms as an atom or group of atoms, as shown in Figure 2.4, that is attached to each lattice point to produce the physical crystal structure.

The crystalline structure is formed by connecting the basis to each of these lattice points.

Lattice + basis = crystal structure.

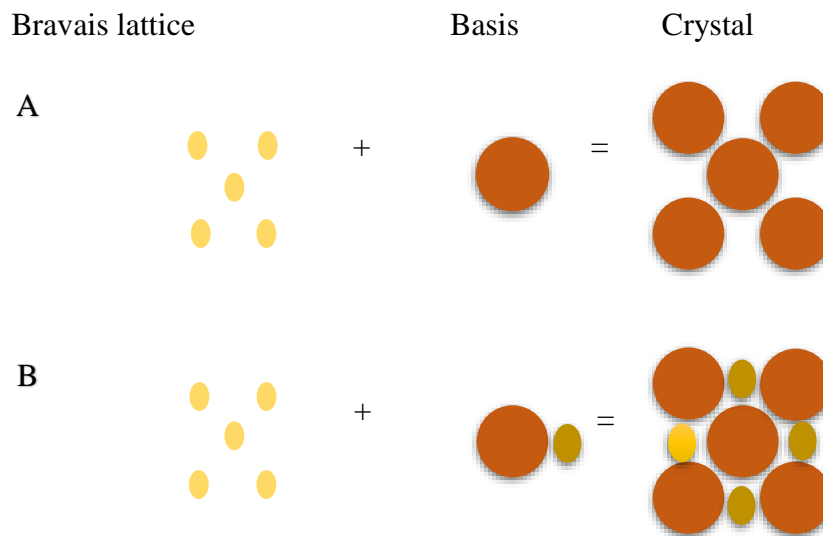


Figure 2.4: Creation of the crystal structure from the combination of lattice and basis. The basis may have one atom (A) or a group of atoms (B).

The lattice is defined by three primitive vectors, \mathbf{a}_1 , \mathbf{a}_2 and \mathbf{a}_3 which allow any point of the lattice C to be acquired by a translation from any point of the lattice R .

$$C = R + c_1\mathbf{a}_1 + c_2\mathbf{a}_2 + c_3\mathbf{a}_3 \quad 2.9$$

where c_1, c_2, c_3 are integers.

The unit cell is a basic building block of the crystal structure with a small repeating entity. If the cell volume formed by the translation vectors \mathbf{a}_1 , \mathbf{a}_2 and \mathbf{a}_3 is the smallest possible, the translation vectors are referred to as primitive. The primitive unit cell is the volume of a cell surrounded by primitive vectors. There is no special method for selecting primitive vectors, however, it is possible to identify more than a group of primitive vectors of a given lattice, and the choice is usually dictated by convenience.

2.4.1 Types of Basic Lattice

A primitive cell is the smallest unit cell that can be repeated in order to form a lattice. A crystal lattice can be thought of as a series of repetitive translations of a primitive cell. The lattice classes are defined by the relationships between the primitive vectors \mathbf{a}_1 , \mathbf{a}_2 and \mathbf{a}_3 , and the angles α , β , and γ between them.

A cubic and hexagonal lattice are the two most important primitive cell types, and they serve as the foundation for all semiconductor structures. The lattice constant, a , is the side dimension of the cube. There are three types of cubic lattice: simple cubic (sc), body-centred cubic (bcc), and face-centred cubic (fcc).

In a simple cubic primitive cell, there is one host atom (point of lattice) at each corner of a cubic unit cell (host atom). Figure 2.5 illustrates a simple cubic lattice formed by $a\mathbf{x}$, $a\mathbf{y}$, and $a\mathbf{z}$, where \mathbf{x} , \mathbf{y} , and \mathbf{z} are unit vectors.

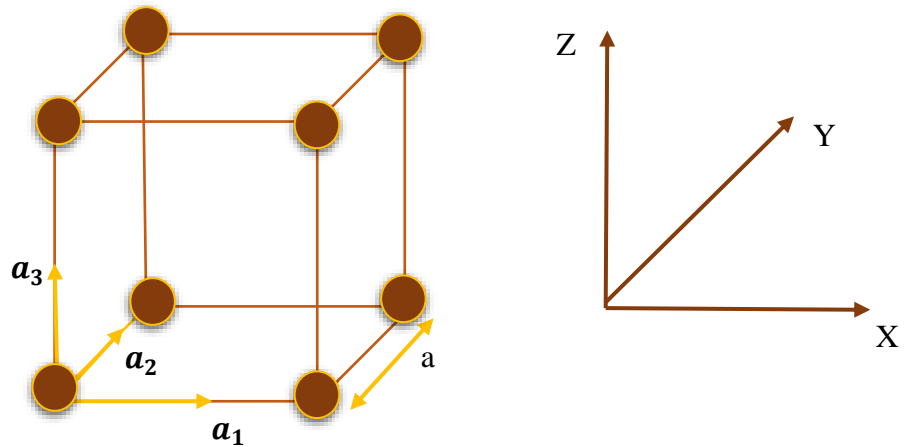


Figure 2.5: A simple cubic lattice (sc) with the primitive vectors.

The body centred cubic (bcc) structure, shown in Figure 2.6, can be created from the simple cubic structure. It has one lattice point at each corner and one atom in the centre of the unit cell body (each atom is bonded with eight other lattice points along the cube body diagonal). A set of primitive vectors for the bcc lattice is given by

$$\mathbf{a}_1 = ax, \mathbf{a}_2 = ay, \mathbf{a}_3 = \frac{a}{2}(x + y + z) \quad 2.10$$

where \mathbf{x} , \mathbf{y} and \mathbf{z} are three orthogonal unit vectors.

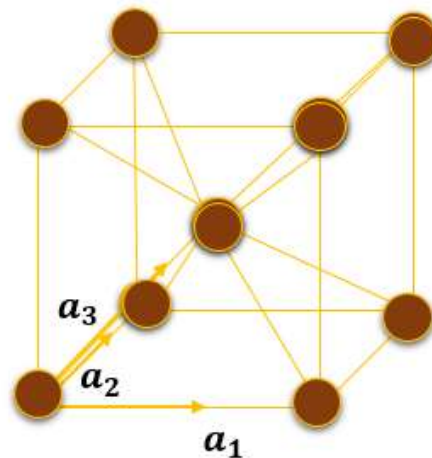


Figure 2.6: The lattice of body centred cubic (bcc) along with a select of primitive vectors.

Face-centred cubic (fcc) structures have one lattice point at each corner, one in the centre of each face, and the lattice points are bonded with those along the face diagonal, as presented in Figure 2.7. The following are a symmetric group of primitive vectors for fcc structure

$$\mathbf{a}_1 = \frac{a}{2} (y + z), \mathbf{a}_2 = \frac{a}{2} (z + x), \mathbf{a}_3 = \frac{a}{2} (x + y) \quad 2.11$$

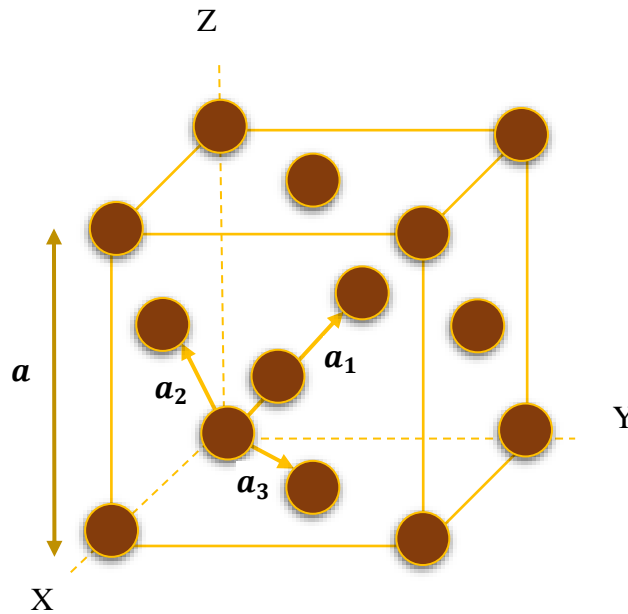


Figure 2.7: The lattice of face centred cubic along with its primitive basis vectors.

Most important semiconductor materials, such as Si and Ge have a diamond-like structure made up of the same atom types as indicated in Figure 2.8. Each atom in the diamond structure forms bonds with four adjacent atoms of the same group. The bonds between atoms in the silicon crystal stretch between fcc sublattices. In the case of III-V and II-VI semiconductor materials with fcc lattices, one fcc lattice is formed from one type of element (for instance, an atom from group III), but the other fcc lattice is formed from the other type of element (for instance, an atom of V group). The elements in the two fcc lattices come from dissimilar groups of the

periodic table. The overall crystal structure is known as the zinc blende lattice. Elements of the same atomic group are positioned on the same fcc lattice in ternary and quaternary semiconductors, whereas all bonds between atoms occur between atoms in dissimilar fcc lattices.

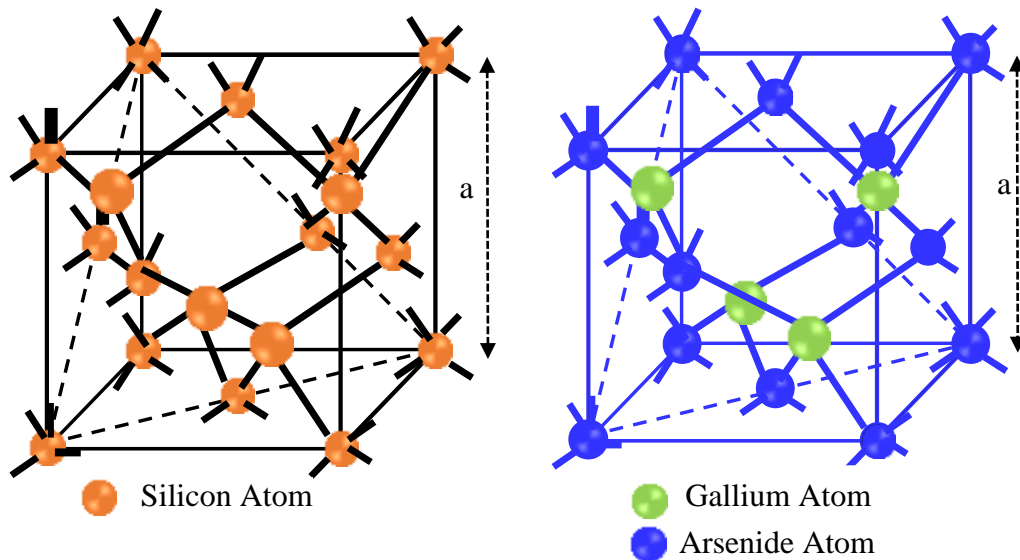


Figure 2.8: Examples of crystal structures (a) diamond for Si. Both types of atomic sites are occupied by Si. (b) Zincblende structure for GaAs. The sites are occupied by Ga and As atoms [2].

For example, in the GaAs crystal shown in Figure 2.8 (b), all Ga atoms are positioned on one of the fcc lattice and bonded to As atoms which are located on the second fcc lattice. As a result, the interatomic distances between neighbouring atoms are less than the lattice constant. The zinc blende structure is found in most common III-V compound materials, such as GaP and GaAs.

2.4.2 Miller Indices for Crystal Planes

In a crystal semiconductor, it is critical to understand the plane or group of planes. The plane on which the devices are manufactured is important because it affects their electrical and optical properties. Before describing a specific surface structure, the crystalline planes must be determined. Miller indices are used in the (hkl) notation to indicate the orientation of crystal planes based on their intercepts with crystallographic reference axes. As for directions, negative indices are often indicated by a bar or minus sign written above the corresponding index, such as $(0\ 0\ \bar{1})$. Each crystal is associated with two lattices: a reciprocal lattice and a crystal lattice. As is well known, a diffraction pattern for crystallisation is a map of the crystal's reciprocal lattice. Three primitive basis vectors, **a**, **b**, and **c**, can be used to describe a crystalline solid. These vectors are defined along the axis (x, y, z) so that the crystal structure remains invariant when vector **R** is translated. The translation vector **R** is defined as the sum of the integral multiples of the three primitive basis vectors (**a**, **b**, and **c**),

$$\mathbf{R} = m\mathbf{a} + n\mathbf{b} + p\mathbf{c} \quad 2.12$$

where m, n, and p are integers and **a**, **b**, and **c** are the primitive vectors

This expression is then used to define the reciprocal lattice basis vectors **a***, **b***, and **c*** in terms of direct lattice basis vectors:

$$\mathbf{a}^* = (\mathbf{b} \times \mathbf{c}) / \mathbf{a} \cdot (\mathbf{b} \times \mathbf{c}) \quad 2.13$$

$$\mathbf{b}^* = (\mathbf{c} \times \mathbf{a}) / \mathbf{a} \cdot (\mathbf{b} \times \mathbf{c}) \quad 2.14$$

$$\mathbf{c}^* = (\mathbf{a} \times \mathbf{b}) / \mathbf{a} \cdot (\mathbf{b} \times \mathbf{c}) \quad 2.15$$

The position vector (\mathbf{g}) in the reciprocal space (d) with components (h,k,l) is perpendicular to the plane with Miller indices (hkl), so it is commonly denoted as \mathbf{g}_{hkl} and can be defined by

$$\mathbf{g}_{hkl} = h\mathbf{a}^* + k\mathbf{b}^* + l\mathbf{c}^* \quad 2.16$$

$$|\mathbf{g}_{hkl}| = 1/d_{hkl} \quad 2.17$$

where, h, k, l are integers and d_{hkl} is the spacing between lattice planes. Figure 2.9 shows an example of various planes in a cubic crystal and their Miller indices. The Miller indices' method is described below.

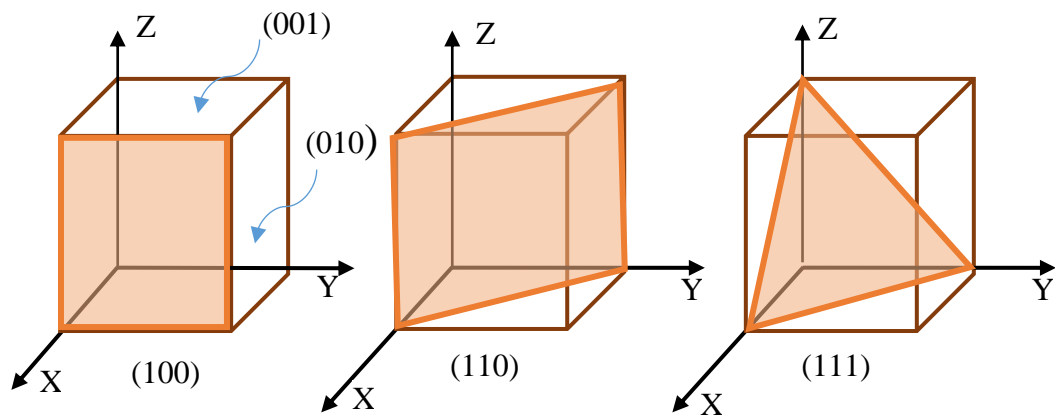


Figure 2.9: Miller indices for some crucial planes in a cubic crystals are presented.

Assuming there is a three-dimensional crystal plane with three basis vectors, \mathbf{x} , \mathbf{y} , and \mathbf{z} , the Miller's indices of this plane can be calculated as follows:

- (i) Determine the intercepts of the planes along three basis vectors.
- (ii) Find the reciprocals of the intercepts along each axis.
- (iii) Reduce the reciprocals of these intercepts to their smallest values in such a way that the smallest three integers have the same ratio.

The results of the three preceding steps are included in parenthesis (hkl) and are referred to as Miller indices for single plane with intercepts at $1/h$, $1/k$, and $1/l$ on the x, y, and z axes, respectively. However, {hkl} represents the Miller indices of a complete set of planes of equal symmetry in a cubic crystal, such as planes (110), ($\bar{1}10$), ($0\bar{1}1$), and so on. The equivalent planes are referred to collectively as {110}. The planes of a cubic crystal system (100), (110), and (111) are known as low index planes because they are only denoted by 0 and 1. Whereas planes with higher values, such as (n11), where n is greater than one, are referred to as high-index planes.

2.4.3 Conventional and Non-Conventional Planes

Over the last decade, there has been a significant increase in interest in the growth of GaAs on high-index planes. The tremendous improvement in the structural, optical, and electrical properties of III-V-based structures grown on high index (n11) planes prompted this interest. The mechanism of epitaxial growth as well as the physics of dopant incorporation can be better understood by studying Molecular Beam Epitaxy (MBE) growth technique development on different-oriented substrates. The use of high Miller index substrate orientations enables the engineering of nanostructured semiconductor properties such as size distribution, shape, emission polarisation, and transition energy, opening up a wide range of design possibilities. The growth of epitaxial layers on high-index planes is a step forward in semiconductor material engineering because it allows for the development of devices with improved properties over devices grown on conventional (100) planes. The fascination with non-conventional semiconductor structures relates to growth, impurity incorporation, lasing performance, electronic

properties, and piezoelectric effects. Non-conventional substrates, for instance, have enabled the fabrication of high-performance InAs/GaAs quantum dot (QD) lasers, ultrahigh mobility two-dimensional hole gases, GaAs/AlGaAs heterostructures, InGaAs QDs with improved piezoelectric effects, and GaMnAs epilayers with altered Mn incorporation and magnetic anisotropies [3, 4]. The possibility of changing and improving the properties of important materials, surface kinetics, growth mechanisms, and impurity incorporation by growing in crystalline orientations other than (100) has incited a lot of interest in these topics. Some exciting properties have emerged in terms of dopant incorporation, piezoelectric effect, microstructure self-organization, overlayer strain, and ternary alloy ordering [5].

Several high index polarised surfaces, such as (311)A [6] and (311)B GaAs [7, 8], have recently received increased attention due to the structures grown on these surfaces having unique properties that improve device performance [8, 9]. When compared to similar samples grown on (100) surfaces, heterostructures grown on (311)A and (311)B GaAs orientation substrates have significantly better optical properties, implying that the starting (311)A and (311)B GaAs surfaces are more stable and smoother [10-12]. It is worth noting that in the case of the GaAs high index planes, A and B refer to the Ga and As surfaces, respectively. The differences between (311)B and (311)A planes can be explained by considering the polarity of the surface [13].

2.5 DIRECT AND INDIRECT ENERGY BANDGAP

In semiconductor physics, based on band structure, materials have either direct bandgap or indirect bandgap. Direct gap semiconductors have different optical properties than indirect gap semiconductors. The material has a direct bandgap if the momentum of the lowest energy state in the conduction band and the highest energy state in the valence band are the same. If they do not match, the material has an indirect bandgap. In materials with a direct bandgap, valence electrons can be excited directly into the conduction band by a photon with an energy greater than the bandgap. However, in materials with an indirect bandgap the electron must pass through an intermediate state and transfer momentum to the crystal lattice. Figures 2.10 (a) and (b) show the most common indirect (Si) and direct (GaAs) bandgap semiconductors.

Direct semiconductors (such as GaAs) have the lowest transition energy for moving an electron from the valence band to the conduction band without changing its momentum. In the case of indirect semiconductors, excitation at the bandgap energy should occur with a change in the electron's momentum which is provided by a phonon. In indirect semiconductors, the only way for interband optical transitions is for the phonon to make a vertical virtual transition at $k = 0$ with the subsequent electron-phonon dispersion. For instance, optical transitions are only allowed if the phonons are emitted or absorbed to maintain crystal momentum [14]. The phonon is absorbed or released to conserve the crystal momentum during optical absorption.

$$E_{electron} = E_{photon} \pm E_{phonon} \quad 2.18$$

$$k_{electron} = \pm k_{phonon} \quad 2.19$$

A similar process occurs in optical emission.

$$E_{photon} = E_{electron} \pm E_{phonon} \quad 2.20$$

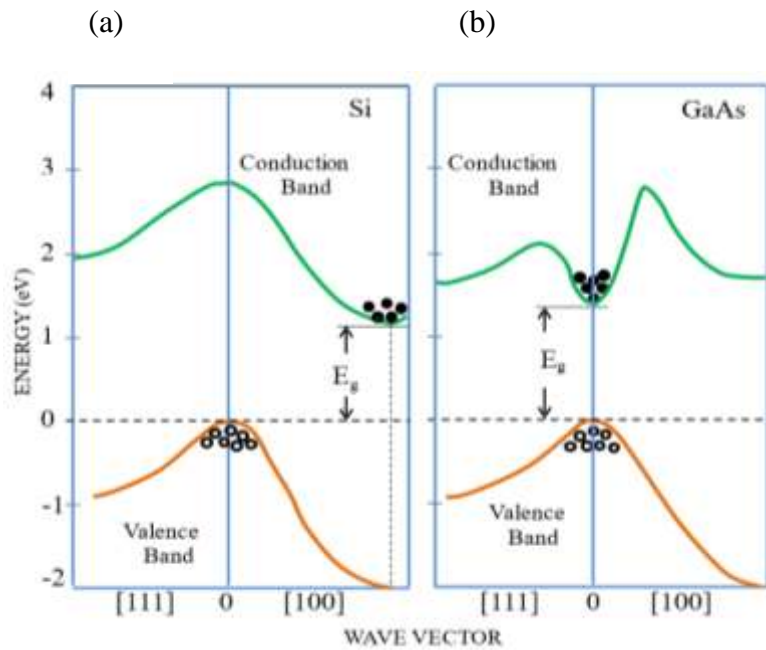


Figure 2.10: Energy-band structures of indirect (Si) and direct (GaAs) bandgap semiconductors with electrons and holes represented by full and open circles, respectively [15].

In bulk silicon for optical transitions, phonons consisting of transverse optical (TO) (~ 56 meV) and transverse acoustic (TA) (~ 18.7 meV) modes [14] play an important role. Nonetheless, it has been demonstrated that zero-phonon optical transitions are partially allowed in silicon nanostructures, such as silicon nanoparticles and porous silicon, and that the oscillator's strength of zero-phonon

transitions is greatly improved. This increases the rate of radiative recombination via direct band-to-band recombination [15-17].

2.6 EFFECT OF TEMPERATURE ON ENERGY BANDGAP

The bandgap energy in semiconductor materials has an inverse relationship with temperature. It tends to decrease as the temperature increases (see Figure 2.11 for Ge, Si and GaAs). The cause of this behaviour is thermal energy, which causes atomic vibrations. When the temperature increases, the amplitude of atomic vibration rises, resulting in greater interatomic spacing. The interaction between phonons (lattice vibrations) and free electrons and holes will also have a minor effect on the bandgap.

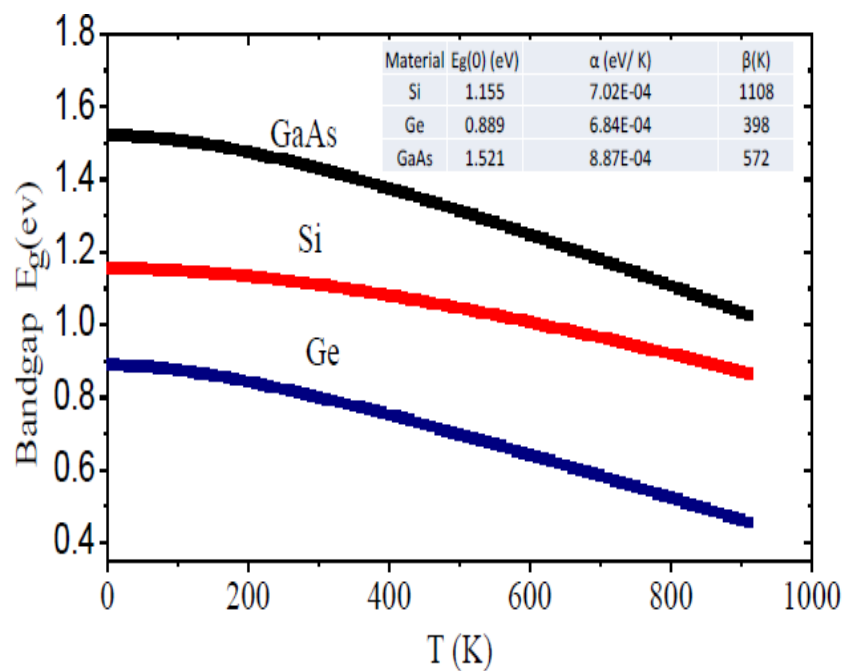


Figure 2.11: The energy bandgap of Ge, Si, and GaAs as a function of temperature [18]. Varshni's parameters for Ge, Si, and GaAs semiconductors are shown in the inset Table.

This effect is determined by the linear expansion coefficient of a material. Increased interatomic spacing reduces the potential seen by electrons in the material. As a result, the size of the energy bandgap shrinks. Applying high compressive (tensile) stress, for example, for direct modulation of the interatomic distance, causes an increase (decrease) in the bandgap. Varshni's formula [18] provides an empirical relationship for the temperature dependence of the energy bandgap.

$$E_g(T) = E_g(0) - \frac{\alpha T^2}{\beta + T} \quad 2.21$$

where $E_g(0)$ denotes the bandgap energy at zero Kelvin. α and β are empirical parameters related to the material. Varshni's parameters for GaAs, Si and Ge semiconductors are shown in the inset Table in Figure 2.12.

2.7 MODIFICATION OF BAND STRUCTURE

The ability to tailor semiconductor bandgap energy is critical for the design of novel electronic devices with superior properties. For bandgap tailoring, also known as bandgap engineering, there are two commonly used approaches. These will be covered briefly in the following section.

2.7.1 Alloys

Semiconductor alloys provide a method for adjusting the bandgap energy magnitude and other material parameters in order to improve and expand the applications of semiconductor devices. The GaAs bandgap, for instance, is too small to emit visible light. The bandgap of GaP, on the other hand, is in the green

part of the spectrum, but it is indirect, therefore the GaP emitter is ineffective without the help of appropriate dopants (e.g., nitrogen) [19]. A well-chosen alloy, such as $\text{GaAs}_x\text{P}_{1-x}$, composed of GaAs and GaP, can retain most of the GaAs properties (e.g., the direct gap), whereas changing the energy of the forbidden gap significantly [20]. Furthermore, the use of alloys contributes to the creation of a material with a suitable lattice constant to be matched to the substrate. Quaternary alloys such as $(\text{In}_{0.53}\text{Ga}_{0.47}\text{As})$ and $(\text{In}_{0.52}\text{Al}_{0.48}\text{As})$ are used to be lattice-matched with InP substrates, which are used as substrates for a variety of devices [21].

Figure 2.12 depicts the bandgap energies of many III-V semiconductors as a function of the lattice constant, including the $\text{GaAs}_{1-x}\text{Bi}_x$ system [22, 23] in green line, which is experimentally predicted over the entire alloying range. Some III-V semiconductors have bandgap energies ranging from 0.18 to 2.4 eV, and the majority of them have a direct gap.

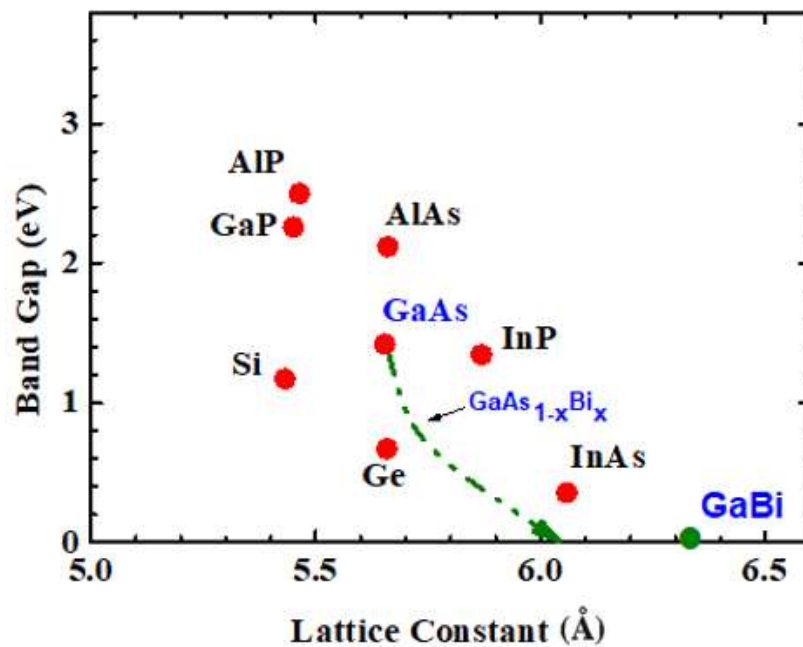


Figure 2.12: Bandgap energy as a function of lattice constant for various III-V semiconductors at room temperature [24].

2.7.1.1 Vegard's Law

Vegard's law is an empirical rule that describes the linear relationship between alloy crystal lattice constants and constituent component concentrations at constant temperature [26]. For example, when an alloy A_xB_{1-x} (x denotes the mole fraction or chemical composition) is formed of a random combination of two elements (these concepts can also be applied to ternary and quaternary alloys), the alloy lattice constant is given by:

$$a_{alloy} = xa_A + (1 - x)a_B \quad 2.22$$

The change in the energy gap in the alloys can be represented by:

$$E_g^{alloy} = (1 - x)E_g^B + xE_g^A \quad 2.23$$

Nonetheless, there is a bowing effect in some alloys caused by an increasing disorder due to alloying. As a result, equation (2.23) is modified by taking the bowing parameter into account (b).

$$E_g^{alloy} = (1 - x)E_g^B + xE_g^A + bx(1 - x) \quad 2.24$$

2.7.1.2 Graded Gap Semiconductor Structures

The chemical composition of semiconductors varies in the classified semiconductor structures, and this difference can affect alloy properties such as the gap energy and the lattice constant. Conversely, in the majority of the classified structures, the

lattice constant does not change significantly. For example, in AB_xC_{1-x} ternary compound semiconductor material, where x is the chemical composition or mole fraction, the AB_xC_{1-x} properties slowly change from AC to AB as x increases from 0 to 1. The lattice constant exhibits linear behaviour with x , whereas the energy gap exhibits non-linear bowing. The gap energy of the compound material AB_xC_{1-x} can be calculated using the following equation:

$$E_{g,ABC}(x) = xE_{g,AB} + (1 - x)E_{g,AC} - bx(1 - x) \quad 2.25$$

where b is the bowing coefficient, which is typically less than 1 eV. The coefficient of bowing value in some compound semiconductors, such as $Al_xGa_{1-x}As$, is so small that the term $(bx(1 - x))$ in the previous equation is insignificant.

2.7.2 Heterostructures

Generally, there are two types of structures, namely homojunction and heterojunction structures. The junction of two identical semiconductor materials produces homojunction structures [27]. Whereas heterojunction structures are formed by stacking two or more different semiconductors. A heterojunction's constituent materials have different energy gaps, atomic or size lattice parameters. Heterostructures provide means to manipulate the behaviour of the holes and electrons by the engineering of the bands. It is frequently used to engineer the electronic energy bands in a variety of solid-state device applications, including semiconductor lasers and solar cells. One important factor in the formation of

heterojunctions is the band alignment of two semiconductor materials. This parameter will be briefly discussed below.

2.7.2.1 Band Alignment

As shown in Figure 2.13, heterojunctions can be classified into three types of band alignment based on how their energy bands are aligned with each other. These are classified as straddled alignment (type I), staggered alignment (type II), and broken gap alignment (type III).

2.7.2.1.1 Straddled Alignment or Type I

In this type of alignment, the bandgap of material B is completely contained within the bandgap of material A, implying that the lowest energy for both electrons and holes occurs in semiconductor B (Figure 2.1 3.a). This type of alignment is common in InGaAs/InP, GaAs/AlGaAs, and InAs/GaAs.

2.7.2.1.2 Staggered Alignment or Type II

This alignment occurs when the lowest energy of the holes occurs in semiconductor A, however, the lowest energy of the electrons occurs in semiconductor B (Figure 2.13.b). A type II heterojunction is typically represented by GaSb/GaAs and GaAsSb/GaInAs.

2.7.2.1.3 Broken Gap Alignment or Type III

Another option for alignment is type III heterostructures, as seen in Figure 2.13.c, where the III and V group elements (such as GaSb/InAs) differ. In type III, one semiconductor's conduction band is located in the lower the valence band of the other semiconductor. It is worth noting that this alignment is also known as a type II misaligned heterojunction.

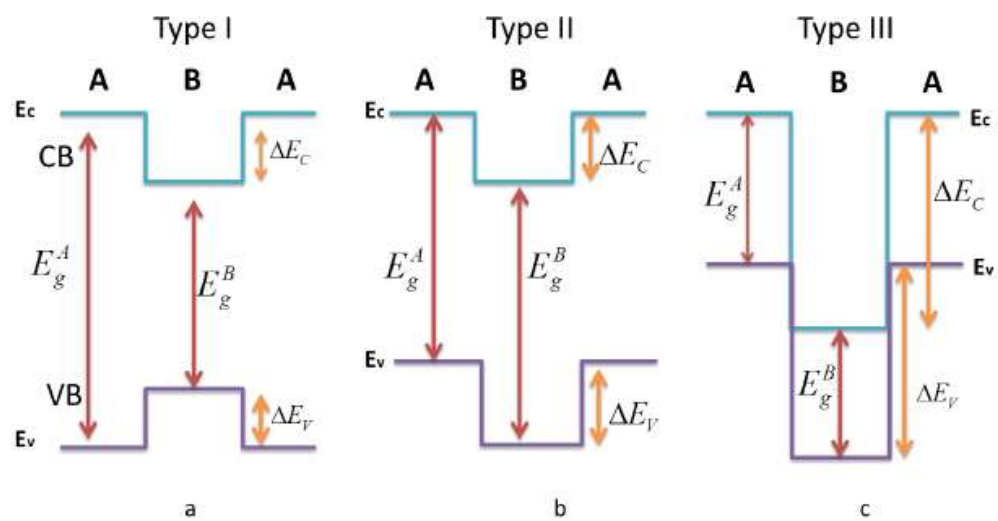


Figure 2.13: Heterojunctions are classified based on their band alignment, where E_C , E_V , E_g , E_C , and E_V represent the materials' conduction band, valence band, energy gap, conduction band offset, and valence band, respectively [27].

2.7.2.2 Anderson's rule

Anderson proposed an electron affinity model in 1962 [28] to calculate the band offset of the perfect heterostructure. The difference in energy between the bottom of the conduction band and the vacuum level is defined as the electron's affinity. Consider two semiconductors A and B with bandgap energies and electron

affinities E_g^A and E_g^B , and χ_A and χ_B , respectively, that have been put into physical contact. The electron affinity model is based on the idea that the energy due to an electron moving from the vacuum level to semiconductor A, then to semiconductor B, and finally back to the vacuum level should be zero. This is demonstrated by:

$$\Delta E_C = \chi_A - \chi_B = \Delta\chi \quad 2.26$$

The bandgap energy difference between the two materials is presented by:

$$\Delta E_g = E_g^B - E_g^A \quad 2.27$$

The valence band offset is given by:

$$\Delta E_V = \Delta E_g - \Delta\chi \quad 2.28$$

The band offset is given by the following expression:

$$\Delta E_g = \Delta E_C + \Delta E_V \quad 2.29$$

It is important to point out that Anderson's rule is fairly valid for some semiconductor pairs but has some limitations for many other materials. Defect states, dislocations, and surface interface states are not included in this model. For instance, using this rule, the theoretical band offset value of the AlAs/GaAs heterostructure is 230 meV, while the experimental value is close to 530meV. The failure of Anderson's model was explained as a result of semiconductor surface dipoles caused by atom readjustments at the semiconductor's surface [29]. These

dipoles have an effect on the electron affinity values and, as a result, the band offset of the heterostructure.

2.8 GENERAL PROPERTIES OF SELECTED SEMICONDUCTORS MATERIALS INVESTIGATED IN THIS WORK

Some of the most significant properties of the semiconductors investigated in this work will be discussed in the following section.

2.8.1 Gallium Arsenide (GaAs)

GaAs is regarded as one of the most technologically significant and extensively researched III-V compound semiconductor material. Although Goldschmidt [30] created the first GaAs material in 1920, its properties were unknown until 1952. It is formed by combining Arsenic (As) group-V and Gallium (Ga) group-III elements from the periodic table. The crystal structure of GaAs is a zinc blende type, as shown in Figure 2.14, with a face-centred cubic lattice (fcc) of As with Ga atoms positioned on the body diagonals. Ga (As) atoms are displaced from the As (Ga) atom by a distance $\left(\frac{a}{4}, \frac{a}{4}, \frac{a}{4}\right)$ along the body diagonal. a is the GaAs lattice constant given by [31]:

$$a = 0.565325 + 3.88 \times 10^{-6} (T - 300K) \text{ nm} \quad 2.30$$

where T is the temperature in Kelvin.

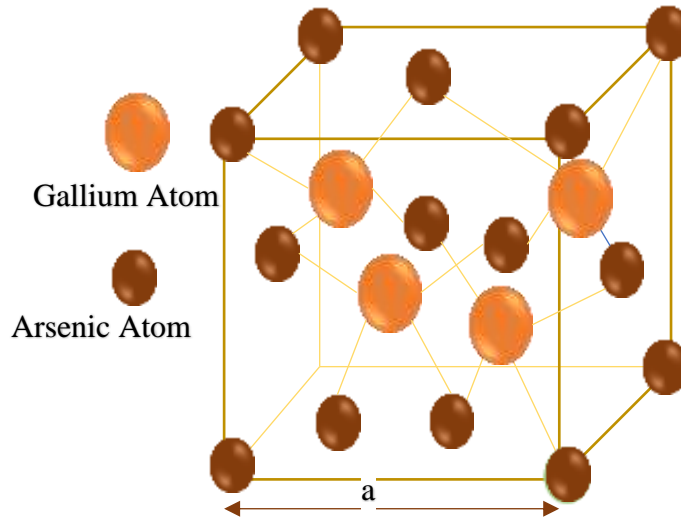


Figure 2.14: GaAs conventional unit cube.

The energy band structure of GaAs is depicted in Figure 2.15. According to this Figure, at $k = 0$, the wave vector of the minima conduction band and the maxima valence band of GaAs have the same value.

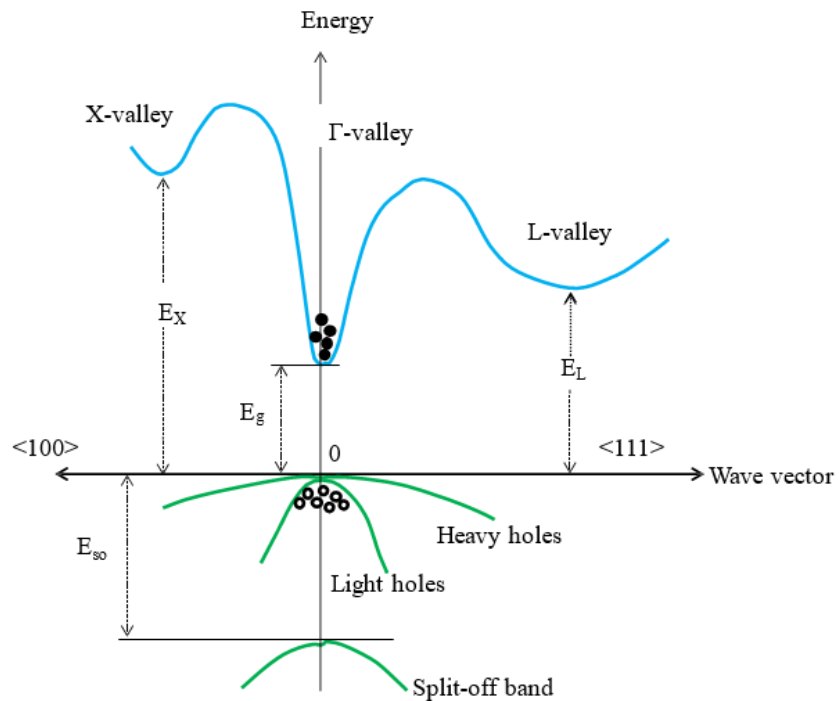


Figure 2.15: The bandgap energy diagram of GaAs is shown for the three different conduction valleys (X, Γ and L).

As a result, the transition of one electron from the valence band to the conduction band requires a change in energy while maintaining momentum. Thus, the nature of the GaAs bandgap is direct according to the bandgap diagram definition. This property ensures excellent GaAs optical properties as well as excellent electron transport in the conduction band. GaAs-based materials, which outperform Si materials in terms of optical and electrical properties, are widely used in optoelectronic and photovoltaic devices. Furthermore, GaAs has higher carrier mobility than Si, making it a suitable and potential candidate for the fabrication of high-frequency devices. At room temperature, the bandgap energy of GaAs is 1.42eV, which corresponds to a wavelength of 0.87 μm [25].

Many techniques have been implemented using GaAs to achieve the 1.30 μm and 1.55 μm emissions required in optical fibres' telecommunication. Adjusting the bandgap through alloying, i.e. creating ternary/quaternary alloys such as InGaAs/InGaAsP [32], is one method for obtaining emissions at these wavelengths. Another common technique is the growth of multiple quantum wells (MQWs) or quantum dots (QDs) with GaAs and other narrower bandgap materials (e.g., InAs) using quantum confinement to control the emission wavelength [33]. Furthermore, because the GaAs energy gap is greater than that of Si, ($E_g^{GaAs} = 1.424\text{eV} > E_g^{Si} = 1.1\text{ eV}$ at 300K), GaAs devices are better suited to operating at higher temperatures than Si devices. Some additional GaAs properties at room temperature are shown in Table 2.3.

Table 2.3: Some important room-temperature properties of GaAs, where hh and lh stand for heavy hole and light hole, respectively [34].

Parameter	GaAs
Crystal Structure	Zincblende
Lattice constant (nm)	0.5653
Crystal density (g/cm ³)	5.360
Energy bandgap (eV) (300K)	1.42
Band type	Direct
Electron effective mass	0.063 m ₀
Hole effective mass	0.62m ₀ (h _h), 0.087m ₀ (l _h)
Dielectric constant (static)	12.85
Specific heat(cal/gK)	0.08
Electron affinity (eV)	4.07

2.8.2 Indium Gallium Arsenide (In_xGa_{1-x}As)

In_xGaAs_{1-x} is a ternary alloy consisting of GaAs and InAs. As is well known, Ga and In are two elements from group III of the periodic table, whereas As is an element from group V. As a result, alloys containing these compounds are referred to as III-V semiconductors with properties intermediate between those of GaAs and InAs. Photonics and electronics have benefited from the use of InGaAs. When In is incorporated into GaAs, the bandgap is reduced by about 12 meV per percent of In [35]. The application of In_xGaAs_{1-x}As alloys as a high-speed and high-sensitivity photodetector, which is a good candidate for optical fibre telecommunications, has attracted the interest of researchers [36]. Pearsall et al. were the first to characterise

single-crystal epitaxially grown $\text{In}_{0.53}\text{Ga}_{0.47}\text{As}$ on (111) and (100) InP substrates [37]. The optical properties of $\text{In}_x\text{GaAs}_{1-x}$ can be modified by varying the proportions of InAs and GaAs, i.e. $\text{In}_{1-x}\text{Ga}_x\text{As}$ [36]. Single crystal epitaxial films of $\text{In}_x\text{GaAs}_{1-x}$ alloy can be deposited on a single crystal substrate of a III-V semiconductor, such as GaAs, InAs, or InP, which have a lattice parameter similar to that of InGaAs alloys. A good match between the lattice constants of the substrate and thin film is required to maintain single crystal properties and avoid strain in the epilayer.

Table 2.4: Some important properties of $\text{In}_{0.5}\text{Ga}_{0.5}\text{As}$ at 300K [36].

Parameter	InGaAs
Lattice constant (nm)	0.5869
Energy bandgap (eV)	0.75
Light-hole effective mass	0.051
Electron mobility	$10,000 \text{ cm}^2 \cdot \text{V}^{-1} \cdot \text{s}^{-1}$
Hole mobility	$250 \text{ cm}^2 \cdot \text{V}^{-1} \cdot \text{s}^{-1}$

2.8.3 Dilute Bismide Materials

The $\text{GaAs}_{1-x}\text{Bi}_x$ system has attracted a lot of attention because of its unique optical properties that set it apart from other materials. The addition of a small amount of Bi to GaAs has a significant effect on the bandgap [38] and spin-orbit splitting [39]. The bandgap energy of GaAs alloys is significantly reduced by adding a small amount of Bi (88 meV per percent Bi) [23], while the spin-orbit splitting energy is significantly increased [38, 40]. These remarkable properties make $\text{GaAs}_{1-x}\text{Bi}_x$

alloy a promising material for a wide range of applications, including long wavelength optoelectronics, long infrared emitters, detectors, and spintronic-related devices. K. Ono et al. [41] achieved the first successful growth of dilute Bismide materials using metalorganic vapour phase epitaxy (MOVPE), followed by molecular beam epitaxy (MBE) [23, 42]. Bi is the heaviest element in group V. A Bi atom has a much larger atomic radius and less electronegativity than an As atom. A compressive strain is developed around the atom due to of the enormous size difference between Bi and As atoms. The large reduction in the GaAsBi bandgap is caused by Bi's strong perturbation of the host valence band. Because of the large difference in atomic potential, a localised level near the valence band maxima of GaAs is formed, attracting holes from the valence band. The localised potential of Bi atoms and the surrounding lattice relaxation significantly disturb the electronic band of GaAs, resulting in a variety of qualitative effects. Shallow states appear near the valence band maxima of $\text{GaAs}_{1-x}\text{Bi}_x$ materials, as opposed to GaAsN materials. These states of energy appear near the conduction band minima in GaAsN. The interaction between these energy states, which behave as shallow donors [38], and the valence band charge carriers causes significant bowing of the energy bands. The strong bandgap decrease of GaAs is due to a small percentage of Bi and N which act as isoelectronic impurities. In GaAs, they substitute As atoms. In the case of Bi incorporation, the massive reduction in GaAs bandgap is thought to be caused by the perturbation of the valence band maxima (VBM) and 6p state of the Bi atom [43, 44]. The Bi 6p orbitals are expected to be found near VBM in GaAs. Consequently, the bandgap of GaAs is reduced due to an upward motion of heavy and light hole bands. The split-off band position changes very little, resulting in a massive increase in spin orbit splitting energy [39]. The large

reduction in the bandgap of GaAs with N incorporation, on the other hand, is thought to be caused by a resonant interaction between the conduction band minima and the 2s state of the N atom [45, 46]. A schematic of the band structure of GaAsBi and an analogous GaAsN alloy is shown in Figure 2.16. This illustrates that this case is very different to the case of dilute nitrides, in which the bonding N 2p orbitals are deep in the valence band of GaAs and should not be considered for bandgap reduction. This energetic behaviour of Bi and N isoelectronic impurities can be physically explained by the difference in the low electronegativity of Bi and the large electronegativity of N when compared to As.

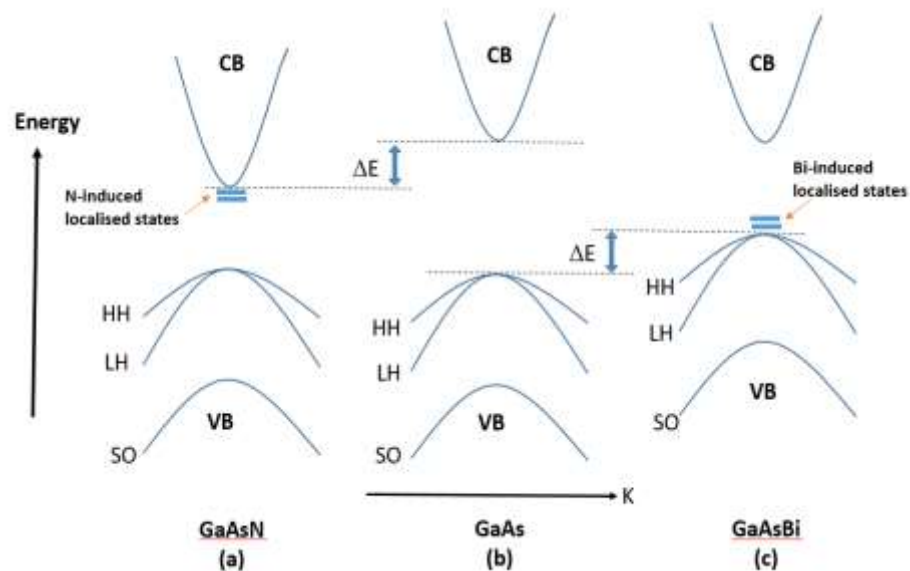


Figure 2.16: Band gap structure of (a) dilute GaAsN, (b) GaAs, and (c) dilute GaAsBi. CB, HH, LH and SO represent the conduction band, heavy holes, light holes, and split off bands, respectively. The position of localized energy states in Bi and N are shown by solid blue lines.

2.8.4 Properties of InGaBiAs

The addition of Bi to InGaAs is expected to result in a much smaller bandgap than GaAsBi [47]. The bandgap in traditional InP-based InGa(Al)As lasers is greater

than the spin-orbit (SO) split energy, which enhances the process of Auger recombination including these energy bands and is detrimental to device performance [48]. It is worth pointing out that Auger recombination is a non-radiative process where the excess energy from the electron-hole recombination is transferred to electrons or holes that are subsequently excited to higher energy states within the same band instead of giving off photons (the radiative process) It is thought that Auger recombination in InGaAsBi can be suppressed by engineering the SO splitting and bandgap. Petropoulos et al. were the first to notice the effect of decreasing the bandgap to 56 meV / percent Bi [49]. Adding heavy Bi atoms to InGaAs host lattice only affects the valence band, so the observed transitions are interpreted as a shift upward of the heavy/light hole bands, while the conduction band and the spin-orbit split band were unaffected, as seen in Figure 2.17. The incorporation of Bi atoms into the InGaAs host lattice results in a decrease of the energy bandgap and an increase of the SO split energy. The incorporation of Bi in an InGaAsBi/GaAs quantum well (QW) has been shown to significantly improve emission wavelength and photoluminescence intensity [50].

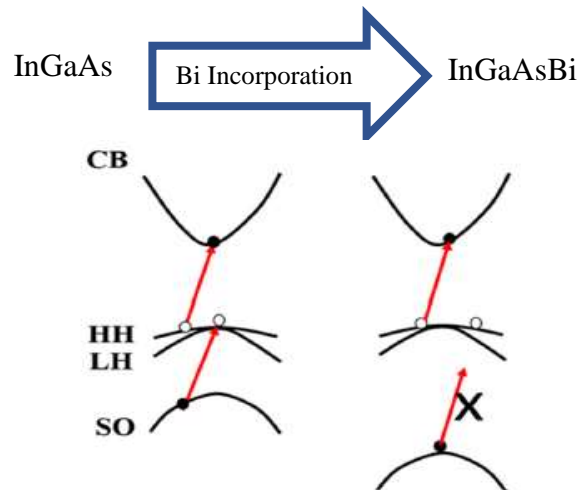


Figure 2.17: Diagram of Bi-related changes in the band structure of InGaAsBi alloys.

2.9 Optical properties of semiconductors

Optical measurements have many unique and attractive features for studying and characterising semiconductor properties. The optical properties of semiconductor materials are commonly classified based on the type of photon incident on the surface of the material, namely scattering, reflection from the material surface, transmission through, or absorption in the material. Generally, incident photons on a semiconductor can excite an electron from the valence band to the conduction band if they have enough energy. The generated electron and hole pair may interact with lattice vibrations (phonons) and electrons from localised defects. As a result, the optical spectra of semiconductor materials can be investigated, providing a significant source of information about the material's optical properties.

2.10 Absorption Processes

Excitation of semiconductor materials with photons of energy greater than the bandgap energy produces an electron-hole pair by optical process. In this case, a photon excites an electron from the valence band to the empty conduction band, as shown in Figure 2.18. When the energy conservation law is applied to the interband transition, the following equation holds:

$$E_f = E_i + \hbar\omega \quad 2.31$$

where E_i is the energy of the initial state in the valence band, E_f is the energy of the final state in the conduction band, and $\hbar\omega$ is the photon energy. For bulk

semiconductors material, there is a continuous series of energy states within the upper and lower bands, so interband transitions are possible over a wide range of frequencies. Nevertheless, the upper and lower limits of the bands, determine the frequency range. Consequently, interband transitions broaden the continuous absorption spectrum from the low energy threshold at E_g to an upper-value.

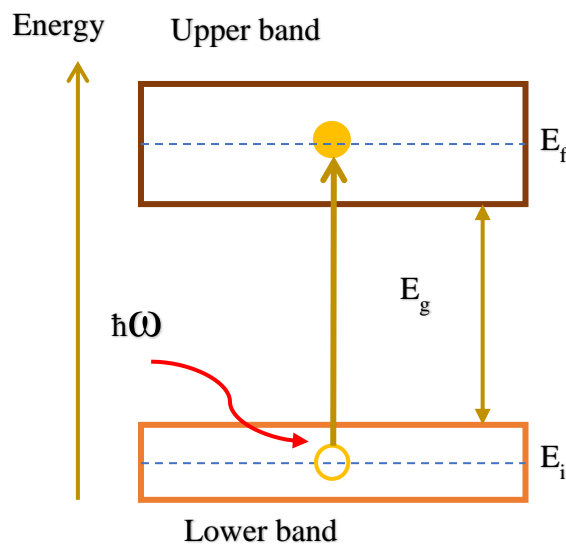


Figure 2.18: Interband optical absorption between an initial energy state E_i in an occupied lower band and a final energy state E_f in an upper band. E_g is the energy difference between the two bands.

For the direct bandgap semiconductors such as GaAs, the absorption coefficient (α) as a function of wavelength (λ) can be expressed as:

$$\alpha(\lambda) = A(\hbar\omega - E_g)^{\frac{1}{2}} \quad 2.32$$

where A is a constant determined by the material properties, E_g is the energy gap and $\hbar\omega$ is the incident photon energy. Figure 2.19 depicts the absorption coefficients of GaAs and Si as a function of incident light energy.

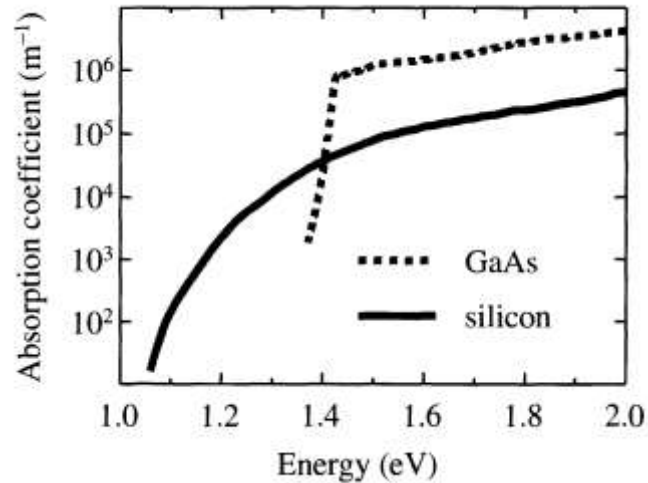


Figure 2.19: Absorption coefficient of GaAs and Si near their band edges as a function of incident light energy (the vertical axis is logarithmic) [51].

2.11 CONCLUSION

This chapter discussed the fundamental concepts of semiconductors, and focused on the most significant properties and applications of GaAs, GaAs_{1-x}Bi_x and In_xGaBi_{1-x}As, which have been investigated optically in this thesis. Additionally, this chapter further emphasises the importance of heterostructures in understanding the optical properties of quantum dots studied in this work.

REFERENCES

- [1] L.A. Coldren, S.W. Corzine, M.L. Mashanovitch, Diode lasers and photonic integrated circuits, John Wiley & Sons, 2012.
- [2] S.M. Sze, Y. Li, K.K. Ng, Physics of semiconductor devices, John wiley & sons, 2021.
- [3] M. Henini, P. Rodgers, P. Crump, B. Gallagher, G. Hill, Growth and electrical transport properties of very high mobility two-dimensional hole gases displaying persistent photoconductivity, Applied physics letters, **65**, 2054-2056 (1994).
- [4] K. Wang, K. Edmonds, L. Zhao, M. Sawicki, R. Campion, B. Gallagher, C. Foxon, GaMnAs grown on (311) GaAs substrates: modified Mn incorporation and new magnetic anisotropies, arXiv preprint cond-mat/0508021, (2005).
- [5] M. Henini, High index surfaces grow novel devices, III-Vs Review, **11**, 48-52 (1998).
- [6] H. Xu, Q. Gong, B. Xu, W. Jiang, J. Wang, W. Zhou, Z. Wang, Structural and optical characteristics of self-organized InAs quantum dots grown on GaAs (3 1 1) A substrates, Journal of crystal growth, **200**, 70-76 (1999).
- [7] M. Henini, Properties and applications of quantum dot heterostructures grown by molecular beam epitaxy, Nanoscale Research Letters, **1**, 32-45 (2006).
- [8] Y. Temko, T. Suzuki, P. Kratzer, K. Jacobi, InAs quantum dots grown on the GaAs (113) A and GaAs (1 1 3) B surfaces: A comparative STM study, Physical Review B, **68**, 165310 (2003).

- [9] L. Wang, M. Li, M. Xiong, L. Zhao, Effect of interfacial bonds on the morphology of InAs QDs grown on GaAs (311) B and (100) substrates, *Nanoscale research letters*, **4**, 689-693 (2009).
- [10] S. Li, G. Cui, Dependence of strength, elongation, and toughness on grain size in metallic structural materials, *Journal of applied physics*, **101**, 083525 (2007).
- [11] A. Polimeni, M. Henini, A. Patane, L. Eaves, P. Main, G. Hill, Optical properties and device applications of (InGa) As self-assembled quantum dots grown on (311) B GaAs substrates, *Applied physics letters*, **73**, 1415-1417 (1998).
- [12] Z. Wang, L. Däweritz, K. Ploog, Molecular-beam epitaxial growth and surface characterization of GaAs (311) B, *Applied Physics Letters*, **78**, 712-714 (2001).
- [13] P.O. Vaccaro, M. Hirai, K. Fujita, T. Watanabe, Optical properties of an nanostructure spontaneously formed on GaAs (311) A-oriented substrates, *Journal of Physics D: Applied Physics*, **29**, 2221 (1996).
- [14] D. Kovalev, H. Heckler, G. Polisski, F. Koch, Optical properties of Si nanocrystals, *physica status solidi (b)*, **215**, 871-932 (1999).
- [15] S. Sze, K. Ng, *Physics of Semiconductor Devices* 3rd ed Wiley, New York, (2007).
- [16] Z. Pu-Qin, H. Dong-Sheng, W. Xing-Long, Quantum confinement of Si nanosphere with radius smaller than 1.2 nm, *Chinese Physics Letters*, **22**, 1492 (2005).
- [17] M. Tabe, M. Kumezawa, Y. Ishikawa, T. Mizuno, Quantum confinement effects in Si quantum well and dot structures fabricated from ultrathin silicon-on-insulator wafers, *Applied surface science*, **175**, 613-618 (2001).

- [18] Y.P. Varshni, Temperature dependence of the energy gap in semiconductors, *physica*, **34**, 149-154 (1967).
- [19] M. Jaros, Electronic properties of semiconductor alloy systems, *Reports on Progress in Physics*, **48**, 1091 (1985).
- [20] A. Peaker, Light Emitting Diodes, *Electronics and Power*, **22**, 789 (1976).
- [21] J.-H. Bahk, Z. Bian, M. Zebarjadi, J.M. Zide, H. Lu, D. Xu, J.P. Feser, G. Zeng, A. Majumdar, A.C. Gossard, Thermoelectric figure of merit of (In_{0.53}Ga_{0.47}As)_{0.8}(In_{0.52}Al_{0.48}As)_{0.2} III-V semiconductor alloys, *Physical Review B*, **81**, 235209 (2010).
- [22] X. Lu, D. Beaton, R. Lewis, T. Tiedje, Y. Zhang, Composition dependence of photoluminescence of GaAs_{1-x}Bi_x alloys, *Applied physics letters*, **95**, 041903 (2009).
- [23] S. Tixier, M. Adamcyk, T. Tiedje, S. Francoeur, A. Mascarenhas, P. Wei, F. Schiettekatte, Molecular beam epitaxy growth of GaAs_{1-x}Bi_x, *Applied physics letters*, **82**, 2245-2247 (2003).
- [24] S. Alhassan, Investigation of structural, electrical and optical properties of doped dilute GaAsBi grown by molecular beam epitaxy, in, University of Nottingham, 2022.
- [25] I. Vurgaftman, J.á. Meyer, L.á. Ram-Mohan, Band parameters for III-V compound semiconductors and their alloys, *Journal of applied physics*, **89**, 5815-5875 (2001).
- [26] A.R. Denton, N.W. Ashcroft, Vegard's law, *Physical review A*, **43**, 3161 (1991).

- [27] V. Palankovski, R. Quay, Analysis and simulation of heterostructure devices, Springer Science & Business Media, 2004.
- [28] R. Anderson, Germanium-gallium arsenide heterojunctions, IBM Journal of Research and Development, **4**, 283-287 (1960).
- [29] H. Kroemer, Nobel Lecture: Quasielectric fields and band offsets: teaching electrons new tricks, Reviews of modern physics, **73**, 783 (2001).
- [30] J. Bernal, The Goldschmidt memorial lecture, Journal of the Chemical Society (Resumed), 2108-2114 (1949).
- [31] R.J.A. Hill, Tunnelling into InAs quantum dots, in, University of Nottingham, 2002.
- [32] P. Sundgren, R.M. von Wurtemberg, J. Berggren, M. Hammar, M. Ghisoni, V. Oscarsson, E. Odling, J. Malmquist, High-performance 1.3 μm InGaAs vertical cavity surface emitting lasers, Electronics Letters, **39**, 1128-1129 (2003).
- [33] H. Liu, I. Sellers, T. Badcock, D. Mowbray, M. Skolnick, K. Groom, M. Gutierrez, M. Hopkinson, J. Ng, J. David, Improved performance of 1.3 μm multilayer InAs quantum-dot lasers using a high-growth-temperature GaAs spacer layer, Applied Physics Letters, **85**, 704-706 (2004).
- [34] J. Blakemore, Semiconducting and other major properties of gallium arsenide, Journal of Applied Physics, **53**, R123-R181 (1982).
- [35] J. Yoshida, T. Kita, O. Wada, K. Oe, Temperature dependence of GaAs $_{1-x}\text{Bi}_x$ band gap studied by photoreflectance spectroscopy, Japanese journal of applied physics, **42**, 371 (2003).

- [36] T. Pearsall, Ga_{0.47}In_{0.53}As: A ternary semiconductor for photodetector applications, *IEEE Journal of Quantum Electronics*, **16**, 709-720 (1980).
- [37] T.P. Pearsall, R. Hopson Jr, Growth and characterization of lattice-matched epitaxial films of Ga_xIn_{1-x}As/InP by liquid-phase epitaxy, *Journal of Applied Physics*, **48**, 4407-4409 (1977).
- [38] S. Francoeur, M.-J. Seong, A. Mascarenhas, S. Tixier, M. Adamcyk, T. Tiedje, Band gap of GaAs_{1-x}Bi_x, 0 < x < 3.6%, *Applied physics letters*, **82**, 3874-3876 (2003).
- [39] B. Fluegel, S. Francoeur, A. Mascarenhas, S. Tixier, E. Young, T. Tiedje, Giant spin-orbit bowing in GaAs_{1-x}Bi_x, *Physical review letters*, **97**, 067205 (2006).
- [40] K. Alberi, O. Dubon, W. Walukiewicz, K. Yu, K. Bertulis, A. Krotkus, Valence band anticrossing in Ga_{1-x}Bi_xAs, *Applied Physics Letters*, **91**, 051909 (2007).
- [41] K. Oe, H. Okamoto, New semiconductor alloy GaAs_{1-x}Bi_x grown by metal organic vapor phase epitaxy, *Japanese journal of applied physics*, **37**, L1283 (1998).
- [42] M. Yoshimoto, W. Huang, Y. Takehara, J. Saraie, A. Chayahara, Y. Horino, K. Oe, New semiconductor GaNAsBi alloy grown by molecular beam epitaxy, *Japanese journal of applied physics*, **43**, L845 (2004).
- [43] A. Janotti, S.-H. Wei, S. Zhang, Theoretical study of the effects of isovalent coalloying of Bi and N in GaAs, *Physical Review B*, **65**, 115203 (2002).

- [44] T. Tiedje, E. Young, A. Mascarenhas, Growth and properties of the dilute bismide semiconductor $\text{GaAs}_{1-x}\text{Bi}_x$ a complementary alloy to the dilute nitrides, *International journal of nanotechnology*, **5**, 963-983 (2008).
- [45] W. Shan, W. Walukiewicz, J. Ager III, E. Haller, J. Geisz, D. Friedman, J. Olson, S.R. Kurtz, Band anticrossing in GaInNAs alloys, *Physical Review Letters*, **82**, 1221 (1999).
- [46] S. Tixier, S. Webster, E. Young, T. Tiedje, S. Francoeur, A. Mascarenhas, P. Wei, F. Schiettekatte, Band gaps of the dilute quaternary alloys $\text{Ga}_x\text{N}_{1-x-y}\text{Bi}_y$ and $\text{Ga}_{1-y}\text{In}_y\text{N}_x\text{As}_{1-x}$, *Applied Physics Letters*, **86**, 112113 (2005).
- [47] V. Halka, W. Freyland, Thermal stability of surface freezing films in Ga-based alloys: An x-ray photoelectron spectroscopy and scanning tunneling microscopy study, *The Journal of chemical physics*, **127**, 034702 (2007).
- [48] X. Chen, Y. Song, L. Zhu, S. Wang, W. Lu, S. Guo, J. Shao, Shallow-terrace-like interface in dilute-bismuth GaSb/AlGaSb single quantum wells evidenced by photoluminescence, *Journal of Applied Physics*, **113**, 153505 (2013).
- [49] J. Petropoulos, Y. Zhong, J. Zide, Optical and electrical characterization of InGaBiAs for use as a mid-infrared optoelectronic material, *Applied Physics Letters*, **99**, 031110 (2011).
- [50] K. Wang, Y. Gu, H. Zhou, L. Zhang, C. Kang, M. Wu, W. Pan, P. Lu, Q. Gong, S. Wang, InPBi single crystals grown by molecular beam epitaxy, *Scientific reports*, **4**, 1-6 (2014).
- [51] E.D. Palik, *Handbook of optical constants of solids*, Academic press, 1998.

CHAPTER 3: THE OPTICAL PROPERTIES AND GROWTH OF LOW DIMENSIONAL SEMICONDUCTOR STRUCTURES

This chapter will present the important concepts of low-dimensional semiconductor structures, including fabrication and properties, which are critical to understanding the optical studies of quantum dots investigated in this study.

3.1 INTRODUCTION

Low-dimensional semiconductor structures (LDSS) are a relatively new field of study in physics. They are defined as zero-, one-, two-, or three-dimensional semiconductor structures with a small scale. Due to the effects of quantum confinement, their optical and electrical properties differ substantially from those of the same material in bulk form. The so-called quantum well is an example of such a structure, in which carriers are restricted to flowing freely in only two dimensions. The interest in the study and preparation of LDSD has energised the science of condensed matter and increased globally. These advanced LDSS enable device engineers to create new electronic and optoelectronic devices. Thin epitaxial layers with nanometre dimensions were first produced in the late 1970s, allowing for an increase in LDSS research. The following are the primary requirements for the ideal LDSS system, which will be implemented in practise depending on the specific applications under consideration:

1. Structural and optical quality: semiconductors produce light when an electron in the conduction band recombines with a hole in the valence band, which is a radiative process. Nonetheless, the presence of defects that form energy states

within the bandgap causes the electron-hole recombination process to occur through these defects which may weaken light emission. When non-radiative processes take over, the optical efficiency, or the number of photons produced for each injected electron and hole decreases. For semiconductor laser applications, nanostructures with low defect numbers are required. Carrier mobility may also suffer as a result of poor structural quality.

2. Size: for a variety of applications, the majority of holes and electrons should be in the lowest energy state, implying negligible thermal excitation to higher states.

The degree of thermal excitation is identified by the ratio of the energy separation of the confined states and the thermal energy $k_B T$, where K_B is the Boltzman constant and T is the temperature. At room temperature, $k_B T$ is 25 meV, and the level separation must be at least three times this value (i.e., 75 meV). The energy spacing between states is dictated by the size of the structure. Increasing the structure size reduces the energy spacing between the confined states. The condition stated above establishes an upper limit for the size of the nanostructures.

3. Growth compatibility: for the mass production of electronic and electro-optical devices, the epitaxial techniques of Molecular Beam Epitaxy (MBE) and Metal-Organic Vapour Phase Epitaxy (MOVPE) are used. Commercialization of nanostructures will be more likely if these techniques can be used to create them.

4. Uniformity: devices typically contain a large number of nanostructures. To create an ideal device, each nanostructure should be the same size, shape, and composition.

5- Confinement potential: in LDSS, the potential wells that confine electrons and holes should be deep. If they are not, huge thermal excitation of carriers out of the nanostructures will happen at high temperatures. In electronic applications, either

holes or electrons trapped or contained within the nanostructure are usually sufficient. Both types of carriers must be confined in electro-optical devices.

6- p-i-n structures: the capacity to insert a nanostructure within a p-i-n structure's intrinsic region allows for carrier extraction or efficient injection.

3.2 QUANTUM CONFINEMENT

The nanostructured materials have unique electronic and optical properties that differ significantly from bulk properties. Because of the tunability of their optical properties due to size variation, they can be used in a variety of optoelectronic applications such as photovoltaic devices, LEDs and lasers. The quantum confinement or quantum size effect is responsible for these unusual properties of semiconductor nanomaterials. Due to the obvious effect of quantum confinement, the optical properties of nanostructures vary with their size. According to Heisenberg's uncertainty principle, the relationship between the uncertainties in position (x) and momentum (P) of a particle confined into a region is given by the following equation:

$$\Delta P_x \Delta x \geq \hbar \quad 3.1$$

where \hbar is Plank's constant.

3.3 DENSITY OF STATES

To define the various characteristics of semiconductors, such as absorption, emissions, and carrier distribution, it is necessary to know how many states are available at each energy. Because of the close proximity of the atoms in solids, their electric fields interact with one another. As a result, energy levels are divided into

a limited number of electronic states [1] . At an energy E , the density of states (DOS) is the number of available electronic states per unit volume per unit energy. The DOS governs the optical and electronic performance of devices. The DOS is determined by the energy and dimensionality of the system in relation to the particle's wave-vector dispersion relation. The electron dispersion relationship in bulk materials is given by:

$$E = \frac{\hbar^2 k^2}{2m_e} \quad 3.2$$

where \hbar is Plank's constant and m_e and k are the effective electron mass and wave vector number, respectively. For example, the effective mass of electrons in GaAs is $m_e = 0.067m_0$, where m_0 is the mass of free electron.

The DOS, $N(E)$, of a three-dimensional (3D) bulk material is given by:

$$N(E) = \frac{\sqrt{2}m_e^{3/2}}{\pi^2 \hbar^2} E^{1/2} \quad 3.3$$

The carrier's movement is confined to a plane by transitioning from three-dimensional (3D) structures to two-dimensional (2D) structures, known as quantum wells (QWs). Thin films, QWs and superlattices are some of the 2D systems. The DOS in 2D systems is modified according to the number of electronic states available and is given by:

$$N(E) = \frac{m_e}{\pi \hbar^2} \quad 3.4$$

As the system dimensions are reduced further, a "quantum wire" or a one-dimensional system is formed (1D). This structure can be found in semiconductor nanowires, nanotubes, and nanorods. The DOS of the quantum wire is as follows:

$$N(E) = \frac{\sqrt{2}m_e^{1/2}}{\pi\hbar} E^{-1/2} \quad 3.5$$

In the case of zero-dimensional (0D) systems, such as quantum dots (QDs), confinement occurs along three dimensions, and the DOS is transformed into a delta function. For QDs, the electrons can only have a limited number of distinct energies. The shape and size of the potential dot influence the state energy and the number of available states.

The DOS of 0D structures is given by:

$$N(E) = \delta(E - E_c) \quad 3.6$$

Figure 3.1 illustrates how the DOS in the conduction band varies with the degree of confinement.

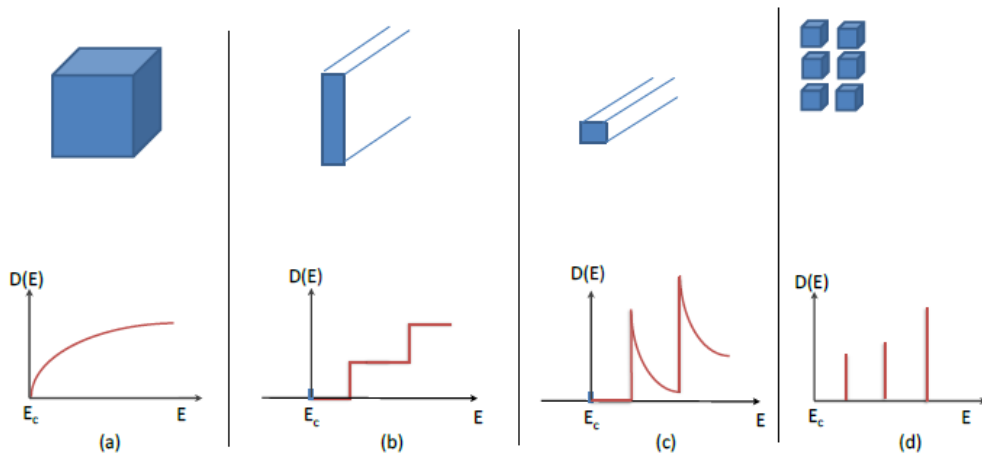


Figure 3.1: (a) DOS $N(E)$ in the conduction band for bulk semiconductor (3D), (b) quantum well (2D), (c) quantum wire (1D), and quantum dot (0D).

3.4 OPTICAL PROCESSES IN LOW DIMENSIONAL SEMICONDUCTOR STRUCTURES

Carrier dynamics and optical processes will be considered only for the case of quantum wells and quantum dots in the following sections.

3.4.1 Absorption in Semiconductor Nanostructures

Semiconductors can absorb a photon by moving the electron between the conduction and valence bands. The absorption strength is determined by the density of states in both bands (i.e. the combined density of states). The combined density of states has a form that is related to the DOS in both the valence and conduction bands and is thus a powerful function of the dimensionality of the system. The absorption will be modified by the quantised energy levels of a nanostructure, resulting in a number of different energy transitions happening between the confined hole and electron states. Another modification occurs because of the effects of excitons, which are electron-hole pairs held together by Coulomb attraction [2]. Since the optical transition can be considered as the creation of an electron-hole pair, Coulomb's attraction increases the absorption rate because it improves the probability of forming the electron-hole pair. For a perfect 2D system, the excitons binding energy increases by a factor of four when compared to bulk values [3].

3.4.2 Photoluminescence Process in Nanostructures

Holes and electrons in a semiconductor can be formed either electrically in a p-n junction or optically with incident photons with energies greater than the bandgap. Extra energies above the band edges are typically used to form holes and electrons.

However, the time required to lose this extra energy is usually much shorter than the time required for electron-hole recombination. As a consequence, the electrons and holes relax on the edges of their band before recombining to produce a photon. As a result, the emission occurs at the energy corresponding to the structure bandgap, with a small distribution due to the thermal energies of electrons and holes. Figure 3.2 shows the effect of quick carrier relaxation in the emission spectrum of a five QWs structure with different widths. Although the wider wells have a number of confined states, only emissions corresponding to the lower energy transition per well are shown.

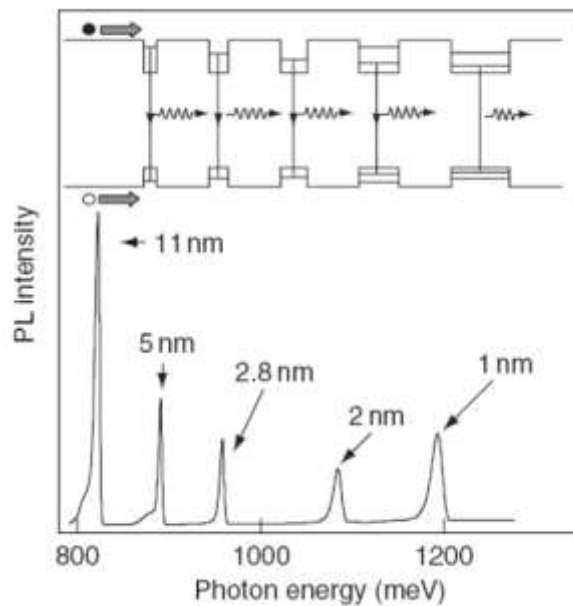


Figure 3.2: Emission spectrum of a $\text{Ga}_{0.47}\text{In}_{0.53}\text{As}/\text{InP}$ QW structure with five different thicknesses of wells. The electronic structure and nature of the optical transitions are depicted in the inset [4].

Higher-energy transitions in a nanostructure can be observed in emission if the density of electrons and holes is sufficiently large that the original electron and hole

states are populated. This can happen under high excitation conditions, when low-energy states become completely occupied and carriers are prohibited from relaxing into them due to the Pauli Exclusion Principle. Figure 3.3 illustrates the emission spectra of a set of self-assembled QDs for various optical excitation powers. Since the average number of holes and electrons in each dot is quite small at low laser power, only the ground state transition (with the lowest energy) is observed. Nonetheless, as power is increased, the ground state with a degeneracy of two is completely occupied, and emission from higher-energy (excited) states is possible. Because of the size non-uniformity of the QDs, variations in shape, composition, and size within a set of QDs result in a large inhomogeneous broadening of the optical spectra. Despite this, the very sharp emissions expected from these 0D nanostructures can be detected by studying a small number of dots.

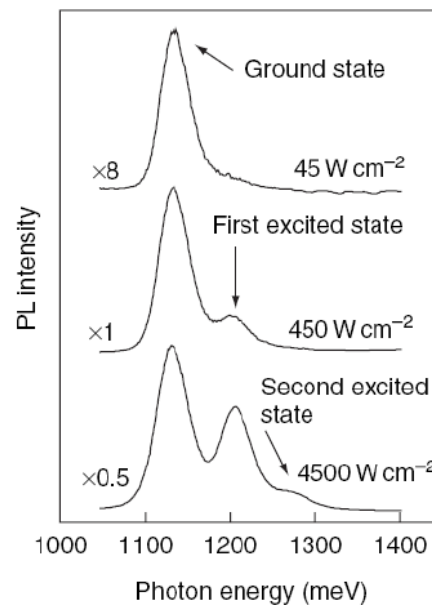


Figure 3.3: An ensemble of emission spectra from InAs self-assembled quantum dots at three different laser power densities. At the highest power, emission from three different transitions is detected. The numbers next to each spectrum represent the relative intensity scale factors [5].

3.5 CARRIER DYNAMICS IN LOW DIMENSIONAL SEMICONDUCTOR STRUCTURES

Carrier dynamics in QD structures are significantly more complex than in bulk materials due to the hetero-interface of two materials and the separate nature of QD levels. Figure 3.4 depicts a simplified diagram of the band of the QD semiconductor structure when excited with light, as observed in a photoluminescence experiment. Excitation is expected to occur in the barrier, i.e. the material surrounding the QDs in this case, for example, GaAs in the InAs/GaAs system. The wetting layer (WL), in which QDs form via a self-assembled growth process, acts as an additional QW in the structure. As a result, various dynamic carrier processes occur including:

1. Excitation of electrons from the barrier's valence band into the conduction band, resulting in free electrons in the conduction band and free holes in the valence band.
2. Relaxation from the barrier to the wetting layer.
3. Carrier capture into QDs.

Capture can occur at higher energy states or at the ground state, with subsequent relaxation. It is also possible that capture will occur directly from barrier states.

4. Relaxation of the carrier through carrier interaction (the so-called Auger effect) or carrier phonon interaction.
5. Carrier trapping and/or nonradiative recombination as a result of carrier transfer from the QDs to nearby deep level traps.
6. Radiative recombination, in which the electron and hole annihilate each other. The energy released during this process is emitted in the form of a photon. Further potential processes include the radiative and nonradiative recombination

of WL carriers, barrier valence/conduction, and thermal escape of holes and electrons from QDs.

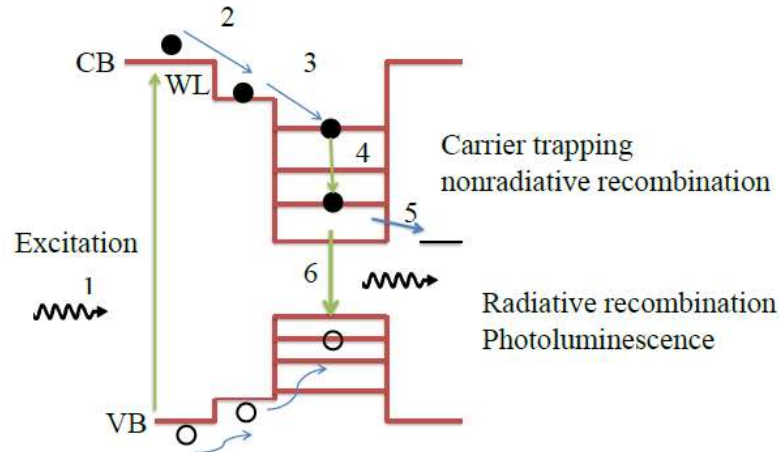


Figure 3.4: A simplified band diagram of a QD structure excited by light, illustrating the various processes described above.

3.6 EPITAXIAL GROWTH OF LOW DIMENSIONAL SEMICONDUCTOR STRUCTURES

For optoelectronic applications, precise growth of high purity crystal semiconductors with low defect density ($5 \times 10^{-3}/\text{cm}^2$ or less) is required. The growth of semiconductor heterostructures includes a technique known as epitaxy, which facilitates deposition and combines single crystal layers with the same crystal structure. Epitaxy is a controlled method for growing a solid film on a crystalline substrate in which the atoms of the growing film adapt to the atomic arrangement of the substrate atoms. Epitaxial growth of III-V compound semiconductors can be achieved using a variety of techniques, including liquid phase epitaxy (LPE), molecular beam epitaxy (MBE), and organic metal vapour phase epitaxy (MOVPE). Because of the much simpler approach of LPE, it was the

preferred method of early semiconductor device production. Both MBE and MOVPE are widely used for the growth of III-V materials, though they can be easily distinguished by their typical applications: both are commonly used as production and research tools; nevertheless, the industry prefers MOVPE due to its commercial appeal. Furthermore, because MBE has a high ability to grow thermodynamically forbidden alloys, it is well suited for research into highly mismatched alloys such as GaAsBi. In the case of the MBE method, the materials are evaporated in ultra-high vacuum (UHV), where epilayers crystallise when the atoms hit the hot substrate. Since MBE operates under UHV conditions, simultaneous characterisation of the growing film is possible, making this technique very popular in research settings. Nonetheless, the growth rate is too slow, limiting the film thickness that can be grown. MOVPE, on the other hand, is a chemical method for the growth of semiconducting materials that does not require a high vacuum such as MBE and has a higher growth rate in general than MBE. As a result, MOVPE is a preferred method for producing devices with large thicknesses.

3.6.1 Molecular Beam Epitaxy

MBE is an epitaxial process that involves one or more thermal reactions of atoms or molecules with a crystalline surface under UHV conditions, typically within 5×10^{-11} mbar (atmospheric pressure is around 1000 mbar) [6]. The MBE growth method has the advantage of allowing for precise control of both doping profiles and chemical compositions. MBE has the ability to create single-crystal multilayer structures with atomic layer dimensions. As a result, the MBE method allows for

the precise fabrication of semiconductor heterostructures with thin layers ranging from a fraction of a micron to a monolayer (one layer of Ga and one layer of As for the case of GaAs). The growth rate is typically around 1 μ m per hour, which translates to one monolayer per second. MBE's advantages include the ability to achieve extremely abrupt interfaces between different materials, good control of layer thickness, the ability to scale the process for mass production and good reproducibility. Elements such as Ga, As, Al, and others that make up a heterostructure can be evaporated using furnaces with orifices directed toward the substrate but protected by shutters. This is the gas Knudsen or molecular-flow regime, and the furnaces are known as Knudsen or K-cells. The molecules that emerge from the K-cells do not diffuse as they would in a gas, but instead form a molecular beam that moves in straight lines without colliding until they collide with the substrate (the mean free path of molecules between collisions is much greater than the size of the chamber at UHV condition). The substrate holder rotates continuously to achieve uniform epitaxial layers (e.g., 0.5 % difference in thickness and 1% variation in doping). The temperature of each furnace has the ability to control the beam of each element. Growth begins as soon as the shutters are opened. Dopants are added by using additional cells. The most common donor atom is Si, which belongs to the fourth group of the periodic table. However, Si may act as a donor or acceptor in III-V compound materials, depending on which host atom it replaces. It typically acts as a donor in the traditional (100) GaAs substrate, but it can also act as an acceptor by growing on a surface other than the (100) plane such as (311)A. Beryllium is commonly used as an acceptor in III-V semiconductors.

3.6.2 MBE Growth of Bi Based III-V Structures

Because of the large difference in atomic size between bismuth and arsenic, MBE growth of $\text{GaAs}_{1-x}\text{Bi}_x$ requires non-standard growth conditions. In GaAs, for example, the lowest impurity and defect-related luminescence emissions are observed for a growth temperature (substrate temperature), T_G , between 550-600°C. The MBE growth of GaAsBi, on the other hand, requires much lower substrate temperatures because Bi does not appear to incorporate significantly above approximately 350°C [7]. In addition, the V/III flux ratio must be low. When the V/III ratio exceeds 1.8, the incorporation of Bi decreases rapidly. Although there are significant growth constraints for the successful synthesis of $\text{GaAs}_{1-x}\text{Bi}_x$ alloys using MBE, it has been proposed that Bi can be incorporated in significant amounts: the highest reported value to date is $x = 22\%$ [8]. The ability of Bi atoms to act as a particularly effective surfactant on the surface during growth (Bi atoms alter the surface chemistry and defect structure during the III-V semiconductors growth by MBE and MOCVD) is responsible for the ability to grow GaAsBi away from nominal GaAs stoichiometry and avoid the negative effects typically observed in GaAs grown at low temperatures. Bi must maintain a constant presence on the surface throughout the growth period in order to function effectively as a surfactant. On the other hand, the tendency of Bi atoms to cluster within the GaAs matrix [9-11] and, in some cases, form Bi-based droplets during growth [12-14] inhibits Bi homogeneous incorporation. Excess Bi can self-segregate to the surface, where it can group unevenly and form droplets. More importantly, the presence of a GaAsBi growth window provides a guide to the growth of alloys with various compositions by controlling critical parameters such as V-III flux ratios and substrate temperature [15].

3.6.3 Growth of Quantum Well Structures

A QW is an energy potential well within a semiconductor structure that is sufficiently thin to confine carrier movement on a length-scale comparable to their de Broglie wavelength, which is approximately 30 nm for an electron in GaAs at room temperature. Carriers' electronic and optical properties are defined in this case by quantum mechanical aspects of their behaviour that are not observable in bulk structures. A diagram of the most basic types of QWs that can be grown is shown in Figure 3.5. In this case, a GaAs/AlGaAs structure is grown on a GaAs substrate, as shown in Figure 3.5(a). The structure is made up of a GaAs layer with a thickness d sandwiched between much thicker layers of the alloy semiconductor AlGaAs, where d is chosen to be comparable to the de Broglie wavelength. GaAs and $\text{Al}_x\text{Ga}_{1-x}\text{As}$ are lattice matched within 0.1% for all x values, making GaAs/ $\text{Al}_x\text{Ga}_{1-x}\text{As}$ materials unique among III-V semiconductors. Because of this property, the growth of GaAs/ $\text{Al}_x\text{Ga}_{1-x}\text{As}$ heterostructures is simple and free of defects. At room temperature, the bandgaps of the two materials range from 1.42 eV for $x = 0$ to 2.168 eV for $x = 1$. The transition from direct to indirect bandgap occurs for AlGaAs materials at a certain value of Al content ($x = 0.44$), and the energy gap can be calculated using equation 3.7.

$$E_{g,\text{Al}_x\text{Ga}_{1-x}\text{As}} = x \cdot E_g(\text{GaAs}) + (1 - x) \cdot E_g(\text{AlAs}) \quad 3.7$$

The band discontinuity ratio between GaAs and $\text{Al}_x\text{Ga}_{1-x}\text{As}$ is unaffected by alloy composition (ΔE_c and ΔE_v are constant fractions, while ΔE_g varies with x). In the case of a typical barrier, an Al content of 30% ($x = 0.3$) is adopted. $\Delta E_g = 0.374$ eV for this composition, and ΔE_c and ΔE_v are 0.247 eV and 0.127 eV, respectively

[16]. An external light source with photon energy greater than the effective band gap produces excess electron–hole pairs by excitation of electrons from the valence band to the conduction band. Excited electrons quickly lose their excess energy and thermalize to the sub-band edges to take up Fermi energy distributions. After excitation, the electrons recombine to empty valence band states by spontaneous emission. The shape of the spectrum corresponds to the thermal distribution of carriers in the bands. Figure 3.5 (b) illustrates a transition of an electron between an occupied state at E_1 in the $n_z = 1$ sub-band in the conduction band and an empty state (i.e., a hole) at E_2 in the $n_z = 1$ sub-band in the valence band, resulting in emission of a photon of energy $h\nu = E_1 - E_2$ as required by energy conservation. This spontaneous emission process requires external excitation such as illumination, referred to as photoluminescence [17].

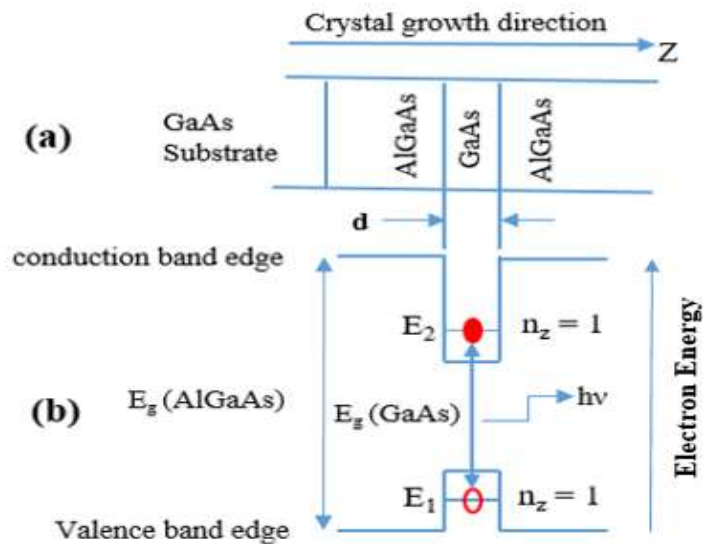


Figure 3.5: (a) A single GaAs/AlGaAs QW is depicted. The QW is formed by a thin GaAs layer sandwiched between two AlGaAs layers with a wider bandgap. (b) Spatial variation of the valence band and the conduction band, as well as the optical transition of an electron from a state in the $n_z = 1$ conduction sub-band to an empty state (hole) in the $n_z = 1$ valence sub-band, resulting in the emission of a photon with energy $h\nu = E_2 - E_1$.

3.6.4 Growth of Quantum Wires

One notable method for fabricating quantum wires or dots is to begin with a QW, which provides confinement along one direction. Then, by leaving ridges or mesas, selectively remove material to form wires or dots. Material removal is accomplished using electron-beam lithography, followed by etching. This method has the advantage of allowing the creation of any desired shape. However, because the electron beam must be scanned serially on surface, writing large area patterns is time consuming. Figure 3.6 depicts the formation of quantum wires. The standard QW layer can be patterned and etched to leave a free-standing strip of QW using photo- or electron- beam lithography. The latter may or may not be filled with barrier material overgrowth (in this case $\text{Ga}_{1-x}\text{Al}_x\text{As}$). As in QW, any charge carriers are still confined along the growth axis (z-axis) of the heterostructure, but they are now confined along an additional direction, either along x- or y-axis, depending on the lithography process. Within the confinement axis approximation, the wire can still be described by a parabolic dispersion relationship given by equation 3.2, which is analogous to bulk and in-plane motion within a QW.

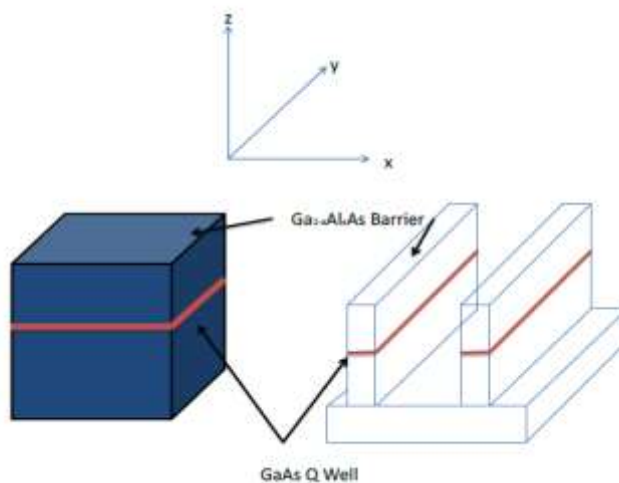


Figure 3.6: Schematic diagram showing the fabrication of a quantum wire.

3.6.5 Growth of Quantum Dots

Semiconductor quantum dots (QDs) have received a lot of attention in recent years due to their enormous potential in both applications and fundamental research [18, 19]. Especially, with the progress of epitaxial growth technology, it is now possible to precisely control the quantum dots in terms of size, composition, and density to achieve desired electrical and optical properties. Quantum dots may be the best candidate for the next generation of photonics devices, such as high-performance lasers and photodetectors. Semiconductor quantum dots have unique discrete states due to the three-dimensional confinement. It is widely acknowledged that quantum dots lasers have excellent temperature stability and low threshold currents due to their higher density of states as compared to quantum wells. QD detectors can cover a very wide range of wavelengths due to the different separate energy states in QDs based on their inter-band and inter-sub band transitions. QDs can be considered as "fake atoms" in basic research because they have separate energy states like atoms or molecules. As a result, different structures of QDs can be created in order to investigate different quantum effects or discover novel phenomena.

Over the last 20 years, few techniques have been used to fabricate QDs, such as lithography-based techniques that combine high-resolution electron beam lithography and etching, which have some drawbacks as described below:

1. Limitation of size prevents the observation of strong quantization effects.
2. Defect formation as a result of etching
3. Size non-uniformity.
4. Interfaces of poor quality.

5. Damage to the bulk crystal.

Stranski-Krastanov (SK) growth in lattice-mismatched systems is a novel and appealing method of fabricating defect-free 10 nm scale QDs. The SK technique involves growing a semiconductor thin layer on a substrate with a different lattice constant than the epilayer. In the SK growth method, the mismatched epitaxy is initially accommodated by biaxial compression in a layer-by-layer (2D) growth region known as the wetting layer. After a few monolayers are deposited, the strain energy increases, and the formation of islands (0D) becomes more advantageous than planar growth.

In such a system, the transition between coherently strained 2D growth and the onset of 0D island growth occurs after the deposition of a "critical thickness" epitaxial material (d_c). This critical thickness is calculated as follows:

$$d_c \cong \frac{a_s}{2|\varepsilon|} \quad 3.8$$

where a_s is the lattice constant of the substrate material. ε is the strain between the two materials which is defined as:

$$\varepsilon = \frac{a_s - a_l}{a_l} \quad 3.9$$

where a_l is the lattice constant of the epilayer.

This critical thickness (d_c) decreases as the lattice mismatch ($a_s - a_l$) between the epitaxial material and the substrate increases. The Stranski-Krastanov growth mode refers to the transition from purely 2D to 3D growth during the deposition of the strained epitaxial layer. Figure 3.7 depicts the SK growth mode of self-assembled quantum dots. In the first two phases of Figure 3.7 (a, b), a strained but uniform

layer of InAs grows with the same lattice parameter as the GaAs substrate. This results in the formation of the so-called wetting layer, which is a narrow QW. Strain, as shown in Figure 3.7.c, makes it energetically favourable for the formation of InAs 3D islands beyond the critical thickness.

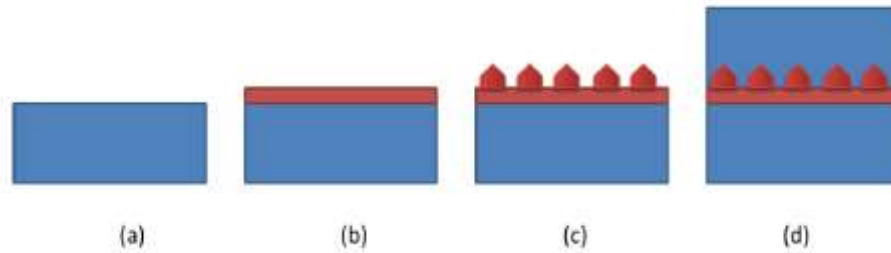


Figure 3.7: Stranski-Krastanov self-assembled QD growth mode (a)-(d) show the sequential stages of the growth of InAs/GaAs QDs. (a) depicts only the GaAs substrate; (b) InAs is deposited on the substrate: a thin, uniform layer grows, forming a narrow quantum well known as the wetting layer; (c) beyond a certain layer thickness, the strain caused by the lattice constant mismatch between the materials causes small islands of InAs to form; and (d) a capping layer of GaAs is grown over the dots for optical characterisation.

QDs form in the case of InAs/GaAs when approximately 1.7 monolayers (MLs) of InAs have been deposited. The critical thickness (d_c) increases as the indium composition decreases. For $\text{In}_{0.5}\text{Ga}_{0.5}\text{As}/\text{GaAs}$ QDs, for instance, d_c is around 4 MLs. It has been discovered that the lowest In composition that can support islanding of the $\text{In}_x\text{Ga}_{1-x}\text{As}$ layer is 25%. One advantage of SK growth of QDs, which is an in-situ technique, is that no processing is required. Because the dots are grown in situ, the homogeneous surface morphology is preserved, and defects are avoided. The underlying issue with this method is the size non-uniformity (about 10%) and the position uncontrollability of the QDs. Size control and arrangement of self-organized 0D structures are thought to be very important for obtaining excellent structural

properties. Modifying growth parameters such as deposition rates and temperature, the composition, size, shape and surface density of the dots can be controlled. The SK mode has been used to fabricate self-assembled quantum dots (SAQDs) from a variety of semiconductor materials, including III-V semiconductors ($\text{In}_x\text{Ga}_{1-x}\text{As}/\text{GaAs}$, $\text{In}_x\text{Ga}_{1-x}\text{As}/\text{AlGaAs}$, InP/GaInP), II-VI materials (CdSe/ZnSe) and wide bandgap nitrides (GaN/AlGaN).

3.7 CONCLUSION

Important concepts of low-dimensional semiconductor structures were presented in this chapter. Optical processes and carrier dynamics were also discussed only for the case of quantum wells and quantum dots. In addition, MBE growth technique, which was used to grow all samples investigated in this thesis was described. Furthermore, the fabrication process of self-assembled quantum dots studied in this thesis, which is critical to understanding their optical properties, was discussed in this work.

REFERENCES

- [1] A. Fox, Optoelectronics in quantum well structures, *Contemporary physics*, **37**, 111-125 (1996).
- [2] D. Miller, D. Chemla, D. Eilenberger, P. Smith, A. Gossard, W. Tsang, Large room-temperature optical nonlinearity in GaAs/Ga $_{1-x}$ Al $_x$ As multiple quantum well structures, *Applied Physics Letters*, **41**, 679-681 (1982).
- [3] R. Kelsall, I.W. Hamley, M. Geoghegan, *Nanoscale science and technology*, John Wiley & Sons, 2005.
- [4] M. Steer, D. Mowbray, W. Tribe, M. Skolnick, M. Sturge, M. Hopkinson, A. Cullis, Whitehouse, CR, R. Murray, Electronic energy levels and energy relaxation mechanisms in self-organized InAs/GaAs quantum dots, *Physical Review B*, **54**, 17738 (1996).
- [5] M.A. Herman, H. Sitter, *High-Vacuum Growth and Processing Systems*, in: *Molecular Beam Epitaxy*, Springer, 1996, pp. 81-134.
- [6] M. Yoshimoto, S. Murata, A. Chayahara, Y. Horino, J. Saraie, K. Oe, Metastable GaAsBi alloy grown by molecular beam epitaxy, *Japanese Journal of Applied Physics*, **42**, L1235 (2003).
- [7] R. Lewis, M. Masnadi-Shirazi, T. Tiedje, Growth of high Bi concentration GaAs $_{1-x}$ Bi $_x$ by molecular beam epitaxy, *Applied Physics Letters*, **101**, 082112 (2012).
- [8] G. Ciatto, M. Thomasset, F. Glas, X. Lu, T. Tiedje, Formation and vanishing of short range ordering in GaAs $_{1-x}$ Bi $_x$ thin films, *Physical Review B*, **82**, 201304 (2010).

- [9] G. Ciatto, E. Young, F. Glas, J. Chen, R.A. Mori, T. Tiedje, Spatial correlation between Bi atoms in dilute GaAs $1-x$ Bi x : from random distribution to Bi pairing and clustering, *Physical Review B*, **78**, 035325 (2008).
- [10] D. Sales, E. Guerrero, J. Rodrigo, P. Galindo, A. Yáñez, M. Shafi, A. Khatab, R. Mari, M. Henini, S. Novikov, Distribution of bismuth atoms in epitaxial GaAsBi, *Applied Physics Letters*, **98**, 101902 (2011).
- [11] G. Vardar, S. Paleg, M. Warren, M. Kang, S. Jeon, R. Goldman, Mechanisms of droplet formation and Bi incorporation during molecular beam epitaxy of GaAsBi, *Applied Physics Letters*, **102**, 042106 (2013).
- [12] X. Lu, D. Beaton, R. Lewis, T. Tiedje, M. Whitwick, Effect of molecular beam epitaxy growth conditions on the Bi content of GaAs $1-x$ Bi x , *Applied Physics Letters*, **92**, 192110 (2008).
- [13] I. Moussa, H. Fitouri, A. Rebey, B. El Jani, Atmospheric-pressure metalorganic vapour phase epitaxy optimization of GaAsBi alloy, *Thin Solid Films*, **516**, 8372-8376 (2008).
- [14] A. Ptak, R. France, D. Beaton, K. Alberi, J. Simon, A. Mascarenhas, C.-S. Jiang, Kinetically limited growth of GaAsBi by molecular-beam epitaxy, *Journal of Crystal Growth*, **338**, 107-110 (2012).
- [15] P. Blood, SEMICONDUCTOR PHYSICS| Quantum Wells and GaAs-Based Structures, (2005).
- [16] L. Jacak, P. Hawrylak, A. Wojs, Quantum dots, (1998).
- [17] A.B.F. KHATAB, Optical properties of nanostructured semiconductors grown by MBE on non-conventional GaAs substrates, University of Nottingham. Nottingham, (2014).

[18] D. Bimberg, M. Grundmann, N.N. Ledentsov, Quantum dot heterostructures, John Wiley & Sons, 1999.

[19] D.G. Deppe, H. Huang, O.B. Shchekin, Modulation characteristics of quantum-dot lasers: The influence of p-type doping and the electronic density of states on obtaining high speed, IEEE Journal of Quantum Electronics, **38**, 1587-1593 (2002).

CHAPTER 4: EXPERIMENTAL TECHNIQUES

This chapter describes the experimental methods used to investigate the optical and structural properties of the semiconductor structures studied in this thesis, namely photoluminescence (PL) spectroscopy, X-ray diffraction (XRD), scanning electron microscopy (SEM) and Raman spectroscopy. The experimental systems (hardware and software) are also presented. The growth of the samples and gamma radiation conditions used in this study are described in the relevant chapters.

4.1 PHOTOLUMINESCENCE

4.1.1 Principles of Photoluminescence

This section will look at photons re-emitted by interband luminescence after the semiconductor has been excited by a photon with an energy greater than the bandgap (E_g) of the semiconductor under investigation. Some physical processes in photoluminescence are more complex than those in absorption. This is because the mechanisms of energy relaxation in solids are closely related to light generation by luminescence. The thermal distributions of electrons and holes within their bands influence the shape of the emission spectrum.

In a photoluminescence experiment, incident light from a laser with energy above the material's bandgap is absorbed, exciting an electron from the valence band (VB) to the conduction band (CB) and producing an electron-hole pair. Following this optical excitation, holes and electrons develop spatially and temporally with characteristic times based on several relaxation processes, as shown in Table 4.1 [1].

Table 4.1: Fundamental processes in semiconductors.

Microscopic Process	Characteristic times (sec)
Carrier-carrier scattering	10^{-15} - 10^{-12}
Intervalley Scattering	10^{-14}
Intervalley Scattering	10^{-13}
Carrier-optical phonon thermalization	10^{-12}
Optical phonon-acoustic phonon interaction	10^{-11}
Carrier diffusion	10^{-11}
Auger recombination (when carrier density $>10^{20}$ cm $^{-3}$)	10^{-10}
Radiative recombination	10^{-9}
Lattice heat diffusion	10^{-8}

The electron-hole pair will then be thermalized by scattering mechanisms before recombining and emitting a photon with an energy (wavelength) corresponding to the bandgap. This process is known as band-to-band radiative recombination, and it is presented in Figure. 4.1(a) for a direct bandgap system. Photo-excited electron-hole pairs can also recombine non-radiatively via a defect state in the bandgap, as illustrated in Figure. 4.1(b). Unintentional impurities (e.g. oxygen, carbon) and defects caused by dislocations and point defects during growth (clustering, vacancy or interstitial) can cause defect states within the bandgap. The energy emitted by carriers recombining via defect states is converted into crystal vibrations and heat (phonons). As a result, the intensity of the PL emission will be closely associated with the density of the defects that reduce the emission. Moreover, the main PL spectral parameters are closely related to the properties of the material, and PL

intensities provide useful information about the efficiency of radiative recombination. For device applications, it is important to understand the competition between radiative and non-radiative recombination processes. The measurement of PL spectra at different excitation intensities can also influence the nature of recombination; for example, a relatively high excitation intensity will significantly perturb the occupation of states within the VB and CB and shift the radiation energy produced by recombination.

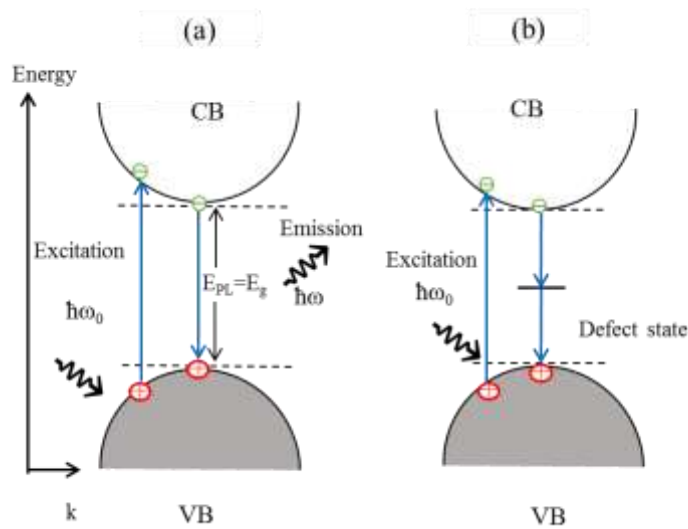


Figure 4.1: The basic mechanisms of recombination after photo-excitation are depicted in a schematic diagram. Carrier recombination processes demonstrating (a) band-to-band radiative recombination and (b) non-radiative recombination via defect states between the CB and the VB.

The Einstein coefficient A defines the rate of spontaneous emission of radiative transitions between two levels as illustrated in Figure 4.2 and is given by:

$$A = \frac{1}{\tau_R} \tag{4.1}$$

where τ_R is natural radiative lifetime of the excited state.

The radiative emission rate, if the upper level has a population N at time t , is given by:

$$\left(\frac{dN}{dt}\right)_{radiative} = -AN \quad 4.2$$

This rate equation can be resolved to give:

$$N(t) = N(0) \exp(-At) = N(0) \exp\left(-\frac{t}{\tau_R}\right) \quad 4.3$$

The Einstein coefficient A is directly proportional to the B coefficient, which gives the probability of absorption [2].

$$A = \frac{8\pi h\nu^3}{c^3} B \quad 4.4$$

where c is speed of light, ν frequency of radiation and h is Planck constant.

This equation states that transitions with a high probability of absorption also have a high probability of emission.

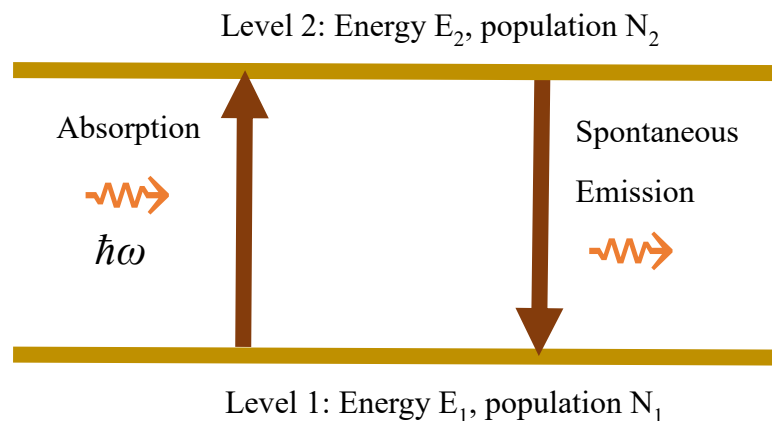


Figure 4.2: Spontaneous emission and absorption, transitions between two levels of an atom in the presence of electromagnetic radiation.

The relationships between the Einstein coefficients A and B expressed by equation 4.2 have been derived for an atom in equilibrium with black body radiation.

The luminescence intensity (I) can be written at frequency (ν) as follows:

$$I(h\nu) \propto |M|^2 g(h\nu) \times \text{Level occupancy factor} \quad 4.5$$

where the level occupancy factor indicates the possibility that the relevant lower level is empty and the upper level is occupied.

The occupancy conditions for photon emission between the separate energy levels E_1 and E_2 are described as follows: a valence band state of energy E_1 is emptied (filled with a hole) and a conduction band state of energy E_2 is filled with an electron.

Fermi functions f_c and f_v corresponding to the conduction and valence bands, respectively, specify the probabilities that these occupancy conditions are satisfied for different values of E_1 and E_2 . The probability $f_e(\nu)$ that the emission condition is satisfied for a photon of energy $h\nu$ is the product of the probabilities that the upper state to be full and that the lower state to be empty.

$$f_e(\nu) = f_c(E_2)[1 - f_v(E_1)] \quad 4.6$$

The light is emitted between the electron and hole states that are thermally occupied and will consequently only be emitted within a narrow energy range from the lowest levels in the excited state band. In contrast, photons can be absorbed into any state within the excited state band, regardless of how far above the bottom of the band they are. In addition to radiative emission, the electron can lose energy as heat by emitting phonons, or it can transfer energy to defects known as traps. If

these non-radiative processes occur on a faster time scale than the radiative transitions, only a very small number of photons will be released. The efficiency of luminescence η_R is given in this case by:

$$\eta_R = \frac{1}{1 + \tau_R/\tau_{NR}} \quad 4.7$$

where τ_R and τ_{NR} are the radiative and non-radiative lifetimes, respectively.

When $\tau_R \gg \tau_{NR}$, η_R is then too small and the light emission is not efficient. As a result, effective luminescence requires that the radiative lifetime be smaller than the non-radiative lifetime [3].

PL is defined as the spontaneous emission of light from a material that is being optically excited. In 1888 Wiedemann introduced the term "luminescence" where the literal translation from Latin of this term is "weak glow". The prefix photo demonstrates that this luminescence is caused by photoexcitation. Luminescence can happen for a variety of reasons and for varying lengths of time. When a photon is absorbed by a material, the resulting luminescence is classified into two types: fluorescence and phosphorescence. In the case of fast emission (ns time scale), luminescence is known as fluorescence, whereas slow emission (hours or even days) is known as phosphorescence.

PL spectroscopy is a technique for determining the impact of defects and impurities on the physical optical properties of a material. It provides information on the energy states and the quality of semiconductor structures containing quantum wells, wires, or dots. In the case of PL in semiconductors, the excitation is carried out using an optical source with a higher energy than the investigated sample's bandgap. The photons are absorbed by the material, where they excite electrons from the valence band to the conduction band, resulting in electron-hole pairs. The

number of electron-hole excited pairs varies with the intensity of the incident photons. Excitons may form when holes and electrons are relaxed to their band edges. By the end of the process, these pairs can either radiatively recombine by emitting photons or non-radioactively recombine via defects, surface, or Auger recombination. As a result, the photon spectrum emitted provides useful information about the electronic properties of materials, such as bandgap and defect density. Figure 4.3 illustrates an electron transition from the valence band (VB) to the conduction band (CB) via optical excitation (Figure 4.3 (a)), followed by relaxation to the band's edge (Figure 4.3 (b)). After that, an electron-hole pair is formed, and a photon is emitted (Figure. 4.3 (c)).

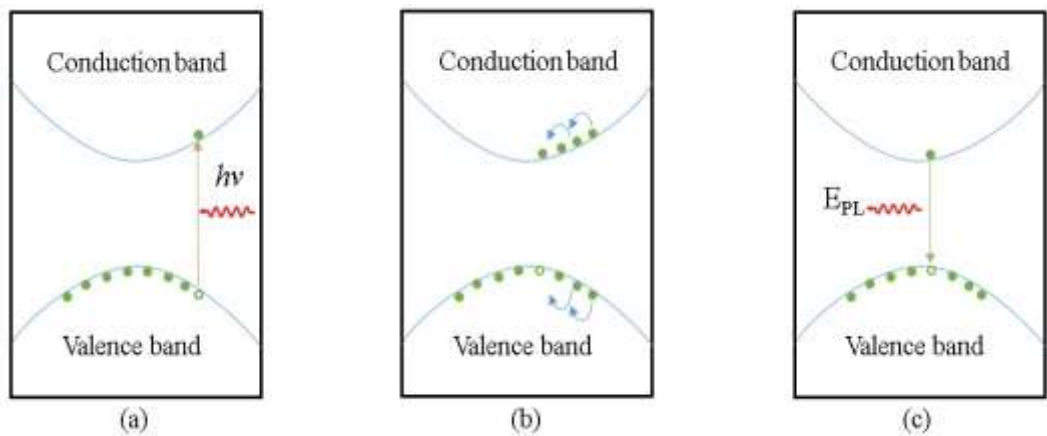


Figure 4.3: Illustration of the processes involved in PL (a) photo-excitation from the valence band to the conduction band, (b) intra-band relaxation and (c) recombination, which leads to PL emission [4].

A rich source of information about the photoexcited material is provided by collecting and analysing the emitted light. The PL spectrum gives the energies of photons emitted, which is a direct indicator of the levels of electronic energies. The PL intensity provides a measure of the relative rates of radiative and non-radiative

recombination. For device applications, understanding the competition between radiative and non-radiative recombination paths is important.

The PL technique is simple, versatile, and non-destructive, and does not require any sample preparation or environmental control. Since the sample is optically excited, no junctions or electrical contacts are required, and high resistivity materials present no real challenges. For this property, the PL technique is well suited for investigating samples with higher resistivity. In the same situation, another advantage of the PL is that the luminescence can be examined in various regions of the sample's surface. The main disadvantage of PL technique is its reliance on optical transitions: the sample under investigation should emit photons. Some semiconductors, such as indirect bandgap semiconductors, have essentially very low PL efficiency because the valence band maximum and the conduction band minimum do not have the same value in momentum space. These materials' relaxed states are thus based on non-radiative recombination processes. In general, PL cannot be used to accurately estimate the density of traps and impurities. When these level states are radiative, they are easily identified in the PL spectrum, and the intensity of the PL peaks provides a relative measure of their presence in the sample. Nonetheless, the absolute density of these states is measured differently [5].

4.1.2 System Hardware Implementation

The block diagram and images of the PL system used in this study are depicted in Figures 4.4, 4.5, 4.6, 4.7 and 4.8. The following sections describe some key components of the PL system which operates at temperatures ranging from 10K to 300K.

4.1.2.1 Spectrometer and Detectors

The emitted photoluminescence was scattered using a grating spectrometer to allow for spectral investigation. The spectrometer used in this study is an Andor 500i spectrometer with a focal length of 500 mm and an aperture of F/6.5 (see Figure 4.4). The Shamrock 500i spectrometer, which is fitted with a CCD camera, features a triple grating turret that makes it simple to select and exchange gratings. The triple grating turret can be easily removed or replaced by a different turret with new gratings. The gratings are interchangeable indexed triple turret with three distinct gratings (300 grooves/mm at 3000 nm blaze, 600 grooves/mm at 2000 nm blaze, and 1200 grooves/mm at 500 nm blaze). The slit widths for entry and exit can be manually or motorised adjusted from 10 μm to 2.5 mm. The CCD camera detector fitted in the spectrometer exit port converts incident photons to electronic signals, allowing it to cover a wide range of wavelengths [6].

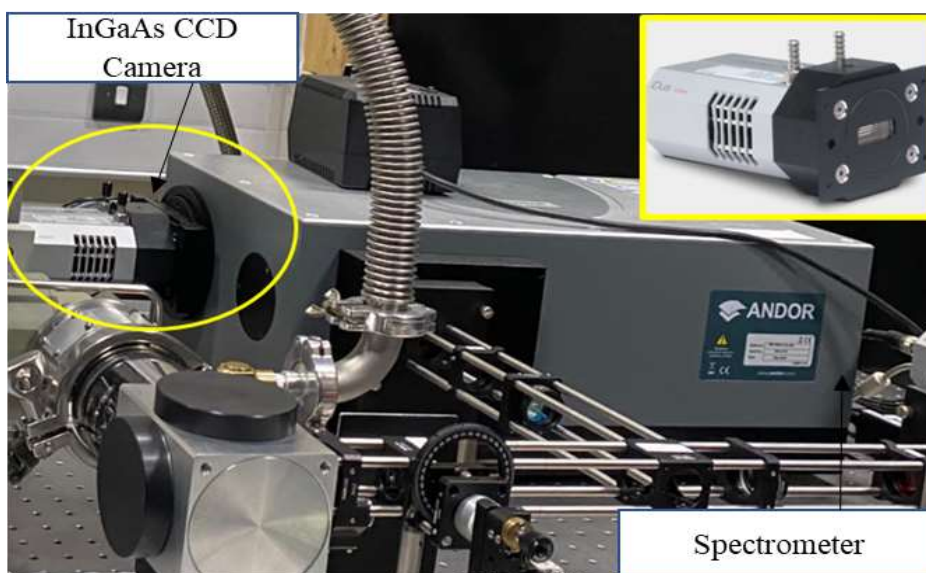


Figure 4.4: Photograph of the Andor Shamrock 500i spectrometer and InGaAs CCD camera fitted to the exit of the spectrometer.

The InGaAs and Si CCD detectors used in the PL system have high sensitivity and can cover optical wavelength ranges of 600 nm - 1.7 μm and 300 nm - 1000 nm, respectively (see Figure 4.5). In this study only the InGaAs detector was used.

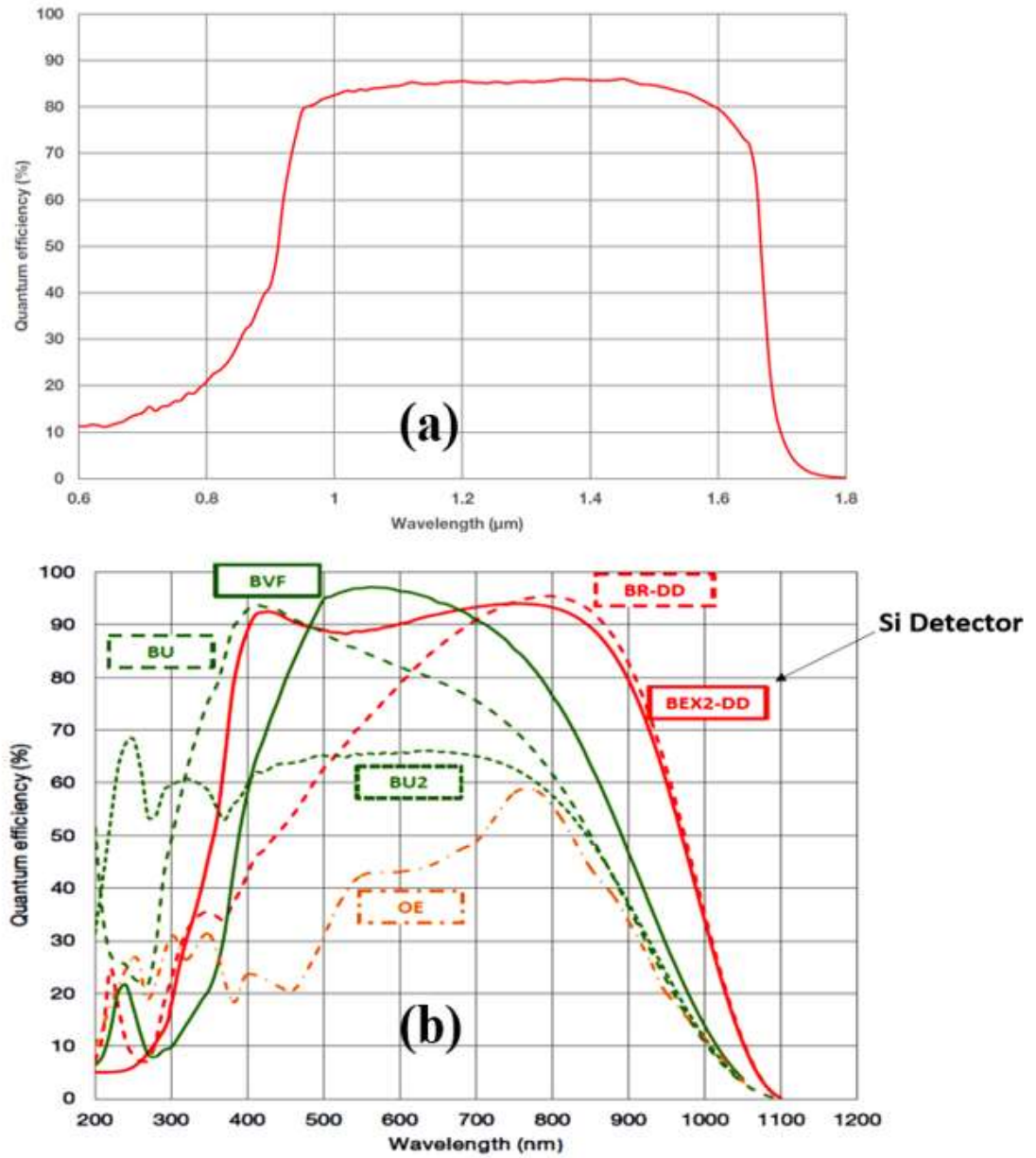


Figure 4.5: The efficiency response curves of (a) InGaAs CCD detector and (b) Si CCD detector.

4.1.2.2 Lasers and Optics

To excite the sample, the PL system uses three types of laser sources, blue, green, and red lasers with wavelengths of 473 nm, 532 nm and 655 nm, respectively. The laser power incident on the sample is controlled manually using a neutral density filter. A beam splitter is used to shine the laser onto the sample and direct the PL signal to the appropriate spectrometer (one fitted with an InGaAs CCD and the other with a Si CCD). In addition, a long pass filter is installed in front of each monochromator entrance slit to eliminate undesirable high-order lines of the laser light. The PL setup also includes a number of optics, such as lenses and mirrors, to focus the PL signal onto the entry slit of the selected spectrometer and the laser light onto the sample. Figures 4.6 and 4.7 depict the setup configuration of the PL system used in this work.

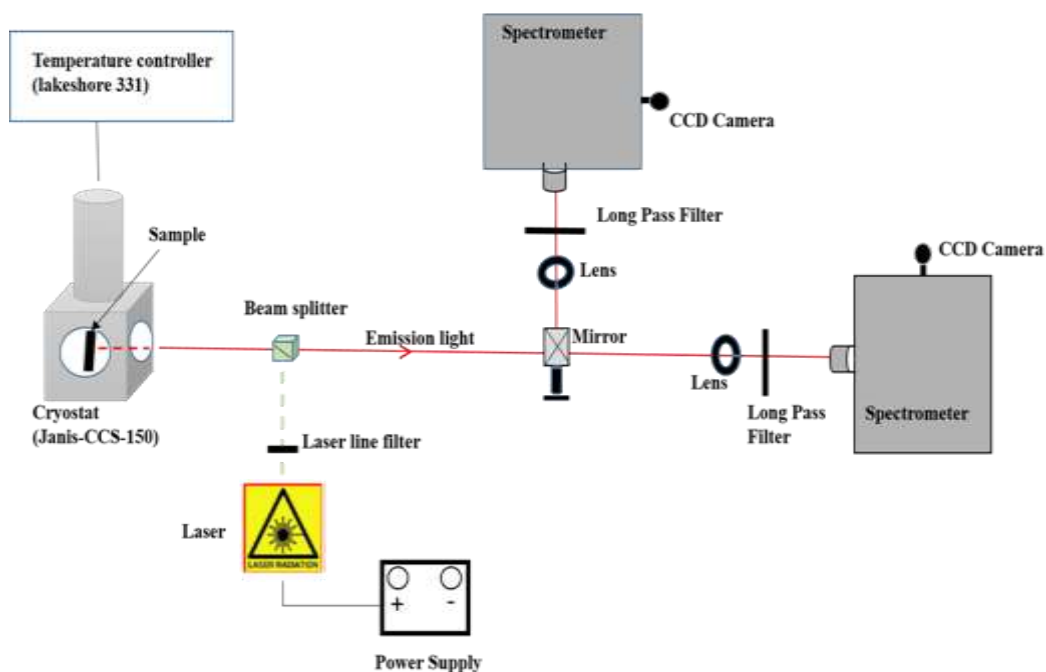


Figure 4.6: A schematic diagram of the photoluminescence apparatus.

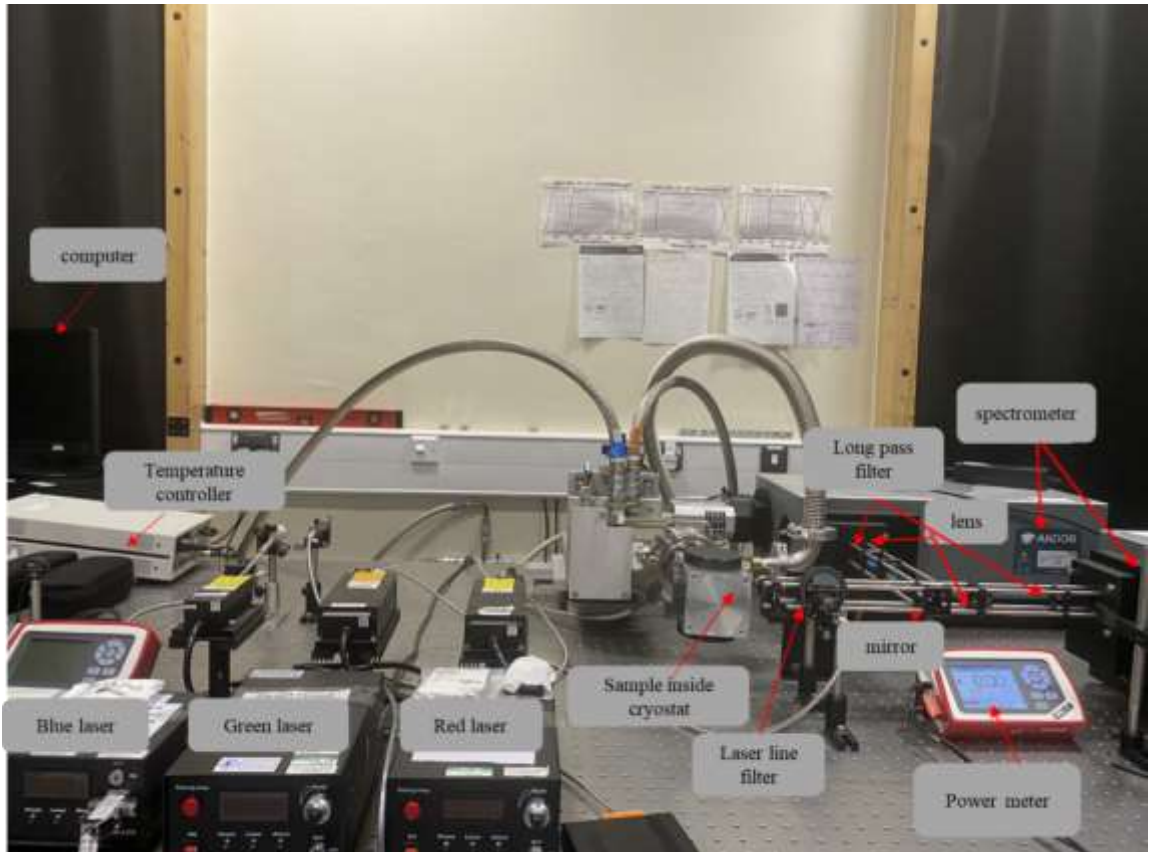


Figure 4.7: Photograph of the photoluminescence apparatus.

4.1.2.3 Cryostat and Temperature Controller

A state-of-the-art cryostat, model Janis CCS-150, was used for temperature-dependent PL measurements. A temperature controller, model Lake Shore 331, and a cryostat have been installed to control the temperature of the samples. Furthermore, thermal sensors and a built-in sample holder are also included (see Figure 4.8). The refrigeration principle is based on a closed-cycle flow of helium gas (He) through a compressor, which produces temperatures ranging from 10K to 300K.

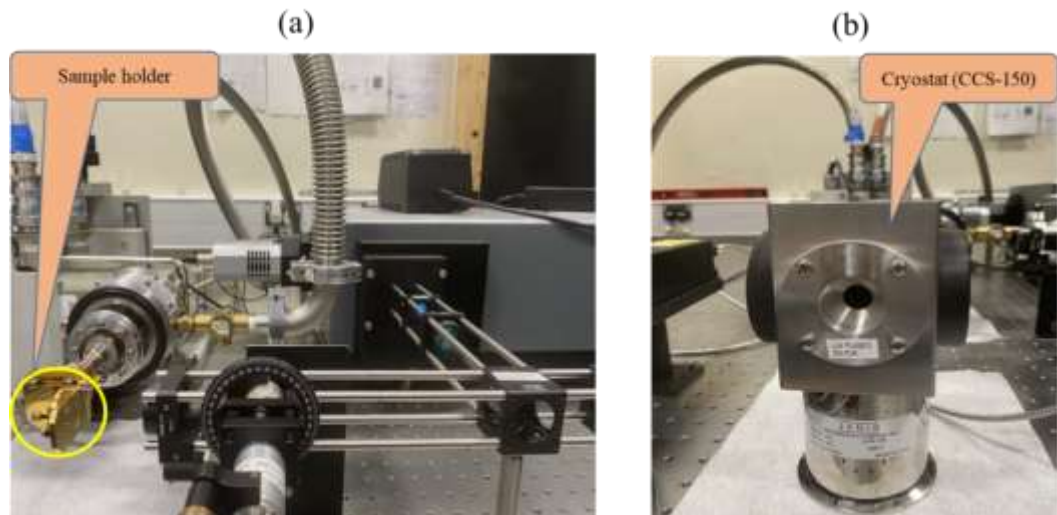


Figure 4.8: Photograph of (a) sample holder, (b) cryostat model Janis CCS-150.

4.1.2.4 Computer Interface

The spectrometer and CCD cameras are connected to a computer via USB ports and used Windows 10 platform.

4.1.2.5 System Controlling Software

The equipment of the PL system is remotely controlled using Andor's Solis software. It has several features for data acquisition as well as monitoring and controlling of the various PL system components. The software, for instance, can control the turret's three gratings, side input slits, shutters, CCD cameras and spectrometers.

4.1.3 Photoluminescence Measurements

This section provides some key details about the PL measurements performed for the study described in this thesis. Low-temperature photoluminescence measurements were carried out at temperatures ranging from 10 K to 300 K using

a variety of excitation sources with varying power ranges, as described in sections 4.1.1. The samples are mounted in a closed cycle Helium-cooled cryostat. The PL system's excitation light was generated by a solid-state green laser with a wavelength of 532 nm and an energy of approximately 2.33 eV over a wide power output range. It is important to note that the energy of the green laser used exceeds the band gap of the materials investigated and only small excitation laser powers (few mW) were used to produce good PL signals. However, the signal-to-noise is determined also by the quality of the material and detector sensitivity. In this experiment, InGaAs detector which covers the infrared range was used. Finally, the spectrum is recorded and stored in the computer.

4.2 STRUCTURAL CHARACTERIZATION

X-ray diffraction (XRD), scanning electron microscopy (SEM) and Raman spectroscopy techniques were used in order to obtain important information about the epitaxial layers such as composition, thickness, and strain in bulk materials and quantum dots.

4.2.1 X-ray Diffraction

4.2.1.1 Principle of XRD

X-ray diffraction (XRD) is one of the most common methods for characterising epitaxially grown semiconductor layers. XRD provides a measure of the material's long-range order. X-rays can penetrate the depth of the sample surface and provide valuable information about material composition, thickness, quality, strain, and relaxation (mismatch). X-rays are appropriate for this purpose because their wavelength ($= 1.54 \text{ \AA}$ produced by a Cu source) is comparable to the distance

between the atoms in the crystal. An incident X-ray beam on a crystal lattice will be diffracted and interfere with itself, resulting in constructive and destructive interference. The diffraction of an X-ray beam by crystal lattice planes is shown in Figure 4.9. In case of the x-rays of wavelength λ incident on the parallel planes of atoms, with a spacing d between the planes, the peaks of Bragg (constructive interference) occur when the law of Bragg is satisfied:

$$n\lambda_{hkl} = 2d_{hkl}\sin(\theta_B) \quad 4.8$$

where n is an integer, θ_B represents the angle of Bragg and hkl are Miller indices for the set of planes analysed.

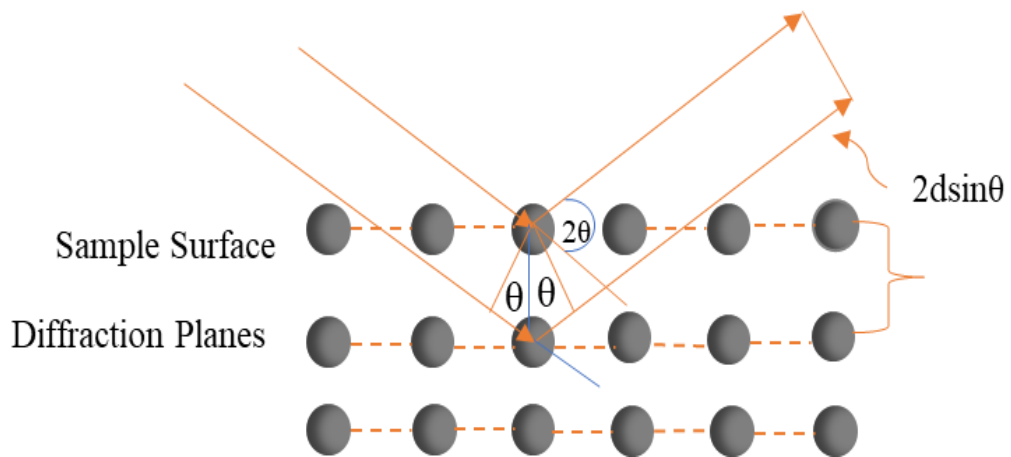


Figure 4.9: A geometrical diagram depicting the diffraction of an X-ray beam by crystal lattice planes. Orange arrowheads represent X-ray beam wave fronts, where deeper penetrating X-rays returning from diffraction planes have shifted wavefront.

To undergo constructive interference for the diffracted X-ray beam, the difference in distance travelled by the diffracted waves must be an integer multiple of wavelengths. Diffraction measured away from the Bragg angle will have a very low intensity, forming a Bragg peak with a finite linewidth. The greater the number of

diffraction planes, the greater the diffraction intensity and the narrower the measured peak width. Peak linewidths will approach the bulk crystal limit with improved lattice perfection and will broaden in the presence of defects such as structural disorder and dislocations.

XRD will show two Bragg peaks in close proximity that correspond to the substrate and epilayer lattice parameters for a compressively strained epitaxial growth on a substrate. This is due to the vertical deformation of the lattice cell in the epilayer when it is lattice matched to the substrate in the growth plane. A diagram of the possible strain states in a compressively strained film is shown in Figure 4.10. Using equation 4.8, the layer with the larger lattice parameter will diffract at a smaller angle, resulting in negative peak splitting (with respect to the substrate), whereas the layer with the smaller lattice parameter will diffract at a larger angle, resulting in positive peak splitting (with respect to the substrate). XRD measurements, when combined with Vegard's law [7], which describes the relationship between composition and an alloy lattice parameter, allows for an accurate assessment of the composition of ternary alloys (such as $\text{GaAs}_{1-x}\text{Bi}_x$).

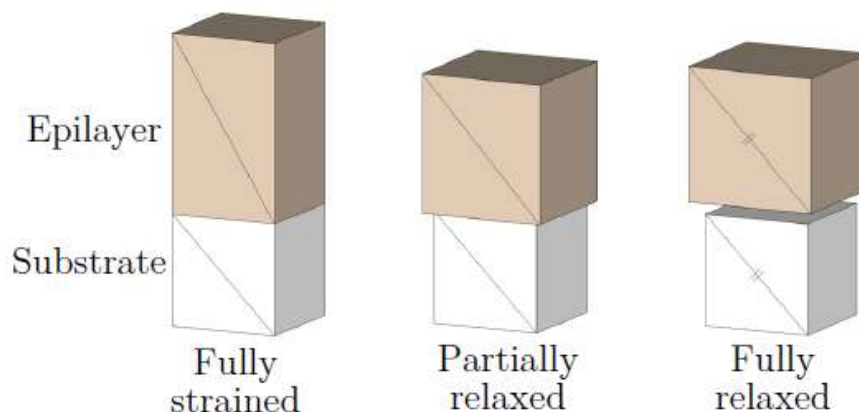


Figure 4.10: A diagram showing the various biaxial compressive strain states for a cubic epitaxial film with a lattice parameter larger than the substrate material [8].

4.2.2 Scanning Electron Microscopy (SEM)

Scanning Electron Microscopy (SEM) is a powerful technique for high-resolution analysis of a wide range of materials. An SEM is a type of electron microscope that uses a fine beam of focused electrons to scan the surface of a sample. The microscope records information about the interaction between the electrons and the sample, creating a magnified image. SEM has the potential to magnify an image up to 2 million times. In SEM, a focused beam of electrons is directed onto a specimen by an electron gun. Electron interactions with the elements in the specimen reveal the chemical composition and structure of the specimen. The electron beam scans the specimen using a raster pattern from top to bottom and side to side. This causes the electrons from the beam (primary electrons) to scatter at the surface of the specimen, resulting in secondary electrons, backscattered electrons, and characteristic X-rays. For SEM imaging, data, which is collected over surface areas ranging from few tens of nm up to few mm, is subsequently collated to form two-dimensional greyscale electron images [9].

Important components of all SEMs are shown in Figure 4.11 and includes the following [10, 11]:

1. Electron source (or gun) that generates electrons at the top of the microscope column.
2. Anode that has a positive charge, attracting the electrons to form a beam.
3. The condenser lens which controls the size of the beam and determines the number of electrons in the beam. The size of the beam will define the resolution of the image.

4. Scanning coils that deflect the beam along x and y axes in order to scan in a raster fashion over the surface of the sample.
5. Objective lens which is the last lens in the sequence of lenses that generate the electron beam. As this lens is closest to the sample, it focuses the beam to a very small spot on the sample.

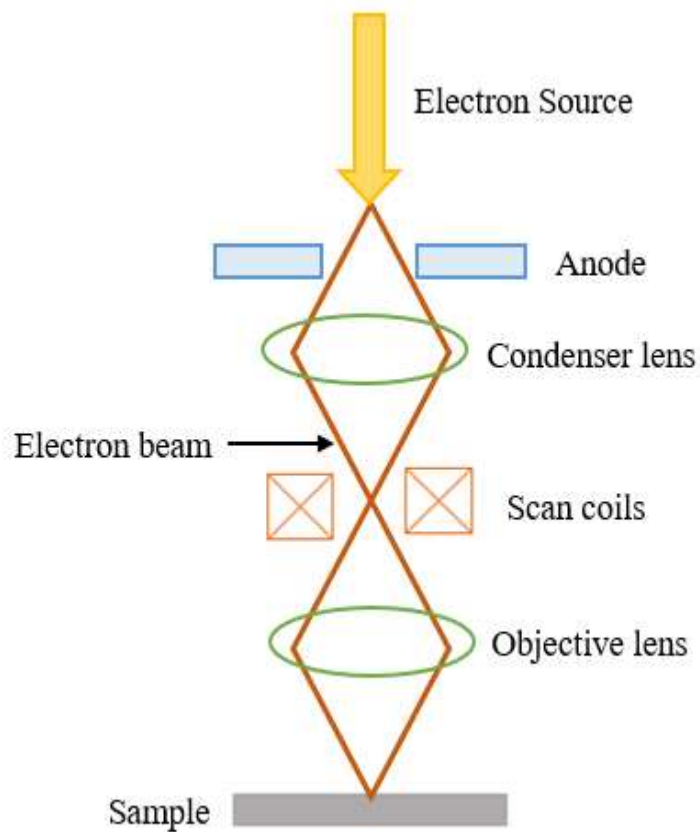


Figure 4.11: schematic diagram of scanning electron microscopy (SEM) components.

4.2.3 Raman Spectroscopy

Raman spectroscopy is used to investigate material properties such as chemical structure and crystallinity. It is based on inelastic light scattering (Raman scattering), in which the scattered light has a different wavelength than the incident

light. When a semiconductor is illuminated with monochromatic light, the majority of the scattered light has the same wavelength. However, only a small portion of the scattered light has a wavelength that differs from the incident wavelength [4]. Raman scattering is classified into two types as shown in Figure 4.12: Stokes scattering and Anti-Stokes scattering. Both types contain information about the material and its molecular composition.

1. Stokes scattering: the photon transfers energy to the molecule. The emitted photon has a lower energy than the absorbed photon.
2. Anti-Stokes scattering: the molecule transfers energy to the photon. The emitted photon has a higher energy than the absorbed photon.

In addition to inelastic scattering, elastic scattering can also appear. Elastic scattering at the same energy as the incident radiation is named Rayleigh scattering. Light scattering is a two-photon process in which one photon is absorbed and another photon is emitted at the same time. Figure 4.12 shows that the photons are most often emitted with the same frequency as the incident photon (Rayleigh scattering), however, photons sometimes lose or gain energy due to molecular interactions and are thus frequency shifted (Figure 4.12a). In Rayleigh scattering, the excited radiation field of molecular electrons matches the frequency of incident photons, therefore when the photon is emitted, the molecule returns to its previous electronic ground state. On the other hand, Stokes scattering and anti-Stokes scattering, are inelastic processes in which molecular electrons oscillate in response to photon excitation [12, 13]. The previous and the resulting electronic ground states are distinct. The emitted photon is frequency-shifted, and the difference from the incident frequency reflects energy that corresponds to specific molecular vibrational frequencies (Figure 4.12b). At thermal equilibrium, molecules in the

electronic ground state are more frequent, thus photons predominantly experience a Stokes shift [4], which is used in majority of Raman applications. In general, only a small part from about every 10^6 – 10^8 photons is inelastically scattered [12, 14].

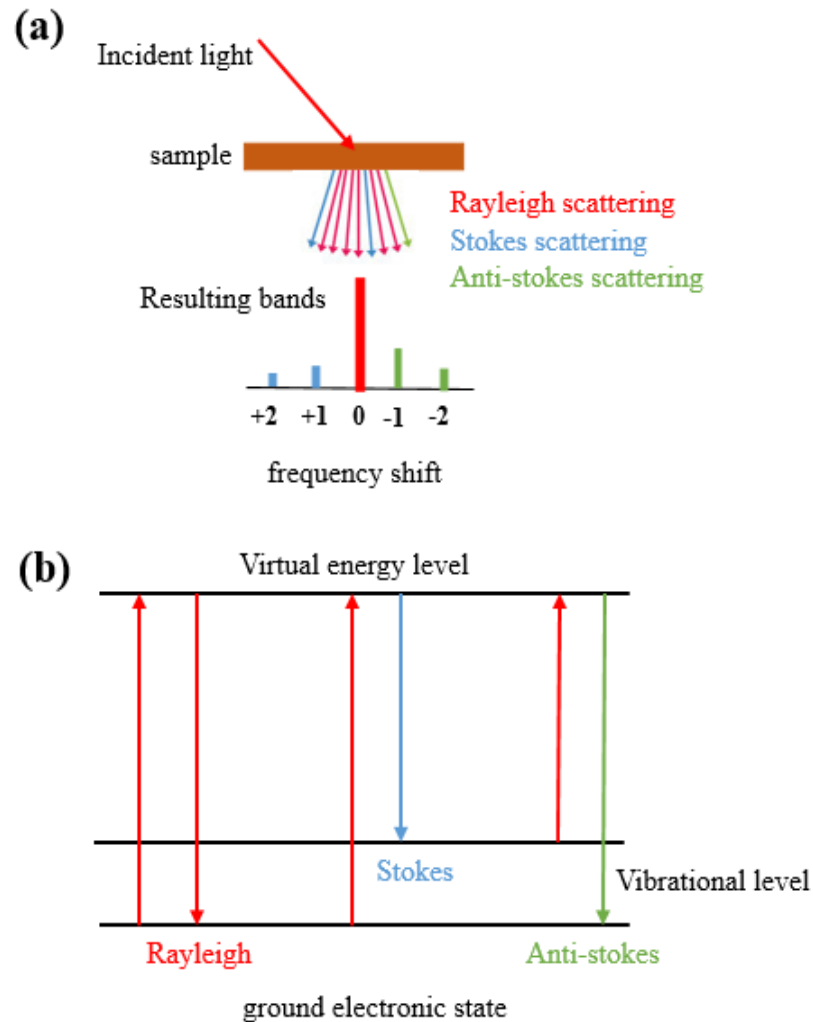


Figure 4.12: Types of light scattering. (a) Raleigh, Stokes, and anti-Stokes scattering and the resulting frequency shift relative to the incident light. (b) Molecular energy levels corresponding to the type of light scattering.

REFERENCES

- [1] J. Shah, Hot electrons and phonons under high intensity photoexcitation of semiconductors, *Solid-State Electronics*, **21**, 43-50 (1978).
- [2] M. Fox, Optical properties of solids, in, *American Association of Physics Teachers*, 2002.
- [3] H. Alghamdi, Optical and structural properties of GaAsBi and InGaBiAs nanostructured semiconductors grown by Molecular Beam Epitaxy, in, *University of Nottingham*, 2020.
- [4] F. Al Mashary, Investigation of the Electrical Properties of Transparent Conductive Oxides Thin Semiconductor Films Grown by Various Techniques, in, *University of Nottingham*, 2019.
- [5] T.H. Gfroerer, Photoluminescence in analysis of surfaces and interfaces, *Encyclopedia of analytical chemistry*, **67**, 3810 (2000).
- [6] S. Alhassan, Investigation of structural, electrical and optical properties of doped dilute GaAsBi grown by molecular beam epitaxy, in, *University of Nottingham*, 2022.
- [7] L. Vegard, *Zeitschrift für Physik a Hadrons and Nuclei, Physics and Astronomy*, **5**, 17-26 (1921).
- [8] J. Steele, Structural and optical studies of GaAs_{1-x}Bi_x and p-Bi₂O₃ for optoelectronic devices, (2015).
- [9] L. Larby, A. Lundberg, Primary Study of the Phase Relationship in the MgO-"V₂O₃" System at 1873 K and pO₂= 10⁻¹¹ atm, in, 2018.
- [10] R.F. Egerton, *Physical principles of electron microscopy*, Springer, 2005.
- [11] L. Reimer, *Transmission electron microscopy: physics of image formation and microanalysis*, Springer, 2013.

- [12] E. Brauchle, K. Schenke-Layland, Raman spectroscopy in biomedicine—non-invasive in vitro analysis of cells and extracellular matrix components in tissues, *Biotechnology journal*, **8**, 288-297 (2013).
- [13] I. Georgakoudi, W.L. Rice, M. Hronik-Tupaj, D.L. Kaplan, Optical spectroscopy and imaging for the noninvasive evaluation of engineered tissues, *Tissue Engineering Part B: Reviews*, **14**, 321-340 (2008).
- [14] M.M. Mariani, V. Deckert, Raman Spectroscopy: Principles, Benefits, and Applications, *Methods in Physical Chemistry*, 419-444 (2012).

CHAPTER 5: THE EFFECT OF GROWTH TEMPERATURE ON THE STRUCTURAL AND OPTICAL PROPERTIES OF DILUTE GaAs_{1-x}Bi_x EPILAYERS GROWN BY MOLECULAR BEAM EPITAXY

This chapter presents a detailed analysis of the effect of the growth temperature on the structural and optical properties of GaAs_{1-x}Bi_x epitaxial layers grown by Molecular Beam Epitaxy (MBE) on conventional (100) GaAs substrates using various techniques such as X-ray diffraction (XRD), Scanning Electron Microscopy (SEM), Raman spectroscopy and its associated hole concentration and photoluminescence (PL). In addition, a brief literature review is presented.

5.1 INTRODUCTION

Dilute III-V bismide semiconductors materials such as GaAs_{1-x}Bi_x alloys display strong reduction in the band gap when only a small percentage of bismuth atoms is incorporated into the lattice of the host material like GaAs which has a band gap energy of 1.424 eV at 300 K. Particularly, a few percent of Bi incorporated into GaAs, i.e. GaAs_{1-x}Bi_x with x being the Bi composition, leads to a giant bowing in the band gap energy (~ 88 meV/%Bi) [1], as well as an increase of the spin-orbit band splitting which helps reduce the non-radiative Auger recombination [2, 3]. In addition, the electron spin properties, which depend critically on the spin-orbit (SO) interaction, can be tuned in dilute bismides, making them suitable candidates for spintronic applications. It is important to note that the conduction band is barely affected by the Bi atoms. These remarkable properties such as reduction of the band

gap make $\text{GaAs}_{1-x}\text{Bi}_x$ a suitable material for several device applications such as multi-junction solar cells [4], photonic devices [1] and long-wavelength optoelectronic devices [5]. It is well known that the growth temperature of III-V alloys can significantly influence their crystalline quality. In fact, substitutional incorporation of Bi into the host lattice of III-V compounds requires low temperature growth. However, the growth of $\text{GaAs}_{1-x}\text{Bi}_x$ is more complicated than the growth of conventional III-V alloys. This is mainly due to the high tendency of Bi to surface segregate during growth, which requires the growth temperature to be lowered to ($< 400\text{ }^\circ\text{C}$) [6]. Low growth temperature of GaAs causes an increased density of defects as well as it leads to degradation of the optical quality of the alloys [6]. For instance, growing GaAs at temperatures lower than the optimal growth temperatures ($\sim 580\text{--}600\text{ }^\circ\text{C}$) leads to the creation of many point defects, such as As-antisites (As_{Ga}), As-interstitials (As_i) and Ga vacancies [7, 8]. Additionally, it is found that as the growth temperature decreases deep level defects are generated in GaAs and their concentrations are enhanced [7, 9]. Nevertheless, using Bi as a surfactant during the growth of GaAs at low temperatures has proven to enhance surface migration, to reduce the density of defects and to suppress the formation of traps in GaAs. However, in $\text{GaAs}_{1-x}\text{Bi}_x$ epilayers where Bi is substituting an arsenic atom, Bi related defects are created. To promote the Bi incorporation, the alloy needs to be grown using comparatively lower temperatures, and modified V/III flux ratios [10, 11]. By growing at $200\text{ }^\circ\text{C}$ using MBE, Lewis et al. reported a record Bi concentration of 22% [12]. However, the growth at low temperatures can generate more defects and inferior surface quality which deteriorates device efficiency. In the case of metalorganic vapour-phase epitaxy (MOVPE) growth, the Bi concentration is lower (3.5–3.7%) for an epilayer [13,

14], and 14% in structures with compositional inhomogeneity [15] since a comparatively higher growth temperature is required to decompose the organic precursor molecules. Recently, Jacobson et al. suggested that Bi solubility can be improved by the strain state of the epitaxial layer: Bi incorporation becomes more favourable if the growing epitaxial film is under tensile strain [16]. This concept allows increasing the Bi content without compromising the optimal growth temperature and provides an opportunity to grow an epilayer lattice matched to GaAs substrate. So far, the concept has been demonstrated for GaAsPBi alloys grown by MOVPE [17, 18]. Forghani et al showed that the quaternary alloy can be pseudomorphically grown on GaAs substrate with a reduced band gap of 1.01–1.11 eV, while Nattermann et al reported the first photoluminescence measurement of the quaternary alloy [18]. However, one of the key parameters that limits the Bi incorporation is the growth temperature. MBE allows for lower optimal growth temperature than MOVPE, hence a greater Bi incorporation in the epitaxial layer. From studies of the temperature dependent PL intensity, it was found that the growth temperature affects the density of shallow and deep electronic states in the band gap [19]. An order of magnitude increase in the hole trap concentration in GaAs_{1-x}Bi_x was reported when the growth temperature was decreased from 370 °C to 330 °C [9]. Hence, the optimization of GaAs_{1-x}Bi_x growth conditions to enhance the optical and electrical quality of the alloy is still a challenge. An in-depth study of the fundamental properties of GaAs_{1-x}Bi_x is strongly needed in order to explore its potential for commercial usage [6]. This work reports a systematic study of the effect of the growth temperature of GaAs_{1-x}Bi_x epilayers grown on semi-insulating (100) GaAs substrates by MBE on their structural and optical

properties by using XRD, SEM, photoluminescence, hole concentration and Raman measurements.

5.2 EXPERIMENTAL DETAILS

The GaAs_{1-x}Bi_x thin layers were grown by Shui-Qing Yu (Department of Electrical Engineering, University of Arkansas, Fayetteville, AR 72701, USA). In the following sections the effects of different growth temperatures on the structural and optical properties of GaAs_{1-x}Bi_x thin films grown on semi-insulating GaAs (100) substrates will be reported.

All GaAs_{1-x}Bi_x thin film samples investigated in this work have been grown by solid-source MBE on semi-insulating (100) GaAs substrates under identical growth conditions to explore the effects of growth temperature, T_G , on the structural and optical properties of the samples. For this purpose, a set of seven GaAs_(1-x)Bi_x epilayers were grown at $T_G = 300\text{ }^\circ\text{C}$, $310\text{ }^\circ\text{C}$, $320\text{ }^\circ\text{C}$, $325\text{ }^\circ\text{C}$, $340\text{ }^\circ\text{C}$, $345\text{ }^\circ\text{C}$ and $365\text{ }^\circ\text{C}$ and labelled as A, B, C, D, E, F and G, respectively, as shown in Table 5.1. The samples were first heated to a temperature of $610\text{ }^\circ\text{C}$ for 10 minutes to desorb the native oxide layer from the substrate surface. After that, an undoped GaAs buffer layer with a thickness of a 400 nm was formed at a growth temperature of $580\text{ }^\circ\text{C}$ and a growth rate of 1 monolayer per second. This was followed by a 20 min growth interruption during which the sample was cooled down to the appropriate T_G and the growth rate lowered to ~ 0.1 monolayer per second. After that, a 300 nm GaAs_{1-x}Bi_x layer was deposited using a relatively large Bi flux that was twice that of As, while maintaining an approximately equal flux of As and Ga. This places the growth conditions well within the Bi saturation regime, where an alloying limit is imposed by the low miscibility of Bi into GaAs. More detailed

information on the growth of $\text{GaAs}_{1-x}\text{Bi}_x$ is reported in Ref. [20]. The Raman measurements were performed by employing a Horiba Lab RAM Evolution micro spectrometer at room temperature using a 532 nm laser line. Laser excitation powers of 5.35 mW and 0.107 mW, were used to obtain data about the correlation of Bi concentration with PL results and the hole concentration, respectively. In addition, SEM data was acquired using a Helios Nano lab 650, FEI Company.

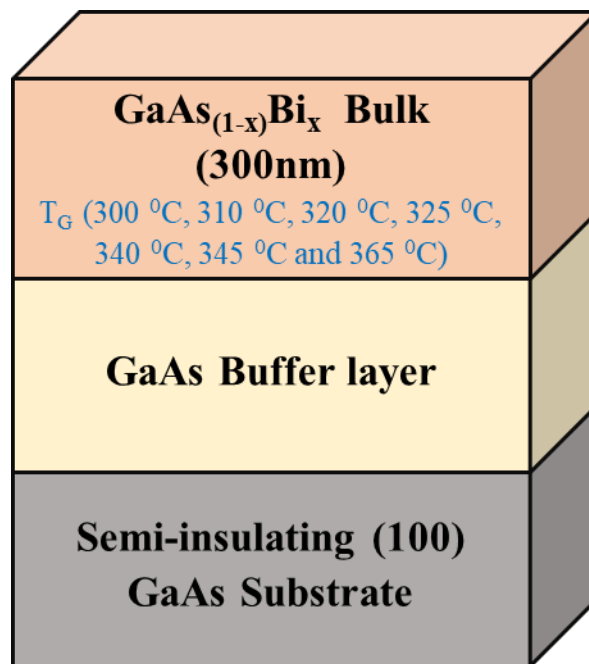


Figure 5.1: Schematic structure of the $\text{GaAs}_{1-x}\text{Bi}_x$ epilayers grown on (100) GaAs substrates.

Table 5.1: $\text{GaAs}_{1-x}\text{Bi}_x$ thin film samples investigated in this study.

Sample	A	B	C	D	E	F	G
T_G (°C)	300	310	320	325	340	345	365

5.3 RESULTS AND DISCUSSION

5.3.1 Structural Characteristics

5.3.1.1 X-ray Diffraction (XRD)

Figure 5.2 shows the XRD pattern for sample E ($T_G=340\text{ }^\circ\text{C}$) with a Bi concentration of 4.4%. The XRD pattern shows three well defined peaks located at 31.63° , 65.53° and 66.05° which are associated with the diffraction planes of (002) and (004) of $\text{GaAs}_{1-x}\text{Bi}_x$ and (004) of GaAs, respectively.

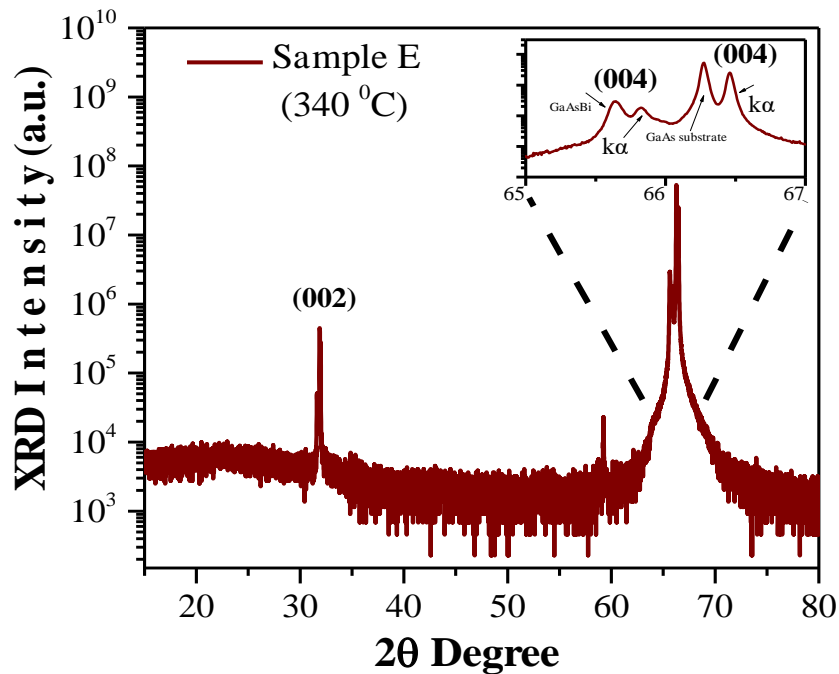


Figure 5.2: Diffraction pattern in the $\theta - 2\theta$ scan of X-ray diffraction measurement for sample E doped with Bi concentration of 4.4%. The inset shows the diffraction pattern in the region between $2\theta = 65.5^\circ$ and 67° , where two peaks are associated with $\text{GaAs}_{1-x}\text{Bi}_x$ and GaAs, and the other two additional peaks are due to the copper $k\alpha$ line originating from the copper target.

The detailed data shown in the inset of Figure 5.2 was used to find the trend of the displacement of the characteristic peak, (004), as a function of the concentration of

Bi. Figure 5.3 shows the XRD patterns obtained for all samples between $2\theta = 65^\circ$ and 67° . It is clearly seen that there is a displacement of the peak between 65.5° and 66° as a function of the bismuth concentration/growth temperature. Figure 5.4 illustrates the shift of the characteristic peak of XRD as a function of the concentration of Bi. It is important to point out the linear trend of $\text{GaAs}_{1-x}\text{Bi}_x$ (004) peak displacement as a function of Bi concentration.

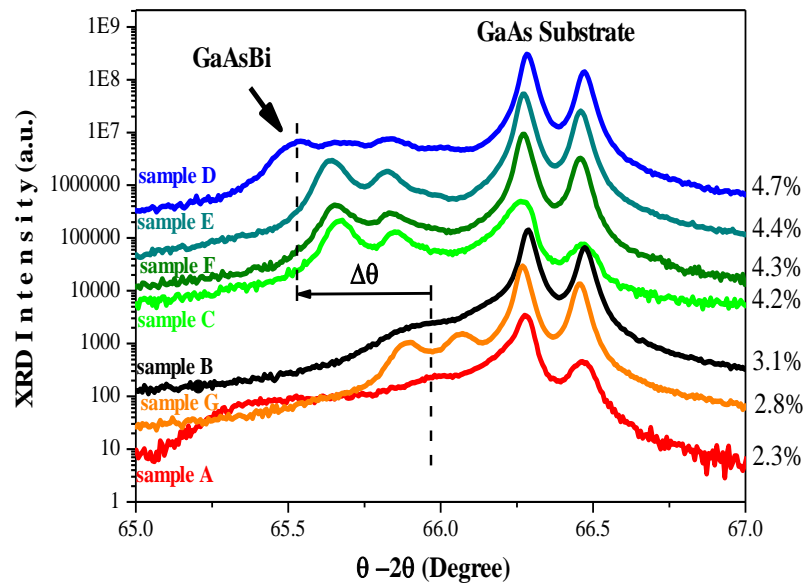


Figure 5.3: XRD patterns obtained for all samples between $2\theta = 65^\circ$ and 67° .

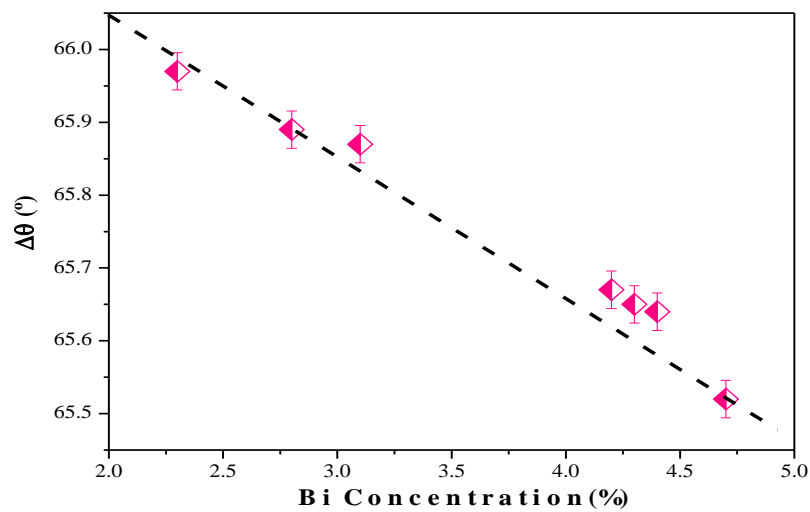


Figure 5.4: Displacement of characteristic peak (004) as a function of bismuth concentration.

5.3.1.2 Scanning Electron Microscopy (SEM)

Figure 5.5 shows the SEM images of the surfaces of all $\text{GaAs}_{1-x}\text{Bi}_x$ samples grown on (100) GaAs substrates at different growth temperatures.

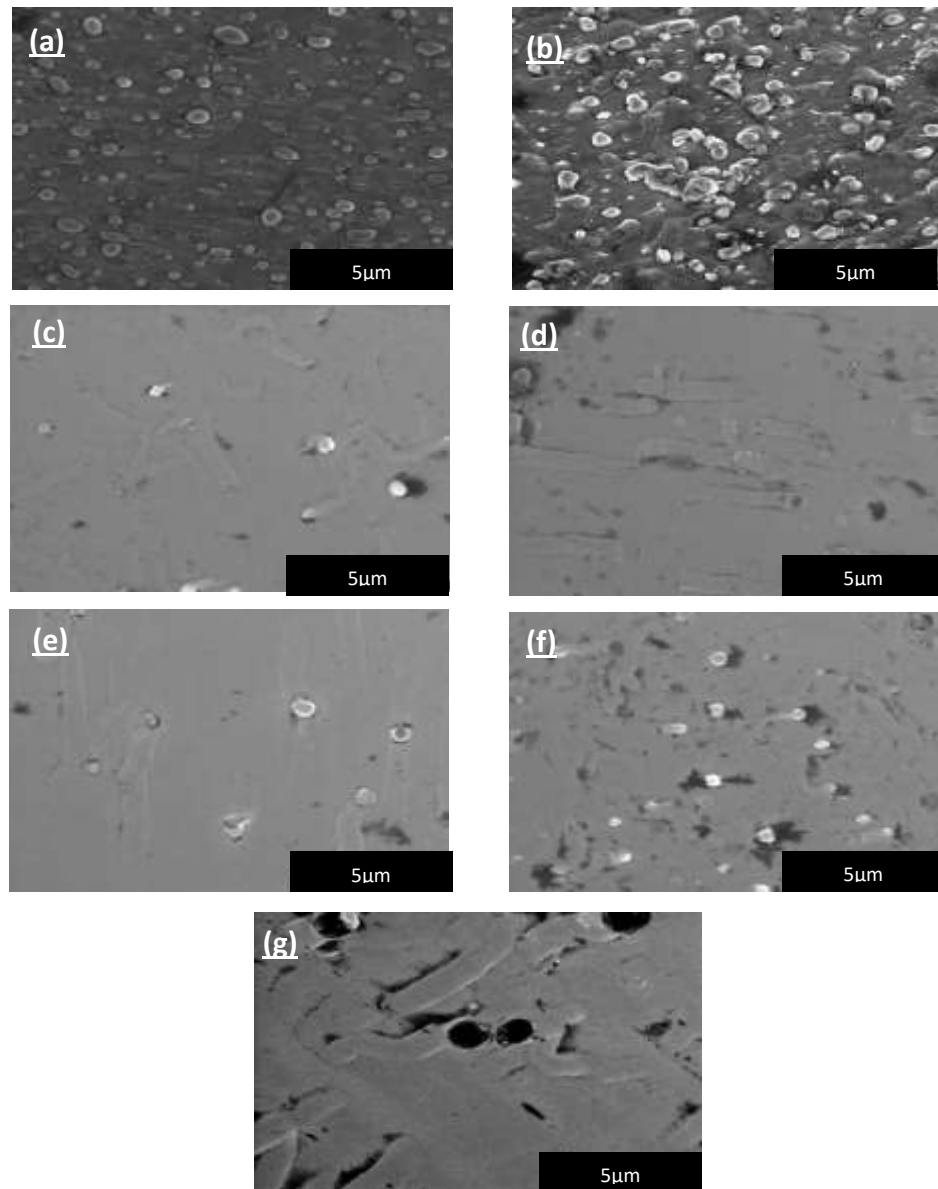


Figure 5.5: SEM images of the surfaces of $\text{GaAs}_{1-x}\text{Bi}_x$ samples grown on (100) GaAs substrates (a) sample A ($T_G=300$ °C), (b) sample B ($T_G=310$ °C), (c) sample C ($T_G=320$ °C), (d) sample D ($T_G=325$ °C), (e) sample E ($T_G=340$ °C), (f) sample F ($T_G=345$ °C), (g) sample G ($T_G=365$ °C). The A (a) and B (b) samples exhibit many droplets, while the samples C (c) to G (g) both droplets and self-aligned trailing nanotracks are present.

The scanning electron microscopy (SEM) data was acquired using a Helios Nanolab 650, FEI Company. Figure 5.5 shows the SEM images of the surfaces of $\text{GaAs}_{1-x}\text{Bi}_x$ samples where droplets are clearly observed. The growth mechanism of these droplets has been the object of study in many works [21, 22]. These Bi droplets, which are formed during the MBE growth of the $\text{GaAs}_{1-x}\text{Bi}_x$ epilayer, are in general associated with the non-uniformities of the thickness and composition of the growing layer. In fact, as expected, the samples with the highest surface concentrations of droplets are those with the lowest concentrations of Bi, as evidenced by SEM images shown in Figures 5.5 (a), (b) and (g).

This means that for these growth temperatures a lower concentration of Bi was incorporated into the GaAs host lattice. On the other hand, sample D, which was grown at 325 °C, has the highest concentration of bismuth (4.7%). As can be seen from Figure 5.5 (d), this sample has the lowest number of both surface droplets and self-aligned trailing nanotracks. Especially for sample G, as shown in Figure 5.5 (g), the self-aligned trailing tracks are wider with black drops at their ends, indicating that bismuth was not effectively incorporated into the GaAs host lattice. Interestingly, sample G grown at the highest temperature (365 °C) is among the samples has also a low concentration of bismuth (2.8%), in agreement with the PL and Raman results which will be discussed in the following sections.

5.3.2 Optical Properties

5.3.2.1 Raman Spectroscopy

Hall effect measurement is one of the most common methods used to determine the charge carriers' concentration in semiconductors, which is important for device fabrication. However, this technique requires the formation of Ohmic contacts which can alter the properties of the samples or even damage them. Alternatively, Raman spectroscopy is a versatile tool that can be used to determine the hole concentrations in Bi-doped GaAs samples without electrical contacts. The generation of hole carriers in $\text{GaAs}_{1-x}\text{Bi}_x$ is due to the fact that Bi atoms create a localised state near the valence band. These resonant localized Bi states interact with the valence band of GaAs. In this sense, the hole concentration can be determined with a good accuracy using the relative intensities ratio of the unscreened longitudinal optical (ULO) phonon and the longitudinal optical phonon-hole-plasmon-coupled (LOPC) modes. Figure 5.6 shows the characteristic Raman spectra of $\text{GaAs}_{1-x}\text{Bi}_x$ at room temperature. The spectra displays the Raman typical bands of GaAs in the range of $200\text{-}350\text{ cm}^{-1}$ [23]. The bottom of Figure 5.6 shows the deconvolution using Lorentzian functions, which display the Raman bands associated with the transverse optical (TO) phonon and longitudinal optical (LO) phonon located at $\sim 263\text{ cm}^{-1}$ and $\sim 286\text{ cm}^{-1}$, respectively [24]. In addition, a broader asymmetric band around 269 cm^{-1} due to the LOPC modes overlaps the TO phonon peak at $\sim 267\text{ cm}^{-1}$. Furthermore, a vibrational mode at $\sim 285\text{ cm}^{-1}$ near the LO phonon peak is observed [23]. Previous studies showed that the Raman scattering signals from the LO and LOPC phonon follow the same Raman selection rules, indicating that the observed LOPC modes are also phonon-like [25]. Interestingly, as the content of Bi increases first there is a slight redshift and then a

blueshift of the LO phonon (for guide to the eyes, see the two black vertical dashed lines in Figure 5.6a), which can be explained by the Bi-induced tensile and/or compressive stress [4]. Besides, as Bi concentration increases, the intensity of the phonon mode located at $\sim 287 \text{ cm}^{-1}$ becomes larger [23]. Figure 5.6b also shows a very interesting result, where Raman intensity of this mode exhibit a linear dependence as a function of the Bi concentration. This Raman band has been assigned to the disorder activated mode or a Fröhlich mode [26, 27].

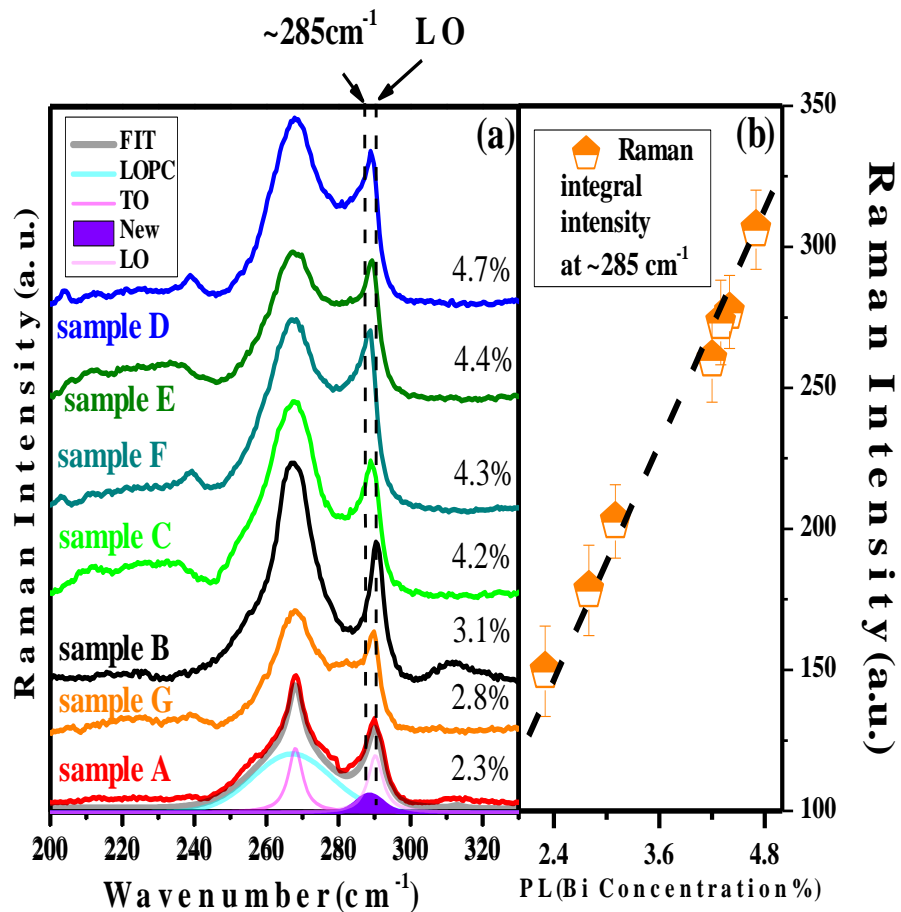


Figure 5.6: (a) Raman spectra from $\text{GaAs}_{1-x}\text{Bi}_x$ samples having different Bi concentrations. (b) Raman intensity from peak at $\sim 285 \text{ cm}^{-1}$ as function of Bi concentration shows a linear dependence.

Figure 5.7 (a) shows the hole concentrations as a function of bismuth concentration of the $\text{GaAs}_{1-x}\text{Bi}_x$ samples. The results indicate that the concentration of holes in the $\text{GaAs}_{1-x}\text{Bi}_x$ samples increases proportionally until bismuth content reaches 4.2%, then decreases and increases again. In Figure 5.7 (b) are plotted the Raman shift of LO mode from the $\text{GaAs}_{1-x}\text{Bi}_x$ samples. As can be seen in Figure 5.7 (b), an evident frequency shift of the LO mode is observed as a function of Bi concentration. First, to obtain the hole concentration from Raman spectroscopy, it is necessary to relate the relative intensities of the longitudinal optical (LO) and longitudinal optical phonon-hole-plasmon-coupled (LOPC) phonon modes using the followings equations [24, 25].

$$p = \frac{8\varepsilon_0\varepsilon_s\alpha^2\phi_B}{e \left[\ln \left(1 + \frac{\zeta_A}{\zeta_S} \right) \right]} \quad 5.1$$

where ε_0 is the vacuum permittivity, ε_s is the static dielectric constant, α is the absorption coefficient and ϕ_B is the surface potential barrier [28]. Since the values of α , ε_s and ϕ_B for $\text{GaAs}_{1-x}\text{Bi}_x$ are not available, those of GaAs were used, $\varepsilon_s = 12.8$, $\phi_B = 0.5$ eV and $\alpha \approx 231 \times 10^3 \text{ cm}^{-1}$, for the excitation wavelength of 532 nm [24, 29, 30]. $\zeta_A = A_{LO}/A_{LOPC}$ is the ratio of the integrated intensity of the unscreened longitudinal optical ULO mode and the longitudinal optical phonon-hole-plasmon-coupled (LOPC) mode in the Raman spectrum. $\zeta_S = I_{LO}/I_{LOPC}$ is the relative Raman scattering efficiencies of the pure longitudinal optical (LO) phonons and the coupled mode in a volume element. By comparing the efficiencies of the modes I_{LO} and I_{LOPC} at different excitation energies, one can obtain $\zeta_S = 2$ [23, 24].

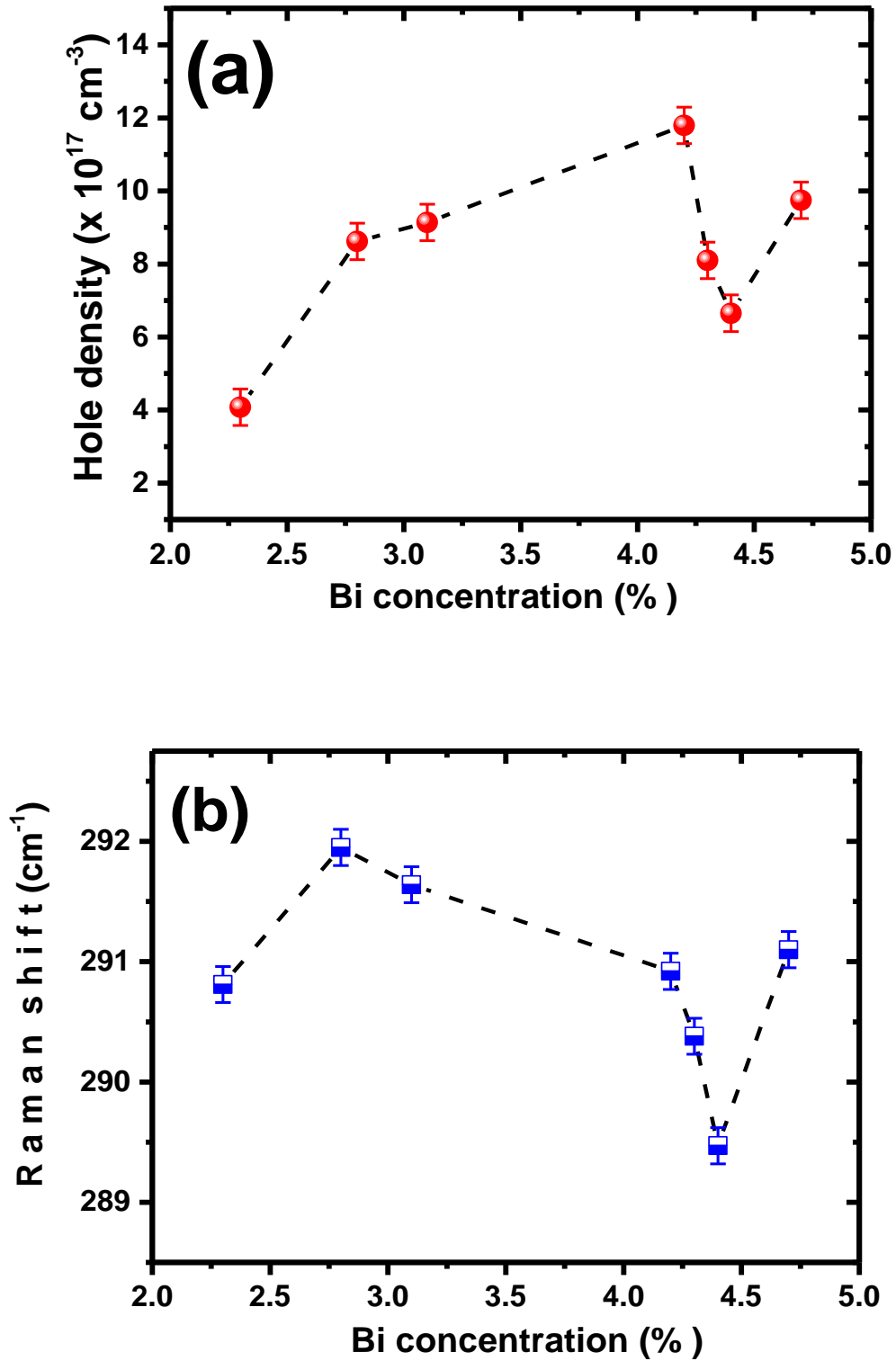


Figure 5.7: (a) The hole concentration (calculated from equation 5.1) versus Bi content for $\text{GaAs}_{1-x}\text{Bi}_x$ epilayer samples. (b) Raman shifts of LO mode versus Bi concentration for all $\text{GaAs}_{1-x}\text{Bi}_x$ thin films samples.

5.3.2.2 Photoluminescence

5.3.2.2.1 Low-Temperature Photoluminescence of GaAs_{1-x}Bi_x Thin Film Samples

This section will report on the optical properties of GaAs_{1-x}Bi_x thin films grown on the conventional (100) GaAs substrates at different growth temperatures, namely A ($T_G=300$ °C), B ($T_G=310$ °C), C ($T_G=320$ °C), D ($T_G=325$ °C), E ($T_G=340$ °C), F ($T_G=345$ °C) and G ($T_G=365$ °C). The effects of growth temperature on the optical properties of GaAs_{1-x}Bi_x layers were investigated by photoluminescence spectroscopy measurements at various temperatures and excitation powers. PL measurements are performed using a green laser (532 nm) with pump powers ranging from 0.5 mW to 65 mW. The samples are mounted within a Janis closed-loop helium cryostat where the temperature was controlled from 10 K to 300 K. The PL spectra are obtained using a high-resolution spectrometer and an InGaAs CCD detector. The PL intensity provides a measure of the radiative and nonradiative recombination relative rates.

Figure 5.8 (a) shows the PL spectra at low temperature of 10 K for all GaAs_{1-x}Bi_x samples grown on (100) GaAs substrates at different growth temperatures and at a laser excitation power $P_{EXC} = 16$ mW (0.91 W/cm²). Overall, the PL peaks at 1.30 eV, 1.23 eV, 1.14 eV, 1.09 eV, 1.12 eV, 1.13 eV and 1.26 eV are related to GaAs_{1-x}Bi_x samples A, B, C, D, E, F and G, respectively. It is worth noting that the GaAs_{1-x}Bi_x PL emission of the sample A ($T_G=300$ °C) is the weakest and the broadest amongst all samples. Consequently, Gaussian fitting was applied for this sample in order to determine the peak energy. Figure 5.8 (b) illustrates the Gaussian fitting of the PL spectra of sample A at 10K and a laser excitation power $P_{EXC} = 60$ mW. The Gaussian fitting shows three peaks with emission energies at 1.3 eV, 1.34 eV and

1.38 eV. The PL emission energy found at 1.3 eV (see green peak in Figure 5.8.b) is related to GaAs_{1-x}Bi_x and the peaks between 1.34 eV and 1.4 eV could be due to some defects.

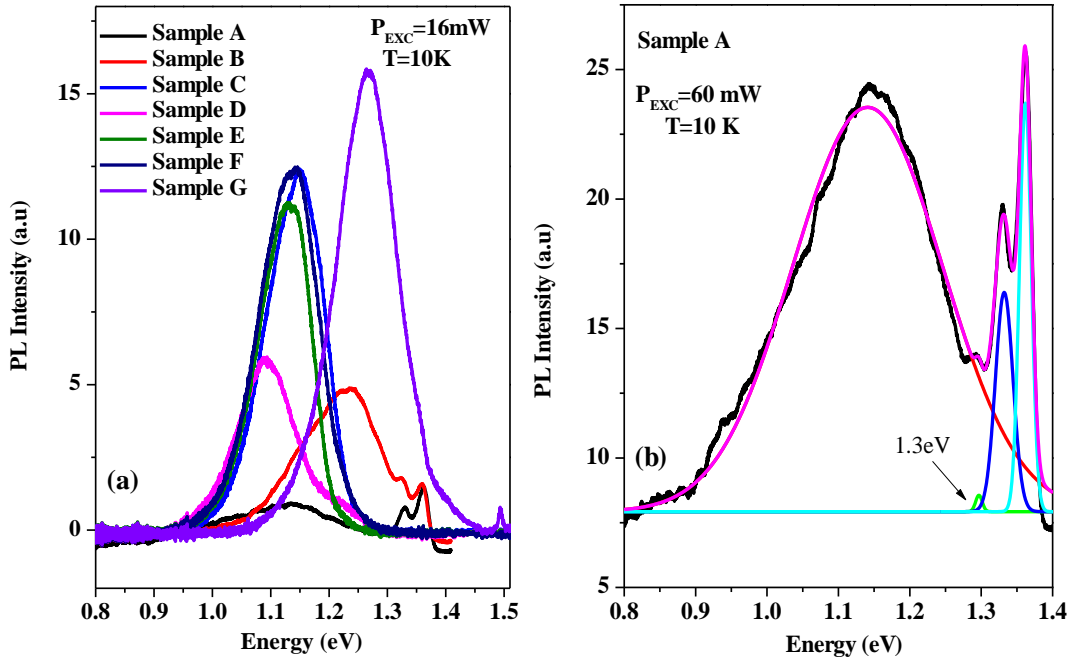


Figure 5.8: (a) 10 K PL spectra of the GaAs_{1-x}Bi_x epilayers grown on (100) GaAs substrates for samples A, B, C, D, E, F and G., using a green laser (532 nm) with $P_{\text{EXC}} = 16 \text{ mW}$ and (b) Gaussian fitting of PL spectra of sample A (GaAs_{1-x}Bi_x epilayer grown on (100) GaAs substrates at $T_{\text{G}} = 300 \text{ }^{\circ}\text{C}$). Measurements were taken at 10 K and $P_{\text{EXC}} = 60 \text{ mW}$.

A small increase of $10 \text{ }^{\circ}\text{C}$ in the growth temperature from $300 \text{ }^{\circ}\text{C}$ (sample A) to $310 \text{ }^{\circ}\text{C}$ (sample B) improved the PL intensity of sample B by 2.6 times as compared to sample A. However, a large enhancement by a factor of 5.6 in the GaAs_{1-x}Bi_x PL intensity was observed by further increasing the growth temperature above $310 \text{ }^{\circ}\text{C}$. These PL results could be explained by the competition mechanisms that generate and reduce structural defects. For example, when the growth temperature is lower

than the optimal GaAs growth temperature ($T_G = 400\text{-}630\text{ }^\circ\text{C}$), native defects which are attributed to nonradiative energy states such as Ga vacancies and As antisites are typically created in the material [31, 32]. On the other hand, Lu et al reported [33] that at the low growth temperatures required to incorporate a small amount of Bi ($x < 0.045$) during GaAs growth, Bi atoms induce localized states close to the maximum of the valence band (MVB) because of Bi-pair and Bi-cluster formation. These localized states behave as trapping centres for bound holes, which can recombine radiatively. At the same time, Bi can behave as a surfactant, which enhances the quality of the material by decreasing the defects because of the low growth temperature used [11]. One mechanism decreases the carrier loss by nonradiative centres for samples A and B (when $T_G \leq 310\text{ }^\circ\text{C}$), and the other mechanisms improve the efficiency of the PL (when $T_G \geq 320\text{ }^\circ\text{C}$) for samples C, D, E, F and G. In this work, sample A which was grown at the lowest growth temperature of $300\text{ }^\circ\text{C}$ has higher density of defects than the other samples as evidenced by the lower PL intensity. Figures 5.9 and 5.10 show that at low temperature (10 K) and a laser excitation power of 16 mW, the PL spectra exhibit two different behaviours depending on the growth temperatures: (i) a red shift of 21 meV of the PL peak from 1.3 eV ($T_G=300\text{ }^\circ\text{C}$) to 1.09 eV ($T_G=325\text{ }^\circ\text{C}$) was observed when the growth temperature was increased (see Figures 5.9a and 5.10a); (ii) a blue shift of 17 meV of the PL peak from 1.09 eV ($T_G=325\text{ }^\circ\text{C}$) to 1.26 eV ($T_G=365\text{ }^\circ\text{C}$) was noted as the growth temperature increased as shown in Figures 5.9b and 5.10b. These findings are in good agreement with Raman results which showed that as the content of Bi increases, first there is a slight redshift and then a blueshift of the LO phonon, which can be explained by the Bi-induced tensile and/or compressive stress [4].

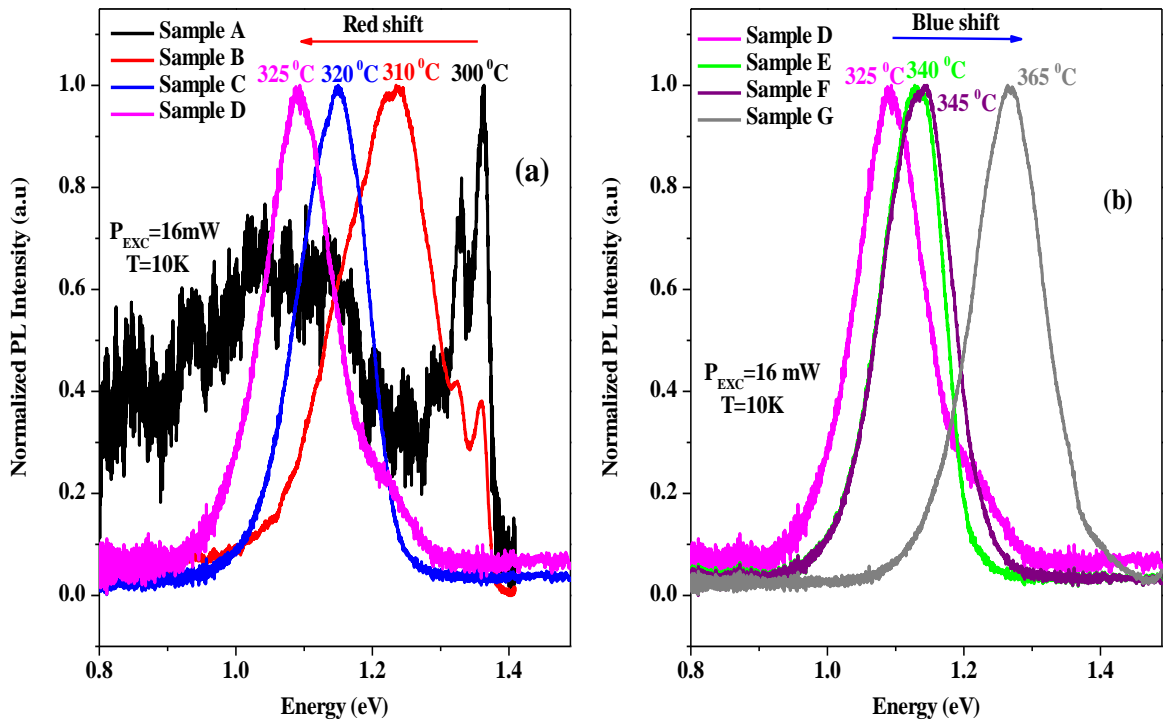


Figure 5.9: Normalised 10 K PL spectra of the GaAs_{1-x}Bi_x epilayers grown on (100) GaAs substrates for (a) samples A, B, C and D; (b) samples D, E, F and G. A green laser (532 nm) with $P_{\text{EXC}}=16\text{ mW}$ (0.91 W/cm^2) was used.

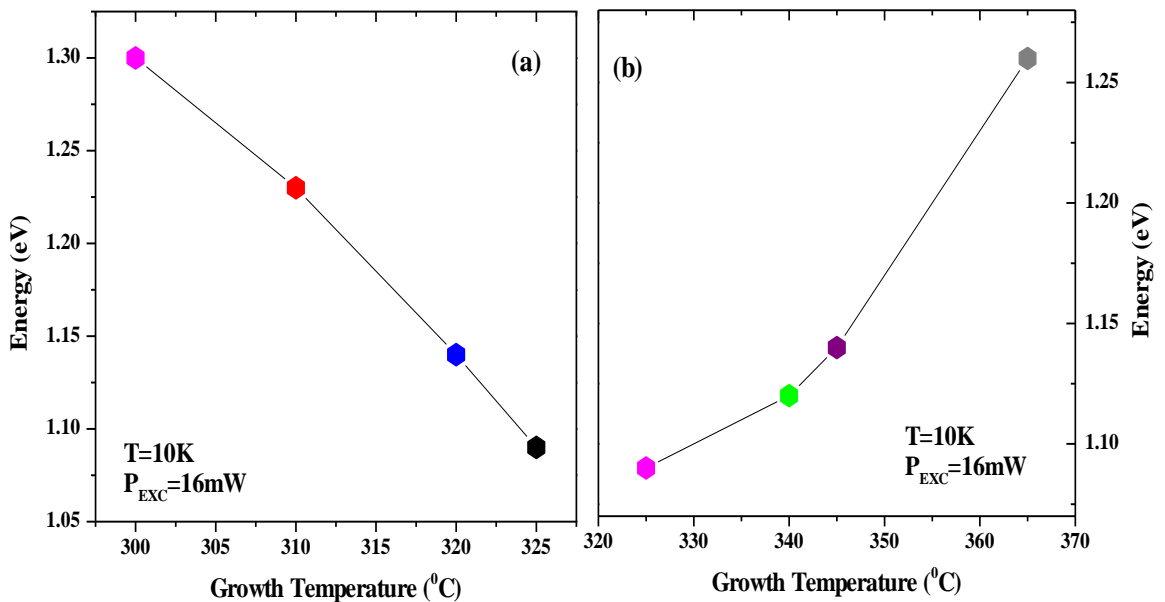


Figure 5.10: PL peak energy for samples grown on (100) GaAs substrates at different growth temperatures for (a) samples A-D; (b); samples D-G. Measurements were taken at 10 K with $P_{\text{EXC}}=16\text{ mW}$.

These results indicate that even a very small change in the growth temperature affects the PL emission energy, meaning that the bismuth incorporation into the host lattice of GaAs is very sensitive to the growth temperature. The PL results evidence that the growth temperature of GaAs_{1-x}Bi_x thin films plays an important role in the Bi incorporation and the optical quality of the samples. To determine the effective Bi composition (x) incorporated in each GaAs_{1-x}Bi_x sample grown at different growth temperatures, it is assumed that the substitutional Bi causes a reduction of the bandgap of GaAs at room temperature by 88 meV per % of Bi [34]. Figure 5.11 shows the growth temperature dependence of the PL peak energy at 10 K and the estimated energies at room temperature (300 K).

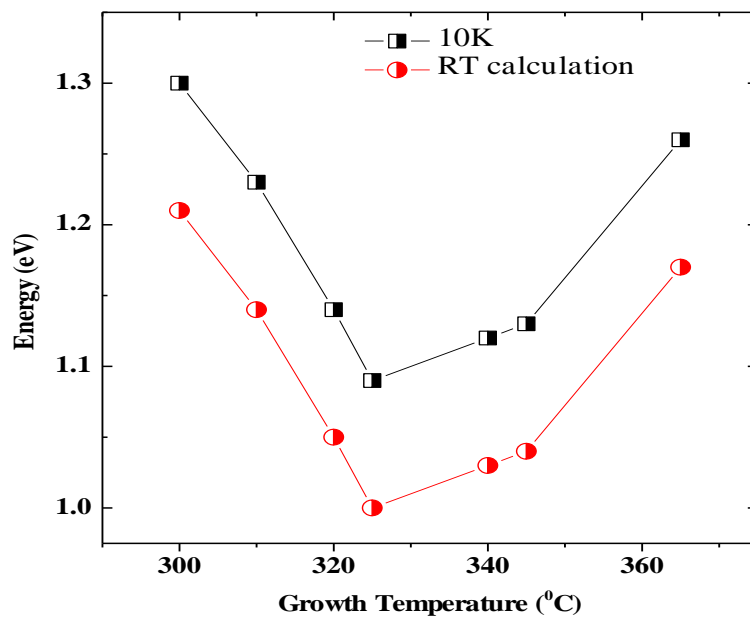


Figure 5.11: The PL peak energy as a function of growth temperature at 10 K and estimated PL peak energy at 300 K (RT= room temperature) for all GaAs_{1-x}Bi_x samples investigated in this study.

Figure 5.12 illustrates the Bi composition as a function of growth temperature for all samples investigated in this study using PL technique. The Bi concentrations were determined from PL measurements and the calculations are presented in Table 5.2. In PL measurements, emission occurs between the conduction band (CB) and the vacant state at the maximum of the valence band (VB). It was observed that the percentage of Bi incorporation increases as the growth temperature increases from 300 °C to 325 °C. However, for $T_G > 325$ °C, the percentage of Bi incorporation decreases. The optimum growth temperature for maximum Bi concentration ($x=4.7\%$) was found to be for sample D ($T_G=325$ °C), whereas sample A ($T_G=300$ °C) has the lowest Bi concentration and optical quality.

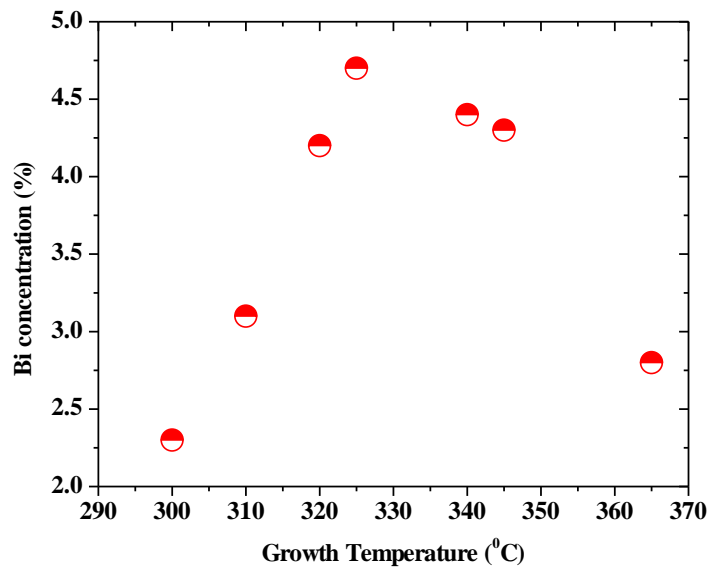


Figure 5.12: Bi composition as a function of growth temperature for GaAsBi samples investigated in this study. Measurements were taken at $P_{EXC}= 16$ mW. The Bi concentrations in the studied samples were determined from PL measurements as presented in Table 5.2.

Table 5.2: Bi concentrations for all GaAs_{1-x}Bi_x epilayer samples as determined from PL. ΔE is the difference between the bandgap of GaAs (1.42 eV) and the estimated GaAs_{1-x}Bi_x PL peak energy at room temperature.

Sample Labelled	Growth Temperature (°C)	PL Peak Energy at 10K (eV)	Estimated PL Peak Energy at 300K (eV)	Bi concentration from PL $X (\%) = \Delta E / 0.088$
A	300	1.30	1.21	2.3
B	310	1.23	1.14	3.1
C	320	1.14	1.05	4.2
D	325	1.09	1	4.7
E	340	1.12	1.03	4.4
F	345	1.13	1.04	4.3
G	365	1.26	1.17	2.8

The PL emissions at low temperatures were observed in an energy range distinct of the expected bandgap reduction. Therefore, other contributions such as strain and/or Bi-defect level-band related transitions could explain the observed differences in PL peak position for different growth temperatures of GaAs_{1-x}Bi_x samples. The giant reduction in the band gap energy of GaAs_{1-x}Bi_x alloys has been described using a valence band (VB) anti-crossing interaction between the Bi level and the host GaAs VB. Additionally, the low temperature PL peak is also expected to present an energy shift for samples under different strain conditions (compressive versus tensile), due to changes in the structure of the band. In samples with compressive strain usually the PL peak is redshifted with respect to the

expected band gap of GaAs [35] . On the other hand, the presence of Bi-related localized states close to the VB edge also causes a redshift in the PL peak since the exciton localized recombination changes the PL line shape by exhibiting an asymmetric characteristic with a low energy tail, which usually dominates the excitonic recombination processes at low temperatures. The origin of these localized states is attributed with the formation of Bi-related complexes and alloy disorder in GaAs_{1-x}Bi_x. Figure 5.13 shows the PL spectra of GaAs_{1-x}Bi_x thin films with various Bi concentrations at 10 K and excitation power of 16 mW.

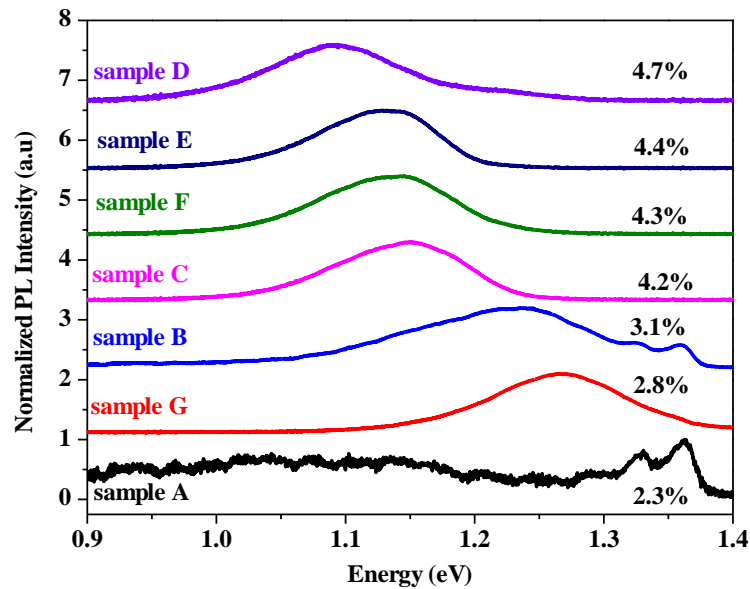


Figure 5.13: PL spectra of GaAs_{1-x}Bi_x thin films having various Bi concentrations grown on (100) GaAs substrates. The measurements were carried out at 10 K using a green laser (532 nm) and P_{EXC}= 16 mW (0.91 W/cm²).

The PL peak shifts to lower energies (redshift of PL peak energy) with increasing Bi concentration from 2.3% to 4.7% evidencing a reduction of the bandgap with Bi content as expected. Fahrettin et al [36] reported that the bandgap of GaAs_(1-x)Bi_x

red shifts with increasing Bi composition is due to the stronger interaction between valence band and localized Bi level.

5.3.2.2.2 Excitation Power Dependence of Photoluminescence of GaAs_{(1-x)Bi_x} Epilayers Grown at Different Growth Temperatures

Figure 5.14 shows the PL spectra at 10 K as a function of laser excitation power.

The results show no blue shifts was observed for all samples.

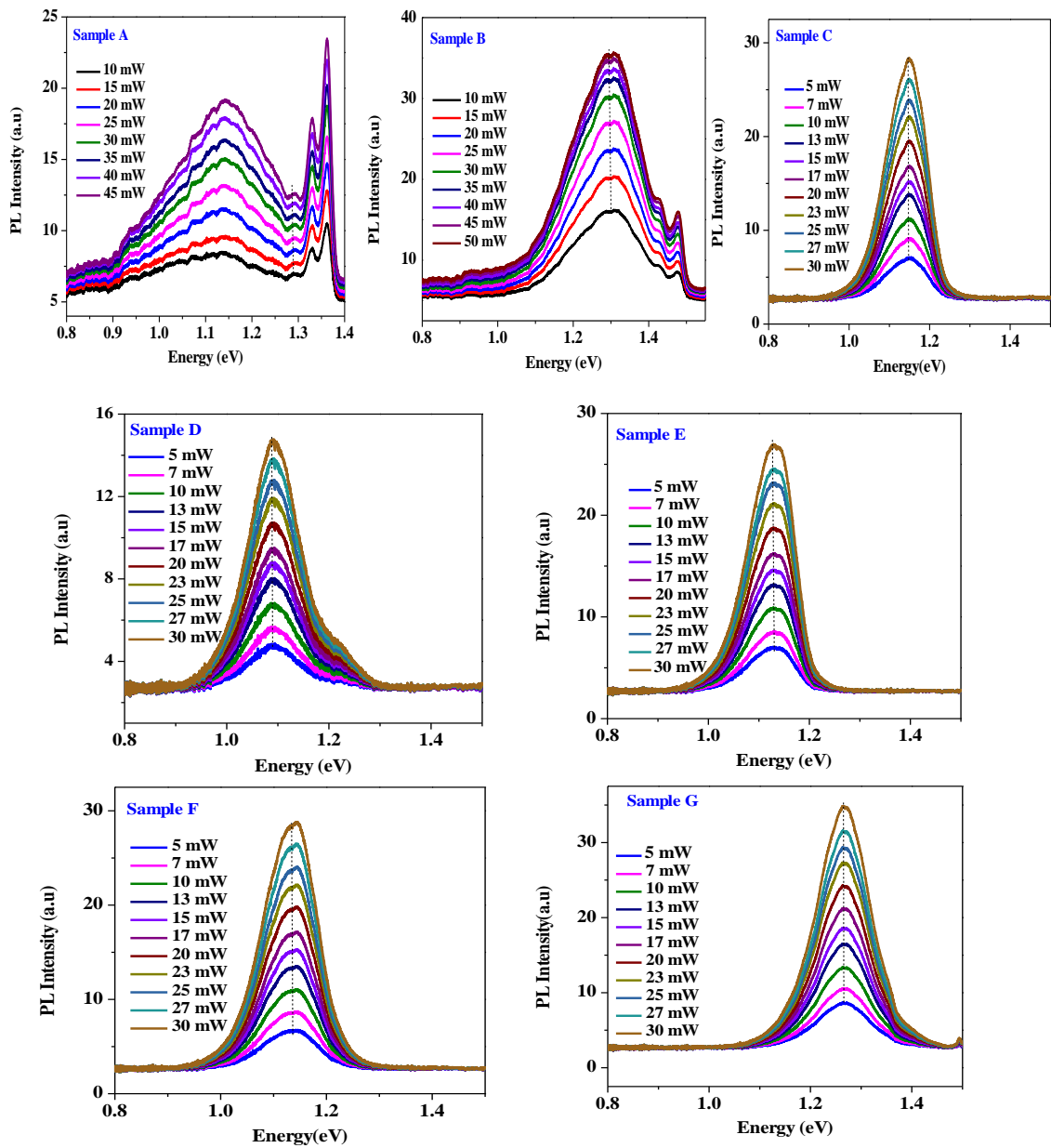


Figure 5.14: Laser excitation power dependence of 10 K PL spectra of GaAs_{1-x}Bi_x epilayers grown on (100) substrates at different temperatures.

To study the effects of carrier localization, the laser power dependence of PL spectra of all samples grown at different temperatures was investigated and is shown in Figure 5.15. The results show that no shift of the GaAs_{1-x}Bi_x PL peaks was observed when P_{EXC} increased from 1 mW to 30 mW.

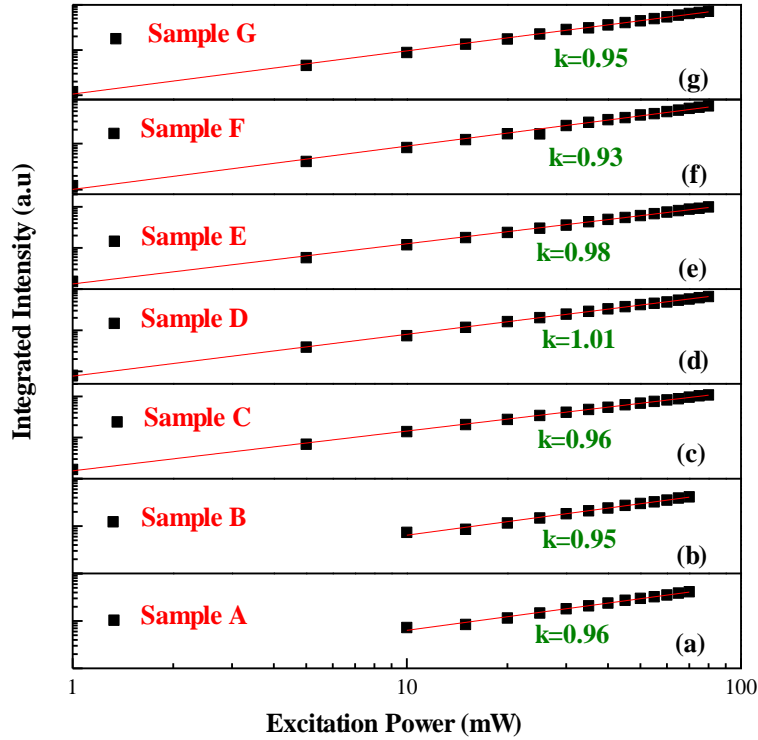


Figure 5.15: 10 K Integrated PL intensity (I_{PL}) as a function of P_{EXC} for GaAs_{1-x}Bi_x samples grown at different temperatures. The solid lines illustrate the fitting curves using equation: $I_{PL} = \beta P_{EXC}^k$.

At low temperatures, the PL from GaAs_{1-x}Bi_x material with reasonably good crystalline quality is governed by near band edge photoluminescence (NBEPL) [37]. It has been shown that the fundamental recombination processes can be determined from the behaviour of the PL intensity as a function of the excitation power [38]. To analyse the emission from GaAs_{1-x}Bi_x epilayers grown at different

temperatures, the integrated PL intensity (I_{PL}) was plotted as a function of P_{EXC} from 1 mW to 65 mW as shown in Figures 5.15 (a–g). The fitting curves using the power law $I_{PL} = \beta P_{EXC}^k$ [37] are also shown as red solid lines. I_{PL} is the integrated PL intensity and β and k are fitting parameters. It was found that the integrated luminescence intensity (I_{PL}) of the NBEPL emission lines is proportional to L^k , where L is the power of the exciting laser radiation. For exciton like transitions, and free-to-bound and donor-acceptor pair transitions $1 < k < 2$ and $k < 1$, respectively [31, 39]. As shown in Figure 5.15, all $\text{GaAs}_{1-x}\text{Bi}_x$ thin film samples show a linear dependence of I_{PL} versus P_{EXC} over the whole excitation powers range 1 mW – 65 mW, indicating one process for carrier radiative recombination as a function of P_{EXC} . Table 5.3 summarises the obtained k values for all samples. In general, k values of ≈ 1 were obtained for most samples.

Table 5.3: k values obtained for all $\text{GaAs}_{1-x}\text{Bi}_x$ samples grown at different temperatures. The measurements were taken at 10 K with laser excitation powers ranging from 1 mW to 65 mW.

Samples	Growth temperature ($^{\circ}\text{C}$)	k
A	300	0.96 ± 0.02
B	310	0.95 ± 0.02
C	320	0.96 ± 0.06
D	325	1.01 ± 0.05
E	340	0.98 ± 0.01
F	345	0.93 ± 0.02
G	365	0.95 ± 0.01

5.3.2.2.3 Temperature Dependence of Photoluminescence of GaAs_{1-x}Bi_x Thin Films Grown at Different Temperatures

In order to gain additional information about the properties of GaAs_{1-x}Bi_x thin film grown on (100) GaAs planes at different temperatures, the temperature dependence of the PL spectra were also studied over the temperature range 10 K to 200 K. The excitation energy was 2.33 eV (532 nm), and the excitation power was kept at 10 mW to avoid any localized states saturation.

The GaAs_{1-x}Bi_x PL peaks of samples A and B were not detected at temperatures above 40 K (not shown in Figure 5.16). These results are consistent with the SEM data which demonstrated that samples A ($T_G=300$ °C) and B ($T_G=310$ °C) have the highest surface concentrations of droplets and the lowest concentrations of Bi, evidencing that for these low growth temperatures the incorporation of Bi into GaAs host lattice is low. The PL spectra of GaAs_{1-x}Bi_x samples C, D, E, F and G are shown in Figure 5.16 (a), (b), (c), (d) and (e), respectively.

The results show that the PL intensity of GaAs_{1-x}Bi_x samples grown at different growth temperatures quenches at different temperatures. It is clearly seen that there is a redshift of PL peak energy because of the bandgap energy decreases with the increase of temperature in all samples. The shape of the PL spectra exhibits an asymmetric characteristic with a low energy tail which is commonly observed in highly mismatched alloys. In addition, no PL signal could be detected in samples C, D, E, F and G above temperatures of 200 K, 170 K, 190 K, 200 K and 190 K, respectively. Furthermore, the monotonous redshift with increasing temperature can be observed and the PL spectra gets broader for all samples.

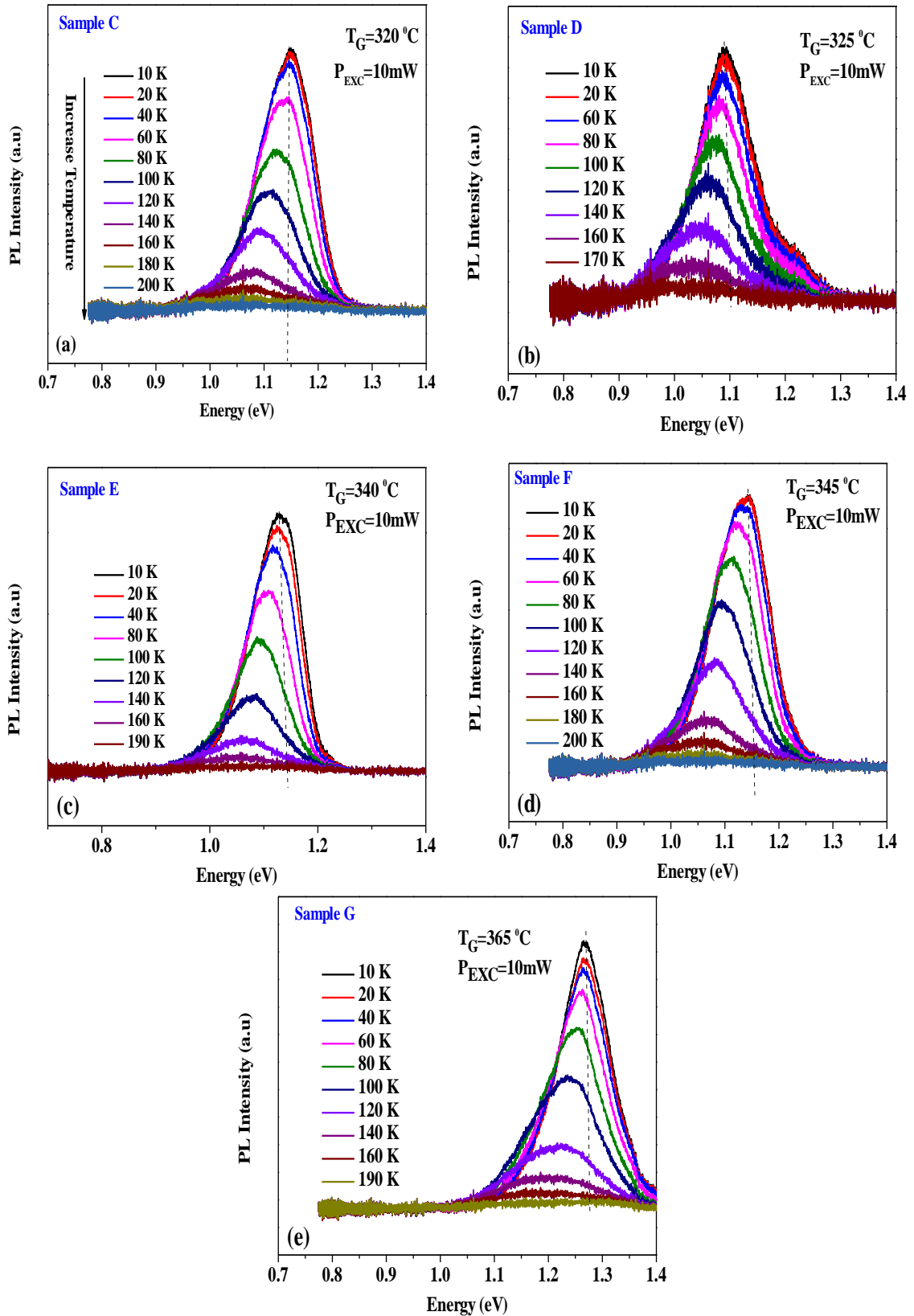


Figure 5.16: Temperature dependence of PL spectra of GaAs_{1-x}Bi_x thin films grown on (100) GaAs substrates at different growth temperatures for a laser power excitation $P_{EXC} = 10$ mW.

Representative plots of the measured temperature dependent PL spectra are shown in Figure 5.17 (a) and (b) for incident excitation power of 5 mW and 15 mW, respectively.

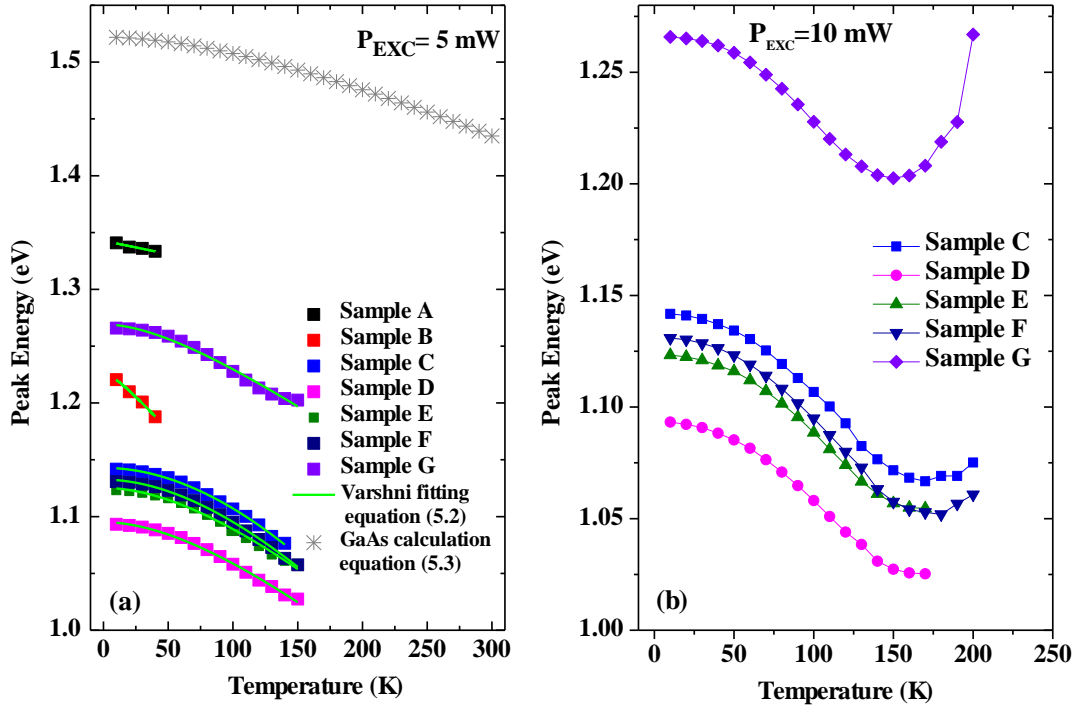


Figure 5.17: (a) PL peak energy as a function of temperature and Varshni fittings for samples A, B, C, D, E, F and G. The solid green lines are calculated according to the Varshni's equation 5.2. Bandgap energy versus temperature of GaAs is calculated from Ref [40]. All measurements were taken at an excitation power of 5 mW; (b) PL peak energy as a function of temperature of samples C, D, E, F and G. All measurements were taken at an excitation power of 15 mW.

As clearly seen in Figure 5.17(a), the PL intensity of the $\text{GaAs}_{1-x}\text{Bi}_x$ samples A and B quenches at 40 K for laser powers of 5mW. The peak luminescence energy as a function of temperature is highly dependent on the incident excitation power [41]. For a 5 mW laser excitation power, no evidence of the characteristic S-shape is seen under this low power condition due to the quenching of the $\text{GaAs}_{1-x}\text{Bi}_x$ PL peaks that occurs at a temperature of $\sim 150 \text{ K}$. Usually the S-shape behaviour is observed

at high temperatures between (150 K- 200 K). Therefore, the PL peak energy versus temperature plot can be fitted using the empirical Varshni relation. Figure 5.17 (a) presents the temperature evolution of the band gap energy with the Varshni model fitting of thin films GaAs_{1-x}Bi_x samples grown at different substrate temperatures. The symbols in Figure 5.17 (a) are the experimental results, and the solid curves are the fitting obtained by using the empirical Varshni equation:

$$E_g(T) = E_g(0) - \frac{\alpha T^2}{T + \beta} \quad 5.2$$

where α (eV/K) is associated with the electron-phonon interaction, β is the Debye temperature, $E_g(0)$ is the bandgap energy at 0 K. T is the measured temperature. The constant values used for the fitting shown in Figure 5.17 (a) are based on Ref [40]: $\alpha = 0.44 \text{ meVK}^{-1}$ and $\beta = 204 \text{ K}$. Generally, these results are similar to those reported previously on the PL of GaAs_{1-x}Bi_x quantum wells (QWs) grown on (100) GaAs substrates [42, 43]. Furthermore, Blakemore calculated [30] the temperature dependency of the direct energy bandgap E_g of GaAs as shown in Figure 5.17 (a), according to the equation.

$$E_g = 1.522 - [(5.8 \times 10^{-4} - 4T^2 / (T + 300))] \text{ eV} \quad 5.3$$

where E_g is direct energy band gap of GaAs in eV and T absolute temperature in K.

Figure 5.17 (b) shows that for an incident laser excitation power of 15 mW, the well-known S-shape behaviour is observed for samples C, D, E, F and G. The origin of this characteristic red-blue shift (S-shape profile) in the peak luminescence

energy can be explained by considering the carrier distribution amongst the localised density of states (LDOS) at different temperatures.

At low temperatures, both deep and shallow localised states are occupied by electron-hole pairs, and charge carriers which have a small thermal energy remain trapped until they are able to recombine. As the temperature increases electron-hole pairs in the shallow energy states close to the valence band edge gain enough thermal energy to escape and become trapped by deeper level localised states. This behaviour results in a rapid red shift of the PL peak energy and can be seen in Figure 5.17 (b) between temperatures of 10 K - 140 K. As carriers gain greater thermal energy, however, they are able to complete multiple hops between states, allowing carriers to escape the deepest traps and occupy a range of shallower energy states. This leads to a blue shift in the peak emission energy between temperatures of 150 K- 200 K. The S-shape relates to the existence of localized states in the epitaxial layer, thus, the evolution cannot be fitted only by using Varshni's equation. For temperatures above 200 K, the PL intensity is completely quenched. These results are similar to those reported previously on the PL of bulk $\text{GaAs}_{1-x}\text{Bi}_x$ grown on (100) GaAs substrates [41] .

Figure 5.18 shows the plots of the PL full width at half maximum (FWHM), which is a figure of merit of the quality of the samples, as a function of temperature for the temperature range 10 K - 200 K and excitation power of 15 mW. The FWHM for samples C, D, E, F and G are 111 meV, 108 meV, 103 meV, 115 meV and 125 meV, respectively. In this investigation, all samples have similar behaviour which does not change appreciably at low temperatures (10 K - 80 K). However, at high temperatures, a monotonous increase of the FWHM with temperature is observed.

Sample G ($T_G=365$ °C) has the highest FWHM, whereas sample E ($T_G=340$ °C) has the lowest FWHM indicating a higher Bi uniformity and optical quality.

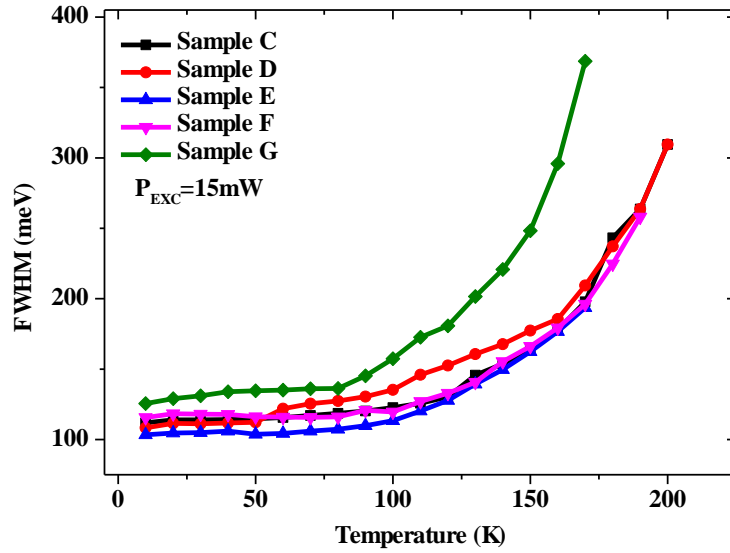


Figure 5.18: FWHM as a function of temperature for GaAs_{1-x}Bi_x epilayers of samples C, D, E, F and G. All measurements were taken at excitation power of 15 mW.

In order to investigate further the nonradiative recombination processes in GaAs_{1-x}Bi_x epilayers for samples C, D, E, F and G, the integrated PL intensity (I_{PL}) as a function of reciprocal temperature is plotted in Figure 5.19. The behaviour is characterized by two different temperature ranges, corresponding to two thermally activated nonradiative recombination processes. The fits are derived by applying the formalism described in Refs [32, 44]. The fit is performed using equation 5.4:

$$I_{PL}(T) = I(0)/[1 + C_1 \exp(-E_1/k_B T) + C_2 \exp(-E_2/k_B T)] \quad 5.4$$

where $I_{PL}(T)$ and $I(0)$ are the PL integrated intensity at temperature T and 0 K, respectively. C_1 and C_2 are constants and are related to the density of nonradiative centres, E_1 and E_2 are the thermal activation energies of these centres, T is the temperature and k_B is the Boltzmann constant. Experimental data were well fitted for all samples as shown in Figure 5.19. The E_1 and E_2 values are reported in Table 5.4. The activation energy E_1 is derived from the slopes of the straight-line portion of the curves in the high temperature region.

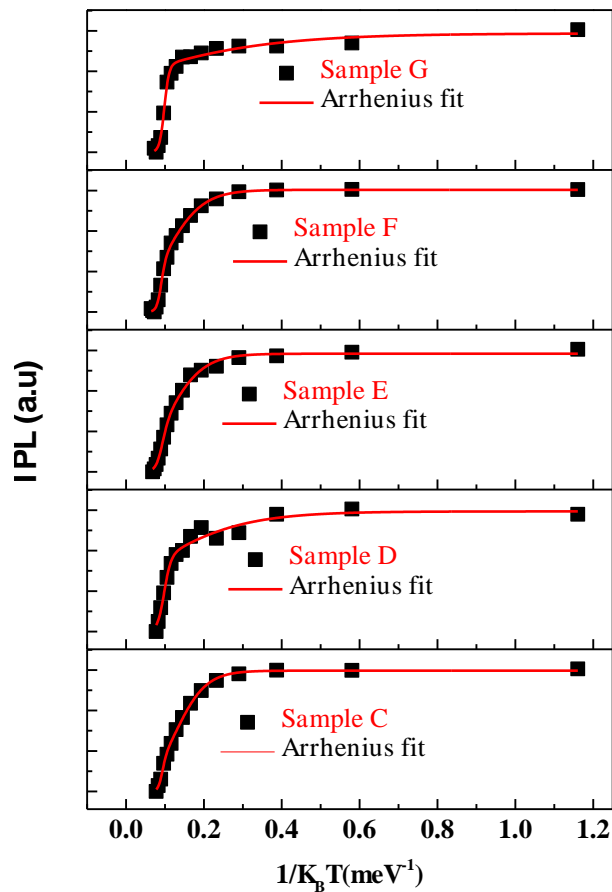


Figure 5.19: Arrhenius plots of integrated PL intensity (IPL) of $\text{GaAs}_{1-x}\text{Bi}_x$ epilayers grown on (100) GaAs substrates for samples C, D, E, F and G. Solid lines illustrate the fit to the experimental data using equation 5.4.

As discussed previously, GaAs_{1-x}Bi_x alloys tend to form localized pairs and clusters, which have different configurations and binding energies [32, 34], alloy disorder, and potential fluctuation. These states are usually associated with two groups with different activation energies in undoped GaAs_{1-x}Bi_x samples: one ranges from 8 to 17 meV and is related to Bi clusters and Bi pairs, and the other energy around 50 meV is related to alloy disorder [34, 44]. As shown in Table 5.4, the E₁ energies ranging between 4 meV and 25 meV are attributed to Bi clusters and Bi pairs as expected. However, the E₂ values ranging from 118 meV to 194 meV indicate that the epilayers have some potential fluctuations, which is consistent with the observed S-shape evolution. Indeed, the presence of localized energy levels in the band gap, which are associated with alloy disorder [45], was reported earlier with a comparatively lower activation energy (75 meV) [34, 45] as compared to the samples investigated in this work (E₂ ranging from 118 meV to 194 meV).

Table 5.4: Arrhenius's parameters obtained from the temperature dependence of the total integrated PL peak intensity of GaAs_{1-x}Bi_x thin films samples.

Samples	Activation energy (meV)	
	E ₁	E ₂
Sample C	25.87	194.91
Sample D	8.21	118.83
Sample E	22.08	125.99
Sample F	21.50	175.83
Sample G	4.92	164.72

5.4 CONCLUSION

The optical properties of GaAs_{1-x}Bi_x epilayers grown on (100) GaAs substrates by Molecular Beam Epitaxy at different growth temperatures were investigated by using SEM, XRD, PL and Raman techniques. The influence of the growth temperature on the optical properties of GaAs_{1-x}Bi_x has been examined systematically. The PL measurements showed that the PL spectra exhibit two different behaviours depending on the growth temperature, namely, red and blue shift were observed as the growth temperature increases from 300 °C to 325 °C, and from 325 °C to 365 °C, respectively. The observed differences in PL peak position for different growth temperatures of GaAs_{1-x}Bi_x samples may indicate contributions from strain and/or Bi-defect level-band related transitions. Moreover, the Bi composition in the studied samples were determined and calculated from PL. The results showed that Bi incorporation into the GaAs host lattice is very sensitive to the growth temperature and varied from 2.3% to 4.7%, and from 4.7 % to 2.8% for a growth temperature in the range 300 °C - 325°C and 325 °C - 365 °C, respectively. This is evidenced by the red shift of the PL peak energy with increasing growth temperature. This result is consistent with Raman measurements which demonstrated that as the content of Bi increases first there is a slight redshift and then a blueshift of the LO phonon peak, which can be explained by the Bi-induced tensile and/or compressive stress. Sample A (T_G= 300 °C) has the lowest Bi concentration and optical quality due higher density of defects than other samples. These results are consistent with SEM data which demonstrated that samples A (T_G=300 °C) have the highest surface concentrations of droplets and the lowest concentrations of Bi, meaning that for these low growth temperatures a lower concentration of Bi was incorporated into the GaAs host lattice. On the other

hand, the optimum growth temperature for maximum Bi incorporation (4.7%) was found to be 325 °C (sample D) which is in good agreement with SEM data which showed that this sample has a lower number of both surface droplets and self-aligned trailing nanotracks. The temperature dependence of the PL spectra in the range 10 K-200 K was also studied. It was found that the peak luminescence energy as a function of temperature is dependent on the incident excitation power. For a 5 mW laser excitation power, no evidence of the characteristic S-shape was observed under such low power condition, and its behaviour was well approximated by the empirical Varshni relation. However, the temperature dependence of PL peak energy at excitation intensity of 15 mW has shown a pronounced S-shape characteristic, which is also typical of the highly mismatched alloys. The S-shaped temperature dependence also originates from the PL of localized states in $\text{GaAs}_{(1-x)}\text{Bi}_x$ in the temperature range of 150 K - 200 K. The integrated PL intensity as a function of inverse temperature confirmed two processes that govern the carrier thermal quenching in the low and high temperature regimes with two activation energies E_1 and E_2 corresponding to Bi clusters and alloy disorder, respectively.

REFERENCES

- [1] S. Francoeur, M.-J. Seong, A. Mascarenhas, S. Tixier, M. Adamcyk, T. Tiedje, Band gap of GaAs $1-x$ Bi x , $0 < x < 3.6\%$, Applied physics letters, 82 (2003) 3874-3876.
- [2] Z. Batool, K. Hild, T. Hosea, X. Lu, T. Tiedje, S. Sweeney, The electronic band structure of GaBiAs/GaAs layers: Influence of strain and band anti-crossing, Journal of Applied Physics, 111 (2012) 113108.
- [3] B. Fluegel, S. Francoeur, A. Mascarenhas, S. Tixier, E. Young, T. Tiedje, Giant spin-orbit bowing in GaAs $1-x$ Bi x , Physical review letters, 97 (2006) 067205.
- [4] Z. Zhou, D.F. Mendes, R.D. Richards, F. Bastiman, J.P. David, Absorption properties of GaAsBi based p-i-n heterojunction diodes, Semiconductor Science and Technology, 30 (2015) 094004.
- [5] V. Pačebutas, K. Bertulis, A. Bičiūnas, A. Krotkus, Low-temperature MBE-grown GaBiAs layers for terahertz optoelectronic applications, physica status solidi c, 6 (2009) 2649-2651.
- [6] X. Lu, D. Beaton, R. Lewis, T. Tiedje, M. Whitwick, Effect of molecular beam epitaxy growth conditions on the Bi content of GaAs $1-x$ Bi x , Applied Physics Letters, 92 (2008) 192110.
- [7] Ł. Gelczuk, J. Kopaczek, T.B. Rockett, R.D. Richards, R. Kudrawiec, Deep-level defects in n-type GaAsBi alloys grown by molecular beam epitaxy at low temperature and their influence on optical properties, Scientific Reports, 7 (2017) 1-11.
- [8] A. Mohmad, F. Bastiman, C. Hunter, J. Ng, S. Sweeney, J. David, The effect of Bi composition to the optical quality of GaAs $1-x$ Bi x , Applied Physics Letters, 99 (2011) 042107.

- [9] P. Mooney, M. Tarun, V. Bahrami-Yekta, T. Tiedje, R. Lewis, M. Masnadi-Shirazi, Defect energy levels in p-type GaAsBi and GaAs grown by MBE at low temperatures, *Semiconductor Science and Technology*, 31 (2016) 065007.
- [10] K. Bertulis, A. Krotkus, G. Aleksejenko, V. Pačebutas, R. Adomavičius, G. Molis, S. Marcinkevičius, GaBiAs: A material for optoelectronic terahertz devices, *Applied physics letters*, 88 (2006) 201112.
- [11] S. Tixier, M. Adamcyk, T. Tiedje, S. Francoeur, A. Mascarenhas, P. Wei, F. Schiettekatte, Molecular beam epitaxy growth of GaAs $1-x$ Bi x , *Applied physics letters*, 82 (2003) 2245-2247.
- [12] R. Lewis, M. Masnadi-Shirazi, T. Tiedje, Growth of high Bi concentration GaAs $1-x$ Bi x by molecular beam epitaxy, *Applied Physics Letters*, 101 (2012) 082112.
- [13] H. Fitouri, I. Moussa, A. Rebey, A. Fouzri, B. El Jani, AP-MOVPE of thin GaAs $1-x$ Bi x alloys, *Journal of crystal growth*, 295 (2006) 114-118.
- [14] I. Moussa, H. Fitouri, A. Rebey, B. El Jani, Atmospheric-pressure metalorganic vapour phase epitaxy optimization of GaAsBi alloy, *Thin Solid Films*, 516 (2008) 8372-8376.
- [15] H. Fitouri, I. Moussa, A. Rebey, B. El Jani, Study of GaAsBi MOVPE growth on (1 0 0) GaAs substrate under high Bi flow rate by high resolution X-ray diffraction, *Microelectronic engineering*, 88 (2011) 476-479.
- [16] H. Jacobsen, B. Puchala, T.F. Kuech, D. Morgan, Ab initio study of the strain dependent thermodynamics of Bi doping in GaAs, *Physical Review B*, 86 (2012) 085207.

- [17] K. Forghani, Y. Guan, M. Losurdo, G. Luo, D. Morgan, S.E. Babcock, A.S. Brown, L.J. Mawst, T. Kuech, GaAs $_{1-y-z}$ PyBiz, an alternative reduced band gap alloy system lattice-matched to GaAs, *Applied Physics Letters*, 105 (2014) 111101.
- [18] L. Nattermann, P. Ludewig, N. Knaub, N. Rosemann, T. Hepp, E. Sterzer, S. Jin, K. Hild, S. Chatterjee, S. Sweeney, MOVPE growth and characterization of quaternary Ga (PAsBi)/GaAs alloys for optoelectronic applications, *Applied Materials Today*, 5 (2016) 209-214.
- [19] V. Bahrami-Yekta, T. Tiedje, M. Masnadi-Shirazi, MBE growth optimization for GaAs $_{1-x}$ Bi $_x$ and dependence of photoluminescence on growth temperature, *Semiconductor Science and Technology*, 30 (2015) 094007.
- [20] J. Steele, J. Horvat, R.A. Lewis, M. Henini, D. Fan, Y.I. Mazur, V. Drogan, P. Grant, S.-Q. Yu, G. Salamo, Mechanism of periodic height variations along self-aligned VLS-grown planar nanostructures, *Nanoscale*, 7 (2015) 20442-20450.
- [21] T. Paulauskas, V. Pačebutas, R. Butkutė, B. Čechavičius, A. Naujokaitis, M. Kamarauskas, M. Skapas, J. Devenson, M. Čaplovičová, V. Vretenár, Atomic-resolution EDX, HAADF, and EELS study of GaAs $_{1-x}$ Bi $_x$ alloys, *Nanoscale Research Letters*, 15 (2020) 1-12.
- [22] G. Vardar, S. Paleg, M. Warren, M. Kang, S. Jeon, R. Goldman, Mechanisms of droplet formation and Bi incorporation during molecular beam epitaxy of GaAsBi, *Applied Physics Letters*, 102 (2013) 042106.
- [23] S. Zhu, W. Qiu, H. Wang, T. Lin, P. Chen, X. Wang, Raman spectroscopic determination of hole concentration in undoped GaAsBi, *Semiconductor Science and Technology*, 34 (2018) 015008.

- [24] M. Seong, S. Chun, H.M. Cheong, N. Samarth, A. Mascarenhas, Spectroscopic determination of hole density in the ferromagnetic semiconductor $\text{Ga}_{1-x}\text{Mn}_x\text{As}$, *Physical Review B*, 66 (2002) 033202.
- [25] J. Steele, R. Lewis, M. Henini, O. Lemine, D. Fan, Y.I. Mazur, V. Dorogan, P. Grant, S.-Q. Yu, G. Salamo, Raman scattering reveals strong LO-phonon-hole-plasmon coupling in nominally undoped GaAsBi: optical determination of carrier concentration, *Optics express*, 22 (2014) 11680-11689.
- [26] D. Schmeltzer, R. Beserman, Localized states in mixed $\text{Ga}_z\text{P}_{1-z}\text{As}$ crystals, *Physical Review B*, 22 (1980) 6330.
- [27] P. Verma, K. Oe, M. Yamada, H. Harima, M. Herms, G. Irmer, Raman studies on $\text{Ga}_{1-x}\text{As}_x\text{Bi}_x$ and $\text{In}_{1-x}\text{As}_x\text{Bi}_x$, *Journal of Applied Physics*, 89 (2001) 1657-1663.
- [28] G. Irmer, M. Wenzel, J. Monecke, Light scattering by a multicomponent plasma coupled with longitudinal-optical phonons: Raman spectra of p-type GaAs: Zn, *Physical Review B*, 56 (1997) 9524.
- [29] D.E. Aspnes, A. Studna, Dielectric functions and optical parameters of si, ge, gap, gaas, gasb, inp, inas, and insb from 1.5 to 6.0 eV, *Physical review B*, 27 (1983) 985.
- [30] J. Blakemore, Semiconducting and other major properties of gallium arsenide, *Journal of Applied Physics*, 53 (1982) R123-R181.
- [31] Q. Kim, D. Langer, Effects of excitation intensity on photoluminescence of pure CdTe, *physica status solidi (b)*, 122 (1984) 263-268.
- [32] S. Mazzucato, P. Boonpeng, H. Carrère, D. Lagarde, A. Arnoult, G. Lacoste, T. Zhang, A. Balocchi, T. Amand, X. Marie, Reduction of defect density by rapid

thermal annealing in GaAsBi studied by time-resolved photoluminescence, *Semiconductor science and technology*, 28 (2013) 022001.

[33] X. Liu, A. Prasad, J. Nishio, E. Weber, Z. Liliental-Weber, W. Walukiewicz, Native point defects in low-temperature-grown GaAs, *Applied Physics Letters*, 67 (1995) 279-281.

[34] S. Alhassan, D. de Souza, A. Alhassni, A. Almunyif, S. Alotaibi, A. Almalki, M. Alhuwayz, I.P. Kazakov, A.V. Klekovkin, V.I. Tsekosh, Investigation of the effect of substrate orientation on the structural, electrical and optical properties of n-type GaAs_{1-x}Bi_x layers grown by Molecular Beam Epitaxy, *Journal of Alloys and Compounds*, 885 (2021) 161019.

[35] D. De Souza, S. Alhassan, S. Alotaibi, A. Alhassni, A. Almunyif, H. Albalawi, I.P. Kazakov, A.V. Klekovkin, S.A. ZinovEv, I.A. Likhachev, Structural and optical properties of n-type and p-type GaAs (1-x) Bi_x thin films grown by molecular beam epitaxy on (311) B GaAs substrates, *Semiconductor Science and Technology*, 36 (2021) 075018.

[36] F. Sarcan, Ö. Dönmez, K. Kara, A. Erol, E. Akalın, M.Ç. Arıkan, H. Makhloufi, A. Arnoult, C. Fontaine, Bismuth-induced effects on optical, lattice vibrational, and structural properties of bulk GaAsBi alloys, *Nanoscale Research Letters*, 9 (2014) 1-7.

[37] T. Schmidt, K. Lischka, W. Zulehner, Excitation-power dependence of the near-band-edge photoluminescence of semiconductors, *Physical Review B*, 45 (1992) 8989.

[38] P. Dean, Photoluminescence as a diagnostic of semiconductors, *Progress in Crystal Growth and Characterization*, 5 (1982) 89-174.

- [39] T. Taguchi, J. Shirafuji, Y. Inuishi, Excitonic emission in cadmium telluride, *physica status solidi (b)*, 68 (1975) 727-738.
- [40] A. Mohmad, F. Bastiman, C. Hunter, R. Richards, S. Sweeney, J. Ng, J. David, B. Majlis, Localization effects and band gap of GaAsBi alloys, *Physica status solidi (b)*, 251 (2014) 1276-1281.
- [41] T. Wilson, N.P. Hylton, Y. Harada, P. Pearce, D. Alonso-Álvarez, A. Mellor, R.D. Richards, J.P. David, N.J. Ekins-Daukes, Assessing the nature of the distribution of localised states in bulk GaAsBi, *Scientific Reports*, 8 (2018) 1-10.
- [42] O. Donmez, A. Erol, M. Arikan, H. Makhloufi, A. Arnoult, C. Fontaine, Optical properties of GaBiAs single quantum well structures grown by MBE, *Semiconductor Science and Technology*, 30 (2015) 094016.
- [43] Y.I. Mazur, V. Dorogan, M. Schmidbauer, G. Tarasov, S. Johnson, X. Lu, M. Ware, S.-Q. Yu, T. Tiedje, G. Salamo, Strong excitation intensity dependence of the photoluminescence line shape in GaAs_{1-x}Bi_x single quantum well samples, *Journal of Applied Physics*, 113 (2013) 144308.
- [44] T. Lu, Z. Ma, C. Du, Y. Fang, H. Wu, Y. Jiang, L. Wang, L. Dai, H. Jia, W. Liu, Temperature-dependent photoluminescence in light-emitting diodes, *Scientific reports*, 4 (2014) 1-7.
- [45] C. Himwas, A. Soison, S. Kijamnajsuk, T. Wongpinij, C. Euaraksakul, S. Panyakeow, S. Kanjanachuchai, GaAsPBi epitaxial layer grown by molecular beam epitaxy, *Semiconductor Science and Technology*, 35 (2020) 095009.

CHAPTER 6: INVESTIGATION OF THE EFFECT OF GAMMA RADIATION ON THE STRUCTURAL AND OPTICAL PROPERTIES OF DILUTE GaAs_{1-x}Bi_x EPILAYERS GROWN AT DIFFERENT GROWTH TEMPERATURES BY MOLECULAR BEAM EPITAXY

This chapter reports the effect of gamma radiation dose on the structural and optical properties of dilute GaAs_{1-x}Bi_x epitaxial layers grown at different substrate temperatures by Molecular Beam Epitaxy (MBE) on conventional (100) GaAs substrates using XRD, hole concentration determined from Raman spectroscopy and PL techniques. Gamma radiation (γ -) was found to influence the electrical and optical properties of GaAs_{1-x}Bi_x epitaxial layers. From Raman measurements it was found that the concentration of holes increased when the samples were irradiated. This result is in good agreement with the photoluminescence results, which showed that the intensity of the main peak increases after irradiation, indicating that the optical properties have improved for all samples. Furthermore, the XRD data showed that for irradiated GaAs_{1-x}Bi_x samples, the crystallographic quality of the samples was slightly worse after irradiation. This is due to the fact that radiation induces several types of defects, including structural defects. This result is consistent with the results of the PL measurements, which demonstrated that the GaAs_{1-x}Bi_x samples exposed to 50 kGy dose have the largest PL full width at half maximum (FWHM) for all irradiated samples. This finding demonstrates that irradiated samples have worse quality compared to non-irradiated samples. The decrease in FWHM confirms a better uniformity of GaAs_{1-x}Bi_x thin films for the non-irradiated samples.

6.1 INTRODUCTION

Electrical and optical properties of III-V semiconductor materials can be altered by intentionally incorporating impurities into the host lattice, and these may significantly influence the performance of electronic and optoelectronic devices. In general, defects can be created in semiconductor materials either intentionally or unintentionally through ionizing irradiation. Radiation induced defects can be divided into two types that are modified by ionizing irradiation: those created initially during growth of the crystal by substitution of a lattice atom with an impurity atom (extrinsic defect) and those created by atomic displacements of a standard lattice site element during irradiation (intrinsic defect). Ionizing radiation creates ions and free electrons, which in turn may be stabilized/trapped by radiation-induced defects before recombination can occur at normal lattice sites [1]. Gamma radiation is an indirectly ionizing and highly energetic electromagnetic radiation, which has a large penetration power. In this sense, ionizing radiation, which can modify the optical and electrical properties of semiconductor materials, may lead to the development of new dosimeters and/or more efficient radiation detectors. Thus, a deep understanding of the effect of gamma radiation on new materials is essential for the improvement of dosimeters. Furthermore, due to radiation in space and the use of electronic devices in satellites, considerable amount of defects can be induced in semiconductors which, in turn, can cause degradation and decrease of the average lifetime of the devices [2].

Several groups have studied the effect of radiation treatment in metal/semiconductor Schottky diodes using a variety of radiation sources, including electron [3], neutron [4], swift heavy ions [5], and gamma radiation [6,

7]. However, the effects of gamma irradiation on GaAs_{1-x}Bi_x thin films grown at different temperatures have not yet been investigated. Gamma irradiation of dilute GaAs_{1-x}Bi_x layers can contribute to a better understanding of the behavior of Bi incorporation into the GaAs host lattice. In this study, the influence of gamma irradiation dose on the structural and optical properties of GaAs_{1-x}Bi_x samples grown by MBE on (100) GaAs substrates is investigated in depth using a variety of methods such as XRD, Raman spectroscopy, hole concentration and PL measurements.

6.2 SAMPLE DETAILS

The samples studied in this work are GaAs_{1-x}Bi_x epilayers grown by solid-source MBE on semi-insulating (100) GaAs substrates at a range of different growth temperatures $T_G = 300\text{ }^\circ\text{C}$, $310\text{ }^\circ\text{C}$, $320\text{ }^\circ\text{C}$, $325\text{ }^\circ\text{C}$, $340\text{ }^\circ\text{C}$, $345\text{ }^\circ\text{C}$ and $365\text{ }^\circ\text{C}$ and labelled as A, B, C, D, E, F and G, respectively, as shown in Chapter 5 (Table 5.1). The layer structure of the GaAs_{1-x}Bi_x samples was illustrated in Figure 5.1 and discussed in Chapter 5 (section 5.2.). Furthermore, the surface of all GaAs_{1-x}Bi_x samples were examined using SEM technique as discussed in Chapter 5 (section 5.3.1.2).

It is important to note that the same piece of each sample mentioned above was measured before and after irradiation. The samples are labelled as NIR (non-irradiated) and IR (irradiated). The gamma radiation dose was 50 kGy. The optical characterization techniques used to investigate these samples are similar to those presented in Chapter 5. The samples were then irradiated with a gamma cell Cobalt Irradiator (dose rate of 1.3 kGy/h) at dose of 50 kGy in the Department of Nuclear Energy at the Federal University of Pernambuco, Brazil. PL spectra of all

GaAs_{1-x}Bi_x samples were investigated as a function of laser power and temperature using a Janis closed-loop helium cryostat. A green laser with a wavelength of 532 nm (2.33 eV) was used to excite the samples. Before subjecting the samples to gamma irradiation, each sample was evaluated using PL measurements to determine whether or not they were uniform. The PL signal was collected in a 0.5 m Andor monochromator fitted with an InGaAs detector. The Raman measurements were performed using a Horiba Lab RAM Evolution micro spectrometer at room temperature using a 532 nm laser line. The laser excitation powers of 5.35 mW and 0.107 mW were used in order to obtain the correlation of Bi concentration with PL results and the hole concentration, respectively.

6.3 RESULTS AND DISCUSSION

6.3.1 Structural Characteristics

Figure 6.1 shows XRD patterns obtained for all samples investigated in this work between $2\theta = 65^{\circ}$ and 67° before and after exposed (50kGy) to gamma radiation. The XRD patterns in Figure 6.1(a) of the NIR samples was discussed in Chapter 5 (section 5.3.1.1). Furthermore, the discussion for XRD data as shown in Figure 6.1(b) of the IR samples is similar to the NIR samples as presented in Chapter 5 (section 5.3.1.1). However, the exception is that the data shown for IR samples, the crystallographic quality of the samples was slightly worse after irradiation. This is due to the fact that radiation induces several types of defects, including structural defects. It is important to note that the signal to noise ratio shown on the XRD plot of the IR samples is less than that shown by the NIR samples.

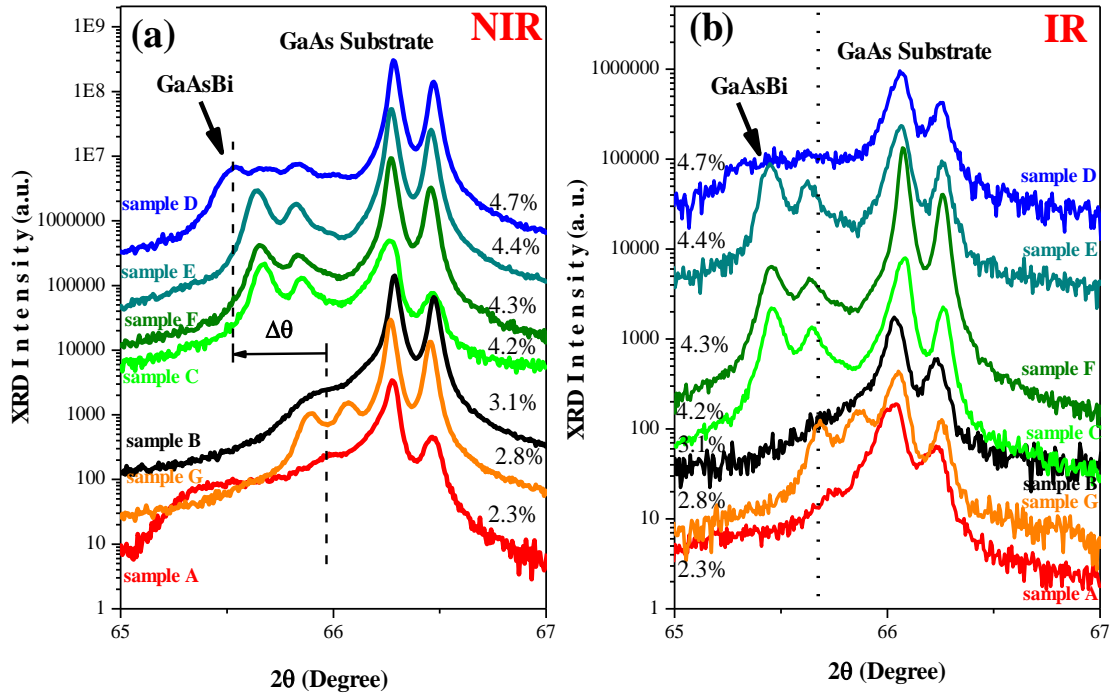


Figure 6.1: XRD patterns obtained for all samples investigated in this study between $2\theta = 65^{\circ}$ and 67° for (a) NIR and (b) IR samples.

6.3.2 Optical Properties

6.3.2.1 Raman Measurements

As discussed in Section 5.3.2.1 of Chapter 5, Raman spectroscopy, can sometimes be considered as an alternative to Hall effect technique which provides a different approach for the determination of charge carrier concentrations without using electrical contacts but the hall measurements also provide a determination of the mobility. In the following, the effect of gamma radiation on Raman spectra and hole concentrations of $\text{GaAs}_{1-x}\text{Bi}_x$ samples irradiated with a 50 kGy dose will be presented. It will be also shown that Raman spectroscopy has proved to be a versatile tool for studying defects in $\text{GaAs}_{1-x}\text{Bi}_x$ samples. It is important to point out that low laser excitation powers were used to perform all Raman measurements. This procedure was adopted because high laser excitation powers may give

incorrect hole concentration values [8]. Sixin et al. showed that laser powers lower than 0.4 mW provides results compatible with other techniques. According to this, in Figure 6.2 (a) and (b) are shown Raman spectra that were obtained using 0.107 mW as the excitation power for the IR and NIR GaAsBi samples.

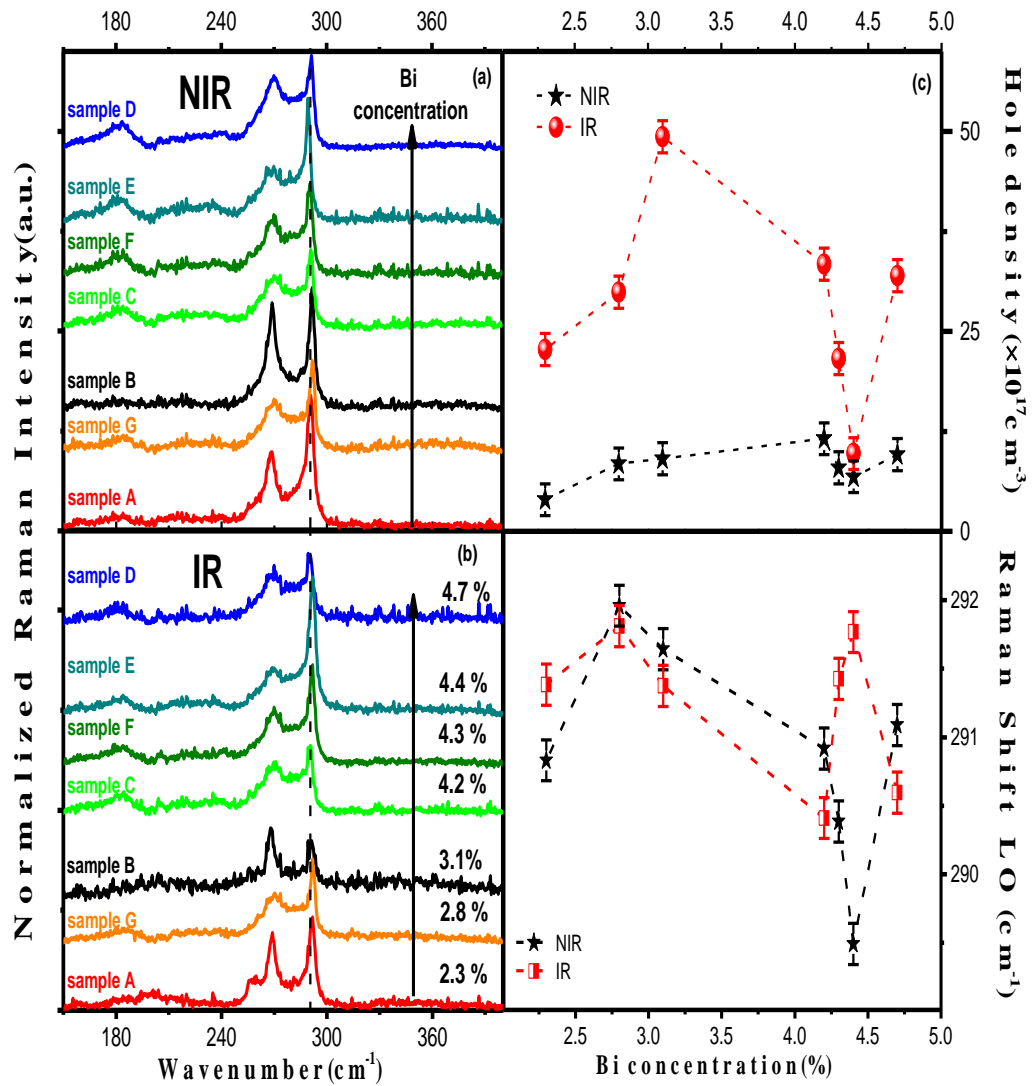


Figure 6.2: Raman spectra from GaAs_{1-x}Bi_x samples having different Bi concentrations. The measurements were performed using 0.107 mW as the excitation power (a) non-irradiated (NIR) samples and (b) Irradiated (IR) samples. (c) The hole concentration (calculated from equation 5.1 in Chapter 5) versus Bi content for IR and NIR samples. (d) Raman shifts of LO mode versus Bi content for the NIR and IR samples.

When carefully comparing the spectra, subtle differences are observed which are evident in the analysis below. The Raman spectra from NIR GaAs_{1-x}Bi_x samples shown in Figure 6.2(a) was discussed in Chapter 5 (section 5.3.2.1). Furthermore, the discussion for the Raman spectra as shown in Figure 6.2(b) of the IR samples is similar to the NIR samples, which is presented in Chapter 5.

Figure 6.2 (c) shows the hole concentrations as a function of bismuth concentration of the NIR samples (black stars) and IR samples (red balls). Note that initially the hole concentration in NIR samples increases proportionally until reaching 4.2% of bismuth, then decreases and finally increases again. It is very important to note from Figure 6.2 (c), that the concentration of holes increased for all samples after radiation. Furthermore, the hole concentrations of the IR samples show a similar behaviour, i.e. increase/decrease/increase, but with a more pronounced trend than the one displayed by the NIR samples. These findings show that these results are consistent with the PL results that will be discussed later, since all samples showed an increase in PL intensity after irradiation.

As is well known, a considerable deformation of the GaAs lattice occurs due the large size of bismuth atoms, which causes an increase in the carrier-phonon coupling. Associated with this, the incorporation of Bi into GaAs host lattice also produces a strong effect on the carrier recombination process due to an increase in the density of localized states [9, 10]. Compressive strain is also commonly observed in GaAs due to bismuth incorporation [9]. These effects caused in the crystal lattice of GaAs due to the incorporation of Bi causes disorder and/or residual strains which alter the frequencies of phonons and their lifetime, and can be

identified by means of Raman spectroscopy [11]. In fact, the GaAs LO Raman mode frequency shifts are deeply related to the compressive and tensile strains, resulting in positive and negative frequency shifts, respectively [12, 13].

In Figure 6.2 (d) are plotted the Raman shift of LO mode from the NIR (black squares) and IR (solid red circles) samples. As can be seen in Figure 6.2 (d), an evident frequency shift of the LO mode is observed as a function of Bi concentration. Interestingly, when comparing NIR and IR samples, a positive or negative frequency shifts in LO mode maybe observed depending on the concentration of Bi. Remarkably, the samples that showed a negative change in the frequency of the LO mode were those that showed the smallest increase in the PL signal after radiation (to be discussed later). This means that these samples showed tensile strains after irradiation. On the other hand, samples with Bi concentrations of 4.3 and 4.4% showed a positive frequency shift of the LO mode after irradiation, indicating that the irradiation caused a compressive strain. More interesting, as will be shown below, the sample with 4.3% of Bi showed the highest increase in the PL signal after irradiation.

6.3.2.2 Photoluminescence

This section will report on the optical properties of $\text{GaAs}_{1-x}\text{Bi}_x$ thin films grown on conventional (100) GaAs substrates at different growth temperatures ($T_G = 300^\circ\text{C} - 365^\circ\text{C}$). Photoluminescence spectroscopy measurements were carried out at a range of temperatures (10 K - 240 K) and excitation powers of 15mW in order to investigate the effects of gamma radiation on the optical properties of the $\text{GaAs}_{1-x}\text{Bi}_x$ epilayers. To verify the effect of ionizing radiation on optical properties of

GaAs_{1-x}Bi_x samples, power dependent PL measurements were carried out. Figures 6.3(a) and 6.3(b) display the PL spectra at 10 K for all GaAs_{1-x}Bi_x samples, namely as-grown and irradiated with a dose of 50 kGys using a laser excitation power of 16 mW (0.91 W/cm²).

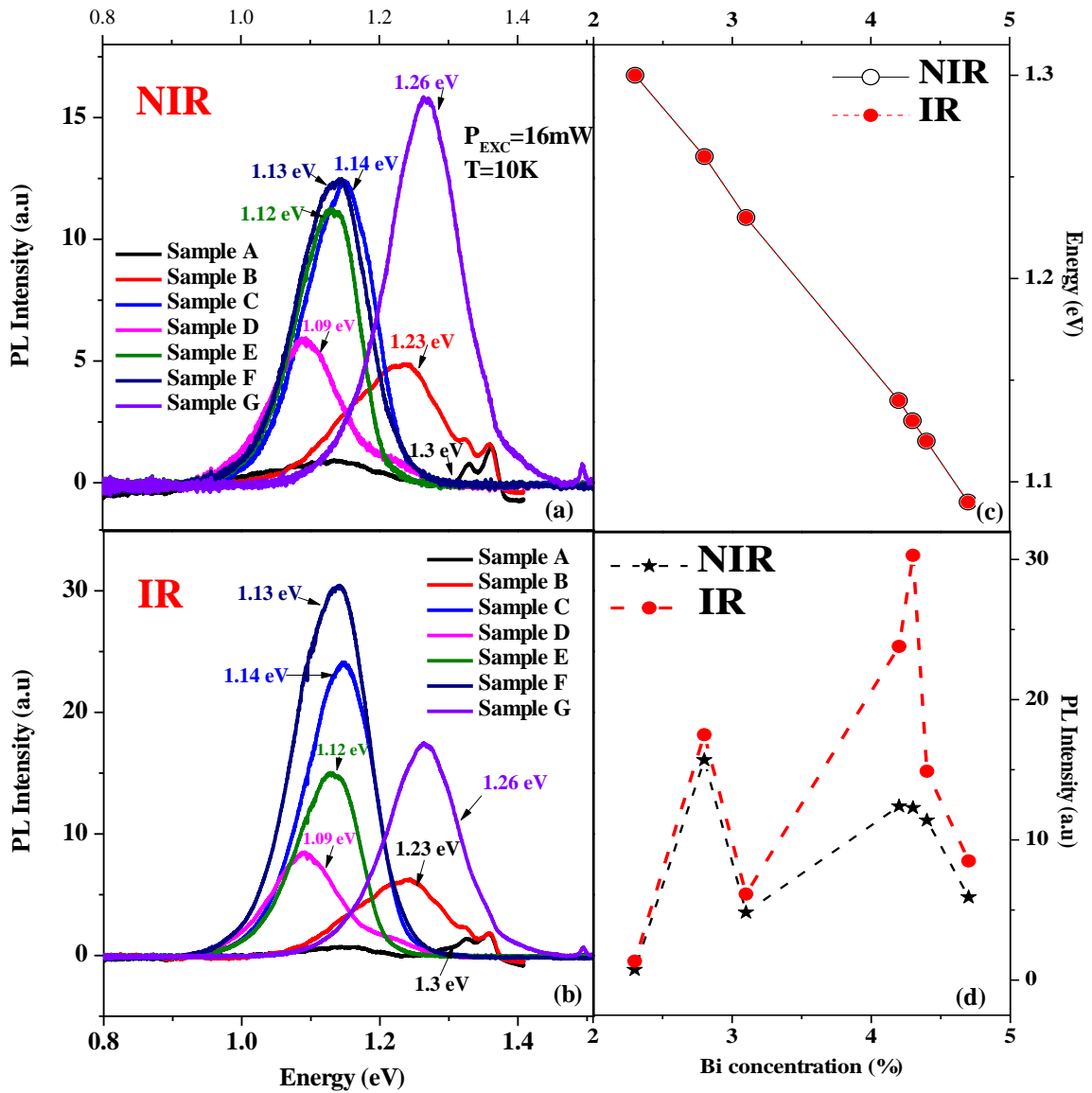


Figure 6.3: 10 K PL spectra of GaAs_{1-x}Bi_x epilayers grown on (100) GaAs substrates for samples A, B, C, D, E, F and G: (a) NIR and (b) IR with 50kGy dose. Bi concentration as a function of (c) PL peak energy and (d) PL intensity for NIR and IR GaAs_{1-x}Bi_x samples. The measurements were carried out using a green laser (532 nm) and $P_{\text{EXC}} = 16 \text{ mW}$.

The PL peaks energies of both NIR and IR samples have the same energies, as can be seen in Figures 6.3 (a) and (b). The PL peaks energies at 1.30 eV, 1.23 eV, 1.14 eV, 1.09 eV, 1.12 eV, 1.13 eV and 1.26 eV are related to $\text{GaAs}_{1-x}\text{Bi}_x$ for samples A, B, C, D, E, F and G, respectively. The effects of gamma radiation on $\text{GaAs}_{1-x}\text{Bi}_x$ thin films is clearly demonstrated in Figures 6.3 (b), (c) and (d) by the following observations: (i) no blue shift of the $\text{GaAs}_{(1-x)}\text{Bi}_x$ thin film PL peak emission energy was observed (see Figure 6.3 (b) and (c)), (ii) there are enhancements of the PL intensities by a factor of 1.06, 1.2, 1.9, 1.4, 1.3, 2.4 and 1.1 for all samples A, B, C, D, E, F and G, respectively (see Figure 6.3d). The latter observation supports the Raman hole concentration results which demonstrated an increase in the carrier concentration for all IR $\text{GaAs}_{1-x}\text{Bi}_x$ samples at 50 kGy dose in comparison with the NIR samples.

Furthermore, the Bi concentration as a function of PL peak energy and PL intensity are shown in Figures 6.3 (c) and (d), respectively, before and after the irradiation process. The Bi concentration was determined based on the PL measurements, which were discussed in Chapter 5 (section 5.3.2.2), along with Figure 5.10 and Table 5.2. Figure 6.3 (c) demonstrates that the PL peak energy versus Bi concentration follows a similar pattern for both NIR and IR irradiated samples. This pattern exhibits a shift to lower energies (a redshift of the PL peak energy) as the Bi concentration increases from 2.3% to 4.7%, demonstrating the reduction of the bandgap that is expected with increasing Bi content. This indicates that the bandgap of $\text{GaAs}_{1-x}\text{Bi}_x$ undergoes a red shift as the composition of Bi increases. This is because of the increased interaction between the valence band and the localized Bi level [14].

As can be seen in Figure 6.3(d), there is also an increase in the PL intensity of all samples, however, this enhancement is largest for the sample with a Bi concentration of 4.3% (sample F). These PL results are also in good agreement with the Raman results, which showed a positive frequency shift of the LO mode after irradiation. This shift in frequency after irradiation indicates that the irradiation caused a compressive strain in the material. However, the samples with a lower Bi concentration showed a smaller increase in the PL signal after being exposed to radiation. These samples had a Bi concentration of 2.3% (sample A), 2.8% (sample G), and 3.1% (sample B). These results are consistent with the findings obtained from the Raman measurements, which demonstrated a decrease in the frequency of the LO mode. After being exposed to ionising radiation, these above samples demonstrated signs of tensile strain. In addition, these results are also in good agreement with SEM data (discussed in Chapter 5), which showed that the samples with the highest surface concentrations of droplets are those with the lowest concentrations of Bi (see SEM images illustrated in Figure 5.5 (a), (b) and (g)). This indicates that for these growth temperatures a lower concentration of Bi was incorporated into the GaAs host lattice.

The temperature dependence of the PL spectra was also studied over the temperature range of 10 K to 240 K in order to gain additional information about the characteristics of IR GaAs_{1-x}Bi_x thin films grown on the (100) GaAs plane at various temperatures. The excitation energy was 2.33 eV (532 nm), and the excitation power was set to 15 mW to avoid saturation of localized states. The PL peaks of IR GaAs_{1-x}Bi_x samples A and B were not detected at temperatures above 40K (not shown in Figure 6.4). However, the PL spectra of IR GaAs_{1-x}Bi_x samples C, D, E, F and G are shown in Figures 6.4 (a), (b), (c), (d) and (e), respectively.

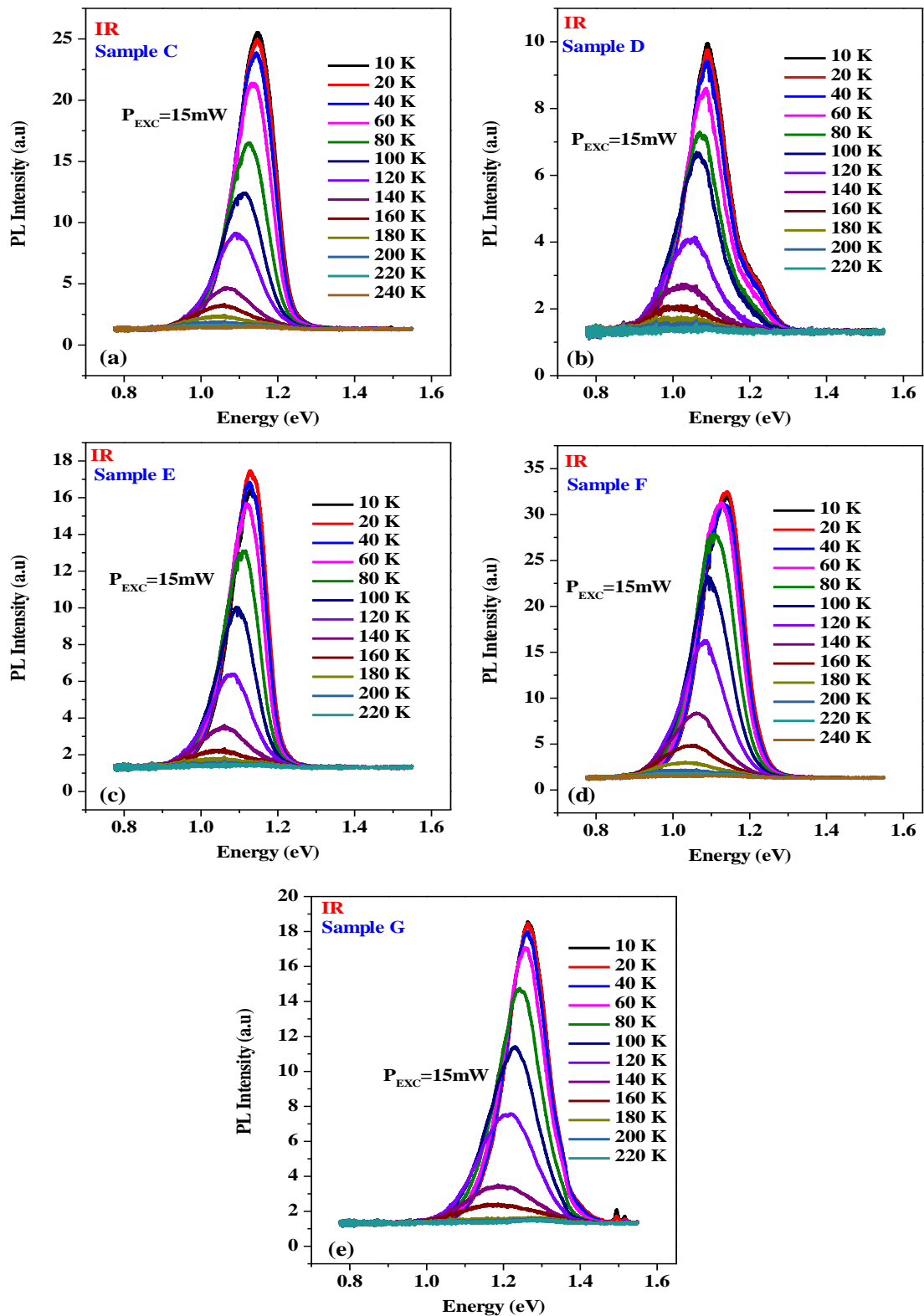


Figure 6.4: Temperature dependence of PL spectra of IR GaAs_{1-x}Bi_x thin films grown on (100) GaAs substrates at different growth temperatures for a laser power excitation $P_{\text{exc}} = 15 \text{ mW}$.

The IR samples A and B showed similar trends as those NIR GaAs_{1-x}Bi_x samples grown at the same temperatures, where the PL peaks disappeared at 40K. On the other hand, the PL spectra extended more in terms of temperature for the samples C, D, E, F and G as compared to the NIR samples, due to an increase of the optical efficiency (PL intensity increased) after irradiation. These results support the Raman results which showed that the concentration of holes increased for all IR samples when compared to NIR ones. The shapes of the PL spectra of IR GaAs_{1-x}Bi_x samples are comparable to those of NIR GaAs_{1-x}Bi_x thin films. The PL spectra exhibit an asymmetric characteristic with a low energy tail, which is typically observed in highly mismatched alloys. Furthermore, no PL signal could be detected in samples C, D, E, F and G above temperatures of 240 K, 220 K, 220 K, 240 K and 220 K, respectively (see Table 6.1). Interestingly, it is important to point out that for NIR samples the PL signal quenched at 200 K, 170 K, 190 K, 200 K and 190 K for samples C, D, E, F and G, respectively (see Table 6.1). This means that, for some samples, the radiation increased the temperature range over which the PL signal can be detected by more than 50 K. In addition, a redshift of PL peak energy with the increase of temperature was observed in IR GaAs_{1-x}Bi_x samples as expected, and the PL emission gets broader for all irradiated samples. Furthermore, the shoulder peak at around 1.2 eV appears for NIR GaAs_{1-x}Bi_x sample D (Figure 5.14 in Chapter 5), which indicates that it is not related to the effect of radiation.

Figure 6.5 illustrates representative plots of the temperature-dependent PL spectra that were measured at an incident excitation power of 15 mW for all (a) NIR GaAs_{1-x}Bi_x epilayers and (b) IR GaAs_{1-x}Bi_x epilayers with a dose of 50 kGy.

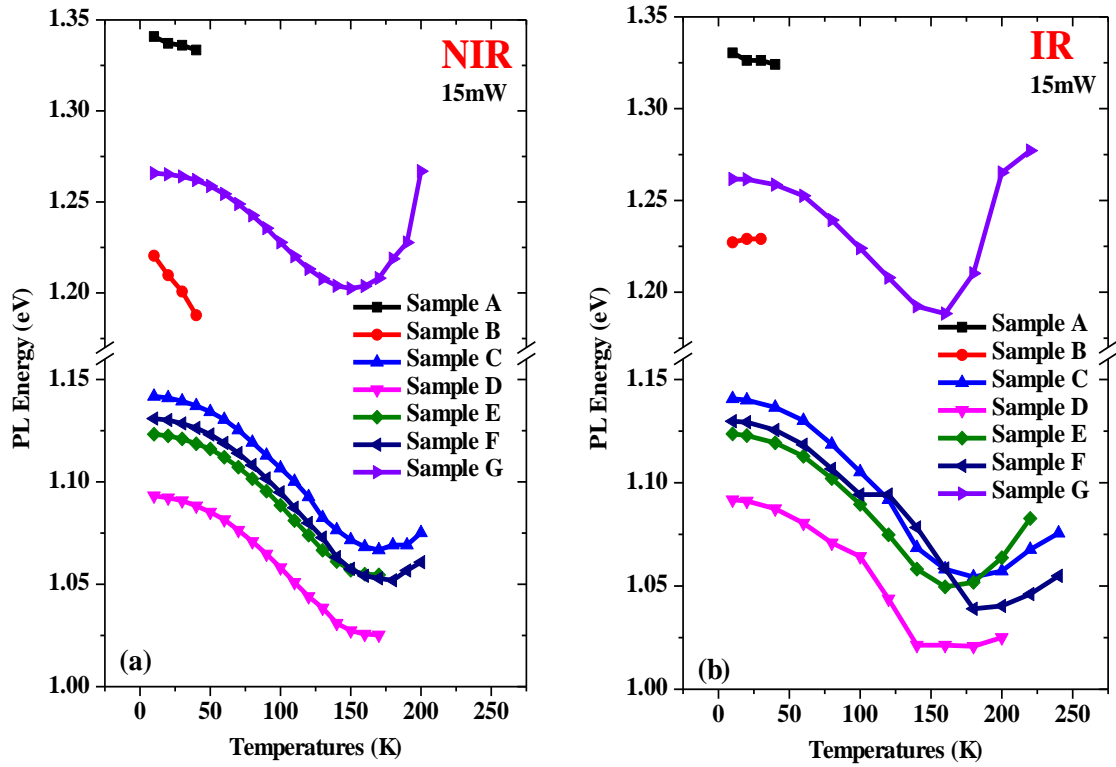


Figure 6.5: (a) PL peak energy as a function of temperature for GaAs_{1-x}Bi_x epilayers grown on (100) GaAs substrates for samples A, B, C, D, E, F and G: (a) NIR samples; (b) IR samples at 50kGy dose. All measurements were taken at an excitation power of 15 mW.

As clearly seen in Figure 6.5, all samples have similar behaviour before and after being exposed to radiation. For example, the PL peaks of the samples A ($T_G=300$ °C) and sample B ($T_G=310$ °C) were not detected at temperatures above 40K for both NIR and IR samples (see black squares and solid red circles in Figures 6.5(a) and (b), respectively). Nonetheless, for an incident laser excitation power of 15 mW, the well-known S-shape behaviour is observed for NIR and IR (50 kGy dose) samples C, D, E, F and G as shown in Figures 6.5(a) and 6.5(b), respectively. The origin of the S-shape profile (red-blue shift) in the PL peak energy can be explained by considering the carrier distribution amongst the localised density of states (LDOS) at different temperatures [15]. The S-shape relates to the existence of

localized states in the epitaxial layer, thus, the evolution cannot be fitted only by using Varshni's equation presented in Chapter 5. When the temperature is higher than 240 K, the PL intensity is completely quenched. These results are consistent with those obtained previously [15] for the PL of bulk $\text{GaAs}_{1-x}\text{Bi}_x$ grown on GaAs (100) substrates. Chapter 5 provides additional information on S-shaped behaviour (Section 5.3.2.2.3). It is important to point out that the PL intensity of the IR samples quenches at higher temperatures than those of the NIR samples as shown in Table 6.1. Consequently, the S-shape behaviour was more evident in the $\text{GaAs}_{1-x}\text{Bi}_x$ samples that were exposed to radiation (see Figure 6.5(b)) compared to those that were not exposed to radiation (see Figure 6.5(a)), due to an increase in the PL intensity, hence optical efficiency, after irradiation. During the interaction of gamma-ray photons with a semiconductor material, several processes can occur. Gamma-rays can be considered as a type of indirect ionizing radiation, which can transfer their energy involving a two-stage process. In the first stage, the photons lose some of their kinetic energy in collisions with secondary charged particles present in the semiconductor through which the radiation passes, and in the second stage, these secondary charged particles lose their energy either through collisions or through radiation emission (e.g., Bremsstrahlung radiation) [1]. This process can release charges (electrons, free radicals) which are trapped at defects in the crystal lattice of a semiconductor material. In this specific case, the substantial difference in atomic size between Bi and As leads to several fascinating optical and structural characteristics in $\text{GaAs}_{1-x}\text{Bi}_x$ (in this alloy Bi substitutes As). Furthermore, Bi acts as an isovalent impurity in GaAs, causing a substantial perturbation in the valence band structure [21]. On this basis, the results presented here suggest that the ionization effect on bismuth is higher when compared to Ga and As atoms in $\text{GaAs}_{1-x}\text{Bi}_x$.

$x\text{Bi}_x$ films. The process of ionization can be comprehended by analysing the relationship between the mass attenuation coefficient (μ) and the reaction cross-section σ (cm^2), i.e, $\mu = N_0\sigma/A$, where N_0 is Avogadro's number (6.02×10^{23}) and A is the atomic weight of the absorber [22]. The atomic weight of Bi, Ga and As are $A^{\text{Bi}} = 208.9804$ u, $A^{\text{As}} = 74.9216$ u and $A^{\text{Ga}} = 69.723$ u, respectively, where u is the atomic mass unit. By considering the cross-section only, it is clear that the cross section of Bi is around three times higher than that of As and Ga ($A^{\text{Bi}}/A^{\text{As}} \sim 2.8$ and $A^{\text{Bi}}/A^{\text{Ga}} \sim 3.0$). This simple analysis suggests that gamma rays interact more strongly with Bi atoms than with the other atoms in the $\text{GaAs}_{1-x}\text{Bi}_x$ alloy. Through the analysis of the Raman results, where it is observed that the density of holes increased for all irradiated samples, this suggestion seems plausible. C. Weiss and colleagues conducted a study on the influence of electron and proton irradiation on the minority carrier lifetime of p-type Ge wafers[23]. According to their investigation, the displacement of a single Ge atom from its lattice position results in the creation of a vacancy and an interstitial atom, also known as a Frenkel pair, occurs on average when exposed to MeV electrons or photons. These defects have the potential to act as recombination centers for electron-hole pairs. In this study, the displacement of Bi atoms from their lattice positions (caused by high-energy photons, which have two primary photon lines at 1.17MeV and 1.32MeV) creates vacancies and interstitial atoms and/or relocates Bi atoms to more energetically favourable positions on the lattice. This occurrence is more probable in the samples investigated in this thesis due to the higher atomic weight of Bi atoms, which is roughly three times greater than that of Ga and As atoms. It is also worth noting that ionizing radiation in semiconductors is typically associated with defects. Recently, Fregolent et al. employed deep level transient spectroscopy to study

defects in n-type GaAs_{1-x}Bi_x layers [24]. They identified six electrically active defects in their samples, two of which are hole traps and only one directly related to Bi. The defect, which could be related to the incorporation of Bi into the host lattice of GaAs and ascribed to the presence of defects near the valence band edge, showed a low hole concentration. Thus, it could be suggested that ionizing radiation can affect this defect level by increasing its concentration. Therewith, the samples' PL signal intensity increases. Finally, heating due to ionizing radiation could also be considered as another possible contribution to the increase in the PL signal of the samples [25]. Gamma radiation can cause a temperature increase which induces structural changes in the GaAs_{1-x}Bi_x alloy. In this case, gamma radiation could cause a kind of thermal annealing, inducing a process of activation of dopants, consequently, contributing to the increase of the PL signal.

Table 6.1: Quenching temperatures and PL FWHM for NIR and IR GaAs_{1-x}Bi_x epilayer samples.

Samples	Growth temperature (° C)	Quenching temperature (K) NIR samples	Quenching temperature (K) of IR samples	FWHM (meV) of NIR samples	FWHM (meV) of IR samples
C	320	200	240	111	113
D	325	170	220	108	111
E	340	190	220	103	104
F	345	200	240	115	118
G	365	190	220	125	128

Figure 6.6 depicts the PL FWHM as a function of temperature from 10 K to 240 K range and excitation power of 15mW. The values of the PL FWHM of the IR samples are higher than those of the NIR samples as shown in Table 6.1.

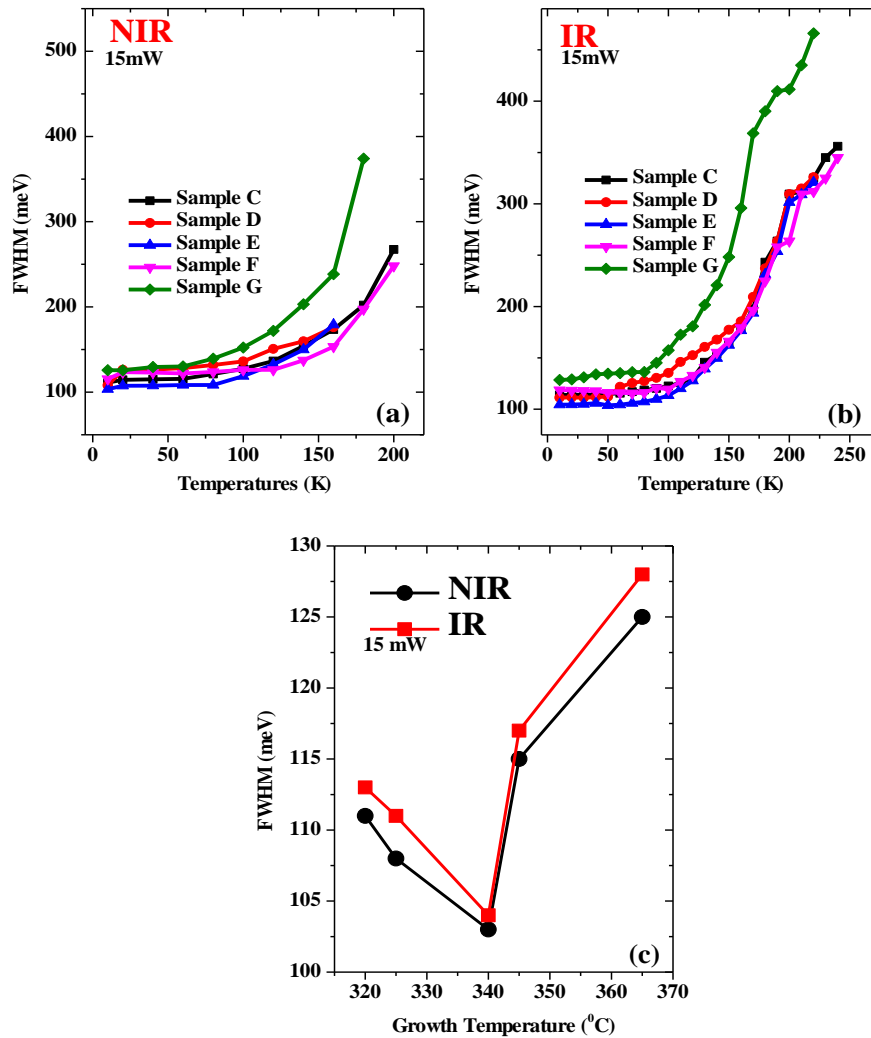


Figure 6.6: FWHM as a function of temperature for GaAs_{1-x}Bi_x epilayers samples C, D, E, F and G for (a) NIR samples; (b) IR samples with 50 kGy dose; (c) FWHM versus growth temperature for GaAs_{1-x}Bi_x epilayers before and after irradiation. All measurements were taken at an excitation power of 15 mW.

The results demonstrated that the FWHM of both NIR and IR samples behave similarly, i.e. does not change appreciably at low temperatures (10 K - 80 K).

However, at high temperatures, the FWHM increases monotonically with temperature. The GaAs_{1-x}Bi_x samples exposed to 50 kGy dose have the highest FWHM for all samples as shown in Figure 6.6(c). This finding demonstrates that IR samples have worse quality compared to NIR samples. The decrease in FWHM confirms a better uniformity of GaAs_{1-x}Bi_x thin films for the NIR samples. This result is consistent with the results of XRD measurements, which demonstrated that for IR samples, the crystallographic quality of the samples was slightly worse after irradiation. This is due to the fact that radiation induces several types of defects, including structural defects. Furthermore, the sample with Bi concentration of 4.4% ($T_G = 340\text{ }^{\circ}\text{C}$) has the lowest FWHM before and after exposure to 50 kGy dose of gamma radiation, indicating a higher Bi uniformity and better optical properties of the thin films. This finding is also in good agreement with Raman measurements that showed a positive frequency shift of the LO mode after irradiation, indicating that the irradiation caused a compressive strain.

However, the sample with Bi concentration of 2.8 % ($T_G = 365\text{ }^{\circ}\text{C}$) has the highest FWHM before and after exposure to 50 kGy dose of gamma radiation. This finding is consistent with the SEM results (discussed in Chapter 5 and illustrated in Figure 5.5 (g)) which demonstrated that the self-aligned trailing tracks are wider with black drops at their ends, indicating that bismuth was not effectively incorporated into the GaAs structure. One possible explanation for all these new optical properties is that only Bi atoms in GaAs_{1-x}Bi_x lattice become highly ionized due to the ionizing effect of gamma irradiation. The three fundamental mechanisms of electromagnetic for gamma radiation interaction such as photo-absorption, Compton scattering, and electron-positron pair production are mostly dominant

on Bi atoms or clusters formed by Bi atoms [16]. The presence of Bi clusters will be shown by analysing the temperature dependence of PL intensity with a modified Arrhenius equation [9, 17, 18], which was described in details in Chapter 5, Section (5.3.2.2.3).

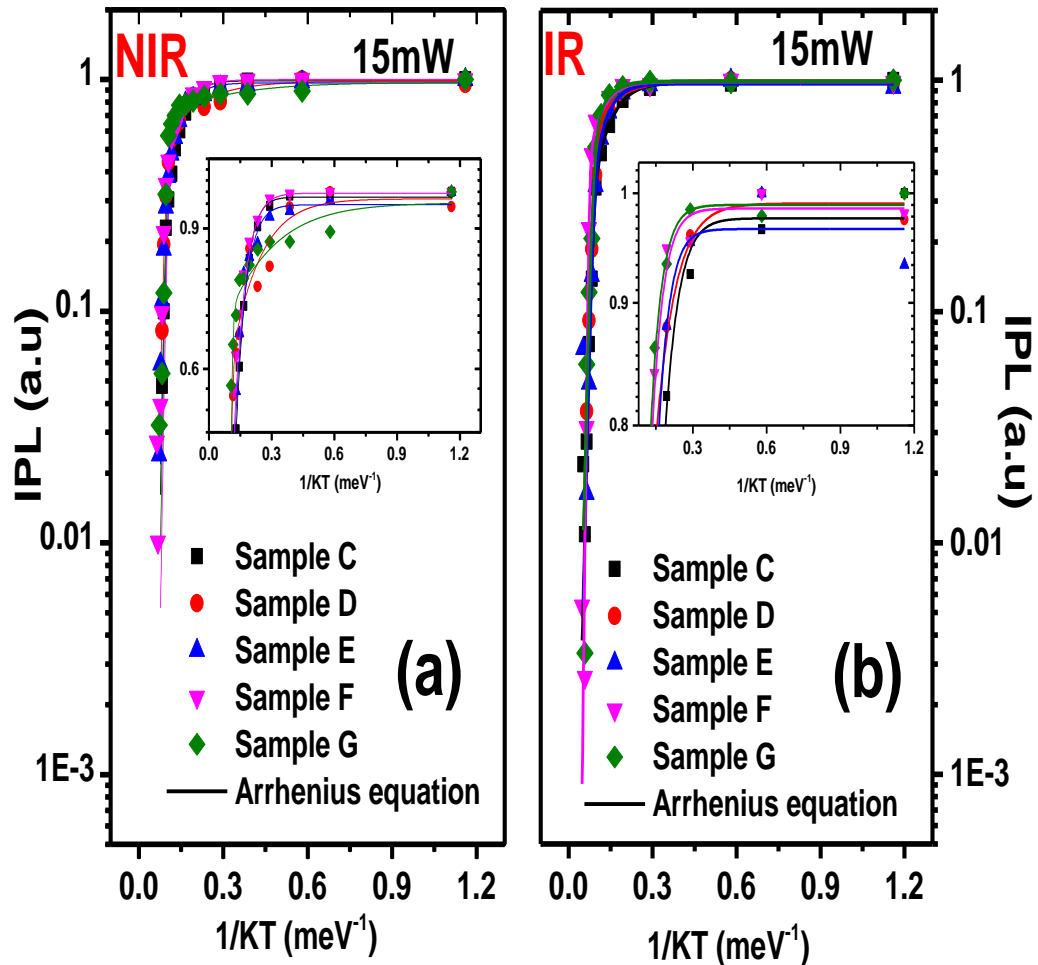


Figure 6.7: Arrhenius plots of integrated PL intensity (IPL) of GaAs_{1-x}Bi_x epilayers, grown on (100) GaAs for samples C, D, E, F and G (a) NIR samples; (b) IR samples. Solid lines illustrate the fit to the experimental data using equation 5.5 presented in Chapter 5. The inserts show zoomed areas of the plots.

Table 6.2 summarises the E_1 and E_2 values for all samples. The activation energies obtained for all samples indicate the formation of Bi clusters and alloy disorder [19]. Indeed, the lower activation energy value (E_1) has been related to Bi cluster and Bi pair formation, while the higher activation energy value (E_2) has been related to the $\text{GaAs}_{1-x}\text{Bi}_x$ alloy disorder [20]. A recent study [9] found very similar behaviour in $\text{GaAs}_{1-x}\text{Bi}_x$ samples. It can be observed that in low-temperature regions, the calculated activation energies E_1 of NIR and IR samples C, D, E, F and G are 25.8 meV, 8.2 meV, 22.1 meV, 21.5 meV and 4.9 meV, and 19.4 meV, 13.5 meV, 23.9 meV, 23.2 meV and 23.3 meV, respectively. All IR samples have larger E_1 activation energies for the low temperature regimes than the NIR samples, except for sample C ($T_G = 320^\circ\text{C}$).

In contrast, in the high temperature regimes all NIR samples have larger E_2 activation energies than the IR samples, except for sample F ($T_G = 345^\circ\text{C}$). It is important to note that the highest E_2 activation energies are found to be in sample F ($T_G = 345^\circ\text{C}$), before and after being exposed to gamma radiation at 175.8 meV and 250.7 meV, respectively. This sample with Bi concentrations of 4.3 % showed a positive frequency shift of the LO mode after irradiation, indicating that the irradiation caused a compressive strain. More interesting is that sample F showed the highest increase in the PL signal after irradiation. Finally, these findings not only indicate and contribute to a better understanding of defects in $\text{GaAs}_{1-x}\text{Bi}_x$, but also demonstrate that these materials can be used as efficient and highly sensitive ionising radiation detectors. More interestingly, the detection of ionizing radiation could be monitored by optical measurements, demonstrating the versatility of this material system [16].

Table 6.2. Arrhenius fitting parameters for NIR and IR samples.

Samples	GaAs _(1-x) Bi _x Samples grown at T _G (°C)	Activation energy (meV)			
		E _{1(NIR)}	E _{2(NIR)}	E _{1(IR)}	E _{2(IR)}
C	320	25.8	194.9	19.4	123.7
D	325	8.2	118.8	13.5	105.4
E	340	22.1	125.9	23.9	122.9
F	345	21.5	175.8	23.2	250.7
G	365	4.9	164.7	23.3	116.7

6.4 CONCLUSION

The effect of gamma radiation dose on the optical properties of GaAs_{1-x}Bi_x epilayers grown on (100) GaAs substrates by Molecular Beam Epitaxy at different growth temperatures were investigated by using XRD, hole concentration, Raman and PL techniques. The PL measurements showed that samples which were subjected to a dose of gamma rays of 50 kGy showed enhanced optical properties in comparison to other samples which had not been irradiated. This result is consistent with Raman measurements which demonstrated that the concentration of holes increased in all IR samples compared to NIR samples. The temperature dependence of the PL spectra in the range 10 K - 240 K was also studied. The temperature dependence of PL peak energy at laser excitation of 15 mW has showed a pronounced S-shape characteristic, which is also typical of the highly mismatched alloys. The S-shape behaviour was more evident in the GaAs_{1-x}Bi_x samples that were exposed to radiation compared to those that were not exposed to

radiation. In addition, it was found that the NIR GaAs_{1-x}Bi_x samples have the lowest FWHM compared to IR samples. This result is consistent with the results of the XRD measurements, which demonstrated that for IR samples, the crystallographic quality of the samples was slightly worse after being exposed to gamma radiation. This is due to the fact that radiation induces several types of defects (i.e. structural defects). Furthermore, it was observed that the signal to noise ratios of XRD spectra of the IR samples is less than those of the NIR samples. Additionally, the sample with Bi concentration of 4.4% ($T_G = 340\text{ }^{\circ}\text{C}$) has the lowest FWHM before and after exposure to 50 kGy dose of gamma radiation, indicating a higher Bi uniformity and better optical properties of the thin films. This finding is also in good agreement with Raman measurements that showed a positive frequency shift of the LO mode after irradiation, indicating that the irradiation caused a compressive strain. Nevertheless, the sample grown at the highest growth temperature ($T_G = 365\text{ }^{\circ}\text{C}$) has the highest FWHM before and after gamma radiation exposure of 50 kGy. This result is consistent with the SEM results, which showed that the self-aligned trailing tracks are wider and have black drops at their ends, indicating that bismuth was not effectively incorporated into the GaAs structure. As a result of these above findings, it can be concluded that these materials have a significant amount of potential for use in ionising radiation detectors that are capable of being monitored using optical as well as electrical measurements. This study highlights an important finding: GaAs_{1-x}Bi_x-based devices with a bismuth concentration ranging from 2.3% to 4.7% exhibit remarkable resistance to radiation doses lower than 50 kGys, with no significant impact on their structural integrity. This result has significant implications for the development of next-generation devices such as multi-junction solar cells, photonic devices, and long-wavelength

optoelectronic devices, which could be utilized in moderate irradiation environments. Additionally, the present research makes valuable contributions to the fundamental understanding that could be helpful for potential future applications of GaAs_{1-x} Bi_x alloys, specifically regarding the impact of ionizing radiation at varying levels of bismuth doping.

REFERENCES

- [1] G. Halverson, Marine isotope stratigraphy, in: Encyclopedia of Scientific Dating Methods, Springer, 2013.
- [2] G.A. Umana-Membreno, J. Dell, G. Parish, B. Nener, L. Faraone, U. Mishra, ^{60}Co gamma irradiation effects on n-GaN Schottky diodes, IEEE Transactions on Electron Devices, 50 (2003) 2326-2334.
- [3] S. Krishnan, G. Sanjeev, M. Pattabi, Electron irradiation effects on the Schottky diode characteristics of p-Si, Nuclear Instruments and Methods in Physics Research Section B: Beam Interactions with Materials and Atoms, 266 (2008) 621-624.
- [4] L. Zhang, Y. Zhang, Y. Zhang, C. Han, Neutron radiation effect on 4H-SiC MESFETs and SBDs, Journal of Semiconductors, 31 (2010) 114006.
- [5] A.T. Sharma, S. Kumar, Y.S. Katharria, D. Kanjilal, Effects of swift heavy ion irradiation on the electrical characteristics of Au/n-GaAs Schottky diodes, Applied surface science, 254 (2007) 459-463.
- [6] N. Al Saqri, J. Felix, M. Aziz, D. Jameel, C. De Araujo, H. Albalawi, F. Al Mashary, H. Alghamdi, D. Taylor, M. Henini, Investigation of the effects of gamma radiation on the electrical properties of dilute GaAs $_{1-x}$ N $_x$ layers grown by Molecular Beam Epitaxy, Current Applied Physics, 15 (2015) 1230-1237.
- [7] Ş. Karataş, A. Türüt, Ş. Altındal, Effects of ^{60}Co γ -ray irradiation on the electrical characteristics of Au/n-GaAs (MS) structures, Nuclear Instruments and Methods in Physics Research Section A: Accelerators, Spectrometers, Detectors and Associated Equipment, 555 (2005) 260-265.
- [8] S. Zhu, W. Qiu, H. Wang, T. Lin, P. Chen, X. Wang, Raman spectroscopic determination of hole concentration in undoped GaAsBi, Semiconductor Science and Technology, 34 (2018) 015008.

- [9] H. Alghamdi, V.O. Gordo, M. Schmidbauer, J.F. Felix, S. Alhassan, A. Alhassni, G.A. Prando, H. Coelho-Júnior, M. Gunes, H.V.A. Galeti, Effect of thermal annealing on the optical and structural properties of (311) B and (001) GaAsBi/GaAs single quantum wells grown by MBE, *Journal of Applied Physics*, 127 (2020) 125704.
- [10] S. Imhof, C. Wagner, A. Thränhardt, A. Chernikov, M. Koch, N.S. Köster, S. Chatterjee, S.W. Koch, O. Rubel, X. Lu, Luminescence dynamics in ga (asbi), *Applied Physics Letters*, 98 (2011) 161104.
- [11] R. Loudon, The Raman effect in crystals, *Advances in Physics*, 13 (1964) 423-482.
- [12] J. Groenen, G. Landa, R. Carles, P. Pizani, M. Gendry, Tensile and compressive strain relief in $\text{In}_x\text{Ga}_{1-x}\text{As}$ epilayers grown on InP probed by Raman scattering, *Journal of applied physics*, 82 (1997) 803-809.
- [13] P. Wickboldt, E. Anastassakis, R. Sauer, M. Cardona, Raman phonon piezospectroscopy in GaAs: Infrared measurements, *Physical Review B*, 35 (1987) 1362.
- [14] F. Sarcan, Ö. Dönmez, K. Kara, A. Erol, E. Akalın, M.Ç. Arıkan, H. Makhoulfi, A. Arnoult, C. Fontaine, Bismuth-induced effects on optical, lattice vibrational, and structural properties of bulk GaAsBi alloys, *Nanoscale Research Letters*, 9 (2014) 1-7.
- [15] T. Wilson, N.P. Hylton, Y. Harada, P. Pearce, D. Alonso-Álvarez, A. Mellor, R.D. Richards, J.P. David, N.J. Ekins-Daukes, Assessing the nature of the distribution of localised states in bulk GaAsBi, *Scientific Reports*, 8 (2018) 1-10.

- [16] S. Alhassan, Investigation of structural, electrical and optical properties of doped dilute GaAsBi grown by molecular beam epitaxy, in, University of Nottingham, 2022.
- [17] S. Olsthoorn, F. Driessen, A. Eijkelenboom, L. Giling, Photoluminescence and photoluminescence excitation spectroscopy of Al_{0.48}In_{0.52}As, Journal of applied physics, 73 (1993) 7798-7803.
- [18] H. Sun, S. Calvez, M. Dawson, J. Gupta, G. Aers, G. Sproule, Thermal quenching mechanism of photoluminescence in 1.55 μ m Ga In N As Sb/Ga (N) As quantum-well structures, Applied physics letters, 89 (2006) 101909.
- [19] M. Usman, C.A. Broderick, A. Lindsay, E.P. O'Reilly, Tight-binding analysis of the electronic structure of dilute bismide alloys of GaP and GaAs, Physical Review B, 84 (2011) 245202.
- [20] S. Sze, K.K. Ng, LEDs and Lasers, Physics of Semiconductor Devices, 3 (2006) 601-657.
- [39] Y. Liu, X. Yi, N.J. Bailey, Z. Zhou, T.B. Rockett, L.W. Lim, C.H. Tan, R.D. Richards, J.P. David, Valence band engineering of GaAsBi for low noise avalanche photodiodes, Nature communications, 12, (2021), 4784.
- [40] G. Nelson, D. Reilly, Gamma-ray interactions with matter, Passive nondestructive analysis of nuclear materials, 2, (1991), 27-42.
- [41] C. Weiss, S. Park, J. Lefèvre, B. Boizot, C. Mohr, O. Cavani, S. Picard, R. Kurstjens, T. Niewelt, S. Janz, Electron and proton irradiation effect on the minority carrier lifetime in SiC passivated p-doped Ge wafers for space photovoltaics, Solar Energy Materials and Solar Cells, 209, (2020), 110430.

- [42] M. Fregolent, M. Buffolo, C. De Santi, S. Hasegawa, J. Matsumura, H. Nishinaka, M. Yoshimoto, G. Meneghesso, E. Zanoni, M. Meneghini, Deep levels and carrier capture kinetics in n-GaAsBi alloys investigated by deep level transient spectroscopy, *Journal of Physics D: Applied Physics*, 54, (2021), 345109.
- [43] S. Aldawood, S. AlGamdi, S.A. Salman, M. AlGarawi, T.S. Alkhuraiji, S.M. Ali, Influence of γ -ray exposure and dose dependent characteristics of (n) PbS-(p) Si hetero-structure, *Journal of Materials Science: Materials in Electronics*, 32, (2021), 11616-11627.

CHAPTER 7: INVESTIGATION OF THE EFFECT OF GAMMA RADIATION ON THE OPTICAL PROPERTIES OF SELF-ASSEMBLED InGaAs QUANTUM DOTS GROWN ON (100) GaAs SUBSTRATES BY MOLECULAR BEAM EPITAXY USING BISMUTH AS A SURFACTANT

This chapter reports the effect of gamma radiation dose (γ -) on the optical properties of self-assembled $\text{In}_{0.52}\text{GaAs}_{0.48}$ quantum dots grown by Molecular Beam Epitaxy (MBE) on semi-insulating (100) GaAs substrates at various growth temperatures with and without exposure to bismuth flux using photoluminescence (PL) technique.

7.1 INTRODUCTION

Self-organized quantum dots (QDs) directly formed via the Stranski-Krastanov (S-K) growth mode have attracted much attention, both for their fundamental physical properties and their potential applications in optoelectronics [1, 2]. As a direct consequence of the SK growth mode, the optimal exploitation of these QDs is limited by the low surface density [3], strain accumulation [4], and size distribution [5]. The characteristics of QDs have been improved using a number of strategies, such as strain-reducing layers [6, 7], strain compensation [8], and post-growth intermixing [9]. There is another alternative technique to control QD size and density during growth which involves the use of a surfactant [10]. D. Guimard et al.[11] demonstrated in their studies that using Sb as surfactant causes an increase in dot density as well as a suppression of coalescence during the growth of InAs QDs grown on GaAs, allowing strong enhancement of PL intensities and emissions above 1.3 μm . As an alternative, bismuth (Bi) typically functions as a surfactant at

high growth temperatures (i.e. substrate temperatures) and can significantly enhance the surface characteristics of III-V semiconductor alloys during III-V growth processes, which result in a smoother surface and larger PL intensity. However, a low growth temperature less than (400 °C) is required to successfully incorporate Bi into GaAs host lattice [12].

High radiation doses have a significant impact on semiconductor performance. When a semiconductor is exposed to high-energy radiation, vacancies, clusters of defects, and dislocations are produced as lattice defects. These defects may result in the development of deep energy levels within the band gap that could act as capture and recombination centres for charge carriers. This could modify the material parameters and hence the properties of devices such as p-i-n detectors and solar cells [13]. These devices such as detectors, are commonly subjected to high radiation doses, therefore a material radiation tolerance is an important factor to consider when selecting detector materials. Accordingly, investigations of the optical properties of these structures that are subjected to high-energy particle irradiation which impacts on the functionality of electronics are of interest. H. Alghamdi et al. [14] reported that the effect of bismuth surfactant on the structural, morphological and optical properties of self-assembled InGaAs quantum dots grown by MBE on GaAs (001) substrates. However, to the best of our knowledge, no previous reports have shown the effect of irradiation on the properties of self-assembled InGaAs quantum dots grown on (100) GaAs substrates using Bi as a surfactant. Therefore, the aim of this work is to study the effect of gamma radiation on the optical properties of self-assembled InGaAs QDs deposited on (100) GaAs substrates by MBE at various temperatures namely, 450 °C, 482 °C and 510 °C, and exposed to a Bi flux during epitaxial growth.

The experimental results demonstrate that the gamma radiation of Bi-mediated growth provides an enhancement of the PL intensity, and no shifts of PL peak energy was observed in the samples irradiated with 30 kGy dose, which are very important properties for the selection of a detector material.

7.2 SAMPLE DETAILS

The $\text{In}_{0.52}\text{Ga}_{0.48}\text{As}$ QDs samples were grown by Prof. Igor Kazakov (Lebedev Physical Institute, Moscow, Russia). All samples investigated in this work were grown by MBE on semi-insulating (100) GaAs substrates using solid sources. Figure 7.1 (a-d) shows the layer structure of the grown samples. After desorption of the oxide layer from the substrate surface, a 160 nm undoped GaAs buffer layer was deposited at a rate of 0.19 nm/s at a growth temperature $T_G = 630$ °C. For sample A (control sample grown without Bi flux), the substrate temperature was ramped down from 630 °C to 510 °C for the formation of $\text{In}_{0.52}\text{Ga}_{0.48}\text{As}$ QDs by growing ~ 5 monolayers (MLs) of InGaAs by pulse deposition of 8xInAs (1s)/GaAs (1s). The beam equivalent pressures (BEP) of In, Ga, and As_4 were 3.6×10^{-7} Torr, 1.7×10^{-7} Torr, and 2.5×10^{-6} Torr, respectively. At the same temperature of 510 °C, a 100 nm undoped GaAs capping layer was grown. Finally, the same InGaAs QDs layer was grown on top of the GaAs cap layer for structural analysis (see Figure 7.1(a)). GaAs was impulse deposited 4 times with a 5 s duration during the substrate temperature (T_G) ramping down to 510 °C over a 400 s period in order to refresh the surface.

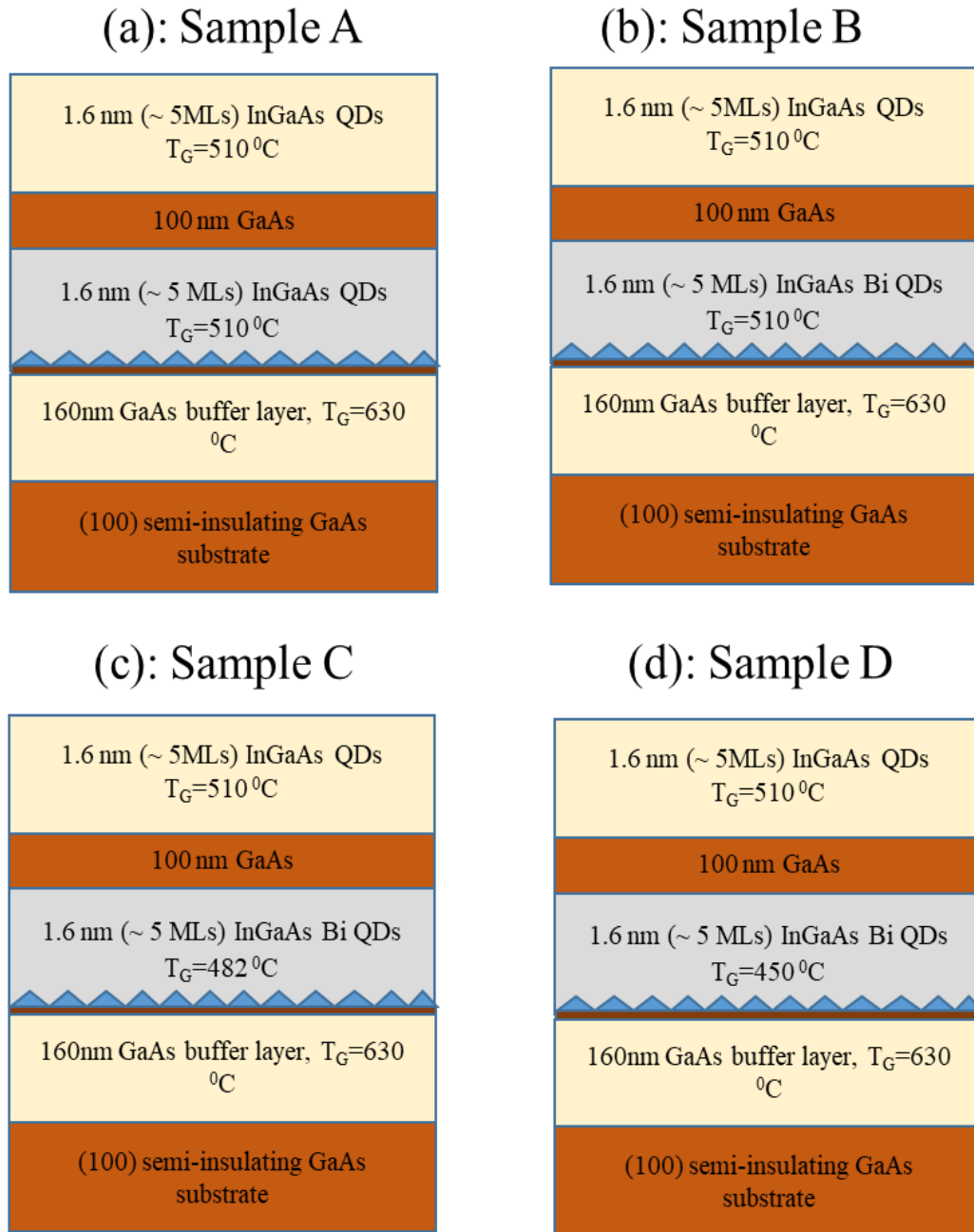


Figure 7.1: Schematic diagram of InGaAs QDs samples grown with and without Bi surfactant at different growth temperatures (T_G): (a) samples grown without Bi surfactant ($T_G=510^\circ\text{C}$); (b) samples grown with Bi surfactant at $T_G=510^\circ\text{C}$, (c) $T_G=482^\circ\text{C}$ and (d) $T_G=450^\circ\text{C}$. The Bi surfactant source was switched on only during the growth of the top and inner InGaAs QDs layers of samples B, C and D.

The growth temperature was measured with a thermocouple located at the back of the substrate holder and an infrared pyrometer Mikron M680, which was used to determine the temperature changes of the substrate at various moments during the transient processes of the growing films. The temperature reference points used in the calibration of the GaAs substrate temperature were determined by Reflection High Energy Electron Diffraction (RHEED), which is one of the most commonly used tool in MBE to calibrate surface temperatures: the amorphous As desorption temperature (250 °C) and transition of surface reconstruction from $(4 \times 4) \rightarrow (2 \times 3) \rightarrow (2 \times 4) \rightarrow (3 \times 6) \rightarrow (4 \times 2)$, observed during heating of the substrate in the absence of As flux at temperatures of 354 °C, 395 °C, 500 °C, and 549 °C, respectively [15]. To investigate the effect of Bi exposure on $\text{In}_x\text{Ga}_{1-x}\text{As}$ QDs, the QDs were deposited using an additional Bi flux with a BEP of 4.5×10^{-8} Torr for the growth of sample B ($T_G = 510$ °C), sample C ($T_G = 482$ °C) and sample D ($T_G = 450$ °C), as presented in Figure 7.1(b)–(d), respectively. The 100 nm undoped GaAs capping layer was grown at the same growth temperature with the Bi source closed (see Figure 7.1 (b–d)).

It is important to note that the Bi source was opened 30 seconds before the deposition of both $\text{In}_x\text{Ga}_{1-x}\text{As}$ layers (the buried layer and the top layer) The flux of Bi atoms to the substrate surface was measured using a control sample consisting of $\text{GaBi}_x\text{As}_{1-x}$ (50 nm)/GaAs grown at a temperature of 285 °C, when no re-evaporation of Bi from the GaAs surface occurs [16]. The Bi and Ga BEP of 4.5×10^{-8} Torr and 6×10^{-8} Torr, respectively, were chosen for the MBE growth of the investigated structures in order to increase the incorporation of Bi into the GaAs host lattice, and thus the content of Bi. The Bi composition was $x = 0.105$, as

determined by X-Ray diffraction (XRD) from the main volume of the grown $\text{In}_x\text{Ga}_{1-x}\text{As}$ layer. As a result, the flux of Bi atoms to the substrate surface during the growth of $\text{In}_x\text{Ga}_{1-x}\text{As}$ QDs was estimated to be 5.8×10^{12} atoms/cm²/s. The flux of group III atoms during QDs growth was about 1.1×10^{14} atoms/cm²/s, i.e. the flux ratio was $\text{Bi/III} \approx 0.05$. Furthermore, it is important to note that there is no Bi incorporation in the grown samples investigated in this chapter because Bi does not incorporate into the host lattice of GaAs and InAs at growth temperatures above ~ 440 °C [12, 17].

The samples were cleaved into two pieces for different irradiation doses (30 kGy and 50 kGy). For this purpose, the samples were then irradiated with a gamma cell Cobalt Irradiator (dose rate of 1.3 kGy/h) at different doses of 30 kGy and 50 kGy at ambient temperature in the presence of air. This process was carried out at the Institute of Physics at the University of Brasília, Brazil.

PL spectra of all $\text{In}_{0.52}\text{Ga}_{0.48}\text{As}$ QDs samples were investigated before (as-grown) and after irradiation as a function of temperature and excitation power. A green laser (532 nm) was used as an excitation power source ranging from 0.5 mW to 30 mW. Prior to exposing the samples to gamma irradiation, all the samples were checked for uniformity using PL measurements. The PL signal was collected in a 0.5 m Andor monochromator fitted with an InGaAs detector. The PL spectra shown in the Figures below (7.2, 7.3, 7.4a, 7.7, 7.8 and 7.9a) are presented using a linear scale divided by 1000 in the intensity axis in order to evidence different effects. Table 7.1 summarizes the samples which were investigated in this Chapter.

Table 7.1: Brief summary of the $\text{In}_{0.52}\text{Ga}_{0.48}\text{As}$ QDs samples investigated in this study.

Samples	Sample Structure $\text{In}_{0.52}\text{Ga}_{0.48}\text{As}$ QDs grown on (100) Semi-insulating GaAs substrate	Growth Temperature ($^{\circ}\text{C}$)
Sample A	with no Bi flux	510
Sample B	with Bi flux	510
Sample C	with Bi flux	482
Sample D	with Bi flux	450

7.3 RESULTS AND DISCUSSION

7.3.1 Effect of Bismuth as a Surfactant and Gamma Radiation on the Optical Properties of $\text{In}_{0.52}\text{Ga}_{0.48}(\text{Bi})\text{As}$ Quantum Dots

In this section, PL measurements were carried out on $\text{In}_{0.52}\text{Ga}_{0.48}\text{As}/\text{GaAs}$ QDs samples, namely as-grown and irradiated with different doses (30 kGy and 50 kGy), grown without Bi flux (sample A) and with Bi surfactant (sample B) at the same substrate temperature of 510°C . It is worth noting that the use of Bi as surfactant during the growth of nanostructures and gamma radiation treatment affect significantly the electrical and optical properties of semiconductor materials. The PL spectra at low temperature (10K) with a laser power excitation $P_{\text{EXC}}=15$ mW of as-grown $\text{In}_{0.52}\text{Ga}_{0.48}\text{As}$ QDs samples (before irradiation) are presented in Figure 7.2 for sample A (grown without Bi) and sample B (grown with Bi).

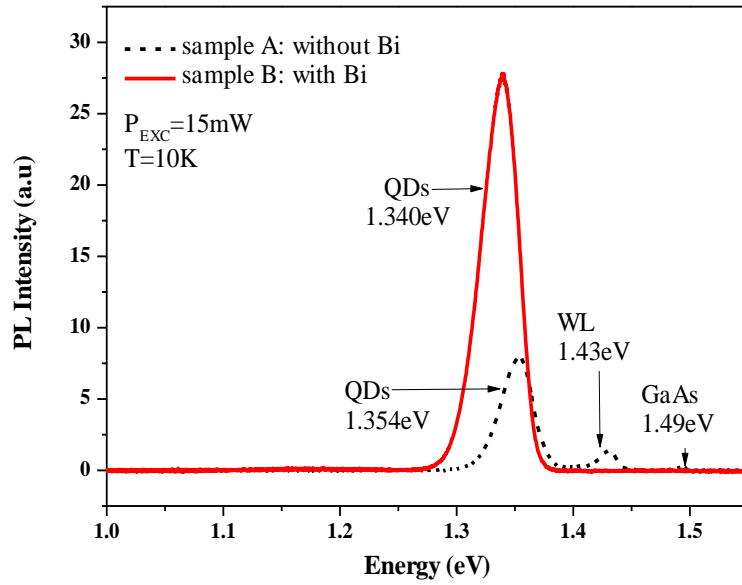


Figure 7.2: PL spectra from $\text{In}_{0.52}\text{Ga}_{0.48}\text{As}$ /GaAs QDs grown without Bi (sample A) and with Bi (sample B) at laser power $P_{\text{EXC}} = 15$ mW and 10 K.

The results show that for sample A, the main peak at 1.354 eV exhibits some asymmetry towards the low-energy side. A clear and sharper PL peak was also observed at high energy at around 1.43 eV. The high-energy peak is attributed to the electron-hole recombination in the wetting layer (WL), whereas the main and lower energy emission is related to the QD ensemble luminescence. In addition, a small peak at 1.49 eV is attributed to the GaAs capping layer/substrate. However, there is one dominant peak observed at around 1.340 eV for sample B. This peak emission is related to the QD ensemble luminescence. The effect of Bi surfactant is clearly demonstrated in Figure 7.2 by the following observations: (i) the QD PL peak red-shifted by 14 meV (from 1.354 eV to 1.340 eV) probably due to the presence of paired QDs which could reduce the quantum confinement, (ii) the PL

peak intensity increased by 3.5 times, (iii) the FWHM decreased from 35 meV to 32 meV and (iv) no signal due the WL was detected in sample B.

As shown in Figure 7.2, the PL peak position of the ground state emission of sample B, grown with Bi as surfactant red-shifted with respect to sample A that was not exposed to Bi flux. Similar results were reported for Bi-mediated growth of InAs QDs [18], which were explained by the fact that QDs are expected to have a lower confinement width due to their dissolution during the capping process [19, 20]. Nevertheless, the presence of Bi atoms can effect this process by suppression of QD dissolution and then increase the size of resulting QDs, which is a similar influence that was obtained when using Sb atoms as surfactant [11, 21].

Moreover, the increase of the PL intensity of sample B shows that the density of defects which act as nonradiative recombination centres was reduced by supplying Bi at a growth temperature of 510 °C, while the reduction of the FWHM confirms a more uniform QD size distribution for this sample. Consequently, the use of Bi as a surfactant can have a profound impact on the optical properties of $\text{In}_{0.52}\text{Ga}_{0.48}\text{As}$ QDs. This result is consistent with previous studies [22, 23] where Bi was confirmed to be an excellent surfactant in InAs QDs growth. More detailed information of as-grown $\text{In}_{0.52}\text{Ga}_{0.48}\text{As}$ QDs using Bi surfactant is reported in Ref [14]. The effect of gamma radiation at different doses (30 kGy and 50 kGy) on the optical properties of $\text{In}_{0.52}\text{Ga}_{0.48}\text{As}$ QDs is clearly evidenced in Figure 7.3 for both samples A and B.

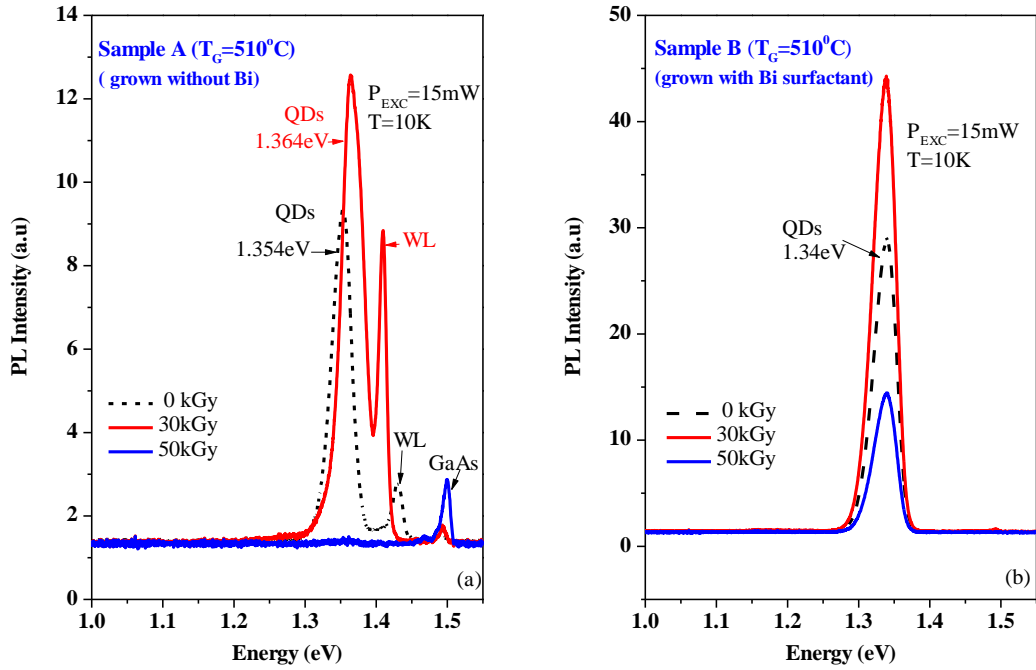


Figure 7.3: 10K PL spectra of as-grown and irradiated $\text{In}_{0.52}\text{Ga}_{0.48}\text{As}/\text{GaAs}$ QDs at different doses (30 kGy and 50 kGy) for (a) grown without being exposed to Bi (sample A); (b) grown with Bi flux (sample B). A green laser (532nm) with $P_{\text{EXC}}=15\text{mW}$ was used.

The results show that for irradiation dose of 30 kGy, the QDs PL emission energy exhibit a blue shift by around 10 meV (from 1.354 eV to 1.364 eV) for sample A (see Figure 7.3 (a)), however, no blue shift is detected in the PL of sample B (see Figure 7.3(b)). In addition, there are significant enhancements of the PL intensities of about 1.3 times and 1.5 times for sample A and sample B, respectively. Interestingly, the PL QDs and WL emissions disappeared after the irradiation dose increased to 50 kGy for sample A. In contrast, for sample B the PL QDs emission is still observed, however, its intensity is reduced by half. In general, gamma radiation treatment has better effect on the QDs sample grown with Bi than the sample grown without a Bi flux. It is worth noting that appropriate irradiation dose

is more efficient to improve the optical quality of alloys without affecting the PL peak energy. In this case, the optimum irradiation dose seems to be 30 kGy, in terms of improvement of the PL intensity. Figure 7.4 shows the PL QDs intensity versus gamma irradiation doses for both samples A and B.

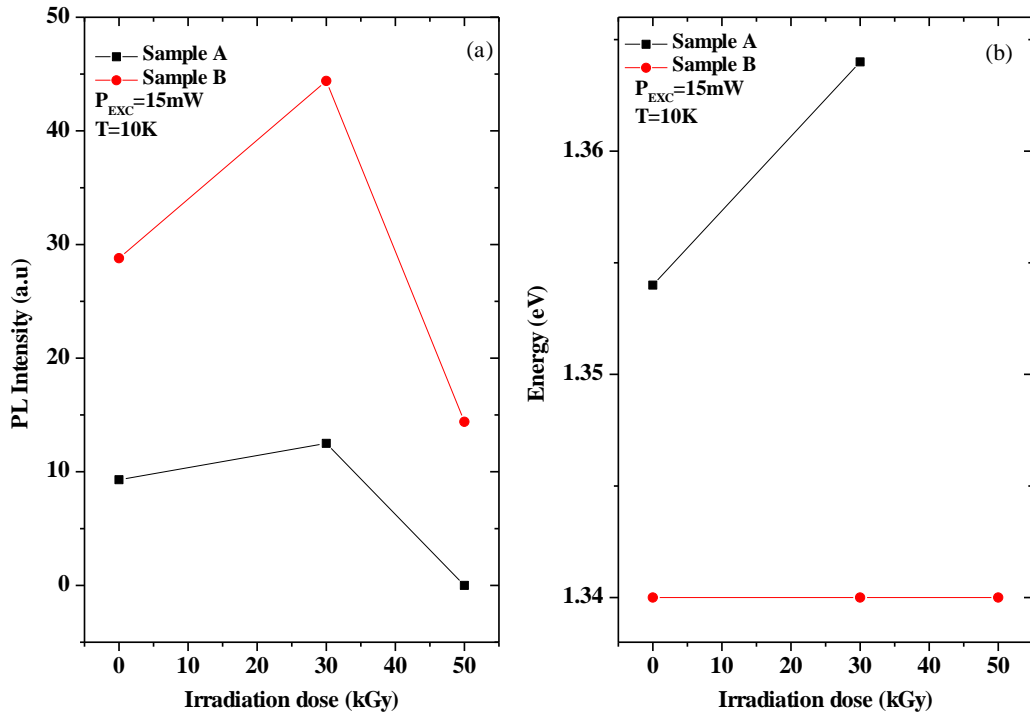


Figure 7.4: Effect of irradiation doses on (a) the QDs PL intensity and (b) PL peak energy of In_{0.52}Ga_{0.48}As QDs. The measurements were taken at 10K with a laser excitation power of 15 mW. A green laser (532nm) was used.

The effect of gamma radiation on the PL QDs intensity is clearly seen in Figure 7.4 (a) by noting the following observations: (i) the optimum irradiation dose is obtained at 30kGy for both samples A and B, (ii) for sample B, the PL QDs intensity is much higher compared to sample A at all irradiated doses. This could be explained by an enhancement of carriers confinement in sample B due to the presence of Bi surfactant. Figure 7.4 (b) shows that there is no blue shift in the PL

QDs emission energy for sample B for all irradiation doses. In contrast, there is a blue shift by 10 meV and the quenching of the PL QDs signal at 30 kGy and 50 kGy, respectively, for sample A.

Table 7.2: Summary of photoluminescence emission parameters of as-grown and irradiated $\text{In}_{0.52}\text{Ga}_{0.48}\text{As}$ QDs grown with and without Bi. The samples were irradiated at different doses.

Samples	Irradiation dose (kGy)	Energy (eV)	Blue shift (meV)	Intensity/1000 (a.u)	Ratio of PL Intensities (Irradiated/Ias-grown)
A (grown without Bi)	0	1.354	-	9.3	1
	30	1.364	10	12.5	1.3
	50	0	0	0	0
B (grown with Bi)	0	1.340	-	28.8	1
	30	1.340	0	44.1	1.5
	50	1.340	0	14.4	0.5

Figure 7.5 shows the PL peak energy as a function of temperature and fitting curves, plotted as solid lines using the Varshni equation, of samples A and B, both as-grown and irradiated in order to understand the effect of the irradiation on their optical properties. Both samples show a red-shift of the PL peak energy with increasing temperatures. The red shift of sample B as compared to sample A can be explained by the higher density of QDs when Bi is used as a surfactant. This

shift agrees well with the calculation using Varshni equation [24, 25] in the whole temperature range, meaning that the PL peak shift is mainly caused by the variation of the InGaAs bandgap.

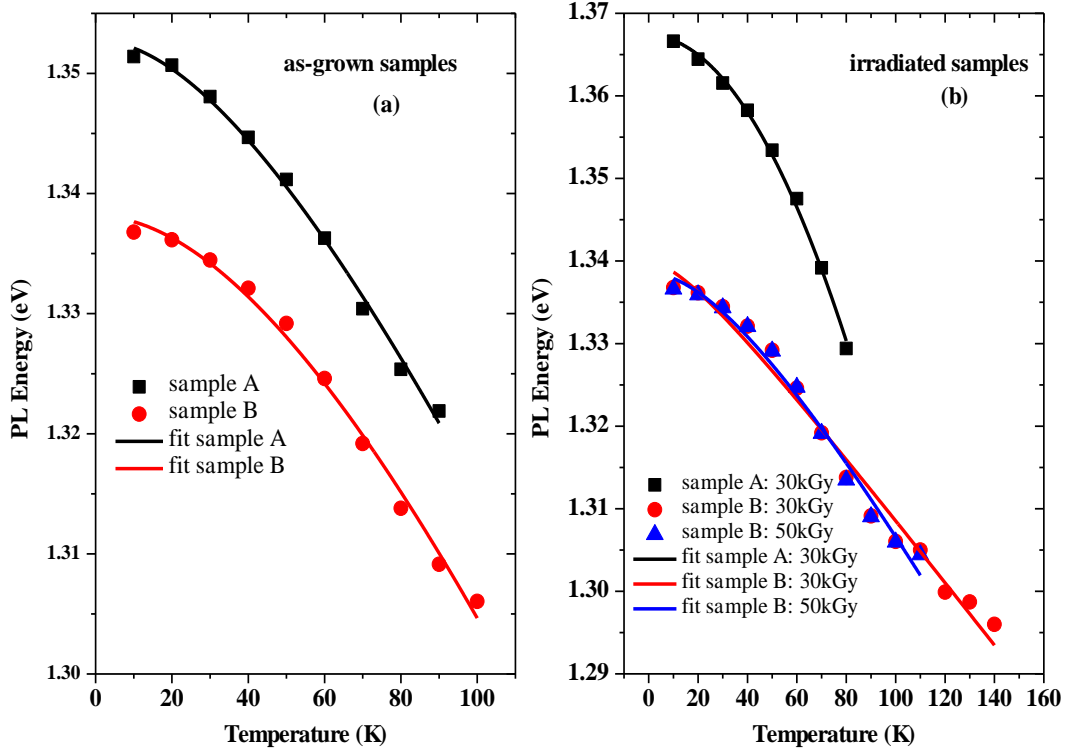


Figure 7.5: Temperature dependent PL peak energy of In_{0.52}Ga_{0.48}As QDs grown without (sample A) and with Bi (sample B) (a) as-grown samples; (b) irradiated samples with 30 kGy and 50 kGy doses. For sample A: no QDs PL energy emission was detected at 50 kGy. All measurements were taken at an excitation laser power of 15 mW.

The red-shift of the PL peak with increasing temperature in QDs systems had previously been observed, and mainly had been attributed to the redistribution of carriers amongst QDs with different sizes [26, 27]. The scattered data in Figure 7.5 are the experimental results and the solid lines are Varshni fitting given by equation 7.1.

$$E_g(T) = E_g(0) - \frac{\alpha T^2}{T + \beta} \quad 7.1$$

where α (eV/K) is related to the electron-phonon interaction, β is the Debye temperature, $E_g(0)$ is the bandgap energy at 0 K, and T is the measured temperature. In this section, the PL spectra of as-grown and irradiated (30 kGy and 50 kGy) QDs samples A and B are recorded at different temperatures in order to gain insight on the change of the QD confinement during the irradiation process that can be influenced by using Bi surfactant. For sample A, when the dose is increased to 50 kGy, no PL signal due to QDs was detected, whereas, for an irradiation dose of 30 kGy a blue shift was observed. In contrast, the QDs PL peak energy for sample B remained constant (1.340 eV) for both doses of 30 kGy and 50 kGy.

As can be seen in Figure 7.5, the effect of radiation on the PL quenching is different for samples A and B. For sample A, the PL signal extends to 90 K (see Figure 7.5(a)), however, after 30 kGy and 50 kGy irradiation doses, the QDs PL signal quenches rapidly at 70 K and no QDs signal was observed, respectively. This quenching of PL in case of irradiated samples could be due to the intermixing effect between the dots and the barrier which results in shallower confining potential and hence faster quenching with increasing temperature. However, the effect of Bi in the irradiated samples is clearly seen in Figure 7.5(b). The PL intensity of Bi-mediated as-grown QDs quenches at 100 K, and show worse thermal stability than samples irradiated with 30 kGy and 50 kGy doses, whose PL quench at 140 K and 110 K, respectively. The detection of the PL at the high temperature of 140 K evidences better carrier confinement when the samples are irradiated with 30 kGy dose. It is important to point out that this is in contrast to sample A (grown without

Bi flux) where the PL signal quenches at lower temperatures when the sample is irradiated with 30 kGy as compared to the non-irradiated sample.

To understand the mechanism of carrier thermal quenching and to have a deeper understanding of the effect of Bi surfactant on the optical properties of as-grown $\text{In}_{0.52}\text{Ga}_{0.48}\text{As}$ QDs and irradiated $\text{In}_{0.52}\text{Ga}_{0.48}\text{As}$ QDs with 30 kGy dose (optimum dose), the integrated PL intensities with an excitation power of 15 mW were plotted in Figure 7.6 as a function of reciprocal temperature.

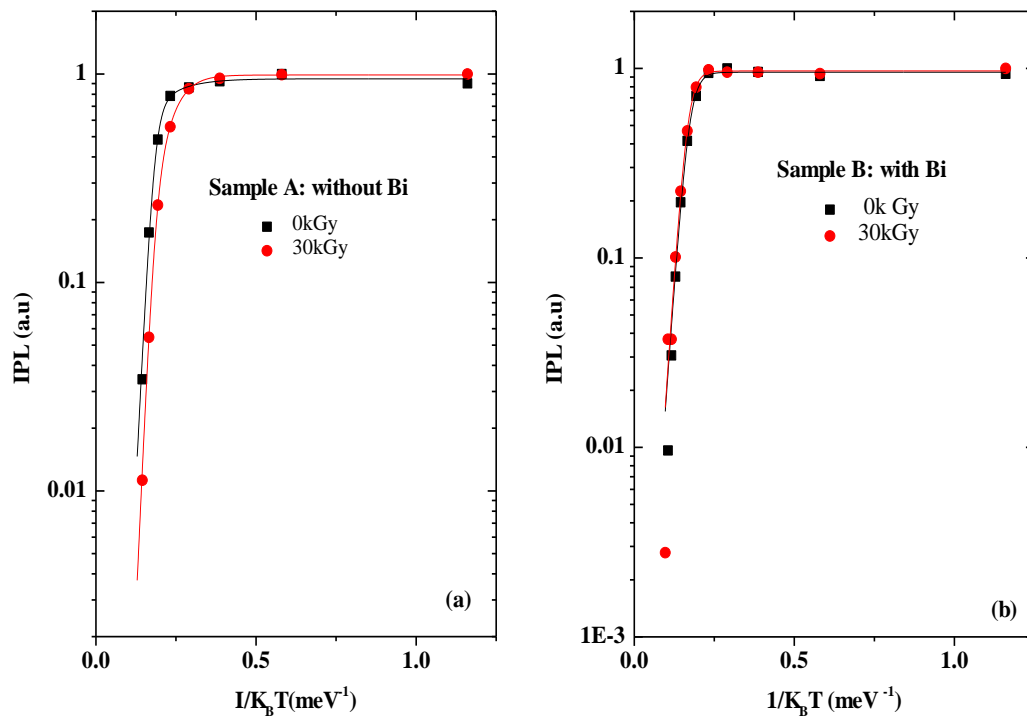


Figure 7.6: Integrated PL intensities as a function of reciprocal temperature for as-grown and 30 kGy irradiated $\text{In}_{0.52}\text{Ga}_{0.48}\text{As}$ QDs grown without (sample A) and with Bi as a surfactant (sample B). The solid lines are the least squares fit of the data.

The experimental data was fitted with a relation involving two nonradiative recombination processes [24].

$$I(T) = I_0/[1 + C_1 \exp(-E_1/(k_B T)) + C_2 \exp(-E_2/(k_B T))] \quad 7.2$$

where C_1 and C_2 represent the strengths of both quenching processes. $I(T)$ and I_0 are the PL integrated intensity at temperature T and 0 K, respectively. k_B is Boltzmann' constant. E_1 and E_2 are the thermal activation energies. As shown in Figure 7.6, experimental data are well fitted, and the fitting parameters calculated from the Arrhenius plots are presented in Table 7.3.

Table 7.3: Fitting parameters for the measured temperature dependent integrated PL intensities of as-grown and 30 kGy irradiated $\text{In}_{0.52}\text{Ga}_{0.48}\text{As}$ QDs of sample A (grown without Bi) and sample B (with Bi surfactant).

Sample	Growth Temperature (°C)	Irradiation dose (kGy)	E1 (meV)	E2 (meV)
Sample A	510	0	71.73	12.88
		30	79.79	23.81
Sample B	510	0	55.05	55
		30	58.29	58.29

It has been suggested that for high-quality $\text{In}_{0.52}\text{Ga}_{0.48}\text{As}$ QDs, the InGaAs WL might serve as a barrier for the carriers' thermal emission [28]. In low-quality material, though, defects will provide further nonradiative channels to reduce the PL and as a result, the thermal activation energy is decreased [28]. In general, E_1 corresponds to the binding energy of carriers [29]. It can be observed that in low-temperature regions, calculated activation energies E_1 of as-grown samples A and B are 71.73 meV and 55.05 meV, respectively, and activation energies E_1 of irradiated samples A and B at 30 kGy dose are 79.79 meV and 58.29 meV,

respectively. Activation energy E_2 of all samples, determined by curve fitting, could be attributed to trapped excitons or carriers thermalizing from localized regions resulting from potential fluctuation in the QDs or thermal excitation of excitons from localized QDs states followed by capture of exciton by defects present in the samples [24]. Overall, the values of activation energies E_1 and E_2 of irradiated $\text{In}_{0.52}\text{Ga}_{0.48}\text{As}$ QDs are highest than those of non-irradiated samples.

7.3.2 Effect of Growth Temperatures and Gamma Radiation on the Optical Properties of $\text{In}_{0.52}\text{Ga}_{0.48}(\text{Bi})\text{As}$ Quantum Dots

Three $\text{In}_{0.52}\text{Ga}_{0.48}(\text{Bi})\text{As}$ QDs samples were grown at different temperatures, namely 510 °C, 482 °C and 450 °C labelled as B, C and D, respectively, using Bi as surfactant. The layer structure and growth conditions (i.e. Bi, Ga and As fluxes) were the same. These samples were irradiated with 30 kGy and 50 kGy doses. The details of the three investigated $\text{In}_{0.52}\text{Ga}_{0.48}(\text{Bi})\text{As}$ QDs samples in this section are summarized in Table 7.4.

Table 7.4: InGaBiAs/GaAs QDs samples grown at various temperatures and irradiated at different doses.

Sample	Irradiation Dose (kGy)	Growth Temperature (° C)
Sample B	30	510
	50	
Sample C	30	482
	50	
Sample D	30	450
	50	

Figure 7.7(a-c) shows a comparison of PL spectra at 10K between $\text{In}_{0.52}\text{Ga}_{0.48}(\text{Bi})\text{As}$ QDs grown at different growth temperatures, namely $T_G=510^\circ\text{C}$, 482°C and 450°C , before and after radiation treatment.

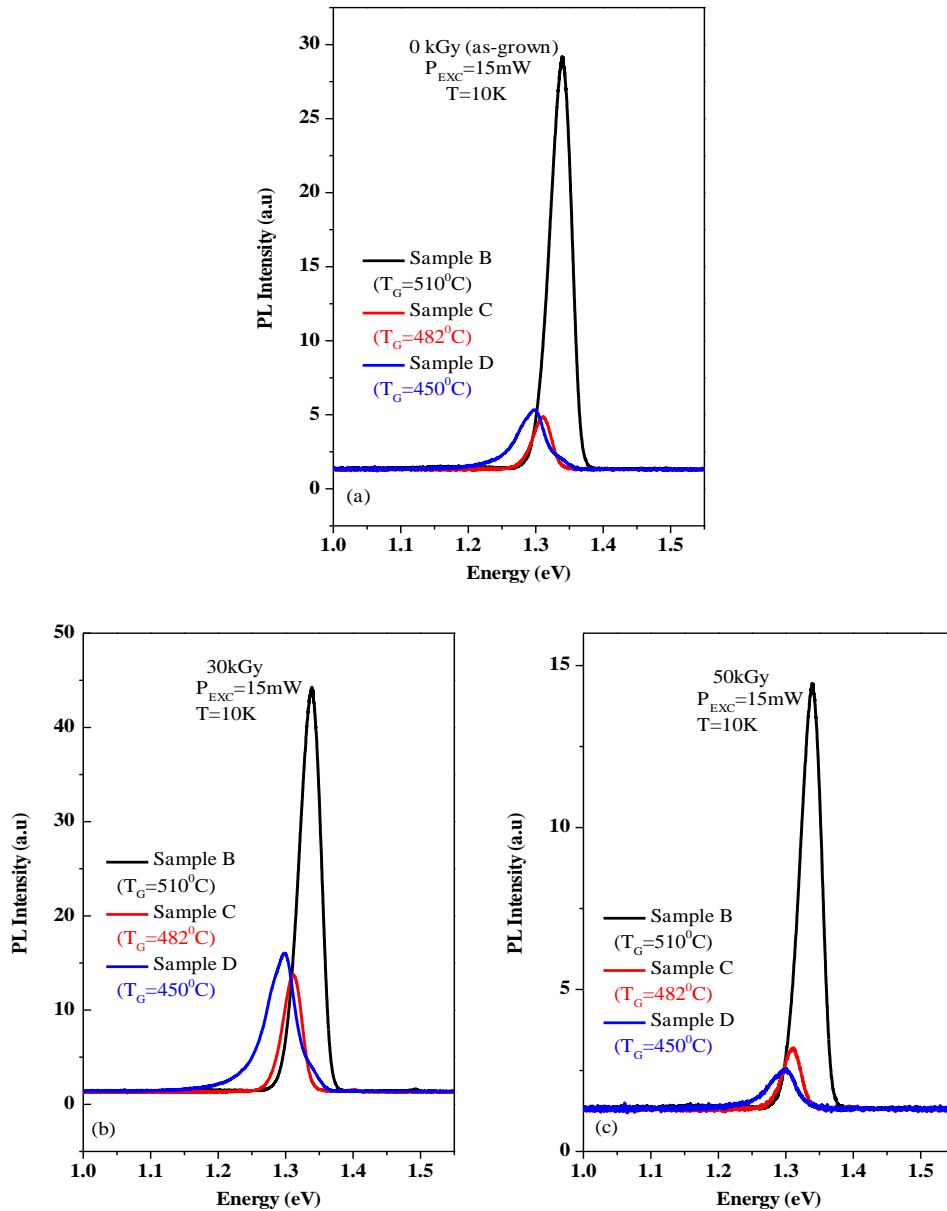


Figure 7.7: PL spectra at 10K and $P_{\text{EXC}} = 15 \text{ mW}$ of $\text{In}_{0.52}\text{Ga}_{0.48}(\text{Bi})\text{As} / \text{GaAs}$ QDs samples: (a) as-grown and irradiated with (b) 30kGy and (c) 50kGy. The $\text{In}_{0.52}\text{Ga}_{0.48}(\text{Bi})\text{As} / \text{GaAs}$ QDs samples were grown at different growth temperatures T_G : sample B ($T_G=510^\circ\text{C}$), sample C ($T_G=482^\circ\text{C}$) and sample D ($T_G=450^\circ\text{C}$).

The effect of Bi surfactant in as-grown (0 kGy) and irradiated samples is clearly demonstrated in Figure 7.7(a-c). All as-grown and irradiated samples show a similar behaviour, i.e. when the growth temperature decreased from 510 °C to 450 °C, the QDs PL peak energy shifted to lower energies. This redshift energy has been observed in InAs/GaAs QDs [14, 19] and was explained by an increase of In atoms surface migration with increasing growth temperatures. Similar results were reported in the literature for InAs/GaAs QDs [14, 30] grown at 475 °C, 485 °C, 492 °C and 500 °C using Bi-mediated growth which was explained by the fact that the QD dimensions became more uniform and homogenous at higher growth temperatures with Bi atoms suppressing the formation of larger dislocated islands. The dot areal density usually decreases at lower growth temperatures and is higher at high temperatures, which reveals essentially the suppression effect of Bi on the surface migration and desorption of In adatoms [14, 30]. The PL intensity of Bi mediated as-grown and irradiated QDs samples grown at the highest temperature is higher than the PL intensity of QDs grown at the lowest temperature, as shown in Figure 7.7 (a-c). The higher PL intensity observed for sample B (grown at 510 °C) could be due to lower density of defects such as point defects (e.g., antisites, interstitials, or vacancies) or dislocated islands formed at the higher growth temperature than the lower growth temperature [14]. These defects could be due to some distortion caused by Bi atoms which might exceed the critical strain to generate these defects [23]. Conversely, a non-monotonic decrease of the PL intensity as the growth temperature decreases is observed in the spectra of as-grown and irradiated samples. In particular, sample C (grown at 482 °C) exhibits the lowest PL intensity as compared to samples grown at 510 °C (sample B) and 450 °C (sample D) except that with an irradiated dose of 50 kGy, the PL intensity is

slightly higher than those deposited at $T_G=482\text{ }^{\circ}\text{C}$ (sample D). Figure 7.8 shows 10K PL spectra of as-grown and irradiated Bi-mediated $\text{In}_{0.52}\text{Ga}_{0.48}(\text{Bi})\text{As}$ QDs deposited at different growth temperatures. The effects of gamma radiation with different doses are clearly seen in Figure 7.8 (a), (b) and (c) for samples B, C and D, respectively.

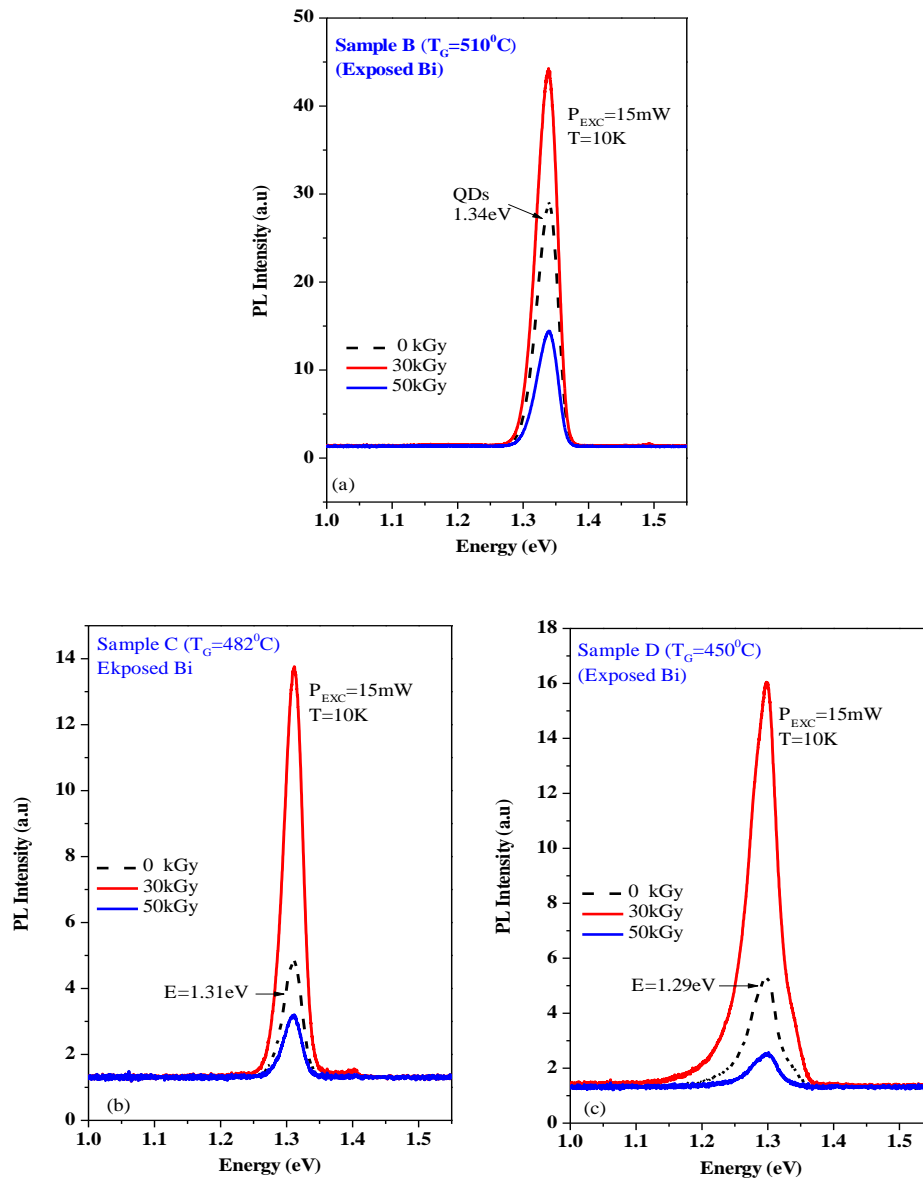


Figure 7.8: 10K PL spectra of as-grown (0 kGy) and irradiated (30 kGy and 50 kGy) $\text{In}_{0.52}\text{Ga}_{0.48}(\text{Bi})\text{As}/\text{GaAs}$ QDs samples (a); sample B ($T_G=510\text{ }^{\circ}\text{C}$); (b) sample C ($T_G=482\text{ }^{\circ}\text{C}$); (c) sample D ($T_G=450\text{ }^{\circ}\text{C}$). A green laser (532nm) with $P_{\text{exc}}=15\text{mW}$ was used.

For an irradiation dose of 30 kGy, it can be noted that (i) no shift was observed in the QDs PL peak energies of sample B (1.34 eV), C (1.31 eV) and D (1.29 eV), (ii) there is a large enhancement in the QDs PL intensities by a factor of 1.5, 2.8 and 3 for sample B, C and D, respectively. However, when samples were irradiated at higher doses of 50 kGy, all samples exhibit a reduction in the QDs PL intensities of about 0.5 times, 1.5 times and 2.1 times for sample B, C and D, respectively. Furthermore, sample B (grown at 510 °C) has higher PL intensities for a gamma radiation treatment with 30 kGy and 50 kGy doses as compared to samples C ($T_G = 482$ °C) and D ($T_G = 450$ °C). Interestingly, the particular radiation dose of 30 kGy resulted in an improvement of the optical properties of all $\text{In}_{0.52}\text{Ga}_{0.48}(\text{Bi})\text{As}$ samples grown with Bi as a surfactant, as evidenced by a large increase in the QDs PL intensity after radiation.

Table 7.5: Summary of photoluminescence emission parameters of as-grown and irradiated $\text{In}_{0.52}\text{Ga}_{0.48}(\text{Bi})\text{As}$ QDs grown with Bi surfactant. The samples were irradiated at different doses.

Samples	Irradiation Dose (kGy)	Energy (eV)	Blue shift (meV)	Intensity/1000 (a.u)	Ratio of PL Intensities (I_{ir}/I_{Nir})
Sample B	0	1.340	-	28.8	1
	30	1.340	0	44.1	1.5
	50	1.340	0	14.4	0.5
Sample C	0	1.310	-	4.8	1
	30	1.310	0	13.7	2.8
	50	1.310	0	3.1	0.6
Sample D	0	1.299	-	5.2	1
	30	1.299	0	15.9	3
	50	1.299	0	2.5	0.4

Figure 7.9 (a) shows the PL QDs intensity versus the growth temperature for different radiation doses. The results indicate that the samples irradiated with a 30 kGy dose have higher PL intensities for all growth temperatures compared to as-grown samples and irradiated samples at 50 kGy dose. However, a decrease of the PL intensity for all growth temperatures is observed at 50 kGy dose. The QDs PL peak energy as a function of irradiation doses is shown in Figure 7.9 (b). It is important to point out that the QDs PL peak emission energy remained constant (no blue shift) for all doses of gamma radiation treatment for sample B (1.34 eV), sample C (1.31 eV) and sample D (1.29 eV).

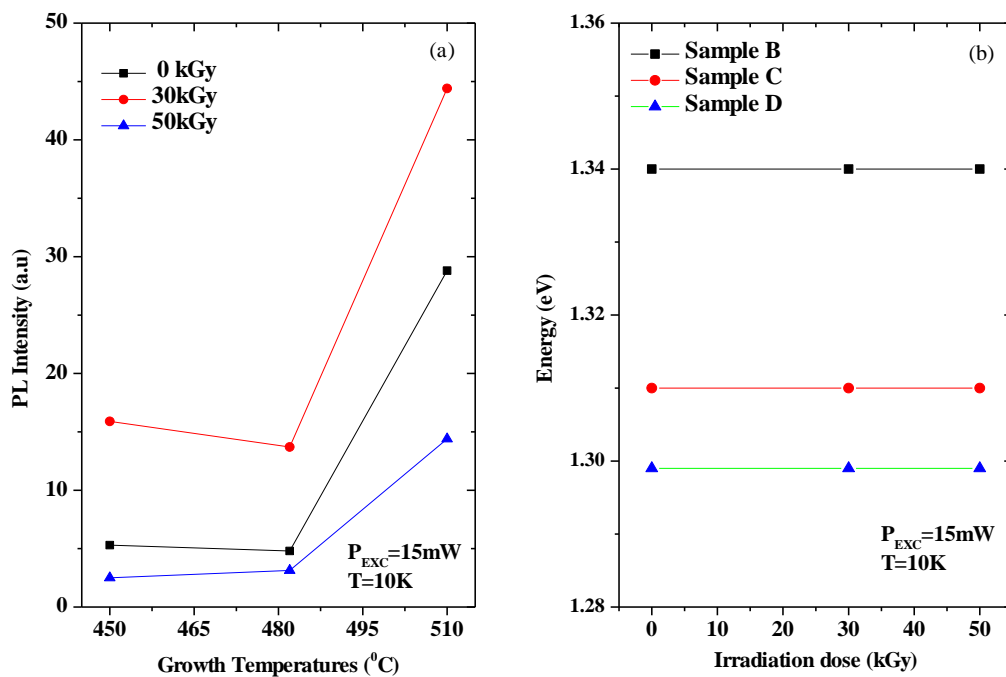


Figure 7.9: (a) the effect of the growth temperature on the PL intensity at different irradiation doses; (b) QDs PL peak energy as a function of irradiation dose for samples grown at different growth temperatures. The measurements were taken at 10K with a laser excitation power of 15mW.

The temperature dependence of the PL peak energy of $\text{In}_{0.52}\text{Ga}_{0.48}(\text{Bi})\text{As}$ QDs deposited at different growth temperatures was studied as shown in Figure 7.10 (a), (b) and (c) for irradiation doses of 0 kGy, 30 kGy and 50 kGy, respectively, in order to investigate the effect of gamma radiation on their optical properties.

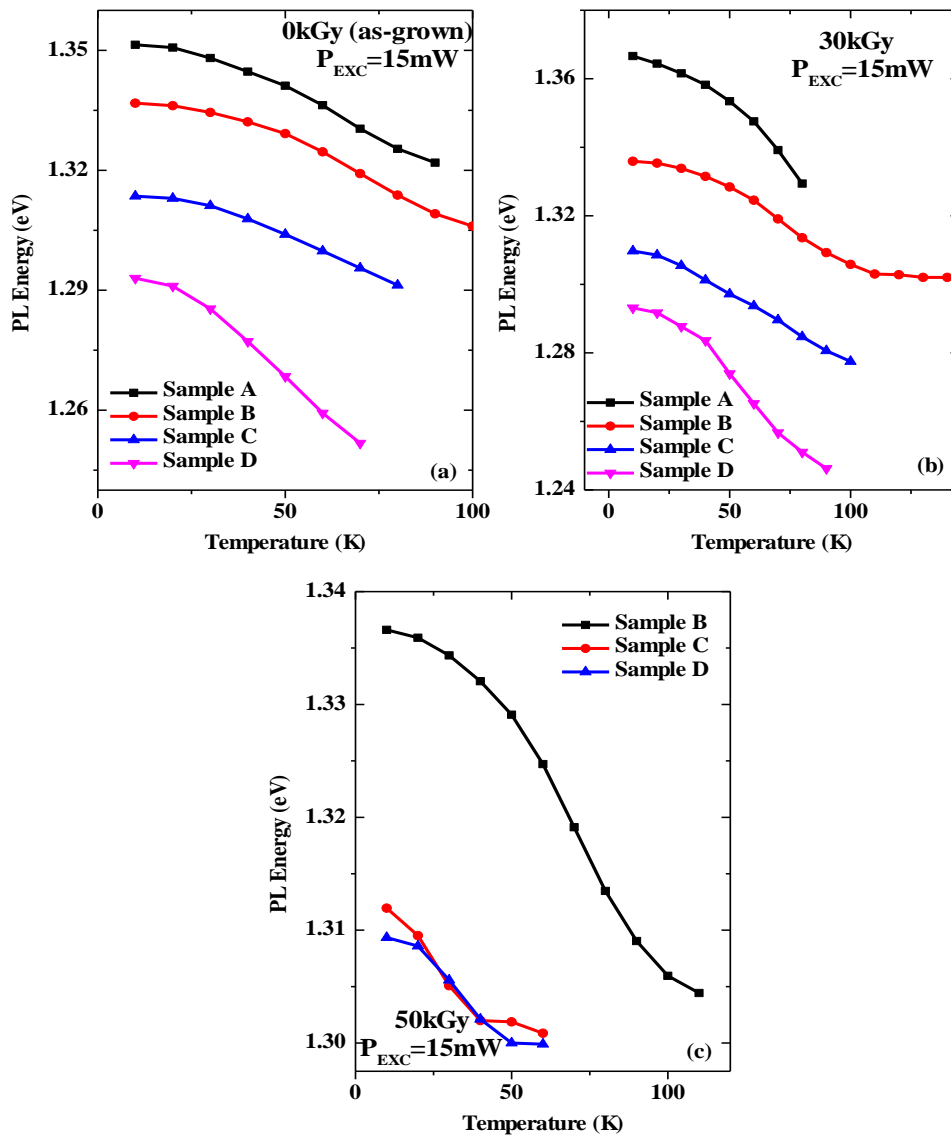


Figure 7.10: Temperature dependent PL peak energy of Bi-mediated $\text{In}_{0.52}\text{Ga}_{0.48}(\text{Bi})\text{As}$ QDs grown at different temperatures T_G : (a) as-grown samples; (b) irradiated samples with 30 kGy dose; (c) irradiated samples with 50 kGy dose. Sample B ($T_G=510^\circ\text{C}$), sample C ($T_G=482^\circ\text{C}$) and sample D ($T_G=450^\circ\text{C}$). Sample A (control sample grown without Bi) grown at $T_G=510^\circ\text{C}$ is also shown for comparison purposes. The laser excitation power $P_{\text{EXC}} = 15 \text{ mW}$.

As can be seen in Figure 7.10, the effect of gamma radiation on the PL quenching is different for the samples grown at different growth temperatures. Only for QDs irradiated with 30 kGy dose, the PL signal persists up to 140 K, 100 K and 90 K for samples B, C and D, respectively. However, at higher doses of 50 kGy, the QDs PL signal quenches rapidly at 120 K, 70 K and 70 K for samples B, C and D, respectively.

As discussed in the previous section, this quenching of PL in the case of gamma irradiated samples could be due to the intermixing effect between the dots and the barrier which results in shallower confining potential and hence faster quenching with increasing temperature. It can be observed that the high PL intensity achieved was for an irradiation dose of 30 kGy, which could be due to fewer defects created at the higher growth temperature than the lower growth temperature. In addition, the QDs grown at different growth temperatures with Bi surfactant show no change in PL peak energy for all radiation doses with respect to those grown without Bi (sample A). It is most probable that this effect could be caused by Bi surfactant. In general, these results indicate that an increase in the growth temperature of QDs results in a significant optical improvement and, therefore, the optimum temperature for Bi-assisted growth in the scope of the QDs' optical properties is 510 °C for either as- grown or irradiated samples.

Figure 7.11 presents the QDs integrated PL intensity of as-grown and irradiated samples with 30 kGy (optimum condition) as a function of inverse temperature for samples grown with Bi surfactant at different growth temperatures of 510 °C (sample B), 482 °C (sample C) and 450 °C (sample D). The experimental data are fitted by using the Arrhenius equation 7.2 (as discussed in previous section.7.3.1). The values of E_1 and E_2 for all samples are summarized in Table 7.6. In general, E_1

corresponds to the binding energy of carriers, whilst E_2 is the energy that is required by carriers to escape out of the quantum confined energy state [29].

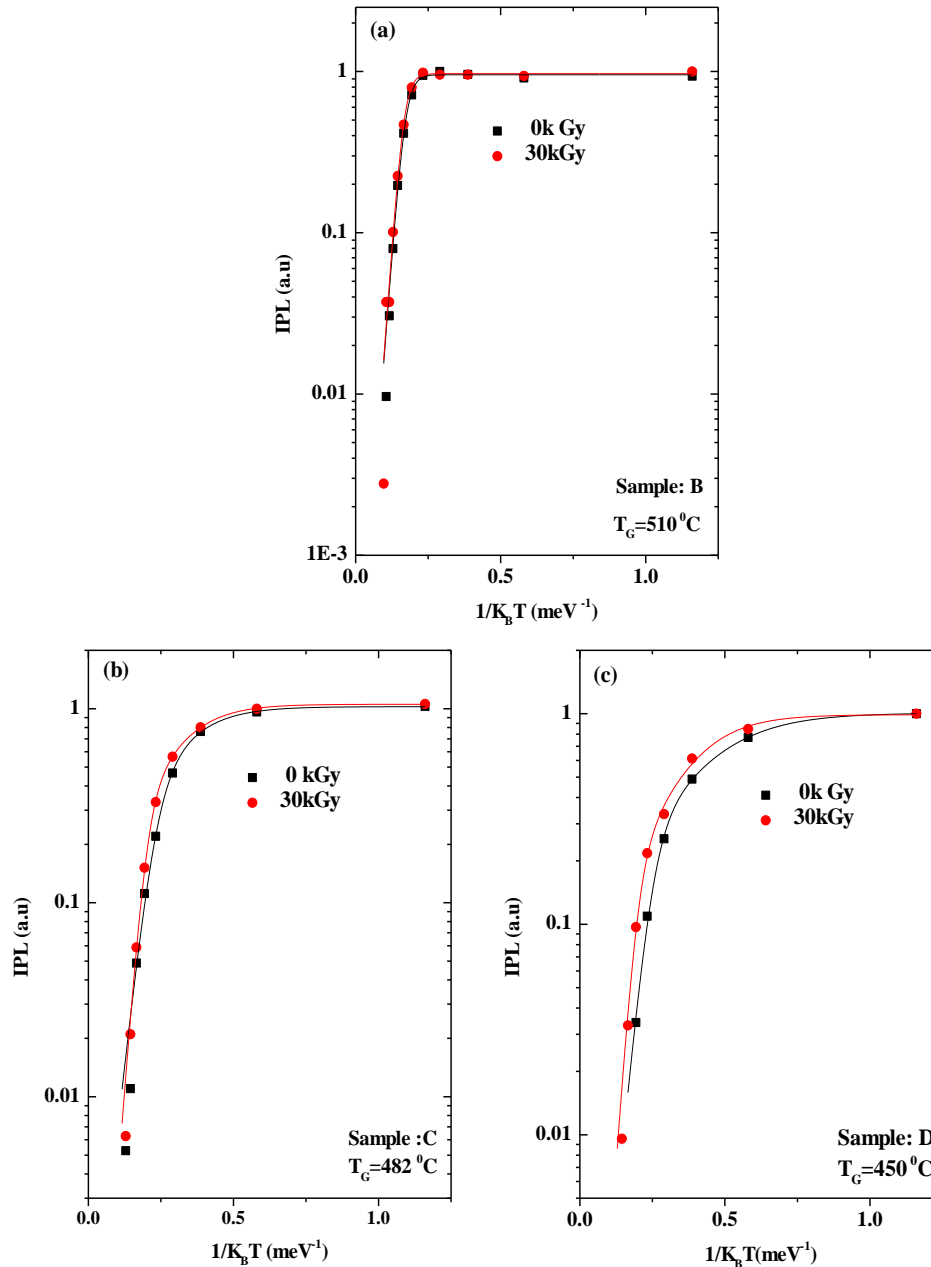


Figure 7.11: Integrated PL intensities for as-grown and 30 kGy dose irradiated (optimum condition) $\text{In}_{0.52}\text{Ga}_{0.48}(\text{Bi})\text{As}$ QDs as a function of reciprocal temperature for (a) sample B ($T_G = 510^\circ\text{C}$); (b) sample C ($T_G = 482^\circ\text{C}$); (c) sample D ($T_G = 450^\circ\text{C}$). The solid lines are the least squares fit of the data. All measurements were taken at a laser excitation power of 15 mW.

All irradiated samples have larger activation energies for both the low and high temperatures regimes than the as-grown samples, indicating that the barrier for carriers escape from QDs is in fact higher than that for as-grown samples. The value of activation energies for as-grown and irradiated sample grown at higher growth temperature 510 °C (sample B) are much higher than those grown at 482 °C (sample C) and 450 °C (sample D) for both the low and high temperatures regimes. The low activation energies for samples C and D are probably the result of the low barrier for carrier transfer amongst QDs [31].

Table 7.6: Fitting parameters for the measured temperature dependent integrated PL intensities of as-grown and 30 kGy irradiated In_{0.52}Ga_{0.48}(Bi)As QDs grown at different temperatures: sample B (T_G=510 °C), sample C (T_G=482 °C) and sample D (T_G=450 °C).

InGa(Bi)As QDs grown with Bi flux	Growth Temperature (°C)	Irradiation Dose (kGy)	E1 (meV)	E2 (meV)
Sample B	510	0	55.05	55
		30	58.29	58.29
Sample C	482	0	31.5	9.1
		30	45.3	9.6
Sample D	450	0	33.12	6.3
		30	44.8	18.4

7.4 CONCLUSION

In summary, the effect of gamma radiation on the optical properties of self-assembled $\text{In}_{0.52}\text{Ga}_{0.48}\text{As}$ QDs grown by MBE on GaAs substrates at various growth temperatures with and without exposure to bismuth flux have been investigated using the PL technique. For sample A (grown without Bi), the main peak of the spectrum was from the dot luminescence at 1.354 eV at 10K with a sharp additional peak observed around 1.43 eV from the wetting layer. The effect of Bi as surfactant on the self-assembled $\text{In}_{0.52}\text{Ga}_{0.48}\text{As} / \text{GaAs}$ QDs has been also investigated. The PL intensity is improved by ~ 3.5 times by introducing Bi as a surfactant. A reduction of the PL peak energy of about 14meV was observed when the $\text{In}_{0.52}\text{Ga}_{0.48}(\text{Bi})\text{As}$ QDs were grown by using Bi as a surfactant (redshift of PL peak), indicating that Bi affects the size of QDs. This is also reflected in its PL intensity and FWHM. Therefore, Bi surfactant can be used to control the morphology of QDs and enhance their optical properties. According to the PL measurements, QDs grown with Bi as surfactant have a higher degree of size uniformity as evidenced by the narrower FWHM.

Furthermore, the effect of gamma radiation with different doses (30kGy and 50kGy) on the self-assembled $\text{In}_{0.52}\text{Ga}_{0.48}\text{As} / \text{GaAs}$ QDs has been also studied. The PL results show that for irradiation dose of 30 kGy, the QDs PL emission energy exhibit a blue shift by around 10 meV for sample A (grown without Bi), however, no blue shift is detected in the PL of QDs for sample B (grown with Bi surfactant). In addition, there are significant enhancements of the PL intensities of about 1.3 times and 1.5 times for sample A and sample B, respectively. Interestingly, the PL QDs and WL emissions disappeared after the irradiation dose increased to 50kGy

for sample A. In contrast, for sample B the PL QDs emission is still observed, however, its intensity is reduced by half. In general, gamma radiation treatment has better effect on the QDs sample grown under a Bi flux than the sample grown without Bi. In this case, the optimum irradiation dose seems to be 30 kGy, in terms of improvement of the PL intensity.

The influence of growth temperature on the optical properties of $\text{In}_{0.52}\text{Ga}_{0.48}(\text{Bi})\text{As}/\text{GaAs}$ QDs has been studied. It was observed that the QDs PL peak red-shifted when the growth temperature decreased from 510 °C to 450 °C. In addition, the effect of gamma radiation with different doses (30 kGy and 50 kGy) on the self-assembled $\text{In}_{0.52}\text{Ga}_{0.48}(\text{Bi})\text{As}/\text{GaAs}$ QDs grown at different growth temperatures has been investigated. For an irradiation dose of 30 kGy, there is a large enhancement in the QDs PL intensities by a factor of 1.5, 2.8 and 3 for sample B, C and D, respectively. However, when samples were irradiated at higher doses of 50 kGy, all samples exhibit a reduction in the QDs PL intensities of about 0.5 times, 1.5 times and 2.1 times for sample B, C and D, respectively. Furthermore, sample B (grown at 510 °C) has higher PL intensities for a gamma radiation treatment with 30 kGy and 50 kGy doses as compared to samples C and D.

Overall, the particular radiation dose of 30 kGy resulted in an improvement of the optical properties of all samples grown with Bi as a surfactant, as evidenced by a large increase in the QDs PL intensity after radiation. Furthermore, growth temperature of 510 °C was found to be optimal before and after exposed to gamma radiation in terms of optical efficiency.

REFERENCES

- [1] L. Asryan, M. Grundmann, N. Ledentsov, O. Stier, R. Suris, D. Bimberg, Maximum modal gain of a self-assembled InAs/GaAs quantum-dot laser, *Journal of Applied Physics*, **90**, 1666-1668 (2001).
- [2] K.A. Sablon, J.W. Little, V. Mitin, A. Sergeev, N. Vagidov, K. Reinhardt, Strong enhancement of solar cell efficiency due to quantum dots with built-in charge, *Nano letters*, **11**, 2311-2317 (2011).
- [3] S.F. Thomassen, T.W. Reenaas, B. Fimland, InAs/GaAs quantum dot density variation across a quarter wafer when grown with substrate rotation, *Journal of crystal growth*, **323**, 223-227 (2011).
- [4] J. Zribi, B. Ilahi, D. Morris, V. Aimez, R. Arès, Chemical beam epitaxy growth and optimization of InAs/GaAs quantum dot multilayers, *Journal of crystal growth*, **384**, 21-26 (2013).
- [5] A. Roshko, T.E. Harvey, B.L. Hyland, S.Y. Lehman, K.D. Cobry, Lateral variations in self-assembled InGaAs quantum dot distributions, *Journal of crystal growth*, **311**, 4109-4115 (2009).
- [6] B. Ilahi, L. Sfaxi, G. Bremond, H. Maaref, Tuning optical properties of high In content InGaAs/GaAs capped InAs quantum dots by post growth rapid thermal annealing, *Materials Science and Engineering: C*, **26**, 971-974 (2006).
- [7] S. Li, J. Bi, M. Li, M. Yang, M. Song, G. Liu, W. Xiong, Y. Li, Y. Fang, C. Chen, Investigation of GaInAs strain reducing layer combined with InAs quantum dots embedded in Ga (In) As subcell of triple junction GaInP/Ga (In) As/Ge solar cell, *Nanoscale Research Letters*, **10**, 1-6 (2015).
- [8] X. Zhang, S. Ganapathy, I. Suemune, H. Kumano, K. Uesugi, Y. Nabetani, T. Matsumoto, Improvement of InAs quantum-dot optical properties by strain

compensation with GaNAs capping layers, *Applied physics letters*, **83**, 4524-4526 (2003).

[9] A. Babiński, J. Jasiński, R. Bożek, A. Szepielow, J. Baranowski, Rapid thermal annealing of InAs/GaAs quantum dots under a GaAs proximity cap, *Applied Physics Letters*, **79**, 2576-2578 (2001).

[10] H. Zhao, A. Malko, Z. Lai, Effect of bismuth on structural and electrical properties of InAs films grown on GaAs substrates by MBE, *Journal of Crystal Growth*, **425**, 89-93 (2015).

[11] D. Guimard, M. Nishioka, S. Tsukamoto, Y. Arakawa, Effect of antimony on the density of InAs/Sb: GaAs (1 0 0) quantum dots grown by metalorganic chemical-vapor deposition, *Journal of crystal growth*, **298**, 548-552 (2007).

[12] K.K. Nagaraja, Y.A. Mityagin, M.P. Telenkov, I.P. Kazakov, GaAs (1-x) Bi x: a promising material for optoelectronics applications, *Critical Reviews in Solid State and Materials Sciences*, **42**, 239-265 (2017).

[13] S.K. Khamari, V. Dixit, T. Ganguli, S. Porwal, S. Singh, S. Kher, R. Sharma, S. Oak, Effect of ^{60}Co γ -ray irradiation on electrical properties of GaAs epilayer and GaAs p-i-n diode, *Nuclear Instruments and Methods in Physics Research Section B: Beam Interactions with Materials and Atoms*, **269**, 272-276 (2011).

[14] H. Alghamdi, A. Alhassni, S. Alhassan, A. Almunyif, A.V. Klekovkin, I.N. Trunkin, A.L. Vasiliev, H.V. Galeti, Y.G. Gobato, I.P. Kazakov, Effect of bismuth surfactant on the structural, morphological and optical properties of self-assembled InGaAs quantum dots grown by Molecular Beam Epitaxy on GaAs (001) substrates, *Journal of Alloys and Compounds*, **905**, 164015 (2022).

- [15] V. Preobrazhenskii, M. Putyato, B. Semyagin, Measurements of parameters of the low-temperature molecular-beam epitaxy of GaAs, *Semiconductors*, **36**, 837-840 (2002).
- [16] R.D. Richards, F. Bastiman, C.J. Hunter, D.F. Mendes, A.R. Mohmad, J.S. Roberts, J.P. David, Molecular beam epitaxy growth of GaAsBi using As₂ and As₄, *Journal of Crystal Growth*, **390**, 120-124 (2014).
- [17] M. Yoshimoto, K. Oe, Molecular beam epitaxy of GaAsBi and related quaternary alloys, in: *Molecular Beam Epitaxy*, Elsevier, 2018, pp. 197-209.
- [18] R.B. Lewis, P. Corfdir, H. Li, J. Herranz, C. Pfüller, O. Brandt, L. Geelhaar, Quantum dot self-assembly driven by a surfactant-induced morphological instability, *Physical Review Letters*, **119**, 086101 (2017).
- [19] A. Hospodková, J. Vyskočil, J. Pangrác, J. Oswald, E. Hulicius, K. Kuldová, Surface processes during growth of InAs/GaAs quantum dot structures monitored by reflectance anisotropy spectroscopy, *Surface Science*, **604**, 318-321 (2010).
- [20] A.D. Utrilla, D.F. Grossi, D.F. Reyes, A. Gonzalo, V. Braza, T. Ben, D. González, A. Guzman, A. Hierro, P.M. Koenraad, Size and shape tunability of self-assembled InAs/GaAs nanostructures through the capping rate, *Applied Surface Science*, **444**, 260-266 (2018).
- [21] T. Matsuura, T. Miyamoto, F. Koyama, Topological characteristics of InAs quantum dot with GaInAs cover using Sb surfactant, *Applied physics letters*, **88**, 183109 (2006).
- [22] D. Fan, Z. Zeng, V.G. Dorogan, Y. Hirono, C. Li, Y.I. Mazur, S.-Q. Yu, S.R. Johnson, Z.M. Wang, G.J. Salamo, Bismuth surfactant mediated growth of InAs quantum dots by molecular beam epitaxy, *Journal of Materials Science: Materials in Electronics*, **24**, 1635-1639 (2013).

- [23] D.F. Reyes, D. Gonzalez, F. Bastiman, L. Dominguez, C.J. Hunter, E. Guerrero, M.A. Roldan, A. Mayoral, J.P. David, D.L. Sales, Photoluminescence enhancement of InAs (Bi) quantum dots by Bi clustering, *Applied Physics Express*, **6**, 042103 (2013).
- [24] A.B.F. KHATAB, Optical properties of nanostructured semiconductors grown by MBE on non-conventional GaAs substrates, University of Nottingham. Nottingham, (2014).
- [25] C. Lobo, R. Leon, InGaAs island shapes and adatom migration behavior on (100),(110),(111), and (311) GaAs surfaces, *Journal of applied physics*, **83**, 4168-4172 (1998).
- [26] M. Hjiri, F. Hassen, H. Maaref, B. Salem, G. Bremond, O. Marty, J. Brault, M. Gendry, Optical properties of self-organized InAs nanostructures grown on InAlAs/InP (0 0 1), *Physica E: Low-dimensional Systems and Nanostructures*, **17**, 180-182 (2003).
- [27] R. Songmuang, S. Kiravittaya, M. Sawadsaringkarn, S. Panyakeow, O.G. Schmidt, Photoluminescence investigation of low-temperature capped self-assembled InAs/GaAs quantum dots, *Journal of crystal Growth*, **251**, 166-171 (2003).
- [28] Z.-Y. Xu, Z.-D. Lu, X. Yang, Z. Yuan, B. Zheng, J. Xu, W. Ge, Y. Wang, J. Wang, L.L. Chang, Carrier relaxation and thermal activation of localized excitons in self-organized InAs multilayers grown on GaAs substrates, *Physical Review B*, **54**, 11528 (1996).
- [29] B. Liang, Q. Yuan, L. Su, Y. Wang, Y. Guo, S. Wang, G. Fu, E. Marega, Y.I. Mazur, M.E. Ware, Correlation between photoluminescence and morphology for

single layer self-assembled InGaAs/GaAs quantum dots, *Optics Express*, **26**, 23107-23118 (2018).

[30] X. Chen, Y. Gu, Y. Ma, S. Chen, M. Tang, Y. Zhang, X. Yu, P. Wang, J. Zhang, J. Wu, Growth mechanisms for InAs/GaAs QDs with and without Bi surfactants, *Materials Research Express*, **6**, 015046 (2018).

[31] H. Alghamdi, Optical and structural properties of GaAsBi and InGaBiAs nanostructured semiconductors grown by Molecular Beam Epitaxy, in, University of Nottingham, 2020.

CHAPTER 8: CONCLUSIONS AND FUTURE WORK

This chapter summarises the research work carried out on (i) the structural and optical properties of dilute bismide III-V semiconductors alloys, namely GaAsBi epilayers grown at different growth temperatures on (100) GaAs substrates, and (ii) the photoluminescence characterisation of InGa(Bi)As/GaAs QDs grown on (100) GaAs planes. XRD, SEM, Raman, hole concentration and PL measurement techniques were used to investigate these alloys. Future work suggestions are also covered in this chapter.

8.1 GaAs_{1-x}Bi_x EPILAYERS

In summary, the influence of the growth temperature on the optical properties of GaAs_{1-x}Bi_x epilayers grown on (100) GaAs substrates by MBE has been examined. The PL measurements revealed that the PL spectra exhibit two distinct behaviours red and blue shifts depending on the growth temperature. The observed differences in PL peak position for different GaAs_{1-x}Bi_x growth temperatures could be attributed to strain and/or Bi-defect level-band related transitions. Indeed, the Bi composition in the studied samples grown at different temperatures were determined and calculated from PL measurements which demonstrated a red-shift and a blue-shift of the PL peak energy corresponding to an increase and a decrease in Bi content, respectively. From the SEM images it was observed that samples with the highest surface concentrations of droplets are those with the lowest concentrations of Bi, and this indicates that for these growth temperatures ($T_G=300$ °C, 310 °C and 365 °C) a lower concentration of Bi was incorporated into the GaAs structure. In contrast, the sample which had the highest concentration of bismuth was grown at 325 °C and has a lower number of droplets and self-aligned trailing

nanotracks on the surface. From Raman measurements it was observed that as the content of Bi increases first there is a slight redshift and then a blueshift of the LO phonon peak, which can be explained by the Bi-induced tensile and/or compressive stress. The temperature dependence of the PL spectra was also studied. It was found that the peak luminescence energy as a function of temperature is dependent on the incident excitation power. For example, the temperature dependence of PL peak energy has shown a pronounced S-shape characteristic at high laser excitation power, however, no evidence of the characteristic S-shape was observed under low laser power conditions. The integrated PL intensity as a function of inverse temperature indicated that two types of defects are present. The first is related to lattice disorder, while the second is related to Bi clusters. In this thesis, the effects of gamma (γ -) irradiation dose on the electrical and optical properties of dilute GaAsBi layers have also been investigated. After irradiation the samples exposed to gamma rays showed enhanced optical properties. Raman measurements demonstrated that the concentration of holes increased after gamma radiation. In addition, XRD data showed that the crystallographic quality of the samples was slightly worse after being exposed to gamma radiation. This finding agrees with the PL FWHM results, which demonstrated an increase of the FWHM after irradiation. This is due to the fact that radiation induces several types of defects, such as structural defects.

8.2 $\text{In}_x\text{GaAs}_{1-x}$ QUANTUM DOTS

In this part of the thesis, the effects of growth temperature (510 °C, 482 °C and 450 °C) and gamma (γ -) irradiation doses (30 kGy and 50 kGy) on the optical properties of InGa(Bi)As QDs grown by MBE on (100) GaAs substrates using Bi as a

surfactant were studied. The experimental results have shown that for irradiation dose of 30 kGy, the QDs PL emission energy exhibit a blue shift for samples grown without Bi, however, no blue shift is detected in the PL of QDs for samples grown with Bi surfactant. In addition, there are significant enhancements of the PL intensities for both samples (i.e. grown with and without Bi) after irradiation with 30kGy dose. Interestingly, the PL QDs and WL emissions disappeared after the irradiation dose increased to 50 kGy for samples grown without Bi (control samples). In contrast, the PL QDs emissions are still observed in the Bi mediated grown samples. Gamma radiation treatment has been found to have an enhanced effect on the optical properties of QDs samples grown under a Bi flux than the samples grown without Bi. In addition, the influence of gamma radiation on InGa(Bi)As/GaAs QDs grown at different substrate temperatures has been also studied. For an irradiation dose of 30 kGy, there is a large enhancement in all QDs PL intensities. However, when samples were irradiated at higher dose of 50 kGy, all samples exhibit a reduction in the QDs PL intensities. The optimum irradiation dose seems to be 30 kGy for all samples grown with Bi surfactant, in terms of improvement of the PL intensity. Furthermore, the growth temperature of 510 °C was found to be optimal in terms of optical efficiency for non-irradiated and irradiated samples grown at this temperature.

8.3 FUTURE WORK SUGGESTIONS

One of the significant advances in semiconductors material engineering is the growth of epitaxial layers on high-index planes. This technique offers an additional degree of freedom to the conventional (100)-grown devices. There are many interests in investigating semiconductor structures epitaxially deposited on non-

(100) planes including growth, optical and electrical properties. However, while most investigations of heterostructures were carried out using the conventional (100) GaAs substrates, there are few studies in comparison that explored non-conventional planes [1, 2, 10, 11]. It is important to point out that semiconductor structures grown on high index GaAs substrates have improved properties as compared to those of similar structures grown on conventional (100) GaAs oriented substrates. These include optical anisotropy [1], high hole mobility [2] and improved optical efficiency [3].

The following suggestions for future research are made based on the experimental results obtained in this thesis and the use of novel index surfaces.

- (i) Although most investigations of $\text{GaAs}_{1-x}\text{Bi}_x$ thin films and devices were performed using the conventional (100) GaAs substrates, there are few studies that explored the growth on high-index planes, which can considerably affect the Bi incorporation into the GaAs host lattice, and the structural, electrical and optical properties of the epilayers [4-8]. Remarkably, Henini et al have shown that Bi incorporation in $\text{GaAs}_{(1-x)}\text{Bi}_x$ thin films can be more enhanced by using (311)B GaAs orientation [4]. However, the effects of substrate orientation and gamma radiation on the structural and optical properties of $\text{GaAs}_{(1-x)}\text{Bi}_x$ alloys grown at different substrate temperatures using non-(100) GaAs planes have not been investigated yet. Therefore, it will be worthwhile to carry out a systematic study to investigate the effects of non-conventional (i.e. non-(100) planes) high-index GaAs substrates and gamma irradiation on the structural, optical and electrical properties of dilute GaAsBi thin epilayer films. The goal of this research would be to determine which

material could be the most suitable for high-performance ionizing radiation detectors. It would also be interesting and important to investigate the effect of different sources as well as different doses of irradiation on these materials. The purpose of this investigation would be to determine whether or not materials and devices based on dilute bismide III-V semiconductors are suitable for use in space applications such as satellite communications.

- (ii) In order to improve the structural, optical and electrical properties of III-V materials and the devices' performance, it is important to understand the nature of the defects introduced by Bi and how to reduce and/or eliminate them. It is common knowledge that the heat treatment process reduces the concentration of defects and/or eliminate completely defects. As a consequence of this, the structural, electrical, and optical properties of materials and devices will be enhanced [9]. In fact, a number of studies have demonstrated that subjecting $\text{GaAs}_{1-x}\text{Bi}_x$ materials to post-growth thermal annealing improves both their structural and optical properties [10-13]. However, the effect of Rapid Thermal Annealing (RTA) at different annealing temperatures on self-assembled InGa(Bi)As QDs using Bi as surfactant has not been investigated yet. Therefore, it is important to perform optical measurements to investigate the annealing effects on InGa(Bi)As QDs in order to improve the quality of the material and understand the effect of these defects on the performance of future devices based on these materials systems.

- (iii) For self-assembled InGa(Bi)As QDs structures, it is worth performing further studies by growing similar nanostructures under the same growth conditions on high index (non-(100) planes) GaAs substrates. This could provide further information on the effects of high index GaAs planes and Bi as surfactant on InGaAs QDs nanostructures. This investigation might help improve the quality and efficiency of semiconductor-based nanostructures needed for future applications in electronic and optoelectronic devices. It is expected that these new bismide-based III-V semiconductor materials will attract a lot of attention from both academia and industry interested in fundamental material research and practical device applications [14, 15].

REFERENCES

- [1] R. Nötzel, Self-organized growth of quantum-dot structures, *Semiconductor Science and Technology*, **11**, 1365 (1996).
- [2] A. Davies, J. Frost, D. Ritchie, D. Peacock, R. Newbury, E. Linfield, M. Pepper, G. Jones, The growth and physics of high mobility two-dimensional hole gases, *Journal of crystal growth*, **111**, 318-322 (1991).
- [3] M. Henini, A. Polimeni, A. Patanè, L. Eaves, P. Main, G. Hill, Effect of the substrate orientation on the self-organisation of (InGa) As/GaAs quantum dots, *Microelectronics journal*, **30**, 319-322 (1999).
- [4] M. Henini, J. Ibáñez, M. Schmidbauer, M. Shafi, S. Novikov, L. Turyanska, S. Molina, D. Sales, M. Chisholm, J. Misiewicz, Molecular beam epitaxy of GaBiAs on (311) B GaAs substrates, *Applied Physics Letters*, **91**, 251909 (2007).
- [5] P.K. Patil, F. Ishikawa, S. Shimomura, GaAsBi/GaAs MQWs MBE growth on (411) GaAs substrate, *Superlattices and Microstructures*, **100**, 1205-1212 (2016).
- [6] G. Prando, V.O. Gordo, J. Puustinen, J. Hilska, H. Alghamdi, G. Som, M. Gunes, M. Akyol, S. Souto, A. Rodrigues, Exciton localization and structural disorder of GaAs_{1-x}Bi_x/GaAs quantum wells grown by molecular beam epitaxy on (311) B GaAs substrates, *Semiconductor Science and Technology*, **33**, 084002 (2018).
- [7] J. Rodrigo, D. Sales, M. Shafi, M. Henini, L. Turyanska, S. Novikov, S. Molina, Effect of annealing on the structural and optical properties of (3 1 1) B GaAsBi layers, *Applied Surface Science*, **256**, 5688-5690 (2010).
- [8] J. Steele, R.A. Lewis, M. Henini, O. Lemine, A. Alkaoud, Raman scattering studies of strain effects in (100) and (311) B GaAs_{1-x}Bi_x epitaxial layers, *Journal of Applied Physics*, **114**, 193516 (2013).

- [9] S. Alhassan, Investigation of structural, electrical and optical properties of doped dilute GaAsBi grown by molecular beam epitaxy, in, University of Nottingham, 2022.
- [10] H. Alghamdi, V.O. Gordo, M. Schmidbauer, J.F. Felix, S. Alhassan, A. Alhassni, G.A. Prando, H. Coelho-Júnior, M. Gunes, H.V.A. Galeti, Effect of thermal annealing on the optical and structural properties of (311) B and (001) GaAsBi/GaAs single quantum wells grown by MBE, *Journal of Applied Physics*, **127**, 125704 (2020).
- [11] P.C. Grant, D. Fan, A. Mosleh, S.-Q. Yu, V.G. Dorogan, M.E. Hawkrige, Y.I. Mazur, M. Benamara, G.J. Salamo, S.R. Johnson, Rapid thermal annealing effect on GaAsBi/GaAs single quantum wells grown by molecular beam epitaxy, *Journal of Vacuum Science & Technology B, Nanotechnology and Microelectronics: Materials, Processing, Measurement, and Phenomena*, **32**, 02C119 (2014).
- [12] O. Lemine, A. Alkaoud, H.A. Galeti, V.O. Gordo, Y.G. Gobato, H. Bouzid, A. Hajry, M. Henini, Thermal annealing effects on the optical and structural properties of (1 0 0) GaAs_{1-x}Bi_x layers grown by molecular beam epitaxy, *Superlattices and Microstructures*, **65**, 48-55 (2014).
- [13] H. Makhoulfi, P. Boonpeng, S. Mazzucato, J. Nicolai, A. Arnoult, T. Hungria, G. Lacoste, C. Gatel, A. Ponchet, H. Carrère, Molecular beam epitaxy and properties of GaAsBi/GaAs quantum wells grown by molecular beam epitaxy: effect of thermal annealing, *Nanoscale Research Letters*, **9**, 1-5 (2014).
- [14] L. Asryan, M. Grundmann, N. Ledentsov, O. Stier, R. Suris, D. Bimberg, Maximum modal gain of a self-assembled InAs/GaAs quantum-dot laser, *Journal of Applied Physics*, **90**, 1666-1668 (2001).

[15] K.A. Sablon, J.W. Little, V. Mitin, A. Sergeev, N. Vagidov, K. Reinhardt, Strong enhancement of solar cell efficiency due to quantum dots with built-in charge, *Nano letters*, **11**, 2311-2317 (2011).